Wetting heterogeneities in porous media

Insights from experiments on the displacement of immiscible fluids

Dissertation
for award of the degree
"Doctor rerum naturalium" (Dr. rer.nat.)
at the Georg-August-Universität Göttingen

within the doctoral program Chemistry
of the Georg-August-University School of Science (GAUSS)

submitted by
Julie Lynette Murison

Göttingen, 2013

Supervisors
Dr. Matthias Schröter (MPIDS Göttingen)
Prof. Dr. Götz Eckold (Univ. Göttingen)
Prof. Dr. Stephan Herminghaus (MPIDS Göttingen)

Members of the Examination Board
Referentin: Prof. Dr. Götz Eckold
Koreferent: Prof. Dr. Stephan Herminghaus

Further members of the Examination Board
Prof. Dr. Martin Sauter (Univ. Göttingen)
Dr. Jean-Christophe Baret (MPIDS Göttingen)
Prof. Dr. Philipp Vana (Univ. Göttingen)
Prof. Dr. Michael Buback (Univ. Göttingen)

Date of the thesis defense: .....

Abstract

Multiphase flow in porous media is an important process for many technical and environmental applications such as fuel cells, oil recovery, CO_2 storage among others. Understanding the rules that govern these flows is essential for planning of CO_2 storage sites, chemical or nuclear waste sites, predicting the viability of new oil reservoirs and preventing contamination of ground water aquifers. Natural porous samples, i.e rocks and soils, have highly heterogeneous pore space, both in geometry and wettability. This complicates experiments on such samples as there is no simple method of characterisation. While it is long known that the wettability of the substrate strongly influences the immiscible flow properties this effect, and in particular the effect of heterogeneous wettability, is poorly characterised.

In this work the first experimental investigation of the domain size of wetting heterogeneities in bead packs is presented, and the effect of these domains on immiscible fluid displacement is discussed. This was accomplished by creating bead packs which had the same overall surface coverages of oil and water wet regions, but differed in the spatial extensions of these domains.

The immiscible flow of water and oil through these samples was characterised by measuring the capillary pressure saturation curve for each type of sample. It was determined that the capillary hysteresis varied monotonically with the spatial extension of the wetting heterogeneities. To relate this measurement to the flow behaviour the invading liquid fronts were then imaged using X-ray microtomography. The front shapes were found to depend on the wetting domain sizes of the samples, with globally smooth fronts obtained for samples with small wetting heterogeneities. Both of these observations can be related to the dissipation of energy of the flow through the medium and it is found that the size of the wetting heterogeneity can control the flow properties.

The lengths scales of the heterogeneities discussed here range from sub-pore to many pores, and in this range are found to be important. However, this is not necessarily true for very small heterogeneities. Towards this goal proof of concept experiments describing how to prepare surfaces with microscopic wetting heterogeneities using polymer brushes are discussed. Polymer brush modified surfaces were also tested as a surface exhibiting stimuli-sensitive wettability.

Contents

Chapter 1

Introduction

1.1 Multiphase flow in porous media

Multiphase flow in porous media can be found everywhere. It is of high importance in energy production, for example in fuel cells [1–3] where hydrogen and oxygen need to be separately delivered to the electrodes, in the presence of water through a polymer electrolyte membrane (PEM). Multiphase pore displacements are also the central principle behind oil recovery [4–8]. The classic picture of drilling a hole in the ground, and creating a geyser of black gold, is pretty far from the truth. Primary oil recovery factors, that is the oil which can be spontaneously recovered, or pumped out as a single fluid are fairly low, with up to 90% of the oil remaining trapped in the reservoir [6, 9]. More commonly oil recovery involves pumping water into the reservoir rock to force the oil out, and the interactions of these two immiscible phases with the rock, determine the amount of extracted oil.

Understanding how two immiscible fluids move through porous media, such as soils or rocks is essential to prevent or ameliorate environmental damage such as ground water contamination [10]. Underground water supplies, or aquifers are porous rock filled with water. These can become contaminated when organic materials, which are used commonly in industry such as chlorinated solvents or alkanes, move through the rock. Understand the mechanisms which govern the transport of these substances can be used to prevent contamination or leakage from a storage site. This is even more important when designing sites for underground storage of chemical and nuclear waste [11]. Underground storage is a hot topic, and there is ever more pressure for CO_2 capture and storage methods to be implemented [12]. Long term, underground storage of CO_2 relies on first, being able to transport the CO_2 into the rock, and secondly trapping it there with minimal leakage. The ability to do both these things requires an understanding of the interactions between the fluid and the rock [13, 14].

The occurrence of extreme weather events such as droughts and flooding puts more pressure on finite clean water supplies. Furthermore, the increasing global population requires new sanitation solutions, particular in developing regions where resources are scarce. Ef-

forts to recycle and decontaminate water, either for drinking, or release back into the natural environment, require enhanced separation and cleaning processes [15]. Filtration methods are ideally suited for these applications, as they are technologically simple to employ, but the currently available filter materials are often not durable to oil water mixtures [16]. Understanding the interaction between the filter materials and the multiple components of the liquid mixtures being separated will allow design of better materials [16, 17], with enhanced separation abilities, and longer lifetimes.

All of these processes, from design of fuel cell membranes, to ensuring the safety of underground chemical storage sites, to optimising oil recovery, share a complexity arising from the interplay between the fluids and the matrix through which they flow. The relative strengths of the interactions of the fluids with the surfaces are called wettability. In the most simple terms, a liquid that spread on a solid surface to form a film, wets the surface. For this liquid, the surface is said to be wettable. In the lab, this is measured by the contact angle a droplet sitting on a surface makes. If the angle is less than 90°, the surface has a high wettability towards that liquid, and if the angle is above 90°, the liquid is non-wetting. Measuring wettability on porous samples is explained in detail in chapter 2. Despite the environmental, and technical importance of these processes, multiphase flow behaviour is poorly characterised [4]. It is known that the wettability of the of the substrate is a major control parameter for multiphase flow [18–22], but this effect is not well understood. Furthermore, porous samples with locally varying wettabilities, i.e partially oil wet, partially water wet, are even less well studied.

Due to the complex nature of the natural samples (rocks, soils and sands) flow experiments performed directly on samples 'from the ground' give diverse results on the wettability conditions required for optimum oil recovery [23]. This is most likely due to poor characterisation of the samples. Natural samples, such as soils, aquifers, or oil reservoirs are known to have large variations in wettability linked to chemical heterogeneities of the rocks or pore space [24–26]. These samples are very complicated, comprised of many materials with different textures, sizes and wettabilities and often require multiple methods for characterisation. Combinations of techniques such as Focussed Ion Beam Scanning Electron Microscopy (FIB-SEM) [27, 28], Environmental Scanning Electron Microscopy (ESEM) [29] and Chemical Force Microscopy (CFM) [25], allow detailed characterisation of the geometry and mineral compositions of small areas of the sample (on the $\sim \mu$m scale). Figure 1.1 shows an example of a chalk sample analysed by Hassenkam and co workers [25], extracted from a reservoir site in the North Sea. The sample displays a high degree of heterogeneity, both physically (shape, roughness), as can be seen by the SEM image, and in wettability, as can be seen in the chemical force map. In highly heterogeneous systems, e.g. carbonate rocks [30] and in general all natural porous

media, characterising the distribution of water and oil wetting surfaces in large enough[1] volumes such as those used in a typical core-flood experiment (on the ∼10 cm scale) would require exhaustive time scales and effort.

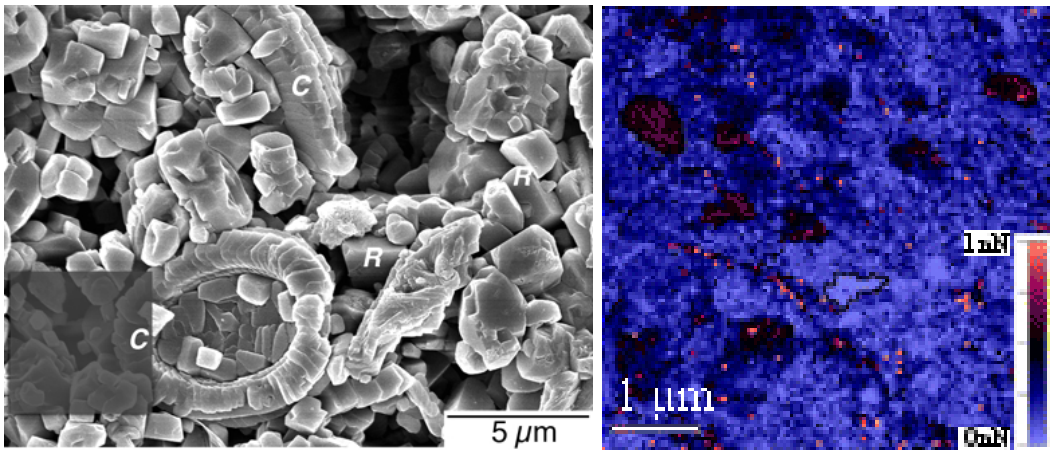

Figure 1.1: Left: Chalk sample from the North Sea shows both geometrical heterogeneity measured by SEM and, Right: chemical heterogeneity, measured using AFM- chemical force mapping shows on the chalk surface hydrophilic regions in blue and hydrophobic regions in red. As can be seen in this figure, the typical sizes of the hydrophobic patches are considerable smaller than a pore. Images reproduced from [25].

Standard laboratory classifications of wettability, i.e contact angle measurements, are not easily applicable to these kinds of samples, and instead the wettability is either guessed [32,33], or estimated from water absorption or permeability measurements [7,34,35]. It is very difficult to isolate the pertinent parameters of these substrates, to determine which properties dictate the flow behaviour.

In order to reduce the complexity of these samples into a few computationally manageable parameters, the general theoretical and numerical approaches use treatments based on average properties of the rock. These simplified approaches also allow for continuum models for two phase flow to be upscaled from the micrometre to the centimetre, and even kilometre length scales to be used for predictive purposes. These simplifications, of the wetting heterogeneities, homogenise different surface energies, or wettabilities, into an average value, either across the whole sample or across several pores [36, 37]. Results from such approaches would suggest that it is the average wettability which controls the flow and a detailed description of the heterogeneities is not required.

However, numerical studies on geometrically heterogeneous models, report that fluid displacement profile obtained from fully described heterogeneous models, are very different from the profile predicted from the averaged sample properties, and that the specific nature of the

[1] 'Large enough' volumes refers to volumes on which the statistical fluctuations in the experiments due to the random nature of porous media are small enough that the flow experiments can be performed with statistically relevant results. This is also referred to as the representative elementary volume (REV) [31]

heterogeneity (size, connectivity, etc.) notably changes the result [38]. Until now, there has been no systematic study of wetting heterogeneities in porous media, and not much attention has been paid to the spatial distributions of wetting patches. Considering the size of these projects (oil reservoirs, ground water aquifers, CO_2 storage, nuclear waste depositories), and the potentially enormous consequences of inaccurate predictions, a more complete description of multiphase flow behaviour is imperative. This thesis describes an experimental investigation to address the impact of wetting heterogeneities in porous media with the aim to contribute to the long-standing need for accurate predictive theories of multiphase flow in porous media [4, 39, 40].

1.2 Previous work on mixed wettability

Experimentally, there are two typical approaches to investigating mixed wettability: the *top down* approach, where experiments are performed directly on natural systems, such as sandstones; or the *bottom up* approach where simplified models, usually bead packs, are used to isolate specific features of interest. Figure 1.2 shows x-ray tomography images of a reservoir sandstone imbibed with oil and water, and a bead pack containing the same liquids. These two samples highlight the differences between the *top down* (complicated real rock samples) and *bottom up* (simple, controlled models) approaches.

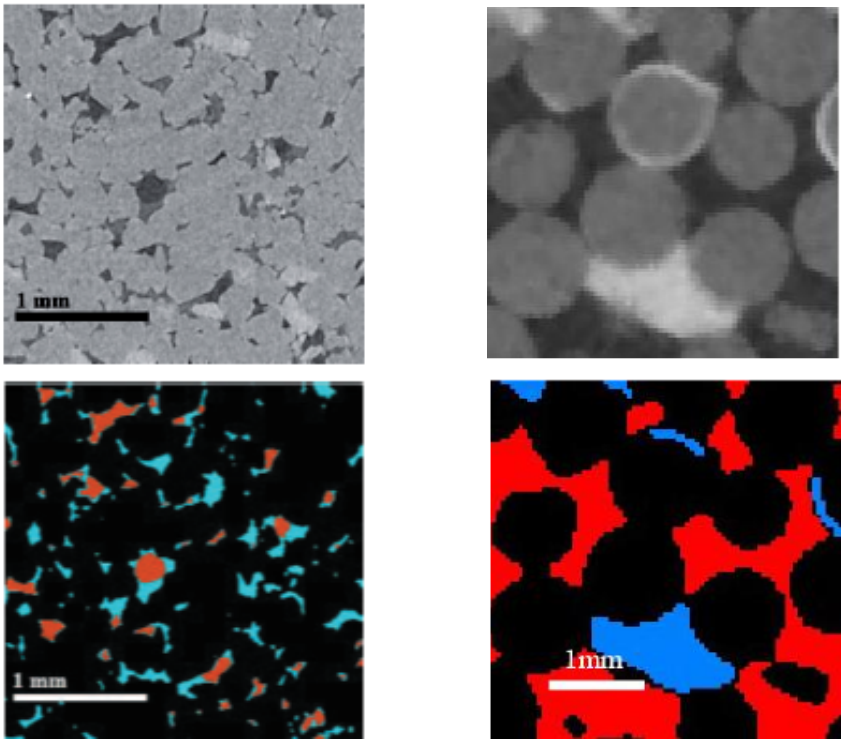

(a) real rock sample (b) bead pack

Figure 1.2: X-ray tomography images, with segmented water (blue) and oil (red) phases shown below for (a) a reservoir rock sample, figure reproduced from [41] and (b) a packing of monodisperse glass beads.

Top down

In top down experiments the focus is to find optimal strategies, for example for efficient oil recovery, based on the analysis of 'real' samples (soils, sands and rocks). What can be seen from figure 1.2 (a) is that even in a small area, there is a wide range of pore sizes, with very different shapes. The distribution of oil (red) and water (blue) inside the pore space suggests there might be a wettability variation, even within single pores. By pumping fluids

in and out of a rock or soil sample and measuring the fluxes and pressures obtained the sample characteristics (i.e average wettability, porosity) can be derived. This measurement is called a capillary pressure saturation curve and is explained in detail in chapter 2. These experiments are typically slow with time scales of weeks per measurement [23, 42]. The low throughput restricts the testing of different conditions, and furthermore relies on the hypothesis that the sample is a representative part of the rock, an assumption that might be flawed in heterogeneous natural systems. Even when samples can be extracted from the area of interest, i.e an oil reservoir or geological storage sight, contamination of these core samples by drilling fluids, and changes in pressure and temperature, often, if not always, lead to systematic errors. The mircoscale distributions of wettability in such systems are unknown [43]. Most oil reservoirs have wettabilities which change from pore to pore, and even on the sub-pore scale due to chemical heterogeneities [4], but there is not yet a technique used to map the wettability pore by pore inside a core. Rather, wettability is inferred from core flooding experiments, and comparisons with numerical simulations. To conclude, at this point in time, the top down approach is simply not applicable to study samples with mixed wettabilities.

Bottom up

In the bottom up approach, model systems are designed and tailored to study the influence of specific parameters of the sample on the flow properties. Two dimensional models of porous media used to experimentally study wettability effects include microfluidic chips [21, 44, 45]. In three dimensions the simplest model porous media, the homogeneous bead pack (as shown in figure 1.2 (b)), is well studied [7, 8, 19, 23, 46–52], even in microgravity [53]. The densest monodisperse beak packs have porosities on the order of 35%, as opposed to consolidated stones, and polydisperse sands and soils, which have much lower porosities. In order to achieve more realistic porosities sintered bead packs have been studied [54], but to the best of my knowledge there have been no studies on sintered packs with mixed wettability. Early work (1959) by Fatt and Klikoff [55], compared experiments with completely water wet beads, samples with a 1:1 mass ratio of oil to water wet beads and a sample with the same ratio of wettability (50% oil wet, 50% water wet), but only the smaller beads were made oil wet. Packings of these beads were filled with water which was then sucked out using an increasing pressure ramp. The results from this experiment are shown in figure 1.3. The shape of the curves for the water wet, and 50% oil wet sand are similar, the major difference being a shift in the pressure at which the water could be sucked out of the packing. The curve for the sample with correlation size and wettability heterogeneity is however completely different, with a notably higher amount of water remaining in the packing even at high water pressures. This observation has been, however, largely ignored by subsequent experimentalists. Instead introducing mixed wettability into simple models has been dealt with almost exclusively by

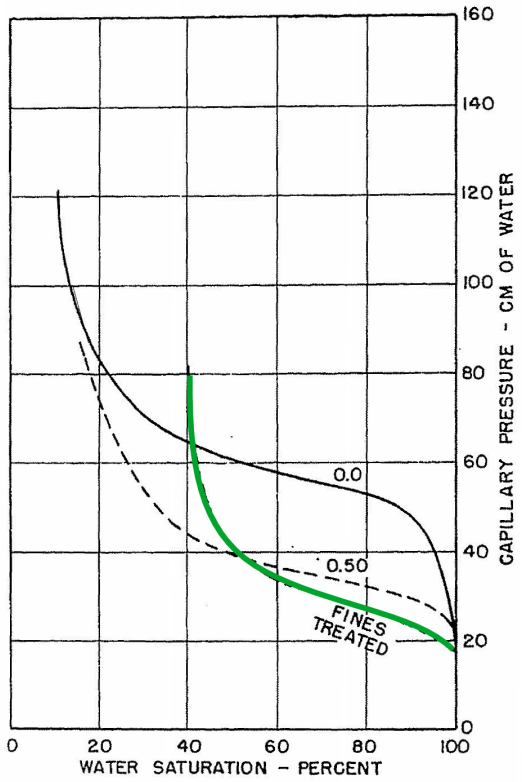

Figure 1.3: Capillary Pressure Saturation curve showing the amount of water sucked out of a packing of beads at different pressures reproduced from [55]. The solid black line represents untreated glass beads (completely water wet). The dashed line shows the curve obtained for the 1:1 oil:water wet beads. The green line, labelled fines treated, shows the curve obtained for a sample with only small oil wetting beads. For a more detailed explanation of this type of measurement see chapter 2.

mixing two kinds of chemically treated monodisperse spheres in different ratios [36,37,42,56–58].

Based on these experiments it has been found that the variations due to mixture composition can be explained by considering the effective wettability of the sample as the average contact angle of the sample [36,37,56]. DiCarlo, Sahni and Blunt [42] worked towards creating samples with the distribution of oil and water wet surfaces more representative of oil reservoirs by ageing bead packs partially saturation with crude oil. The idea being that the surfaces in contact with the oil would experience a wettability change. [29]. Using x-ray imaging of the fluid distributions relative permeabilities of oil and water were measured. However, no strong differences between this 'realistically wet' sample the homogeneous mixture of oil wetting and water wetting sand were observed. It should be noted that they were not able characterise to the spatial distribution of the different wetting surfaces. The composition of the fluids used to modified the 'realistically wet' sand pack was 80% crude oil, 20% brine. At these concentrations, both phases would be percolated [59]. This means that there are continuous

pathways of both oil wetting and water wetting pores, and not mixed wettability within a single pore. This perhaps explains why no difference between the 'realistically wet' simple mixture of oil wetting and water beads, which contains the same bi-continuous paths, and the 'realistic scenario' was observed.

Numerical modelling

Complimentary to the experimental studies there has also been a large effort to understand pore-scale fluid displacements numerically. The typical numerical approach for modelling flow inside porous media uses pore-throat models to represent the porous media. Pore-throat models are created by fitting the largest possible sphere inside a pore space, and connecting it to the surrounding pores by the largest possible cylinders which fit through the connecting gaps. A representation of this, for a bead pack is shown in figure 1.4.

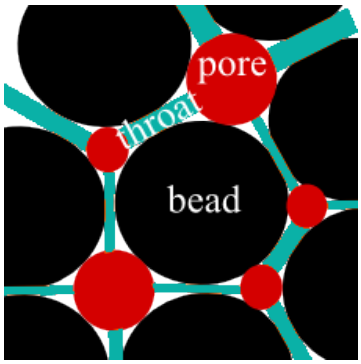

Figure 1.4: A 2D representation of a pore-throat model. The pore space is characterised by the largest sphere (red) which fitted inside a pore space, and is connected to neighbouring pores by the throats, which are characterised as the largest cylinders (green) which can fit between the beads (black).

These models can be created from x-ray tomography images of natural samples, and numerical models with the exact size distributions of the pores and throats can be created. Examples of this method are numerous in the literature [60–68]. An example of the complicated structures which can result from the pore-throat network construction from real rock samples, created by Zhao and Blunt [61], is shown in figure 1.5.

Pore throat networks capture the geometry of the sample, but the wettability information, which cannot be extracted from such tomography images, has to be artificially added to the networks. One way of doing this is individually labelling the pores as oil or water wet. The results from simulations of flow on such networks suggest that the factor which affects the flow behaviour is it is the number of preferentially oil wet pores, and not the strength of the oil-rock interaction [61]. The authors conclude that the pore structure plays a minor role compared to average wettability. However the fact that it is number of pores, and not total average contact angles which dictate permeabilities could also be interpreted that it is wetting heterogeneities, specifically wetting boundaries, and not average wettability which dictate flow

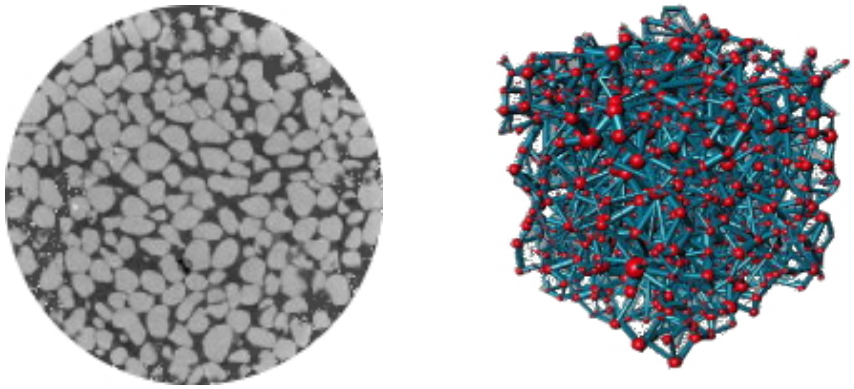

(a) natural sand sample (b) pore-throat network model

Figure 1.5: Example of (a) x-ray tomography image of unconsolidated natural sand and (b) the pore throat model constructed from the 3D image volume. Images were reproduced from [61].

properties. Numerical modelling of mixed wet systems where there is a correlation between pore size and pore wettability have shown that standard industry wettability classification can be significantly off [67] and wetting domain sizes might play a significant role at low capillary numbers [66]. While indicating that length scale is indeed important, to date there has been no systematic study of wetting heterogeneities, in particular to the spatial arrangements of wetting and non wetting surfaces.

State of the art experiments

Both top-down and bottom-up experimental studies are being re-invigorated by new imaging techniques, afford by major recent advances in imaging technology. These techniques, such as X-ray tomography [5, 31, 41, 51, 64, 69], MRI [28, 70, 71] and confocal microscopy [9, 72–74] are allowing ever better imaging of dynamic flow inside the porous media. These experiments are shedding new light on multiphase flow in confined environments, challenging old paradigms about classical flow properties [5] and potentially changing accepted view on these systems. These studies however, focus on the effects of geometry, and how to model geometric heterogeneities [9, 74]. Such an effort is also required to understand how wettability effects immiscible flow.

1.3 Heterogeneous wettability and the LoSal effect

Further complicating the effects of heterogeneous and unknown wettability inside reservoir rocks is the observation that the interaction between the rock/oil/water interface depends also on the salt concentration in the aqueous phase [75–77]. Typically, secondary oil recovery processes are achieved by flooding oil wells with sea water. However, empirically it has been observed that when low salinity water is used, more oil can be released from the rock. This is known as the LoSal effect. The explanation for the increase in oil recovery is a local shift in contact angle at the rock surface towards more water wetting surfaces in the presence of the low salinity water. While there has been a large effort to describe the molecular mechanisms for how this can occur [78–81], the physical mechanisms for droplet release due to such a contact angle change remain unclear. Investigation into larger scale experiments, where multiple ganglia can be trapped, visualised and released are limited by the lack of suitable coatings for bead packs which exhibit a wettability shift in the presence of salt.

1.4 Aims of this work

The open questions regarding the effect of mixed wettability in porous media can be summarised into the following four main questions:

- What is the effect of pore scale wetting heterogeneities on the sample scale flow properties?
- What are useful model porous media systems to investigate this?
- Is there a model surface which mimics the LoSal effect?
- What are the implications for natural systems?

This thesis addresses the above mentioned open questions. This work presents the first experimental study on the role of wetting heterogeneity domain size in mixed-wet bead packs by measuring the wetting characteristics and structure of invading liquid fronts inside heterogeneously wettable porous media. The methods used to measure wettability and image the liquid fronts are explained in chapter 2.

Chapter 3 describes the preparation of mixed wet model systems to investigate the role of heterogeneous wettability. The model samples were designed such that the average wettability of the different samples is kept constant, but the spatial extension of the heterogeneities is systematically varied, from sub-pore scale to clusters of several beads. In this way the effect of the spatial variations can be studied independent of differences in global wettabilities, unlike approaches based upon initial oil saturations [42, 66].

Once the models were created and tested, the effect of the pore scale wetting heterogeneities on the sample scale flow properties was investigated, and the effects of the sizes of the wetting and non-wetting patches on the bead surfaces quantified. Chapter 4 explains the experimental approach used: the measurement of capillary pressure saturation curves. These experiments measure the critical sample scale characteristics on dense bead packs on the centimetre scale. To understand how this impacts the two phase flow properties these experiments are combined with X-ray microtomography where the liquid front of the invading fluid is imaged. The results of the pore structure on the overall flow properties and the effects on the trapped ganglia are described in chapter 5.

This approach will provide guidelines to describe accurately heterogeneous wettabilities in a porous medium, a prerequisite for efficient up scaled models from the pore to reservoir scale. Full mapping of the wetting domain size from much smaller than a pore, to much larger than a pore, in combination with numerical simulations can be used to 'back-characterise' natural, complex samples leading to more accurate predictive modelling. In order to determine the extent of the effects of wetting heterogeneities, methods to produce such heterogeneities on the very small scale are discussed in chapter 6.

Finally, to move towards ever more realistic models for natural systems, and in particular a model surface to mimic the LoSal effect, surfaces are prepared with coatings which react to the surrounding fluid environment. Such systems, with stimuli-sensitive wettability, could potentially be used to investigate droplet remobilisation inside be packs, in order to better understand the LoSal effect. The preparation of stimuli-sensitive surfaces are presented in chapter 6.

Chapter 2

Methods

This chapter describes the general methods used for the experiments and analysis. As this body of work deals with wetting heterogeneities, the wettability must be measured. Ways in which this can be achieved are discussed in section 2.1. The goal of this work is to understand wetting effects in porous media, therefore it is imperative that the wettability of a porous sample can be quantified. This is achieved using capillary pressure saturation curves which measure the global wettability of bead packs. This type of measurement is explained in section 2.2.

To understand the collective properties of the samples used in these experiments, and to visualise what is happening inside them, x-ray tomography imaging is used. A general description of how this works is provided in section 2.3. Finally to extract physical data from the images a series of image processing steps are used. The general work flow is described in section 2.4.

2.1 Measuring wettability

As illustrated in chapter 1 a systematic investigation into the effects of wettability of two phase flow is required. The first question then, is how to measure wettability. This chapter outlines the common approaches used to measure wettability, starting from a flat surface and then moving into porous samples.

2.1.1 Measuring wettability on a flat surface

Wettability is the term used to classify relative strengths of interactions between two fluids and a solid. In simplest terms is refers to the tendency of a fluid to spread on, or wet, a solid surface, displacing the second surrounding fluid, (often referred to as the ambient phase). The natural way to quantify the wettability of a planar surface is to measure the contact angle the interface makes with the solid (fig. 2.1). This angle corresponds to the mechanical

equilibrium between the two fluids and the solid surface. On an ideal surface this angle can be related to difference in surface energies of the solid when in contact with different fluids and is called the Young's contact angle. The Young's contact angle corresponds to the global energy minimum between the three phases in contact. However, due to imperfections (chemical and physical) on real surfaces, experimentally what is measured is the apparent contact angle, which corresponds to a local energy minimum. If the liquid spreads completely over the surface, that is has a contact angle of 0° it is said to wet the surface. Liquids which make a contact angle of more than 30° but less than 90° are said to partially wet the surface, and if the contact angle is greater than 90° the liquid is said to be non wetting.

Contact angles are typically measured using sessile drops, or the captive bubble technique [82]. Both these techniques measure the static contact angle, which in the ideal case (i.e perfect surfaces), also represents the equilibrium configuration of the three phases. When the two fluids used are water, for the drop phase, and air for the ambient phase, the wetting behaviour of the surfaces is referred to as hydrophilic (wetted by water) or hydrophobic (non wetted by water). Clean glass surfaces are hydrophilic, and water droplets which are deposited on top of them will spread. This is not true of dirty glass, e.g a window, where adsorbed organic compounds change the wettability of the surface. A common hydrophobic surface is Teflon, such as a non-stick frying pan, which is not wetted by either water or oil, and is also oleophobic.

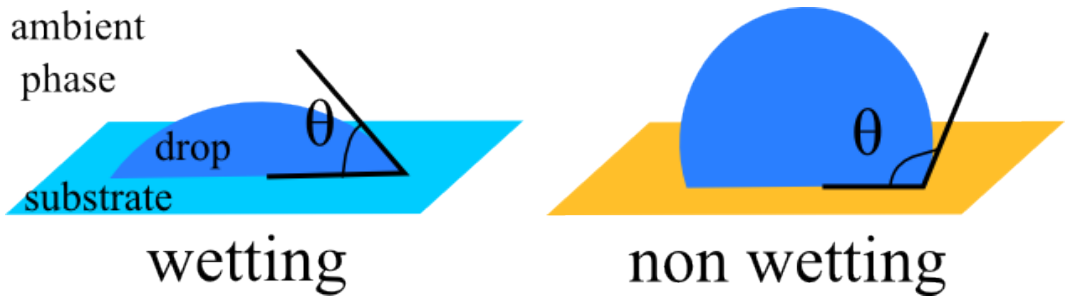

Figure 2.1: Cartoon showing the Young's contact angle for a droplet sitting on top of a partially wetting (left) and non-wetting (right) surface. The wettability is classified by the internal angle the droplet makes with the surface.

The wettability of a surface is dependant on the surface structure, both the chemical and physical composition. A film of organic components on a glass surface can render it hydrophobic, for example a self assembled monolayer a silane on glass, or a thiol on a gold surface. In this thesis films of chlorotrimethylsilane (CTMS) were used to modify glass surfaces. On a flat surface, CTMS monolayers will give a contact angle between air and water of 90° - 100° [83, 84] depending on the film quality. Another common method, and the other method used in this work, of creating hydrophobic surfaces is first coating the substrate with a thin layer of gold, or silver, and then forming a self assembled alkylthiol film. Films created

with hexadecanethiol on gold have contact angles between air and water of approximately 110° [85–87].

Wettability of the substrate does not only depend on the chemical composition of the surface, but also the physical composition. Surface roughness is known to play a large role in the observed contact angle. Theoretical treatments of surface roughness include the Wenzel model [88] which describes the situation when the film really wets the whole surface and the Cassie model [89] which describes a situation where pockets of the ambient phase (i.e air) are trapped under the drop. These methods provide a way of incorporating the effect of surface roughness into the wettability measurement. The interplay between the physical and chemical structure of the surface are used to design superhydrophobic surfaces [90, 91]. These surfaces have contact angles with water which approach 180°.

It is essential to note that for any real system, the ideal energy minimum of the three phases is unlikely to be reached, due to imperfections of the surface on which the contact angle is being measured. Rather, it is more likely that the shape of the droplet corresponds to a mechanical equilibrium and local energy minimum. In this case, the contact angle is related to the work required to in- or decrease the area of the solid being wet by the fluid. Still, it is valid to relate the contact angle to the work necessary to change the wet surface area, as it contains the energy dissipated while moving the three phase contact line.

Due to the existence of these local minima, the measured contact angle ranges between two values. The contact line, which is the line common to the three phases, moves when the angle is larger or smaller than these two particular values, called the advancing and receding contact angles. A sketch of these two angles is shown in figure 2.2

The advancing contact angle, θ_a is the largest angle a droplet forms against a surface before the contact line moves. It is typically measured by increasing the size of a droplet and measuring the largest angle which is formed before the droplet moves. As the droplet volume increases, the contact line remains pinned to the surface and so the angle must increase. As the droplet volume is increased further this becomes unstable and the contact line moves. Similarly the receding angle, θ_r is the smallest angle measured, before the contact line is moving when the volume of a droplet is reduced. The difference between the advancing and receding contact angles is called the contact angle hysteresis. On a very homogeneous substrate, the hysteresis is typically small ($<5°$), but heterogeneity, chemical or physical, leads to an increase of contact line pinning of resulting in an increase in contact angle hysteresis (50° or even higher).

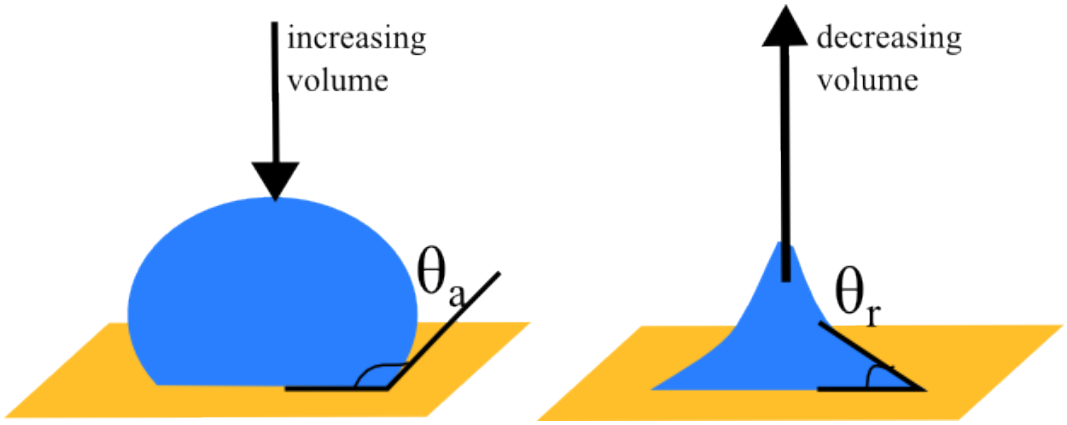

Figure 2.2: Left: the advancing contact angle of a droplet of a surface and Right: the receding contact angle.

2.1.2 Measuring wettability on a sphere

Contact angles are extremely useful to classify wettability on flat homogeneous surfaces, but the problem becomes substantially more difficult when it comes to measuring contact angles on other objects. The problem of measuring contact angles on individually treated beads or microspheres is long standing. If the sphere are large enough, e.g. 1 mm, micro-droplets can be placed on top of them [92], the contact angle can be measured and the spherical geometry of the substrate can be corrected for. However, because the drop should be an order of magnitude smaller than the bead diameter to use this method, it is not easily applicable to small microspheres. Another technique involves placing a sphere at an interface and measuring the penetration depth [93]. Recently methods involving the deformation of the interface [94], or measurement of the dynamics contact lines as a bead is pulled through an interface have been suggested (experiments in progress by Dufour and Baret). These methods are still being developed and there remains no single standard method of determining wettability of single microspheres.

While it is of course most desirable to measure the wettability directly on the object of interest, the difficult and tedium of these measurements generally prohibit sufficient measurements to be made to characterise a statistically significant proportion of the sample of interest. Instead, general practise is to measure the bulk wetting properties of many grains, using techniques such as the Washburn capillary rise method [95] to measure wettability of powders and porous samples.

2.1.3 Capillary wetting

The simplest measure of capillary wetting is called capillary rise. When a capillary is placed inside a bath of liquid, the liquid will spontaneously rise inside the tube, displacing the fluid inside it (usually air), to a given height which depends on the radius and wettability of the tube. A cartoon of this is shown in figure 2.3.

Capillary rise

Capillary rise is defined as the height, h, a liquid rises inside a capillary of radius r (equation2.1).

$$h = \frac{2\gamma cos\theta}{\Delta\rho g r} \tag{2.1}$$

$\Delta\rho$ is the density difference between the two fluids

γ is the interfacial tension between the fluid pair used in the measurements

θ is the contact angle of the fluids with the surface (assuming negligible contact angle hysteresis)

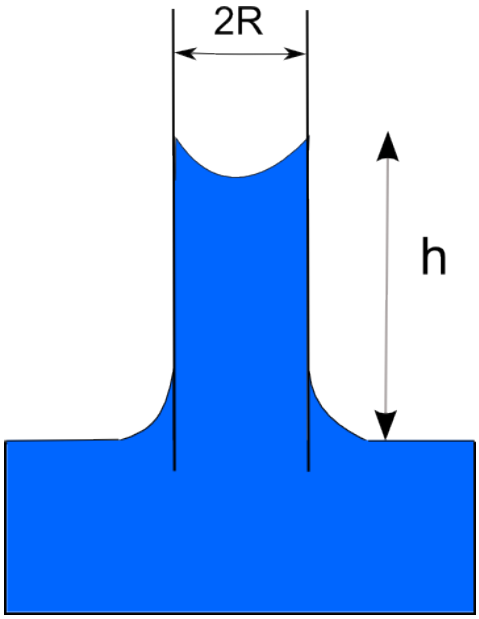

Figure 2.3: Liquid rises inside a capillary to a height h, depending on the radius of the capillary, r, γ the surface tension between the two liquids, and the wetting condition, that is the contact angle between the capillary material, the invading liquid and the displaced phase, θ

r is the capillary radius

Rewriting the equation in terms of the pressure gives

$$P_c = \Delta\rho gh = \frac{2\gamma cos\theta}{r} \tag{2.2}$$

which can be understood as the pressure required for a fluid to invade a capillary of radius r. Both the wetting condition of the surface, and the radius of the capillary determine the pressure required to displace the incumbent fluid.

The capillary rise is the measurement of a single saturation (the height the liquid rises could also be expressed as a volume) of a capillary at a single pressure. This measurement can be extended by varying the pressure and measuring the respective volumes, or saturations of the both phases. These measurements are generally referred to as Capillary Pressure Saturations curves.

2.2 Capillary pressure saturation curves

2.2.1 Introduction to capillary pressure saturation curves

Capillary pressure saturation (CPS) curves are a standard industry measurement for the wetting characteristics of porous media. They are used extensively in this thesis to characterise

the bead samples. This section describes the meaning of these curves. In practise any two liquids can be used, and for ease of measurement one is often air. However in this work, the two immiscible phases used, and discussed are water and oil.

As indicated by the name, capillary pressure saturation curves relate the capillary pressure between the two immiscible fluids and the saturation of one of the phases. The capillary pressure (P_c) is defined as the pressure difference across the interface of two immiscible fluids. There are various conventions used to define it, but for the purposes of this work it is defined as the following:

$$P_c = P_{water} - P_{oil} \tag{2.3}$$

The saturation S is defined as the volume of water divide by the pore volume (i.e the total volume of the porous media multiplied by the porosity of the sample). The capillary pressure saturation curve is obtained by measuring the saturation of the fluids inside the porous media at different applied pressure until the invading phase has entirely invaded the free space, and then once more completely replaced by the original phase. This loop can be repeated several times.

In these loops, water or oil invades the porous medium. In oil engineering, these steps are referred to as 'imbibtion' and 'drainage'. The physical chemistry definition of imbibition refers to the displacement of a non-wetting phase by a wetting one, such as water invasion into a water-wetting rock, or a glass bead pack, displacing oil. Drainage refers to the opposite process, in which teh non-wetting phase displaces a wetting one. This however, becomes quite confusing when talking about mixed wet systems because water invasion into the porous media is simultaneously imbibition and drainage, that is both oil wet pores and water wet pores must be invaded at the same time for the liquid to progress through the sample. These terms are used rather loosely in the literature, with imbibition generically referring to water invasion, regardless of the wettability of the porous medium, and drainage referring to oil invasion. For simplicity, this convention will also be used here.

In the following section, the physical meaning of CPS curves will be explained first for very simple systems, and the be presented for general porous media.

2.2.2 Capillary pressure saturation curves for model systems

The first simple system presented is composed of a single capillary, with negligible contact angle hysteresis. Figure 2.4 shows a schematic of a capillary pressure saturation curve for an ideal capillary. Water invades from the bottom, and at a certain pressure the water is able to displace the oil and fill the capillary. In an ideal case, where there is no contact angle hysteresis, the pressure in which the oil can re-invade the capillary displacing the oil should be the same. In such a system, we would expect to find no hysteresis.

If we consider porous media, due to the different arrangement of grains, there are different

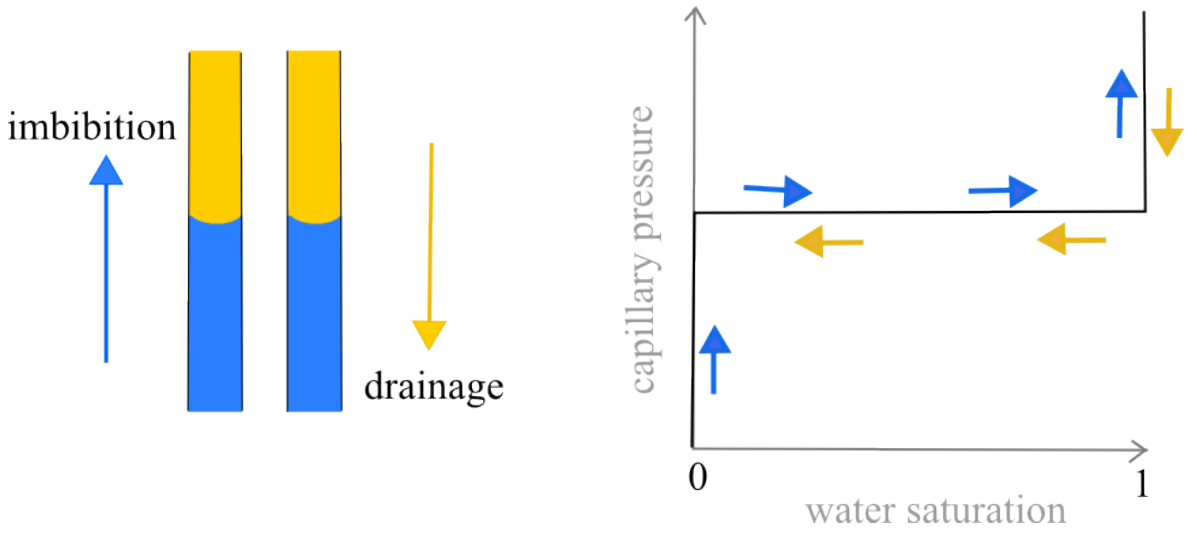

Figure 2.4: Imbibition (water invasion) and drainage (oil invasion) of an ideal capillary (no contact angle hysteresis), with a sketch of a capillary pressure saturation curve for such a system. Imbibition is indicated by the blue arrows, and drainage by the yellow arrows.

pore radii, and so, the channels which the fluid can move have different sizes, and so the heights the fluids would rise in each capillaries are different (see equation 2.2). Conversely, it can be considered that the pressure required to invade capillaries of different sizes are different. The effect of this on the capillary pressure saturation curve is shown in figure 2.5. For the imbibition process liquid is sucked easily into capillaries with smaller radii, whereas for drainage the pressure needed to force the non-wetting liquid into the smaller capillary is higher than a larger one.

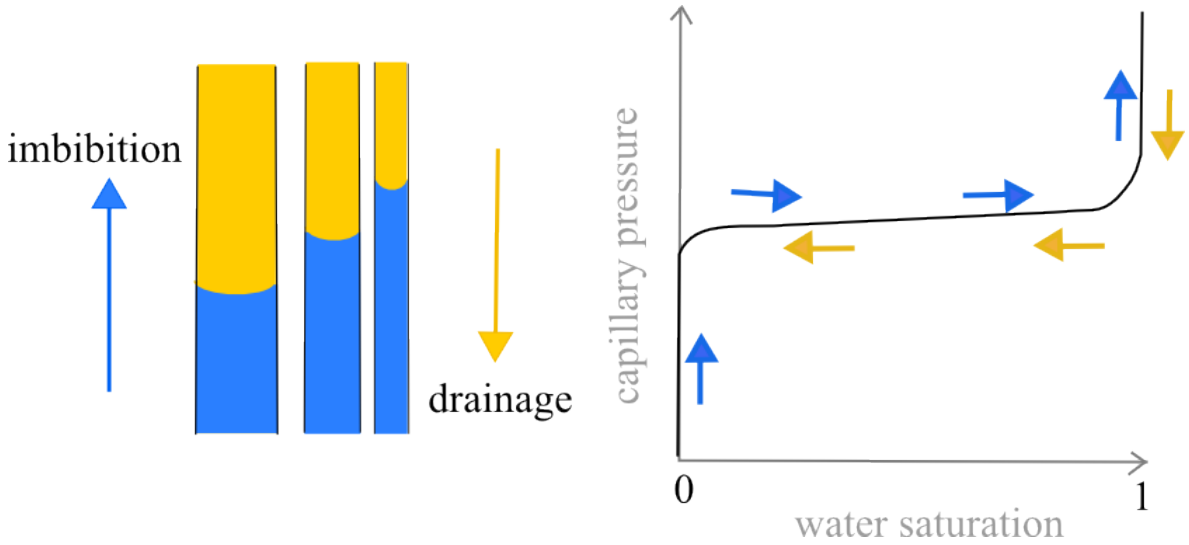

Figure 2.5: Imbibition and drainage of a bundle of capillaries with different sizes. The capillary pressure saturation curve for such a system is shown on the right.

The simplest models of porous media considers it to be a collection of capillaries through which the liquid can flow [96, 97]. Extensions of these models using bundles of capillaries of different sizes to model a stratified porous media (layers made of different sizes beads) are in good agreement with experimental results [74] for single direction flow (i.e either imbibition or drainage).

Increasing the realism of the model further still, channels that form in bead packs are not straight capillaries but rather have non-constant curvature. A sketch of this is shown in figure 2.6. The effect of the non-constant curvature changes the position of the interface depending on whether the pore displacement occurs via imbibition (invasion of the wetting fluid, in this case water) or drainage (invasion of the non-wetting fluid, in this case oil). The different stable positions of the interface at the same capillary pressure causes hysteresis in the capillary pressure saturation curve, even without taking into account the contact angle hysteresis. The interface is advancing step by step. This non-constant advance means that there is a certain applied pressure required for the interface to advance to the next stable position. The 'jumping'of the interface is a non-reversible process and the energy which is dissipated in the process also contributes to the hysteresis of the capillary pressure saturation curve. In porous media this phenomena is knows as Haine's jumps. A formal mathematical description of this process can be found in reference [98].

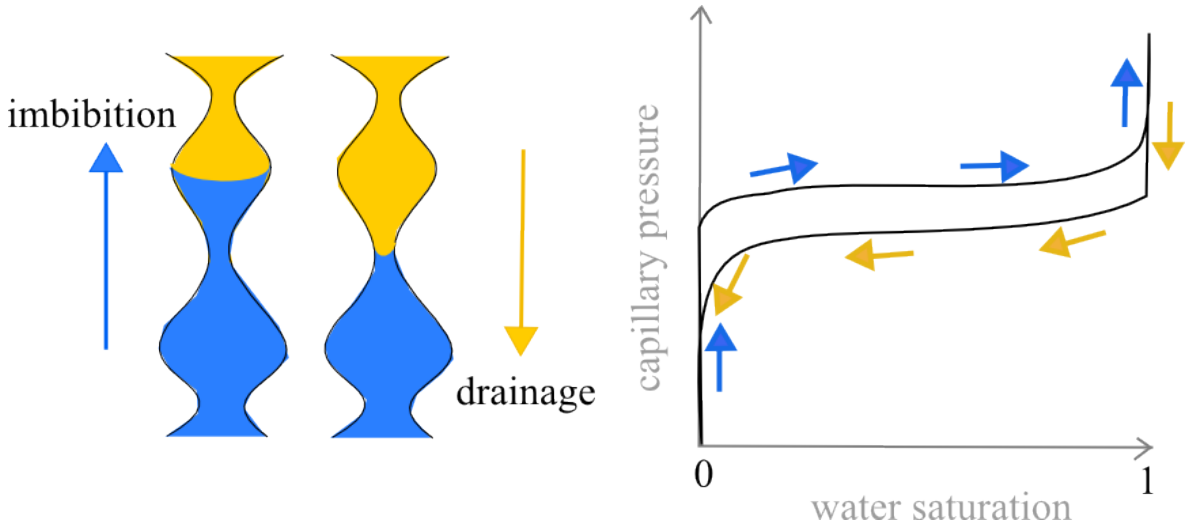

Figure 2.6: Cartoon showing imbibition and drainage of an capillary (no contact angle hysteresis) with a non constant curvature. The different stable positions of the interface, depending on the wetting condition of the invading liquid (i.e imbibition or drainage), leads to a difference in fluid saturations at the sample pressures, shown by the opening of the loop. This is called capillary hysteresis.

Finally, to move from model capillaries to an actual bead pack, it is important to consider the connectivity of pores. A schematic of this is shown in figure 2.7. Rather than straight isolated channels, pores are connected to several neighbouring pores. This leads to two new phenomena: topological changes in the interface, and the trapping of small blobs of liquid in

the packing. Topological changes to the interface can occur when two advancing fronts merge (known as Melrose processes) or an interface is split by an obstacle into two new advancing fronts. Topological changes are irreversible and dissipate energy. These events, as well as the Haine's jump type events caused by the non constant radii of the pores both contribute to the hysteresis between imbibition and drainage processes. The second effect of the network of pores, compared to a bundle of capillaries, is that blobs of liquid may become disconnected from the advancing front and remain trapped into the bead pack. Once a blob, or ganglia, is disconnected from the advancing interface, even at high pressures of the invading liquid it will not be remobilised.[1] This leads to the non-zero saturation values at both ends of the pressure versus saturation curve shown in figure 2.7. It should be noted, that these models all represent the ideal case, where there is no contact angle hysteresis. Contact angle hysteresis is also contributes to energy dissipation of the moving interface, although it is unclear if this is a dominant effect. The effects of contact angle hysteresis are discussed in chapter 4

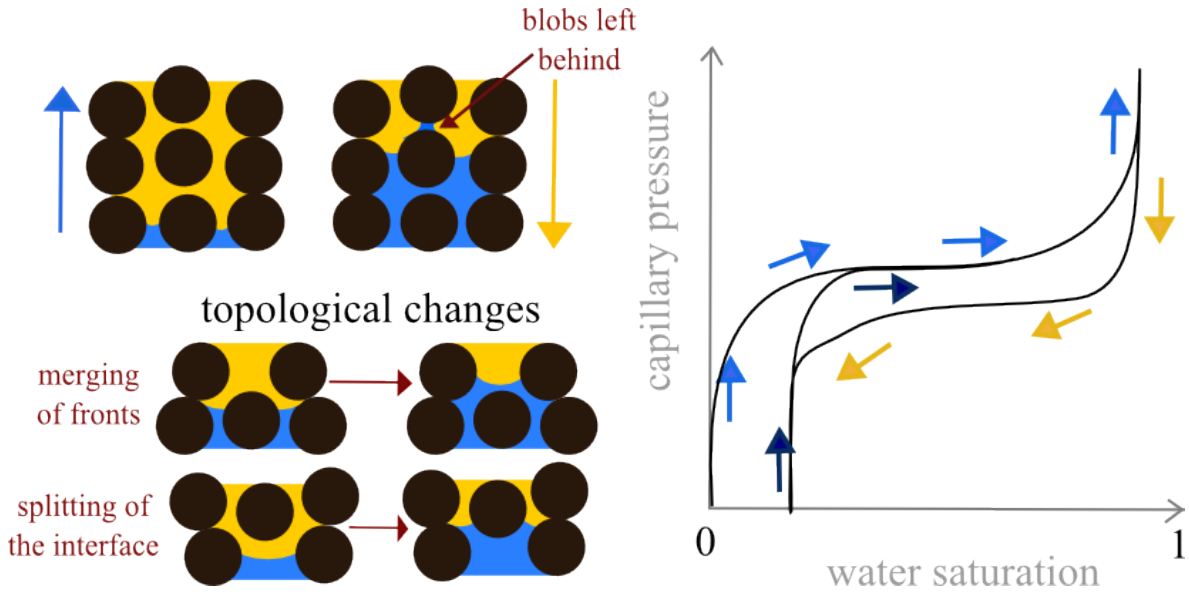

Figure 2.7: Imbibition and Drainage through a bead pack. Top Left: Schematic indicating the trapping of droplets of the defending phase inside a bead pack. This leads to non-zero residual saturations of each phase, even at large pressure. Bottom Left: Cartoon illustrating the topological changes (merging or splitting) of the interface which can occur due to the network like structure of the bead pack. Right: Schematic of a capillary pressure saturation curve for a sample bead pack model. The non zero value of the residual phase results in the the secondary imbibition indicated by the dark blue arrows starting from a non zero value.

Based on the pressure equation (eqn. 2.2) the order of pore displacements can be determined. For the wetting case ($\cos\theta < 1$) the liquid will invade first through the smallest pores, than the larger pores. For the non-wetting case ($\cos\theta > 1$) the liquid will invade first the

[1]Strictly speaking, this is only true in the capillarity dominated regime. In the presence of viscous or inertial forces remobilisation is possible. However, the experiments presented in this work are dominated by capillarity, and this statement holds, that the disconnected droplets will remain trapped.

larger pores and then the smaller ones.

2.2.3 Capillary pressure saturation curves for porous media

In this section, the use of capillary pressure saturation curves in the general case is presented. These curves are typically used to derive unknown characteristics of natural samples such as pore size distributions and wettability. In petroleum engineering, these curves are a standard industry measurement for wetting characteristics of porous media, and two general classification schemes are used, the Amott-Harvey Index [99] and USBM number [49].

Shown in Figure 2.8 is again a schematic of a capillary pressure saturation curve, with the different regimes highlighted. It consists of the primary imbibition curve (indicated with red arrows) which is the initial invasion of the wetting phase into the porous media, then the primary drainage curve (blue and purpose arrows) which is the re-invasion of the original phase. Following the primary imbibition and drainage, it is theoretically predicted that the system enters a constant loop [100]. This loop is referred to as the capillary hysteresis loop. There are two regimes of imbibition and drainage- spontaneous and forced. Spontaneous imbibition/drainage refers to invasion of the liquid into the porous medium at capillary pressures lower than that required to invade the empty cell. These zones are indicated in figure 2.8. In our system, spontaneous imbibition refers to imbibition which takes place at capillary pressures less than zero, where the water is sucked into the porous medium displacing oil, and for drainage at capillary pressure above zero where the oil is spontaneously sucked back into the cell.

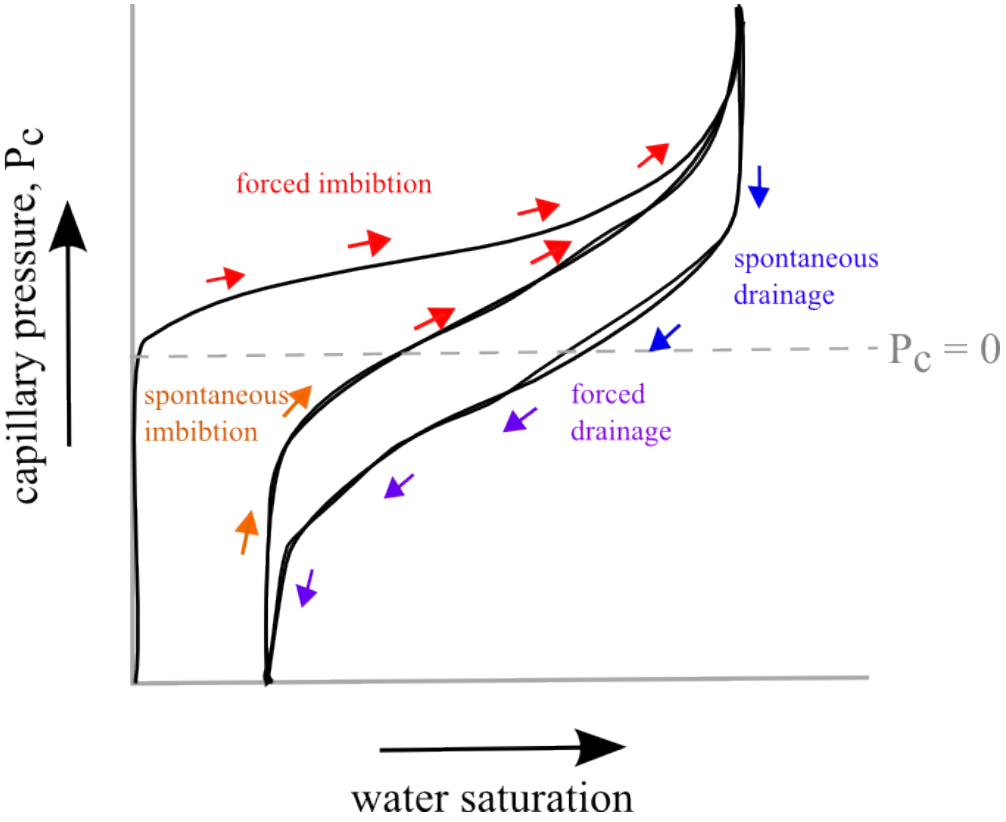

Figure 2.8: Schematic of a capillary pressure saturation curve. The spontaneous and forced imbibition and drainage zones are indicated by the coloured arrows.

Generally speaking the wettability of the sample can be inferred by the position of the CPS curve to the $P_c = 0$ line (grey dashed line in figure 2.8). Curves below the line, which spontaneous imbibe water are classified as water wetting. Samples which curves are above the line, where the water has to be forced inside, are oil wetting and curves which are centred around $P_c = 0$ are either intermediately or mixed wetting. In order to quantitatively characterise sample wettability there are two commonly used classifications of wettability derived from capillary pressure saturation curves. These are the Amott-Harvey Index, and the United States Bureau of Mines index. Both measures are used to quantify the wettability of the sample.

Amott-Harvey index

The Amott-Harvey index, denoted as I, first described in 1959 [99] is a number between -1 and 1 which qualitatively describes the wettability of a rock (or any porous sample) with 1 being strongly water wetting, and -1 being strong oil wetting. A schematic indicating how the Ammot-Harvey index is calculated is shown in figure 2.9.

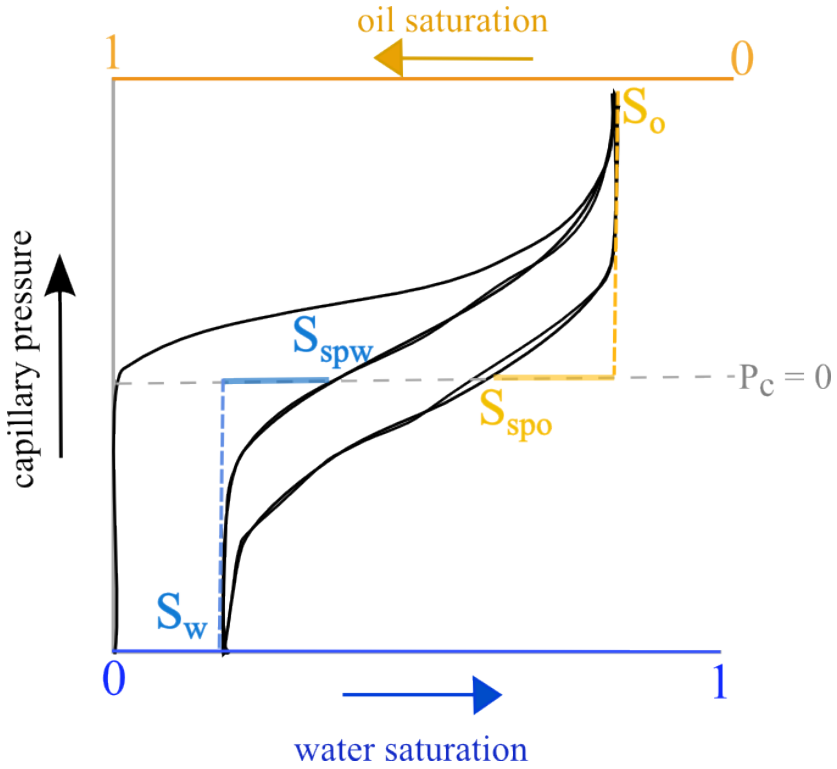

Figure 2.9: Schematic of a capillary pressure saturation curve with marked values used in the calculation of the Amott-Harvey Index

The Amott-Harvey Index is defined as:

$$I_w = \frac{S_{spw} - S_w}{1 - S_w - S_o} \tag{2.4}$$

$$I_o = \frac{S_{spo} - S_o}{1 - S_w - S_o} \tag{2.5}$$

$$I = I_w - I_o \tag{2.6}$$

where

S_{spw} is spontaneous water sorption and corresponds to the point where the secondary imbibtion lines crosses the zero pressure line

S_w is the residual water saturation

S_{spo} is the spontaneous oil sorption, and corresponds to the point where the drainage line cross the zero pressure line

S_o is the residual oil saturation

Looking at the schematic (figure 2.9 is it clear to see that small differences in the crossing points of the zero line can have a major impact on the wettability classification. To avoid

this, an alternative description of wettability is sometimes used which looks at the area under the imbibtion and drainage curves.

USBM numbers

Another description of rock wettability is the United States Bureau of Mines number (USBM). This qualitative characterisation is based on the integrated area under the forced imbibition and drainage parts of the curve, and is shown in equation 2.7 and figure 2.10. It is based on the idea that the area under the curve is equal to the amount of work required to move the fluid interface through the sample. The wettability is then assumed to be linked to the differences in how hard it is to remove the water, compared to how hard it is to remove the oil.

$$W = log(\frac{A1}{A2}) \tag{2.7}$$

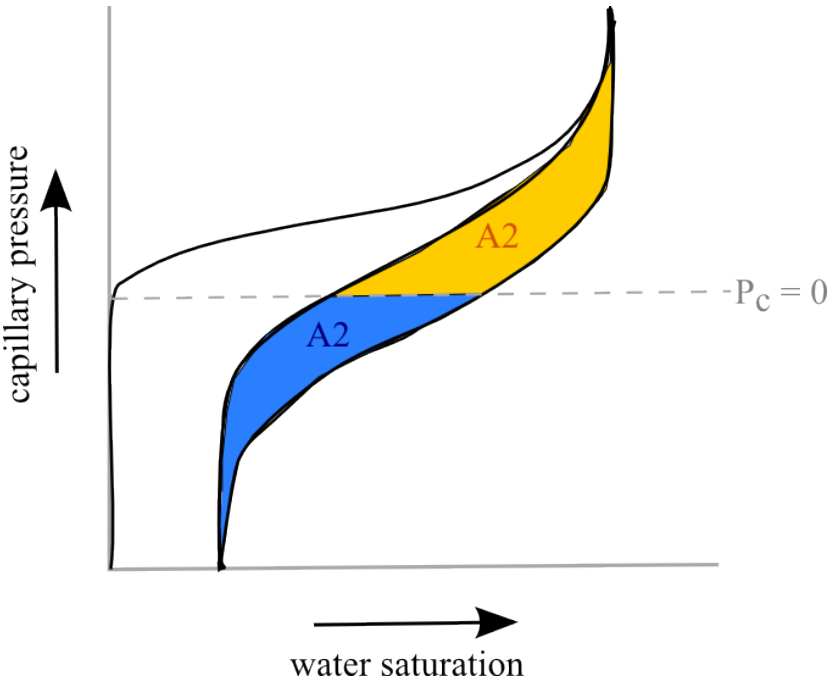

Figure 2.10: Schematic of a capillary pressure saturation curve showing the areas used for the calculation of the USBM number. The forced drainage area is shown in blue and the forced imbibition shown in orange.

Although these measurements, the Amott-Harvey index and USBM number, are considered the industry standard in determining wettability in porous samples of unknown wettability, which is almost always the case with natural samples, there have been many reported limitations of such a classification scheme. For example, the Amott-Harvey and USBM indexes are only applicable within a certain wetting regime, and cannot differentiate between

very water wetting samples of different contact angles [35]. In the cases of mixed (with distinct water and oil wetting regions) or intermediate wetting (contact angles of approximately 90°) both Amott-Harvey and USBM would give the same number. However, the two phase flow properties through two such samples is very different [7, 8, 67].

In order to measure capillary pressure saturation curves there are two other quantities which need to be considered: the capillary length and the capillary number.

The capillary length is given by equation 2.8. The capillary length, is the length scale for an interface which results as the balance between interfacial tension and gravity. In practise, for interfaces which are smaller than the capillary length, the effects of gravity can be effectively ignored. For air/water systems, (and at standard pressures and temperatures) the capillary length is around 2 mm.

$$\lambda_c = \sqrt{\frac{\gamma}{\Delta\rho g}} \tag{2.8}$$

The capillary number is the ratio of viscous forces to surface tension. In general, for systems with small capillary numbers the fluid displacement is dominated by capillary effects (and not viscous effects). In our experiments the capillary number is approximately 10^{-6}, meaning that we are in the capillarity dominated regime. While the overall invasion of the porous media, is said to be quasi-static, fluctuations in the local velocity of the invading fluid, for instance during the Haine's jump, can be significantly higher.

$$Ca = \frac{\mu V}{\gamma} \tag{2.9}$$

The standard analysis of capillary pressure saturation curves assumes that the samples are homogeneous, or that heterogeneity is homogeneously distributed. From a capillary pressure saturation curve along, little can be said about the distribution of the wetting surfaces inside the porous media. This is further exacerbated by the unknown wetting characteristics of the sample. Instead, in this work a controlled sample with mixed wettability, where the distribution of wetting surfaces are known and well characterised is investigated. This approach allows for features of the curves specifically pertaining the wetting domains to be identified. As such a library of curves corresponding to known samples can be created and has potential for a better characterisation of wettability in natural samples.

The was characterised using X-ray tomography. In order to characterise the spatial distributions of wetting surfaces inside the bead packs, and asses the impact of wetting heterogeneities on the immiscible flow characteristics, the sample, and liquid-liquid distributions inside the packing needs to be visualised. This is achieved using X-ray tomography.

2.3 X-ray tomography

X-ray computerised tomography, referred to as X-ray tomography, or simply X-ray CT, is the technique of creating 3D images by taking radiograms (x-ray adsorption images) from every angle of the sample, and then reconstructing the 3D image from all the radiograms. Tomography is widely used in medical diagnostics to create 3D internal images of the body, in a non-destructive way. Medical CT scanners were adapted for use in the material sciences in the late 1980s [101]. A schematic showing the principle of tomography is shown in figure 2.11.

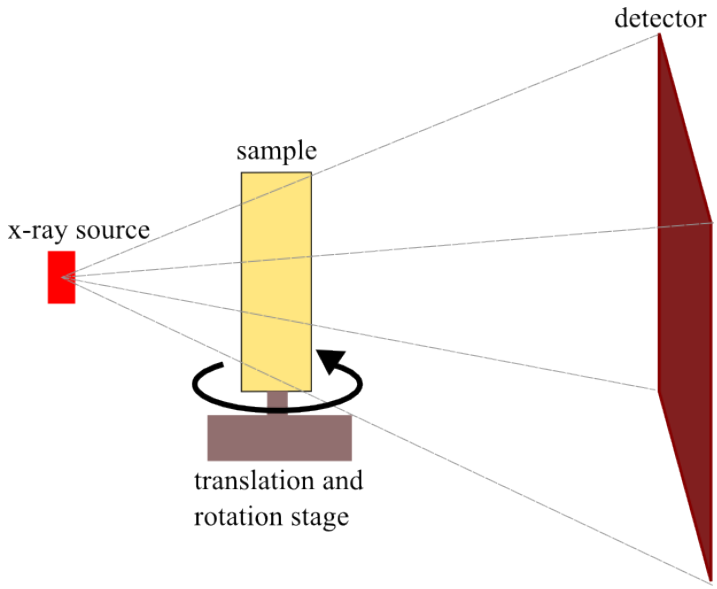

Figure 2.11: (a) Schematic of the tomography set up. A sample is placed in the x-ray beam, and rotated whilst being imaged. The x-ray transmission image at every angle is measured by the detector. These images are then reconstructed into a 3D volume.

Tomography imaging of the samples in this work were acquired in house using the GE Phoenix Nanotom, a commercially available instrument. A picture of the Nanotom and the inside of the Nanotom is shown in figure 2.12. The name Nanotom, refers to the resolution of the instrument, which is able to resolve features down to the ∼900 nm limit.

A sample is placed between the x-ray source and the detector and the absorption of the X-rays by the sample is recorded by the detector which consists of a scintillating layer and a CCD detector. The scintillating layer converts the X-rays into visible light, which are then measured by the CCD detector. The sample is rotated in the beam, and at each angle, a radiogram is recorded. An illustrative example can be seen in figure 2.13. Radiograms of Kinder Surprise Egg are shown for 0, 90, 180 and 270 degrees rotation. For the full image a radiogram is taken at finer steps of 0.5° rotation. These radiograms are then reconstructed into a three dimensional image. The algorithm used is a filter-back projection algorithm and details on the reconstruction algorithm can be found in reference [104]. A 2D slice and the 3D volume rendering of the egg are shown in figure 2.14.

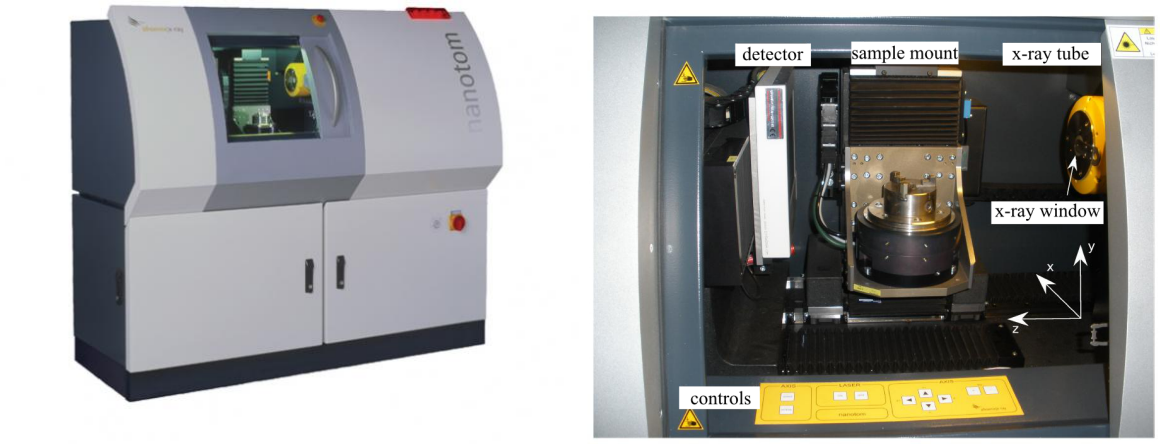

(a) GE Nanotom, photo reproduced from [102] (b) Inside view. Picture adapted from [103]

Figure 2.12: Outside and Inside views of the GE Phoenix Nanotom.

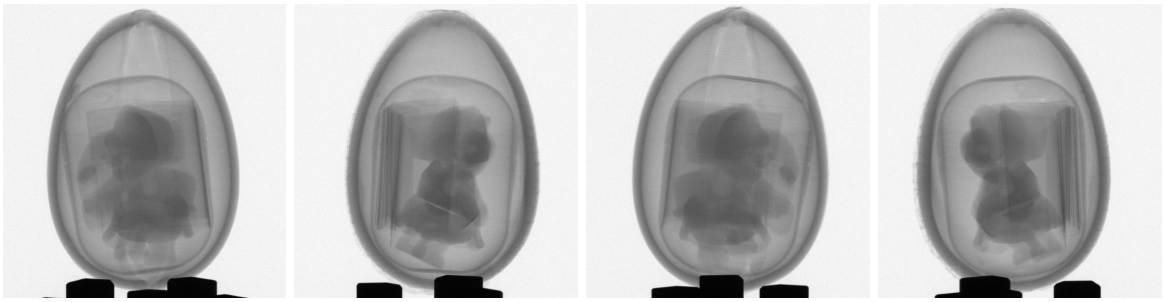

(a) 0° rotation (b) 90° rotation (c) 180° rotation (d) 270° rotation

Figure 2.13: X-ray adsorption images of kinder surprise egg taken at different angles. Images are taken at each angle and then used to reconstruct the 3D image.

The most simple type of X-ray tomography, and the one discussed here is X-ray absorption tomography. In this type of imaging, contrast is achieved between different elements of the image by differing amounts of X-ray absorption. Materials which absorb a lot of X-rays appear dark in the radiograms, but bright in the reconstructed tomography. X-ray absorption depends on the mass attenuation coefficient of the material, which essentially depends on the electronic structure of the material, i.e bigger atoms absorb more X-ray, gold is brighter than aluminium, and the density of the atoms. A familiar example is a medical chest X-ray, where the dense bones which contain large amounts of calcium absorb more X-rays than the surrounding soft tissue (made mostly of water). Just like the medical x-ray, materials which are strong absorbers appear bright in the reconstructed image, and materials which absorb weakly appear dark. The difference in X-ray absorption of different materials means that X-ray imaging is a useful non-destructive way to look inside otherwise non-transparent objects. In the images of the Kinder Surprise egg, the pieces can be easily visualised due to the large

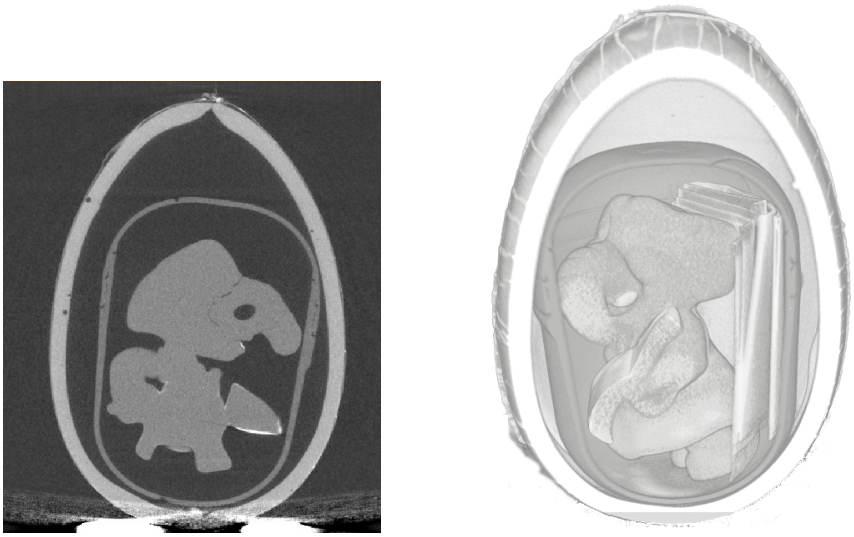

(a) 2D slice (b) 3D volume rendering

Figure 2.14: 3D reconstruction of a Kinder surprise egg a) a 2D slice and b) volume rendering of the grey value data with a cut to show the interior structure

density differences between the air (absorbs very few X-rays) and the chocolate and plastic layers as seen in figure 2.14a. The 3D image is made of voxels, which are volume pixels. The resolution of the image is described by the side length of a voxel.

3D visualisation of the interior structure of an object is aesthetically pleasing and can allow important observations to be made, however to extract real physical data from the images several processing steps are required to transfer the image into something that can be analysed by a computer. The general image processing steps which are used in this work are described in the following section.

X-ray parameters

X-ray images presented in the thesis was acquired with the following protocols. 3D tomography data was collected using GE Nanotom with a tungsten target and a resolution of $16 - 17\,\mu$m per voxel for the imaging of liquid fronts (Chapter 5), and 6 - 12 μm for the sample characterisation (Chapter 3). Data was acquired using a current of 150 μA and a voltage of 150 kV to achieve the best contrast between all phases in the system. 1440 images were collected with an exposure time of 250 ms using 2x2 binning to give a reconstructed file size of 1132 x 1132 x 1152 pixels.

2.4 Image processing

Our eyes are very good at pattern recognition. For example, in the x-ray image of the Kinder Surprise egg, our eyes have no trouble distinguishing the different elements- the outside egg shell, the inside plastic capsule and the small toy inside. To convert this into something that can be read by the computer however, we need to segment each element. This is usually done by a form of grey value segmentation. For illustration purposes, it is useful to continue with the Kinder Surprise analogy as it exhibits all the typical problems that arise during image processing procedures. The generic work flow described in this section is applicable to all of the samples and experiments imaged in this work with x-ray tomography. Image processing and the creation of 3D pictures was done using Avizo-Fire 7.0, a commercially available software package.

2.4.1 Pre-filtering

Prior to further processing, all images are pre-filtered using a 3D-bilateral filter[2] with 500 iterations, which is an edge preserving median filter. This reduces the noise and improves the segmentation quality. A raw image (before filtering) and filtered image are shown in figure 2.15. The filtering step removes a lot of the noise from the bulk of the phases without blurring the boundaries an undesirable side effect common to median or Gaussian filtering). The noise reduction allows for significantly improved segmentation of the images.

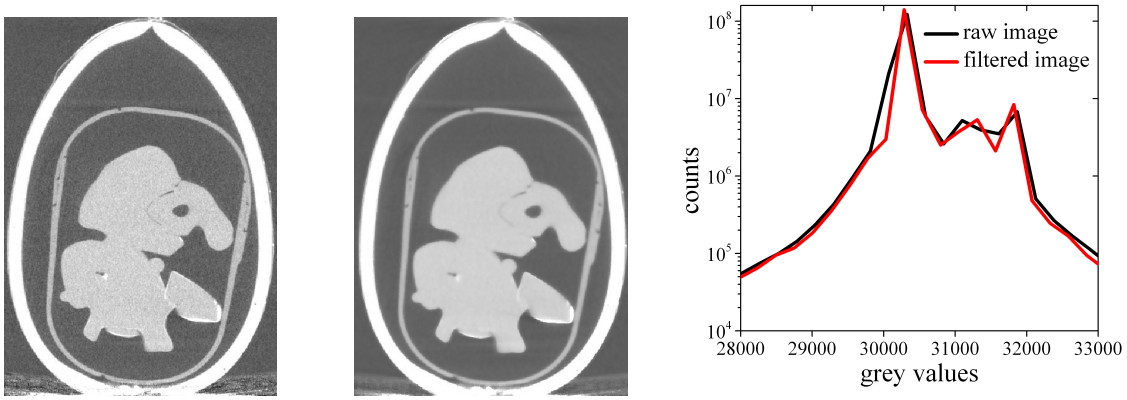

(a) raw image (b) image after filtering (c) grey value histogram

Figure 2.15: (a) 2D slice from the raw tomography of a Kinder Suprise egg and (b) the same image after bilateral filtering. (c) shows the grey value histograms (with a bin size of 300 grey values) of the raw image (black line) and the filtered image (red). The removal of noise causes a sharpening of the peaks enabling an easier segmentation.

[2]Each processing term is explained in the appendix (chapter A) and details of the precise algorithms used can be found in [105].

2.4.2 Segmentation

As seen in the images and the grey value histogram (figure 2.15) there are three phases present, each shade of grey corresponding to a peak on the histogram. The background, the air, is easily separated from the other two phases, however the chocolate egg shell, and the plastic toy inside are much closer in grey values and therefore more difficult to segment. The initial segmentation based upon the the local minimums of the grey values (selecting each separate peak in the histogram) gives a reasonable approximation of the elements we want to extract- with a few defects. This is shown in figure 2.16.

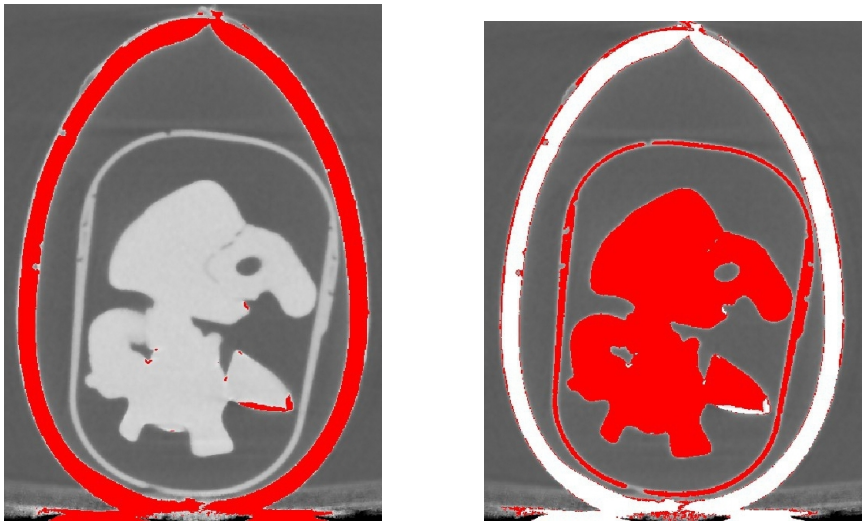

(a) shell segmentation (b) figure segmentation

Figure 2.16: The initial segmentation of the features of the image just using grey value thresholding. The segemented portion of the image is overlaid on the original image in red.

Now there are two binary images (images which consist of 0 s, the black background, and 1 s the red foreground). There are some small errors in the segmentation, for example the small bright sections on the figure correspond to the same grey values as the shell (see figure 2.16a) and the aluminium foil around the egg corresponds to the same grey values as the plastic figure and have therefore been included in the segmentation. These unwanted inclusions can be removed from the binary images using morphological transformations.

The two simplest morphological transforms are erosion and dilation. Erosion refers to the processes where the last layer of voxels of an object are removed and dilation refers to the opposite, in which a layer of voxels is added. These operations are performed with different neighbour criteria to determine what the edge of an object is. This is illustrated using a 2D example shown in figure 2.17. In 2D the neighbour criteria can be 4-neighbours (edge connected) and 8-neighbours (corner connected) is In 3D, these become 6-neighbours (face connectivity), 18-neighbours (edge connectivity) and 26-neighbours (corner connectivity). For very small objects, or objects imaged with a low resolution, the choice of neighbour criteria

does have some effect on the shape of the extracted data. Opening describes a sequence of an erosion and then a dilation step. The result of the opening transformation is that large areas of the image are preserved but the small isolated features, do not survive the erosion step and are removed. Closing refers to the sequence of a dilation and subsequent erosion step. The effect of closing is to fill in holes small gaps between nearly connected objects.

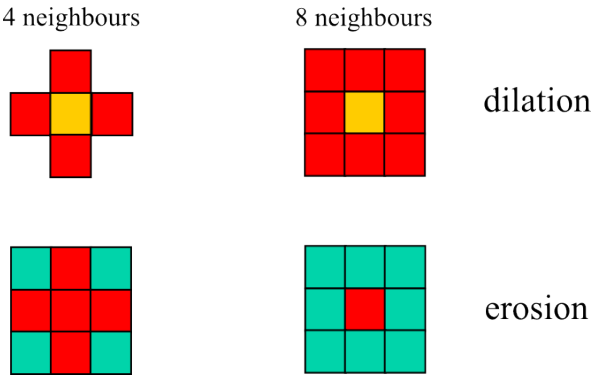

Figure 2.17: A 2D example of dilation and erosion. The dilation is performed on a one pixel object using 4 and 8 neighbour criteria. The yellow square represents the initial pixel and the red squares show the pixels which are added to the object in the dilation step. The erosion is performed on a 3x3 pixel object where the green squares show the pixels which are removed by the erosion step, and the red square s are the final object.

The problems of the foil layer around the shell (see figure 2.16b) and the small inclusions on the figure (see figure 2.16a) can be removed using an opening step using the 18-neighbour criteria. The effect of the opening transformation on the segmented images can be seen in figure 2.18.

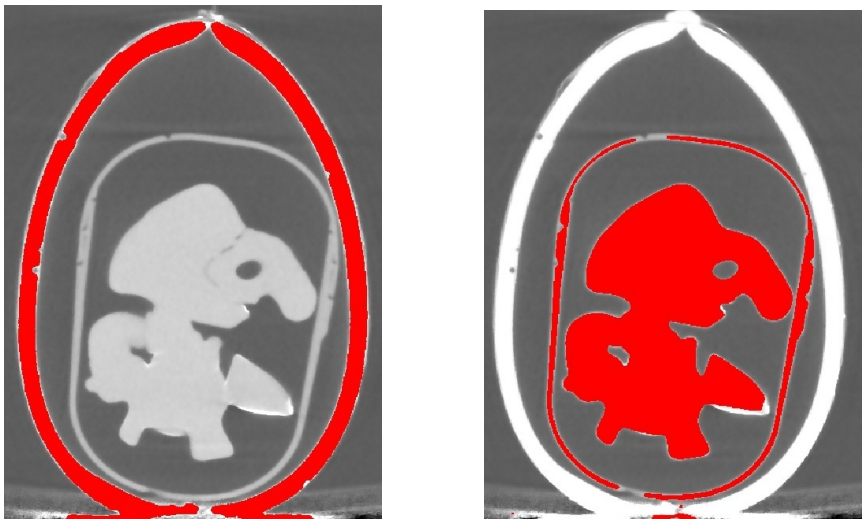

(a) 'opened'figure image (b) 'opened'shell image

Figure 2.18: Opened images (compared to figure 2.16 with small erroneous features removed

In this way, all the separate features of the image that we wish to identify can be extracted. Continuing with further opening steps, the figure can be separated from the plastic capsule inside. The capsule can be isolated by subtracting the figure from the original thresholded image. We can now reconstruct the image from its separate components for analysis. This is shown in figure 2.19

Figure 2.19: 3D Volume rendering of each individual components showing the separately identified features of the image and picture of the object for comparison.

At this point, as there is no analysis needing to be done of the Kinder Surprise object, nothing further will be done to this image. However, the concepts introduced here and in general this work flow; filtering, segmentation, and mophological transformations, is the same work flow applied to the experimental images of bead packs and liquid distributions featured in this work, to obtain the features of interest for analysis.

2.5 Summary

This chapter dealt with two topics. The first is how to measure wettability, not just on a flat surface, but also inside a porous sample. Wettabiliy of porous samples can be measured using Capillary Pressure Saturation Curves. The second method introduced in this chapter was X-ray tomography imaging. Tomography is a non-invasive technique which allows 3D imaging of the internal structure of an object. Combined with several imaging processing steps, the physical features of these images can be extracted and analysed. In order to fully elucidate the two phase flow behaviour through the model porous media used in this study these techniques will be employed to study the effects of wetting heterogeneities on measured wettability and distribution of liquids inside bead packs.

Chapter 3

Design of mixed wet porous media

As demonstrated in chapter 1, what is missing in the literature is a systematic investigation of the spatial distribution of wetting and non wetting surfaces in porous media. Despite continuing interest in understanding the pore scale mechanisms involved in two phase flow in porous media, mixed wet studies to date, do not consider the effects of wetting heterogeneity, but rather focus on average wettability as a control parameter. While some heterogeneities have been introduced in numerical studies, no model systems, experimental or otherwise, containing lengths scales of a size such that multiple heterogeneities can exist with a single pore space have been reported. This chapter will address this problem and describe the design, creation and characterisation of the samples with wetting heterogeneities with lengths that range from sub-pore to spanning multiple pores.

Samples were designed which had the same global compositions allowing direct comparison of the effects of the local wetting distributions independently of any effects of the local wetting distribution independently of any effect caused by overall average wettability. These samples are this all designed such that while the spatial extension of the wetting and non-wetting surfaces change, the overall percentages of wetting surfaces remain constant at 50%. This will test the validity of 'averaging theories'. If average wettability in indeed a the important control parameter of two phase flow than the pore displacements in all of these samples should exhibit the sample characteristics.

To make sure that the flow properties through such samples was robust, and not a peculiarity caused by a particular surface treatment, four different types of surface treatments were used to create hydrophobic surfaces. The resulting coatings have similar contact angles, but are made with different chemical treatments, and have different surface roughness. The preparation of these samples could only involve scalable methods, as for the sample scale properties (measured in Chapters 4 and 5) $\sim$ 3 g of beads are required per experiment. The treated beads were characterised both locally (i.e individually) and as a whole sample. The sample scale characterisation was performed by calculating the wetting correlation ξ, which is proportional to the average size of the wetting domains.

3.1 New kinds of models

The approach presented in this work was to introduce the mixed wettability on the beads themselves. This methodology resulted in samples that contain potentially several wetting heterogeneities inside of a single pore space, something completely new to the literature. A sketch of each type of sample is shown in figure 3.1. The creation of each type of sample is described in section 3.3. The surface modifications are detailed in section 3.2.

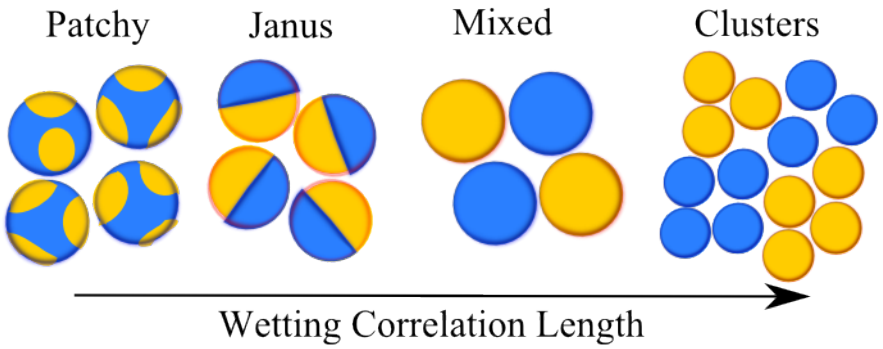

Figure 3.1: Cartoon samples created with different wetting correlation lengths, ξ. The two colours represent the different wettabilities, with blue representing water wet surfaces and yellow signifying oil wet surfaces. This colour convention is used throughout this work.

While is it important to locally characterise each bead (wettability, percentage surface coverage), the flow through the sample will depend on the sample environment as a whole. Therefore is also important to measure the collective properties of each of these samples, by characterisation of bead packs comprising of ∼1,000 modified glass beads. This is accomplished using a minimal descriptor, the wetting correlation length ξ. ξ is a statistical property of the collective surfaces of all the beads. It is defined as the average distance travelled away from the original surface before a surface of the other wettability can be reached. ξ is measured from x-ray tomography images of the different sample types. The calculation of ξ from the tomography images is described in section 3.4.

3.2 Controlling the wettability

To introduce a wetting heterogeneity into the bead packs, the surface of the water wetting glass beads must be modified to become oil wet. The glass beads used were MoSci soda lime glass beads, with diameters of 350 - 425 μm. Four different protocols were used to achieve this: silver, gold, CTMS and Etched. Multiple coatings were used to test the specific effects of chemical functionality and surface roughness. Figure 3.2 shows homogeneously coated gold and silver beads, and uncoated glass beads. The four types of surface treatments used to create hydrophobic domains in the bead packs are 'silver', 'gold', 'CTMS'and 'etched'.

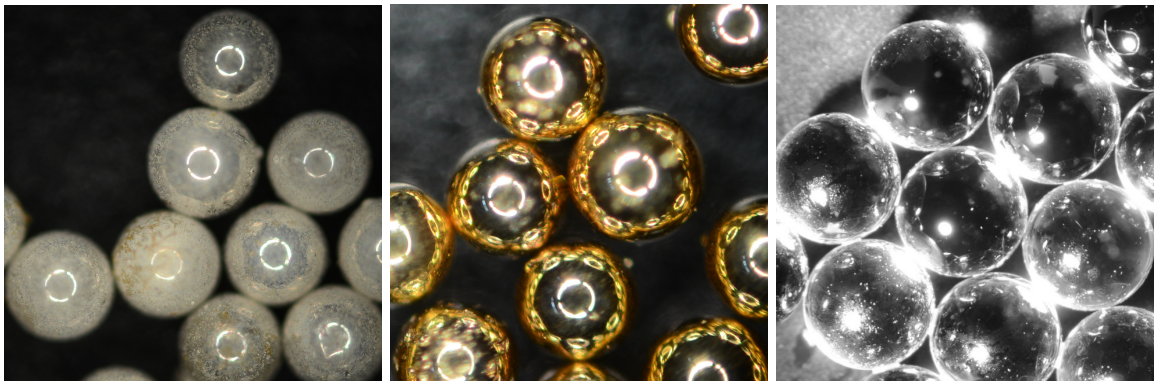

(a) silver coated beads (b) gold coated beads (c) uncoated glass beads

Figure 3.2: Pictures of fully coated beads, 350 μm diameter, with different surface treatments. The difference in surface roughness between the gold, glass and silver beads is clearly visible. [1]

3.2.1 Pre-cleaning

Prior to modification or use all glass beads are cleaned using the 'Hellmanex ' cleaning protocol to remove any adsorbed organic material from the surface. An alternative common method of cleaning glass is the piranha etch, which consists of a 4:1 ratio of concentrated sulphuric acid to hydrogen peroxide. However, the in order to avoid any uncontrolled roughening of the surface, a potential side effect of piranha cleaning the Hellmanex protocol was used instead. The Hellmanex cleaning protocol is as follows: first beads are washed in millipore water, before resting in a 20% solution of Hellmanex detergent for 120 minutes, with periodic agitation of the beads. The detergent is then removed and the beads are rinsed with sufficient millipore water until all foam disappears. The beads are then soaked in 1 M NaOH for 120 minutes, with periodic agitation. Cleaned soda lime glass slides were measured to have a water in oil contact angle of 20°.

[1] Photo credit: Guido Schriever

3.2.2 Silver

Beads classified as 'silver' are created by first coating the glass surface with silver metal and then coated with hexadecanethiol rendering the surface hydrophobic.

To prepare the glass surface of the beads and create a better adhesion between the glass and the deposited silver, the beads are first coated with APETS (3-aminoproplytriethoxysilane) [106]. The silver ions in solution complex with the free amine group of the silane providing surface tethered seeds for the plating process.

50.0 g/L $AgNO_3$ solution, with sufficient NH_4OH (25%) added until all silver has formed the $Ag[NH3]_2$ complex, as indicated by dissolution of all brown $AgNH_3$ precipitate resulting in a clear solution. The reactive mixture is poured over the glass beads. To this solution formaldehyde is added (2.5 mL per 10 mL H_20). The solution is left to plate for 120 min at room temperature.

After cleaning and drying of the newly deposited silver coating, a self assembled monolayer of hexadecanethiol (see figure 3.3) is formed on the silver layer, making the surface hydrophobic. The silvered beads are covered with a 1% (volume) solution of hexadecanethiol in dodecane for 60 min. The beads are then collected and rinsed with isopropanol and dried in the oven at 75°C for approximately 12 hours.

Water in oil contact angles were measured using sessile drops on analogously treated glass slides and determined to be 120° (see figure 3.3).

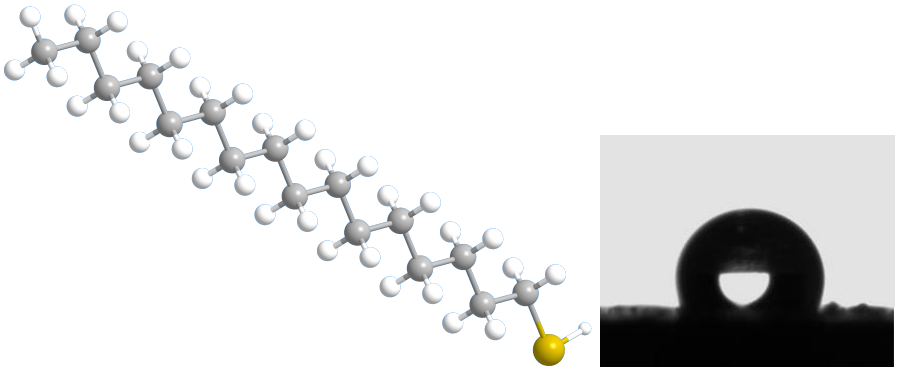

Figure 3.3: Left:3D rendering of a hexadecane thiol molecule. The sulphur atom shown in yellow spontaneously adsorbs to gold and silver surfaces creating a oil-wetting monolayer. Right: A sessile drop contact angle measured of water in hexadecane on a silver-thiol surface

3.2.3 Gold

Gold coated samples were obtained from Creo-Vac Dresden and were created by sputtering with gold resulting in a gold layer approximately 200 nm thick. The gold surfaces were then made hydrophobic by adding hexadecanethiol, in the same treatment as the silver surfaces. Static contact angles measured on analogously treated flat surfaces were measured to be 130°.

3.2.4 CTMS

A CTMS (chlorotrimethylsilane, see figure 3.4) layer was formed upon cleaned glass beads by resting them in a 0.5% volume solution of toluene for 60 minutes at room temperature. The beads were then rinsed in isopropanol and acetone before drying in the oven overnight. Static contact angles measured on analogously treated microscope slides were determined to be 130°.

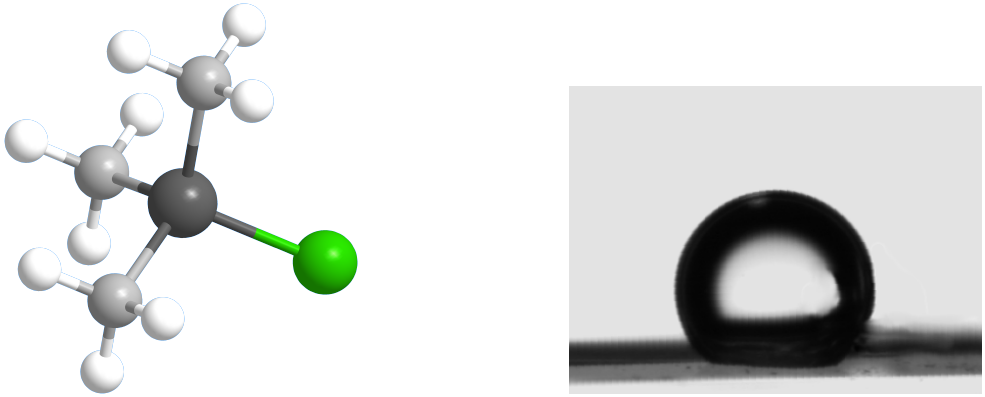

Figure 3.4: Left: 3D rendering of a CTMS molecule. The silane atom (shown dark grey) reacts with Si-OH groups on the glass surface forming a Si-O-Si bond. The methyl groups then point upwards from the glass surface making it hydrophobic. Right: Contact angle measurement of water in oil on a CTMS treated microscope slide.

3.2.5 Etched

In order to investigate the effect of surface roughness, and create an alternative rough sample to compare with the results of the silver coated beads, a glass etching protocol as described in Utermann et.al. [107] was used. A solution of 60 g of glycerol in 140 mL of millipore water was heated at 90°C for 90 minutes. 60 g of NH_4FHF and 10 g of $FeCl_3$ were added to the mixture and thoroughly shaken until dissolved. The mixture was then shaken on a horizontal shaker for 15 min and allowed to cool, and then vortexed (using the vortex genie) for 15 seconds to ensure that all additives were dissolved or dispersed in the solution. The solution was then centrifuged for 15 minutes at 5000 rpm (revolutions per minute) and the clear solution carefully decanted from the sedimented solids. Glass beads were added to the clear etching solution for ten minutes. The solution was then decanted and the glass beads rinsed several times in millipore water and dried overnight in the oven. The rough surfaces were then made hydrophobic using CTMS.

3.2.6 Characterising the Surface Roughness

The surface roughness was characterised using white light interferometry (WLI). These measurements were performed on five beads of each type (gold, silver and etched). Figure 3.6

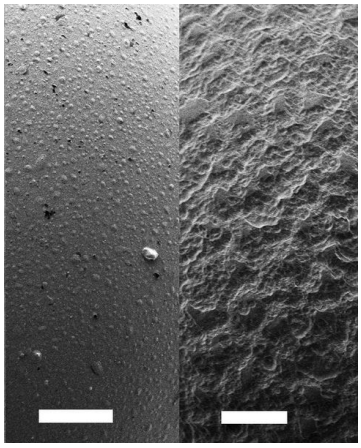

Figure 3.5: SEM image of etched beads, the left panel is a native glass bead, and the right panel is a glass bead that has been etched. Scale bars are 1 μm. Image taken from [107]

shows the surface profiles of a gold, silver and etched glass bead. The gold bead has a smooth surface, and just a few sub-micron defects can be seen on the spherical cap. The silver bead, has an extremely rough surface, with features extending up to 5 μm from the surface. This confirmed what is seen in the optical images (figure 3.2) that the silver surfaces are very rough. The etched glass surfaces are also quite rough, with features of several microns visible in the surface profile.

3.2.7 Stability of the coatings

The stability of the different coatings were tested in two ways. The first was to measure the interfacial tension (IFT) of hexadecane in which the beads had been soaked for more than 24 hours. The IFT of the hexadecane was measured via the pendant drop method against millipore water and did not change substantially from the recorded value of clean IFT. The IFT against time is shown in chapter 4, section 4.1.5. If the coatings were deteriorating in the presence of the hexadecane, the IFT is expected to drop. The second method used was to create layered samples of modified beads and clean glass beads and measure the capillary pressure saturation curve for such a sample. Previous studies had reported that coatings such as OTS (octadecyltriethoxysilane) were unstable in the conditions of the CPS experiment and that after an experiment OTS was found to coat all of the beads in the cell and not only those which had been originally modified. [108]. After the CPS experiment, which lasts more than 24 hours, the beads were removed in their layers so that the originally hydrophilic beads were separated from the originally modified beads. The wettability of these beads was then qualitatively checked by placing the beads into water and oil and observing their behaviour. There was no change in the qualitative wetting behaviour of the beads, the hydrophobically modified beads continued to flocculate in the water and flow in the oil, and the glass beads did not flocculate at all under water.

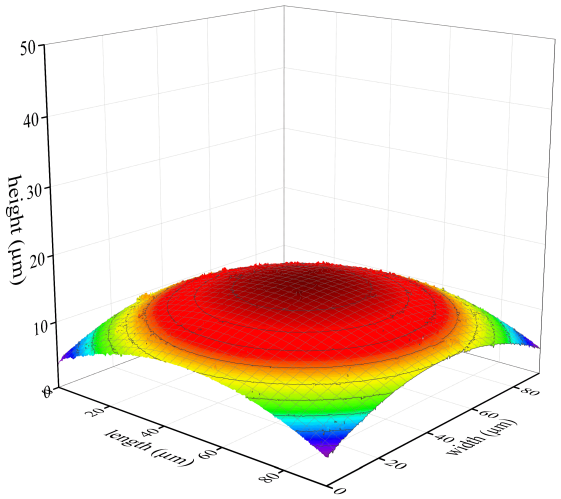

(a) gold bead

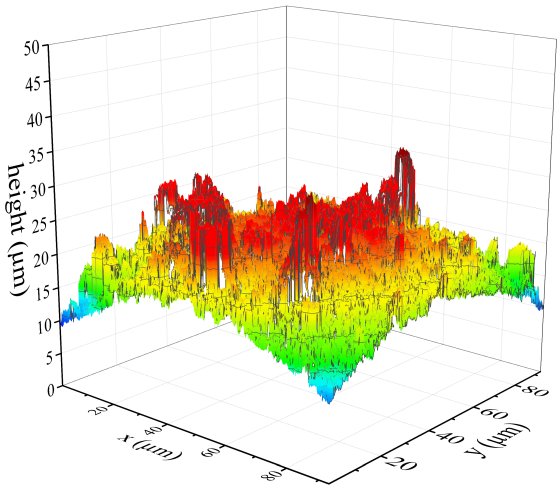

(b) silver bead

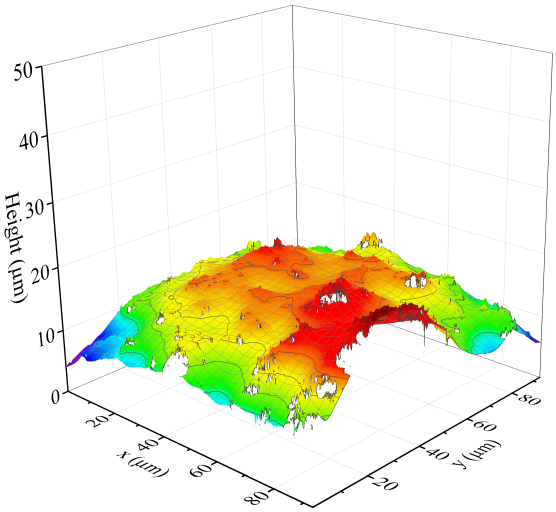

(c) etched glass bead

Figure 3.6: Surface plots of treated beads measured by white light interferometry. The beads have a diameter of 350μm.

These four methods of creating hydrophobic surfaces are used in conjunction with different techniques to control the length scale of the surface modification to create the four model samples depicted in figure 3.1.

3.3 Controlling the length scale

This section outlines the creation of the different length scales used in the investigation. Each of the sample types (patchy, janus, mixed, and clusters) was designed to have different spatial distributions of the wetting surfaces but importantly, an average surface coverage of 50% hydrophobic surfaces in the entire bead pack.

3.3.1 Patchy

Patchy samples are beads which have multiple wetting patches on a single bead. Packings of these beads create samples where within every pore space each pore contains one, or even several wetting heterogeneities.

Patchy samples were made by selectively masking the contact points between grains using liquid bridges. The amount of surface coverage is directly proportional to the liquid content in the bridges [59]. This is illustrated in figure 3.7 where liquid bridges of 1 M CsI solution (for x-ray contrast) in a packing of glass beads were imaged using X-ray tomography.

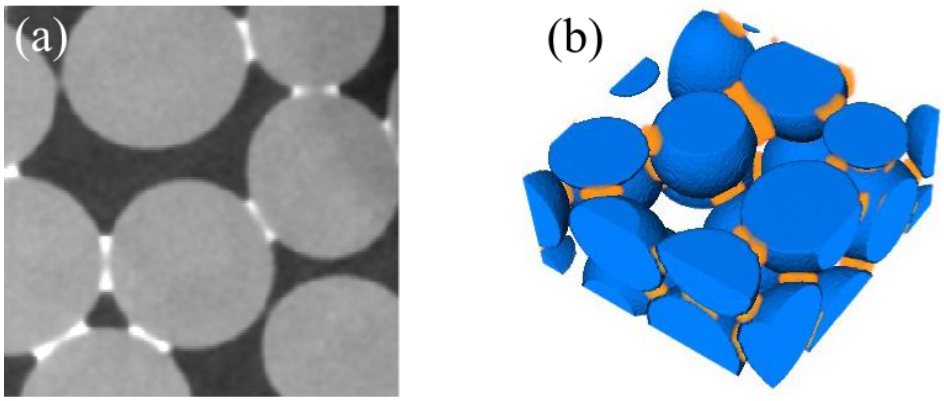

Figure 3.7: (a) 2D slice and (b) 3D volume rendering of X-ray tomography of beads with water bridges made from 1 M CsI for X-ray contrast enhancement to show location of masks

Samples used in this study were created by using the liquid bridges which form between grains as a mask prior to further surface modification. A volume of 2.0% of the total sample volume of hexadecane was used for masking and was stirred through the beads so that the liquid became homogeneously distributed between beads as capillary bridges (as shown in figure 3.7). The sample placed in the freezer and cooled to -20°C, freezing the masking liquid to prevent any movement. The frozen packing was then injected with a 0.5% solution of CTMS (chlorotrimethyl silane) in hexane. Hexane was used as the solvent as the freezing point of hexane ($\sim$ -95 °C) is well below that of hexadecane (16 °C). The frozen porous sample filled with the CTMS in hexane solution was degassed, to ensure that the CTMS reaches all the exposed surfaces of the beads and then left to react for 18 hours in the freezer at -20°C. After this time the sample is warmed to room temperature, the liquids removed

and the beads washed in isopropanol, and dried in the oven. A schematic of the method can been seen in figure 3.8.

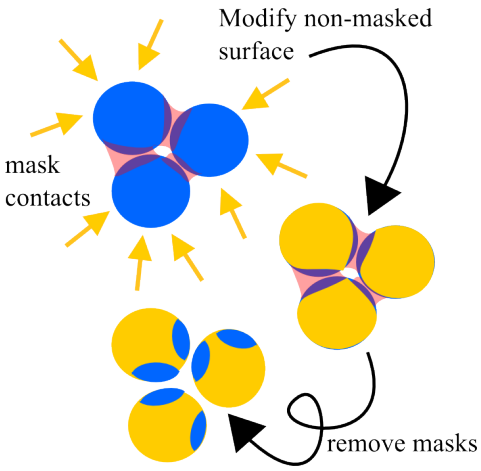

Figure 3.8: Schematic showing the masking of patchy beads to create a length scales smaller than a single pore size

One method of characterising the extent of modified surface of the patchy beads is to measure the surface coverage of the beads by the liquid bridges. Previous work on this issue determined that at a mask volume of 2.5% of a wetting fluid (water) the surface coverage of the beads was approximately 45% [59]. However, the system used here is slightly different, and to ensure that there are no significant side effects caused by using different mask liquid or the freezing step, it is also necessary to measure the amount surface coverage directly on modified beads.

Surface modifications with silanes are particularly unsuited to visual characterisation, either by microscopy of x-ray tomography. In order to characterises the surface coverage, using x-ray tomography samples with x-ray contrast corresponding to the different wetting patches are required. These samples consisted of fully coated silver beads which were masked with hexadecane in the same manner as the silane modified beads. The exposed silver surface was then etched away using a solution of 4:1:1 MeOH:H_2O_2:NH_4OH for five minutes. After cleaning and drying the beads were then dried and imaged using X-ray tomography to visualise the remaining silver surface. In order to determine the correct mask volume, samples with volumes from 1.0% to 2.5% were measured. The sample was imaged with a resolution of 6 μm per voxel to allow high resolution imaging of the surface.

From the X-ray tomography the glass and silver surfaces were extracted (details of the image processing can be found in appendix A), and the surface coverage to mask volume ratio was calculated and is shown in figure 3.9. To match the surface wettability ratios of the other samples, a mask volume of 2.0% was chosen, resulting in a surface coverage of 50 $\pm$ 5%.

As a caveat to this method, it should be mentioned that the etching reaction between the etch solution and silver surfaces is highly exothermic, and forcing this liquid inside bead

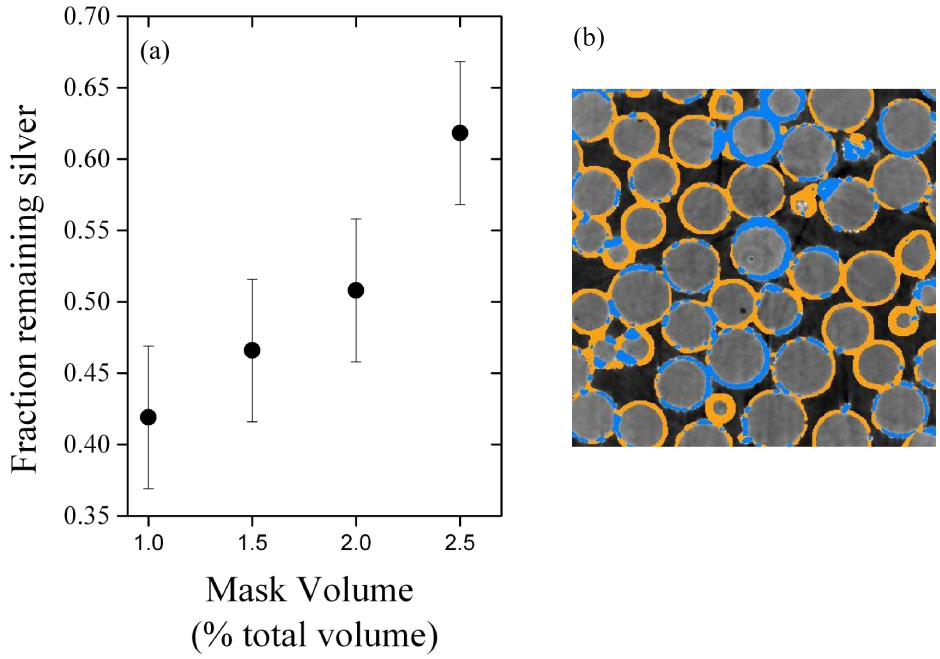

Figure 3.9: a) Calibration of surface coverage to mask volume of etched silver patchy samples. The large error bars arise from the sensitivity of the surface layers segmentation and b) 2D slice of an x-ray tomography of etched silver beads created with a mask volume of 2.0%. The silver surfaces are highlighted in blue and the glass surfaces in orange.

packs with frozen liquid bridges, without destroying the integrity of these masks is not without substantial difficulty. In fact, this could only be achieved on small samples of beads, sufficient for characterisation, but not of the order required for testing of flow properties which requires $\sim$ 3 g of beads. For this reason, only the CTMS modified patchy beads were able to be used for further experiments.

3.3.2 Janus

Janus spheres were created by modifying half of the surface of the spheres. For the different coatings used this was achieved by two masking methods.

Gold janus beads were created by sputtering gold on the top half of beads sitting on a flat surface. The shadowing effect provided by the neighbouring beads preventing the undersides of the beads being coated and resulted in half coated gold spheres. A 3D volume rendering (made from x-ray tomography images) of gold sputtered janus grains can be seen in figure 3.13.

Silver janus grains were created as described by Cassangrande et. al. [109] in which beads are half masked using a thin film of resin (Norlands Optical Adhesive no. 89, a UV curable glue) and the remaining exposed surface is coated. A schematic of such a scheme is shown in figure 3.10.

To ensure there was no lasting wettability alteration of the masked side of the beads, a

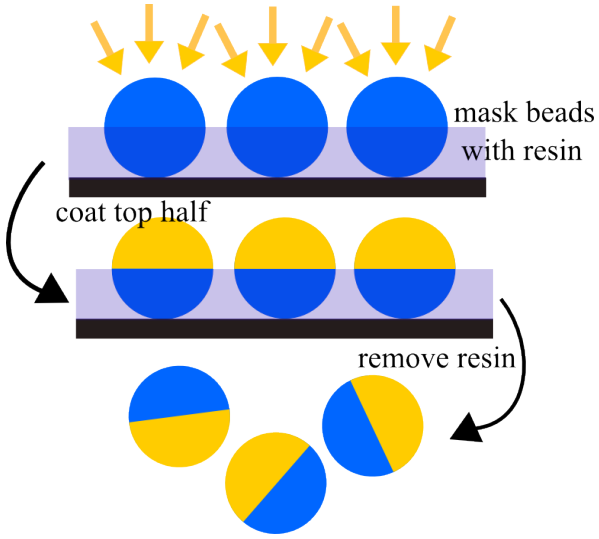

Figure 3.10: Cartoon showing resin protection method of creating janus grains.

control batch of beads was made, where the beads were first embedded in the resin layer, then removed cleaned and dried. The wettability of these beads was measured using a capillary pressure saturation curve and they were found to be as hydrophilic as the straight cleaned glass beads, demonstrating there was no side-effects of the resin.

An alternative method to make janus beads using wax and water emulsions was first trialled, but eventually abandoned due to a low yield of usable grains. Details of this methods can be found in appendix B.

3.3.3 Mixed

These are the easiest of the four samples to create as it involves simply mixtures of hydrophobic and hydrophilic spheres. These are the only types of samples described here which have been previously reported in the literature and around which theories concerning mixed wettabilities have been built. Mixed samples were made with all four surface treatments- gold, silver, CTMS and etched. A 3D volume rendering of a mixed sample is shown in figure 3.13. It was postulated in chapter 1 that mixed wet samples of this type are a special case of heterogeneous wettability, due to the presence of continuous pathways of oil wet and water wet pores. The percolation of both phases of beads is shown in figure 3.11 which shows individual volume renderings of the two kinds of beads. There are continuous pathways of water wettable and oil wettable pores throughout the whole system. It is this dual percolation in mixed samples which is most likely responsible for the agreement between contact angle averaging modelling and mixed-wet bead pack experiments. These creation of these images from X-ray tomography of bead packs is described in section 3.4.

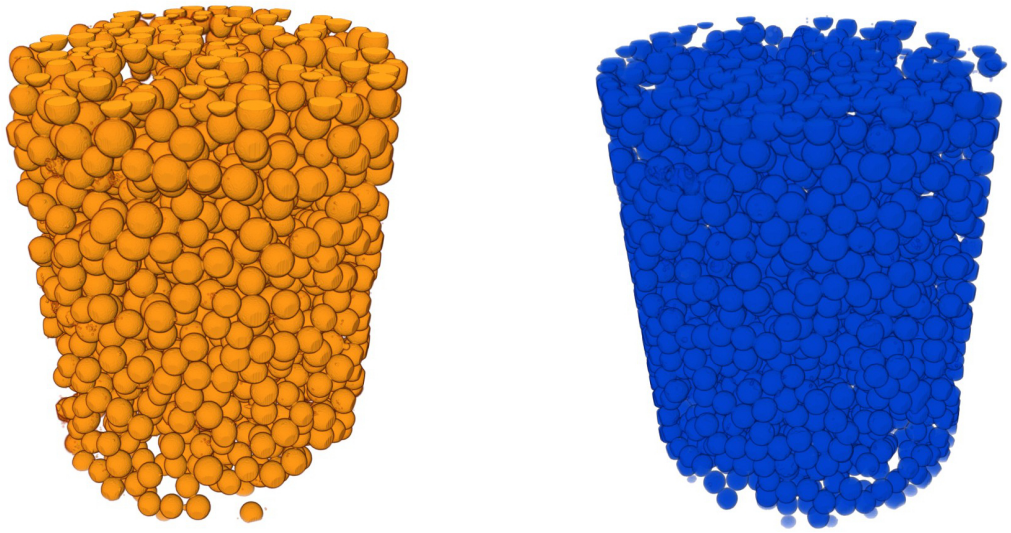

(a) oil wet spheres (b) water wet spheres

Figure 3.11: Both types of spheres, yellow representing oil wetting and blue representing water wetting are displayed here separately. From these images it can been seen that both phases have connected pathways through the packing.

3.3.4 Clusters

Cluster samples were made by sieving wetted beads of homogeneous wettability (both hydrophobic and hydrophilic clusters are prepared) through a 1 mm sieve. The beads were first partially wet with hexadecane so that they stuck together, and the wet mixture sieved to obtained clusters of a defined size. A cartoon of this process is shown in figure 3.12 a. Analysis of cluster size was done by embedding individual clusters in PDMS (polydimethysiloxane) and making X-ray tomography of the clusters. The beads were segmented and each individual bead identified. The 3D renderings of the individual clusters, with identified beads are shown below in figure 3.12 b. The number of beads per cluster was counted for 20 individual clusters. The histogram of the number of beads per cluster is shown in figure 3.12 c. From this small number, it can already been seen that there is a large range of sizes, from 10 beads to more than 60, with the average cluster size estimated to be ∼30 beads. The number of clusters measured in this was was limited due to the difficult of embedding the individual clusters in PDMS and preventing any two clusters from merging.

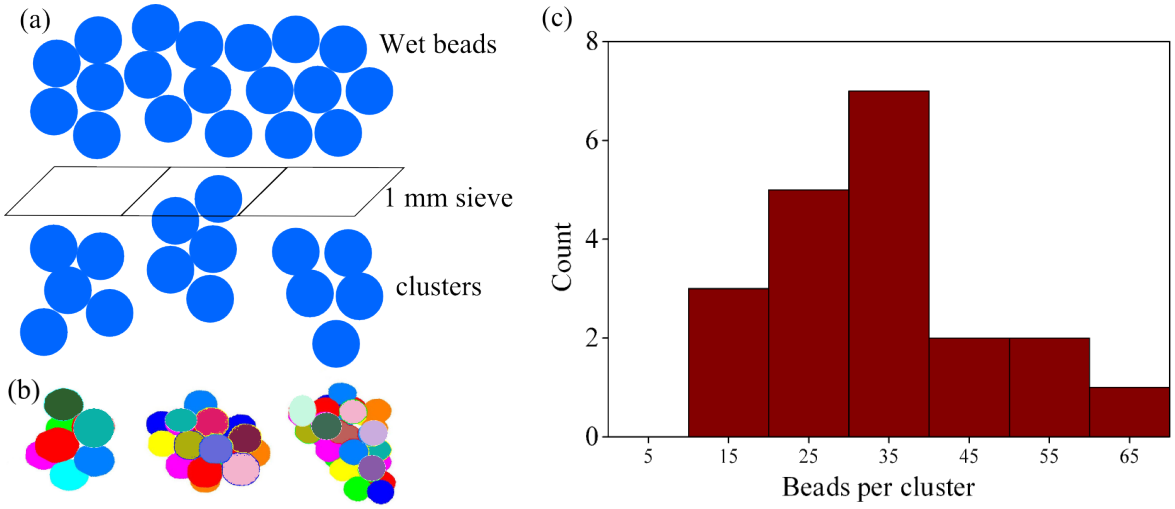

Figure 3.12: (a) Cartoon showing how clusters of a defined size are made by sieving through a 1 mm mesh, (b) volume renderings of individual clusters imaged with x-ray tomography, different colours are used to indicate different beads, and (c) histogram showing the number of beads per cluster.

A 3D volume rendering of X-ray tomography of a cluster sample is shown in figure 3.13. What is clear from the 3D image is that, just like the mixed sample, there are percolating pathways of both types, water and oil wet beads the entire way through the sample. What is also clear from the tomography, is that the packing of such a sample is non-trivial in that the clusters need to remain unbroken during the formation of the sample. To maintain the integrity of the clusters the liquid bridges were frozen after sieving creating solid but brittle clusters. 50% mixtures of oil wet and water wet clusters were made by mixing equal weights of each type of cluster. This was stirred, gently to mix the clusters without breaking them.

The clusters were then transferred into a sample tube. The renderings of individual clusters in figure 3.12 show irregular and anisotropic shapes, and because of this the frozen clusters do not form dense packings. To achieve a density comparable to that of the other samples, of approximately 60% the clusters are compressed using a teflon rod. The pressure exerted on the clusters is sufficient to either melt the frozen hexadecane bridges between the beads, or simply break them. Layer by layer, first filling the sample tube with the mixed clusters, and then by compressing the clusters a dense sample can be built up. This sample is then filled with hexadecane and degassed to remove any air. In order to transfer the dense cluster sample without disturbing the local arrangement of the grains from the cluster formation it is frozen and transferred as a solid block from the preparation sample tube into the measurement tubes (for example for the CPS experiments).

3.3.5 All samples

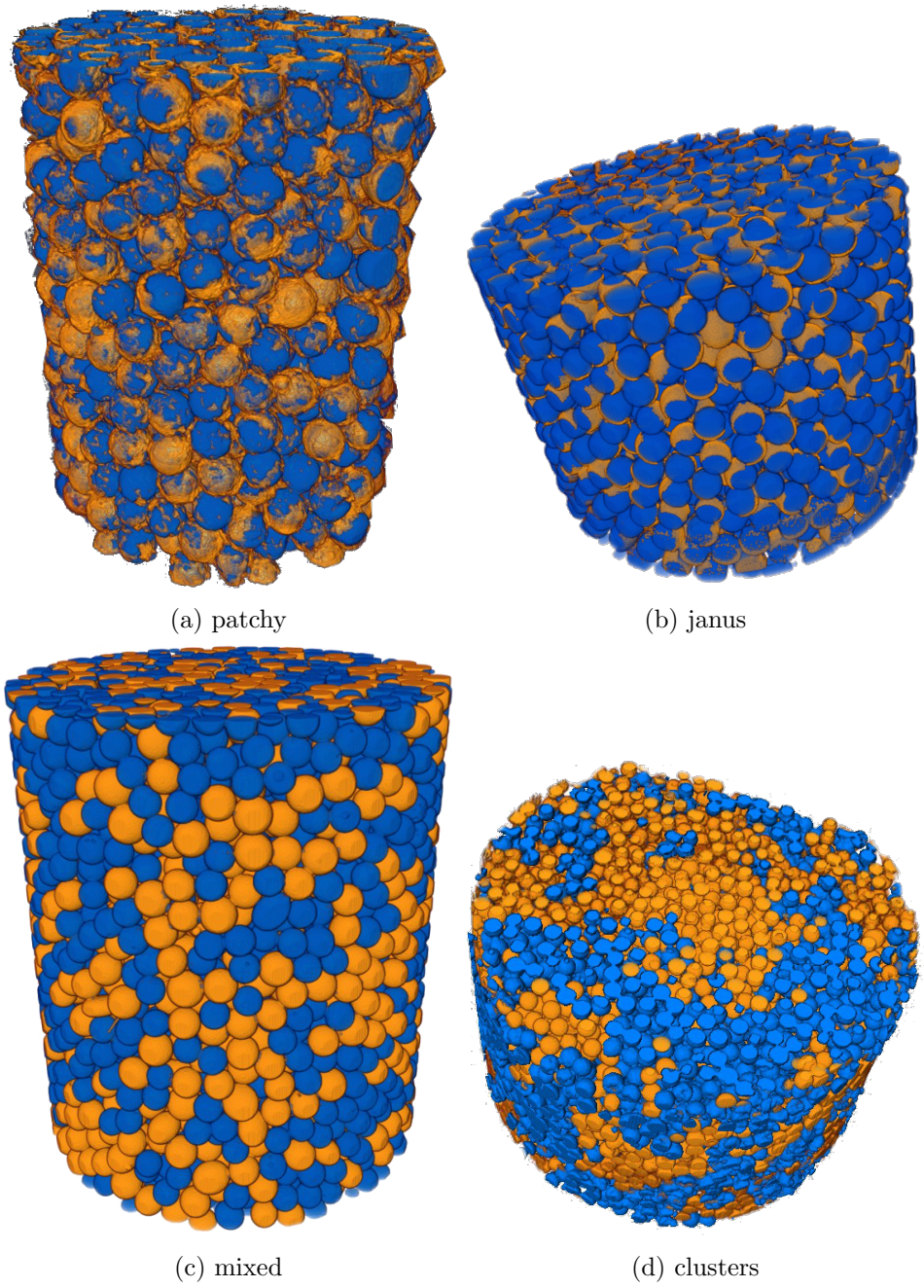

(a) patchy (b) janus

(c) mixed (d) clusters

Figure 3.13: Volume rendering of X-ray tomographies of heterogeneously wetting samples. The samples were dry (no liquid). The beads imaged here are 350-400 μm in diameter. For the patchy and janus samples, with correlation lengths of less than one, there are no (or very few possibilities) of percolating pathways of one wetting surface throughout the whole sample. In the case of the samples with correlation lengths greater than 1 (mixed and clusters), both samples show percolating pathways of water wet and oil wet beads through the entire sample.

Observing the volumes of all of the samples next to one another, as shown in figure 3.13

the differences between the samples are highlighted. What is apparent for both the patchy and janus samples, is that on single bead both types of wetting surfaces are present. For these samples there are no, or very few possibilities for a continuous pathway of one or the other wetting surface from the bottom to the top of the packing. This is in contrast to the mixed and cluster systems which have continuous pathways of both wetting surfaces throughout the packings.

3.4 Characterisation on the sample scale

To understand the flow behaviour through these samples, it is necessary to characterise the spatial distribution of wettabilities throughout the whole sample. This is done by measuring the wetting correlation length, ξ from tomographic images of packings of dry grains. The images were segmented such that each 'wetting phase' was selected separately, set to 1 or 2, and all background voxels were set to zero. 2D slices of the tomographies overlaid with the two segmented wetting surfaces can been seen in figure 3.15. For most of the samples, it is not possible to determined the wettability from the x-ray absorption (i.e silane coatings are not visible by X-ray tomography). To overcome this model samples were designed with X-ray visible markers which have a spatial distribution similar to the wettability distribution of the samples of interest. 2D slices of the tomographies overlaid with the two segmented wettign surfaces can be seen in figure 3.15.

Extraction of features from tomography images is performed using grey value thresholding, as described in chapter 2, section 2.3. In order to be able to differentiate between water wet and oil wet surfaces in the images these features need to have a different X-ray contrast. In the case of the metal coatings, this is relatively straightforward, although, x-ray imaging requires thicker layers of deposited metal than necessary for the wettability modifications. Patchy samples created by the silver etching method could be directly used for the correlation length calculation as the silver is quite thick (1 μm) is much brighter than the glass beads. For janus samples x-ray contrast was achieved by sputtering a thick layer of gold (1 μm) on one hemisphere of the bead, and imaging with a resolution of 11 μm per voxel allowing for clear resolution and segmentation of the modified surface. The mixed and cluster samples which have homogeneously coated beads were imaged using two types of beads with different x-ray contrast: glass and basalt beads. Because the beads were the same size as those used in the experimental measurements and the samples were prepared in identical ways these models represent the mixed and cluster samples prepared with modified glass beads. Mixed and cluster samples were imaged with a resolution of 12 μm per voxel. The different wetting surfaces for each type of sample were extracting using a combination of filtering, segmenting and morphological transformation techniques. The exact protocol used for each sample is described in the appendix (chapter A). The correlation length calculations were performed on samples containing approximately $\sim$1,000 beads. The results of the correlation length calculation for the four types of samples is shown in figure 3.15.

The algorithm used for the correlation calculation compares every voxel to every voxel within a sub-volume of the image. This works by constructing a 3D matrix where the coordinates of the element of the matrix represent the difference in the coordinates between two voxels. Each element of this matrix is a 2D matrix representing the different colour information (AA, AB, BA, BB). The segmented image is converted into a 4 dimensional array containing the coordinates and value of every non-zero voxel (as in the initial calculation).

Unlike a classical auto-correlation each entry in the list is compared with every entry occurring after it, i.e voxel pairs are only compared once, substantially improving the efficiency of the calculation. As each voxel pair is checked the counter for each colour combination in the element of the matrix is incremented according to the voxel combination (i.e AA, AB etc.). After every voxel pair has been checked, the distances between the voxel pair are calculated from the coordinates of the storage matrix. This step allows the distance calculation to be performed only once also greatly improving the efficiency of the calculation. The entire process is depicted in flow chart form in figure 3.14. The distance histograms are converted into probability distribution fucntions by dividing the number of a given type of voxel combinations found at a certain distance by the total number of voxels combinations found at that distance. An example showing how the PDF of AA is calculated is shown in equation 3.1. AB is used to denote both the AB and BA voxel combinations as the order is unimportant.

$$PDF(AA) = \frac{AA}{AA + BB + AB} \tag{3.1}$$

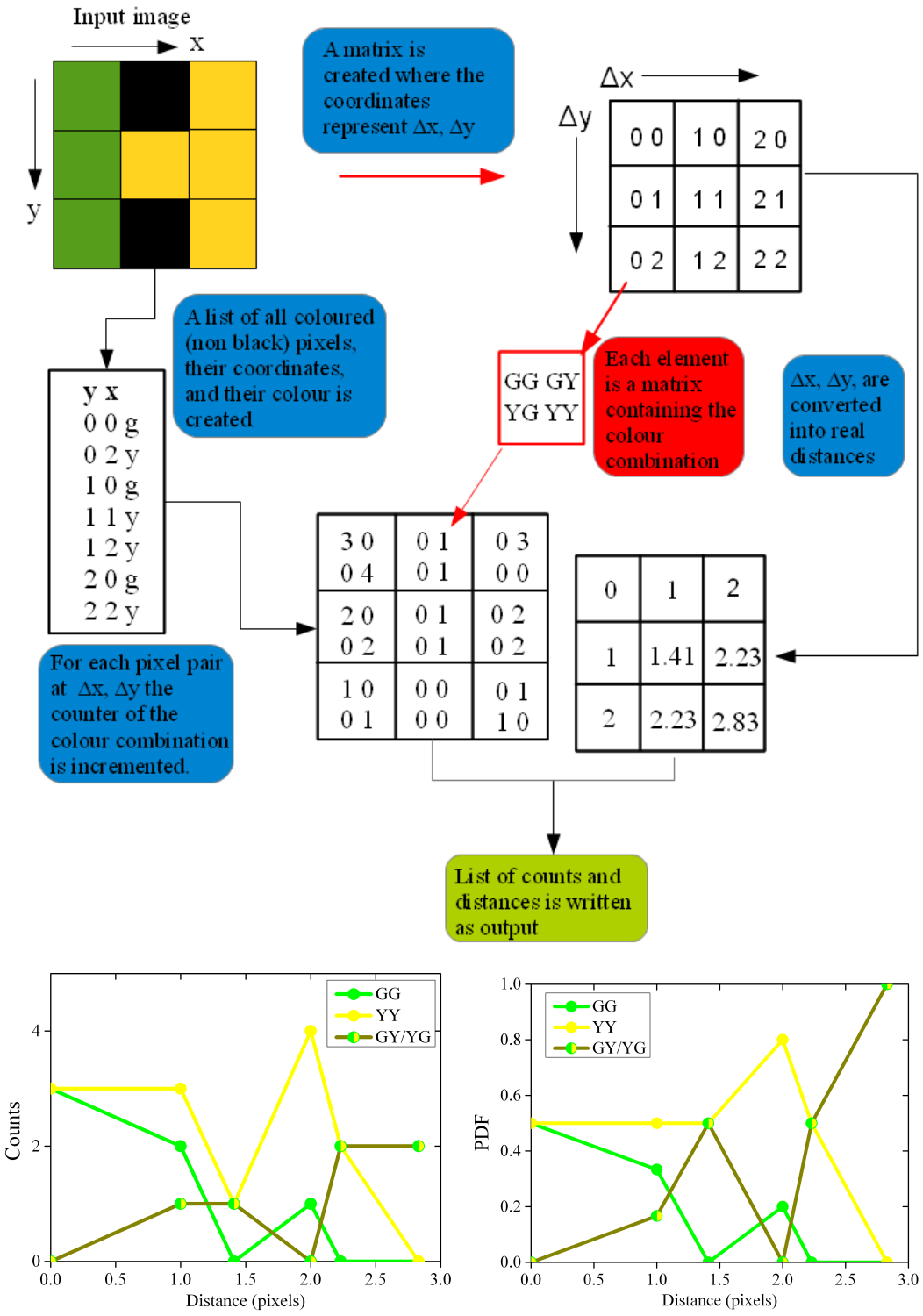

Figure 3.14: Graphical representation of the correlation length calculation for a 2D 3x3 pixel image. The speed of the algorithm is greatly improved by reading each pixel pair only once, and performing the distance calculation only once at the end, rather than for each pixel pair. From the output of the code, the counts and distance information the PDF for each colour can be calculated.

The correlation length code as described above calculates the probability density function of the wetting surfaces. Simply put, the three curves plotted in each graph of figure 3.15 are the probability of being in a certain phase after moving a distance (measured in bead diameters) away from the starting point. The blue and orange curves represent the probabilities to remain in the same phase- starting and ended in either a blue of orange voxel. The black curve represents the probability to change phase, starting in either blue or orange, and ended in the other colour, irrespective of the order. The correlation length is taken as the cross point between the blue and orange and the black curves. At this distance the probability to remain in the original phase (either blue or orange) is the same as to change into the other wetting surface. Now it can be understood that ξ describes the spatial extension of wetting patches.

From the curves shown in figure 3.15, two important pieces of information can be learnt. The first is the value of the correlation length, which is displayed on the figure. The second piece of information is a confirmation of the global distribution of wetting surfaces inside the packing. The values of the blue and orange curves at a distance of zero show the relative numbers of blue and orange voxels extracted from the tomography images. For all samples each colour makes up 50% of the total extracted surface voxels. The composition of the mixed and cluster samples is the most clear, as they are created by weighing set amounts of each kind of bead on an analytical balance. As the volumes of the beads have clear x-ray contrast the segmentation of the beads, and surfaces is relatively straightforward. Because of this, the high amount of confidence in the sample composition, and in the surface segmentation, the variation between the blue and orange curves can be understood as a natural error bar for this measurement.

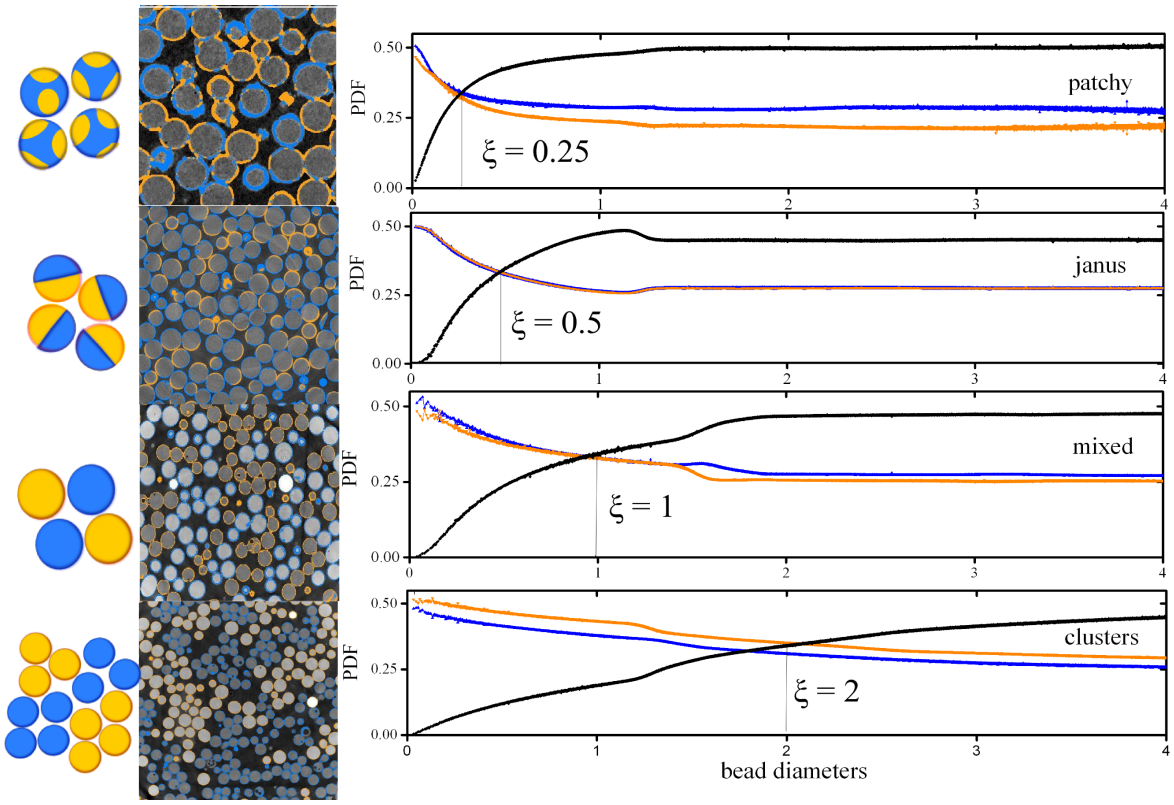

Figure 3.15: The correlation lengths with the cartoons of the sample types and the tomography images used in the calculation are plotted. From top to bottom the samples are patchy, janus, mixed and clusters. The y-axis shows the probability density function to end up in a voxel of the same value (blue or orange) after moving a distance d (x-axis, normalised to a bead diameter). The colours of the curves blue and orange represent the different values of the surfaces and the black curve shows the probability to change from a blue voxel to an orange one. The correlation length ξ is taken as the crossing point between the blue, orange and black curves, and is indicated on the graph.

3.5 Summary

This section has described the preparation and characterisation of a library of samples with spatial distributions of wettability which span the length scales from sub-pore to multiple pores. The wetting heterogeneities have been classified using a simple statistical descriptor called the wetting correlation length. Each type of sample here had a distinct correlation length for each wettability pattern. This is the first time a minimal descriptor has been proposed for mixed wetting porous media. The effect of the correlation length on macroscopic properties of samples of these types of grains will be examined in chapters 4 and 5.

Chapter 4

Capillary pressure saturation experiments

This chapter describes the Capillary Pressure Saturation Experiments used to measure the average wettability and the energy dissipation fluids experience as they are forced through a porous media. The first section describes the experimental apparatus used and the protocol of running an experiment. The second part details the results obtained for the different sample types and explains the differences observed between the samples.

4.1 Experimental

Capillary pressure saturations curves were obtained for the mixed wet samples that were described in chapter 3.

The experimental apparatus was designed and built in house in collaboration with Benoît Semin, and optimised to allow collection of multiple pressure saturation curves per sample. This section describes the experimental set up, choice of materials for the experimental cell, and details the measurement protocol for a Capillary Pressure Saturation curve.

4.1.1 Capillary pressure saturation apparatus

Capillary Pressure Saturation curves were measured using a self-built experimental apparatus, sketched in figure 4.1 and how it looks in the lab in figure 4.2.

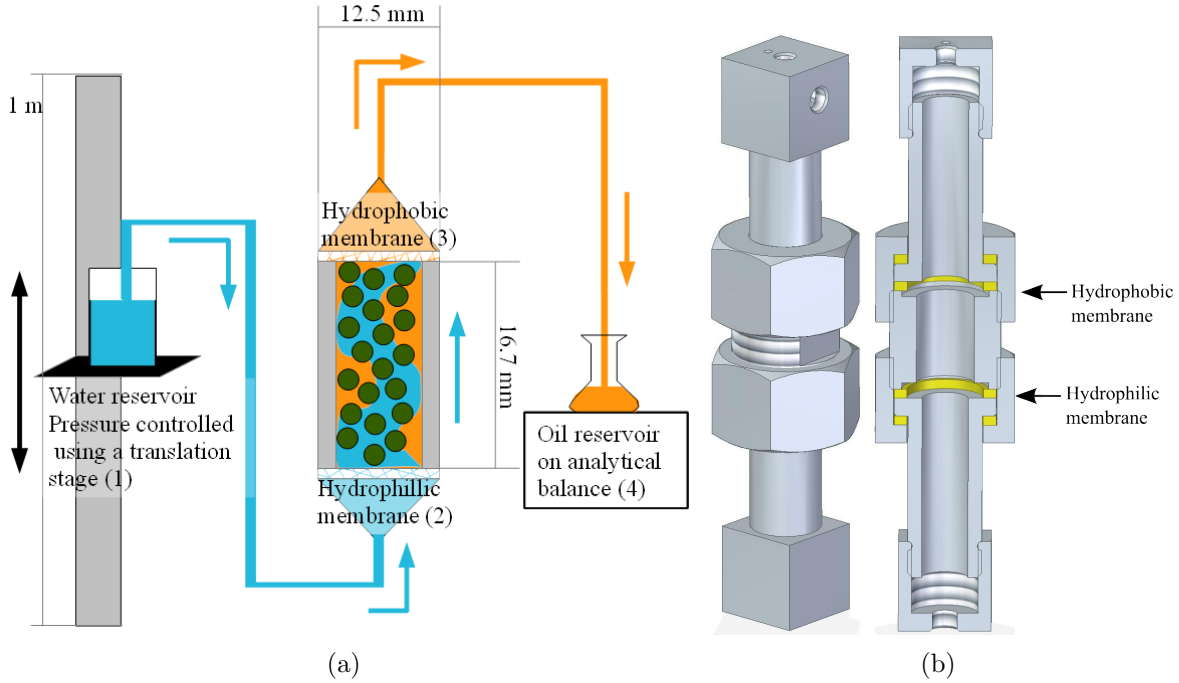

Figure 4.1: Sketch showing (a) the experimental capillary pressure set up and (b) 3D detailed drawing of the measurement cell showing where the membranes are placed. The capillary pressure, $P_c = P_{water}$ - P_{oil}, is set difference in heights between the liquid levels in the water reservoir (1) and oil reservoir (4). The flow of fluids is controlled by a pair of semi-permeable membranes. The hydrophilic membrane (2) allows flow of water, but not oil, and hydrophobic membrane (3) allowing flow of only oil through the membrane. The water pressure is controlled using a translation stage (1) where the height of the water reservoir sets the hydrostatic pressure of water, and the movement of hexadecane in and out of the cell is measured on an analytical mass balance (4).

To obtain the Capillary Pressure Saturation curves, a bead sample is held inside the pressure cell, which has a cylindrical body (see figure 4.1). A hydrophobic membrane is placed at the top part of the sample (permeable to oil but not to water) and a hydrophilic membrane (permeable to water but not to oil) at the bottom. An oil reservoir is connected to the hydrophobic membrane, and a water reservoir to the hydrophilic one. The oil saturation, i.e. the volume of oil between the membranes divided by the total liquid volume, is measured as a function of the pressure difference between the oil and water reservoirs.

In this setup, the cell body is made of brass or polyether ether ketone (PEEK). The latter material is X-ray transparent. The cell consists of a bottom part, a central part containing the beads and a top part. The use of three parts make the filling and cleaning of the cell easier. The beads are contained in a cylinder of diameter 12.5 mm and height 16.7 mm, and these dimensions are the same for both materials. The three parts are indicated in figure 4.1b. In the case of the PEEK cell this cylinder is inside the central part of the cell. In the case of the brass cell, a Teflon cylinder (outer diameter 18 mm) is inserted inside the central part so that the geometry of the bead sample is the same.

The hydrophobic membrane (Fig. 4.1(3)) consists of two layers: a thick membrane (Porex XS-96190, pore size 7-12μm, height 1.5mm which ensures that the membrane is mechanically strong enough and a thin membrane (Sartorius 11806-47-N, PTFE, pore size 0.45μm, height 115-145μm, which prevents any water to flow through it. The two membranes are held together using two magnets (Supermagnete, diameter 3 mm, height 1 mm, nickel coating). The thick membrane is in contact with the beads, because the thin hydrophobic membrane is easily damaged when in contact with the beads. Similarly, the hydrophilic membrane (Fig. 4.1(2)) is made using a thick Porex XS-8259 and a thin Sartorius 25006-47-N polyamide membranes. The thin hydrophilic membrane is in contact with the beads because it is not damaged by bead contact.

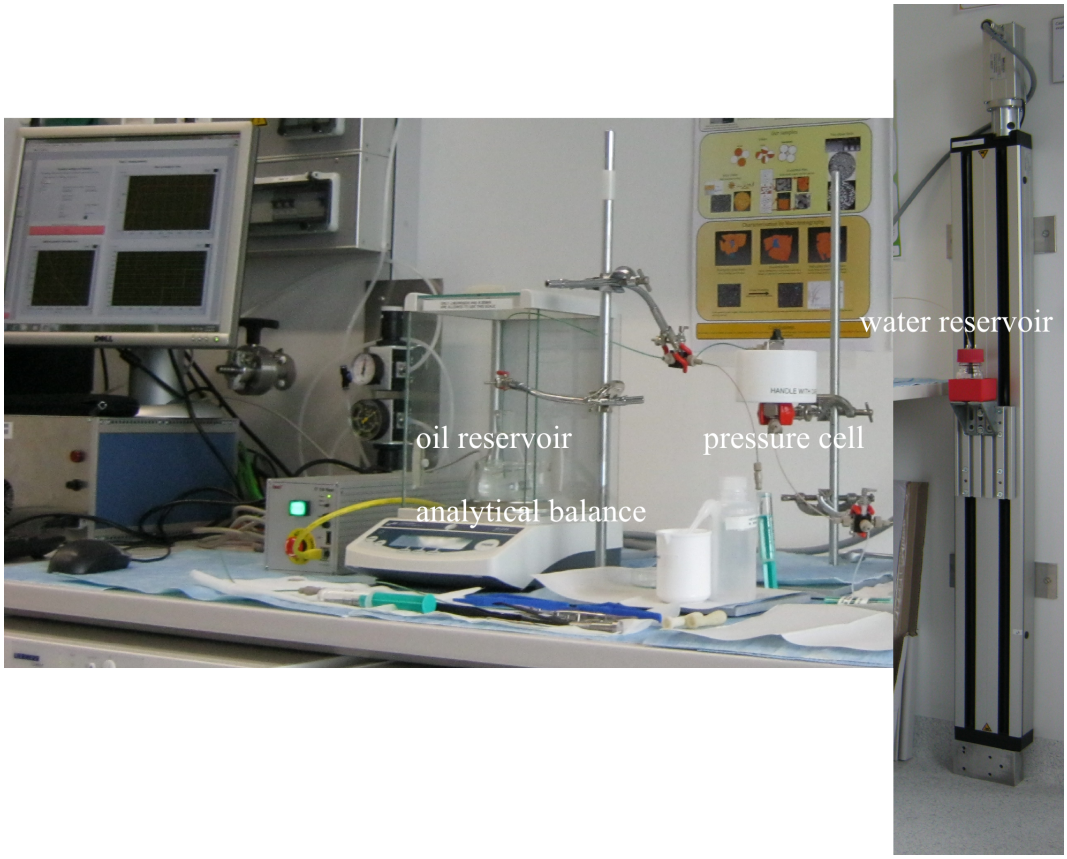

Figure 4.2: Photo of the experimental set up showing the analytical balance with the oil reservoir, and the translation stage with the water reservoir.

The top part of the cell is filled with oil, as is the tubing connecting it to the main oil reservoir, a glass Erlenmeyer, which is open to air. To avoid any force transmission the tubing it fixed under the oil surface, but not touching any of the walls. This tubing is made of PEEK and is bought from Upchurch Scientific: OD 1/16 inch (1.6 mm) , ID 0.03 inch (0.8 mm), length $\sim$ 25 cm. The diameter and length of the PEEK tubing have been chosen to minimize the pressure drop in the tubing, and thus to keep the time scale of an experiment within

1-2 days. The typical flow speed during imbibition is approximately 0.02μ L $\cdot$ s^{-1} (max $\sim$ 0.06μL $\cdot$ s^{-1}).

A 3-way valve (Hamilton HV3) is placed at the middle of the PEEK tubing, which allows us to fill the PEEK tubing. Similarly, the bottom part of the cell is connected to a 250 mL glass bottle open to air through a PEEK tubing (140 cm) with a 3-way valve in the middle part. Both the water and oil reservoirs have large liquid air interface (19.5 and 18 cm^2 respectively), so that the liquid level remain constant (maximum height change of 0.47 mm, which would correspond to a pressure change of 0.05 mbar) with respect to the reservoirs, and so that the Laplace pressure drop at this interface is negligible.

The erlenmayer containing the oil is placed on the plate of a balance (Fig. 4.1(5)) (Denver Scientific, SI-234), 0.1 mg readout) to measure the quantity of oil removed from the the sample as a function of time. The water pressure is set by translating vertically the water reservoir using a 1m high translation stage (Isel, Germany). The balance and the translation stage are computer controlled using a Labview routine.

The two fluid couples used for the experiments are listed, with the properties of the pairs in table 4.1. The second liquid-pair, with the 2 M KI$_{(aq)}$ solution is used for X-ray contrast in visualisng the liquid distributions (chapter 5). The capillary length for the hexadecane-millipore water couple is larger than the height of the cell, and so the effects of gravity on the imbibition/drainage can be safely neglected. In the case of the salt solution, because of the greater density difference between the two liquids, the capillary length is half that of the cell height, meaning that gravitational forces on liquids might play a role during imbibition/drainage. However, as shown in chapter 5 analysis of the invading front morphology showed that under the experimental conditions used, this is not the case.

Liquid pair	$\Delta\rho$ $[kgm^{-3}]$	Interfacial tension initial γ_i $[mNm^{-1}]$	Interfacial tension final γ_f $[mNm^{-1}]$	Capillary Length (mm) λ_c
Hexadecane-Millipore Water	227	51 $\pm$ 1	35 $\pm$ 1	22.9
Hexadecane-2M KI$_{(aq)}$	558	48 $\pm$ 1	45 $\pm$ 2	8.76

Table 4.1: Physical data for the fluid-pairs used for the capillary pressure measurements. The capillary length is calculated using the initial interfacial tension values.

The materials of the experiment have been chosen specifically because they do not release surfactants into the oil or water phases. This was checked by measuring the surface tension between the oil collected above the hydrophobic membrane after an experiment and millipore water. The testing of each component is described in detail in subsection 4.1.5

The temperature of the room is regulated to be $21 + / - 0.5$°C throughout the experiment.

4.1.2 Experimental procedure

Prior to the experimental runs, all air is removed from the system by degassing the beads and the membranes. The sample beads and hydrophobic membrane are degassed in hexadecane and the hydrophilic membrane is degassed in water. Beads are loaded into the cell under oil, to prevent introduction of air, and all tubing is primed with fluid at the beginning of the experiment.

The points of Capillary Pressure Saturation curves correspond to a steady state regime. The aim is to determine the steady saturation for a set of given capillary pressure. The initial state of the sample is in oil. The pressure of the water is increased in equal steps (usually 1 mbar) and oil is produced from the cell. At a given saturation, no more oil is produced with further increasing pressure steps, and this amount of liquid is referred to as the residual oil saturation.

We know the internal volume of the cell is 2.05 mL, that the porosity of the sample is approximately 40%, and that the total fluid volume within the cell is 0.82 mL. The density of hexadecane is 0.77 g/mL. The total mass of hexadecane which can be produced from the cell is therefore $\sim$0.65 g.

The pressure is only increased or decreased (depending on the position in the ramp) when the mass reading on the balance reaches a steady value. It is considered that the saturation reaches a steady value when the mass reading on the balance remains constant within a standard deviation of 0.0005 g during 200 s (see figure 4.3). At this point, the saturation value and the capillary pressure is plotted on the CPS curve and the pressure is increased/decreased.

As a protocol capillary pressures from -20 mbar to +20 mbar and back to -20 mbar by 1 mbar steps is chosen, (a 1 cm vertical translation of the stage corresponds to a 1 mbar pressure change). These loops are repeated 3 to 5 times to reach a steady cycle.

This procedure, which consists in changing the pressure rapidly where the saturation is hardly changing and changing it slowly in the pressure region where the saturation is changing a lot allows significant gains in speed of the CPSC measurement while maintaining a high level of accuracy. This also allows us to make several loops to check the steady behaviour of the system, which is rare in the literature, due to the extensively long time scales otherwise required for such a measurement, which can be matters of weeks per measurement. [23, 42]. At the end of the measurements to beads are collected dried and weighed, and the packing fraction is calculated.

4.1.3 Calibration of the zero capillary pressure

The zero capillary pressure point is calibrated by performing a CPS experiment without beads in the cell. An example of an empty cell experiment is shown in figure 4.4. This allows us to account for the different densities of the liquids used, and eliminates any errors which

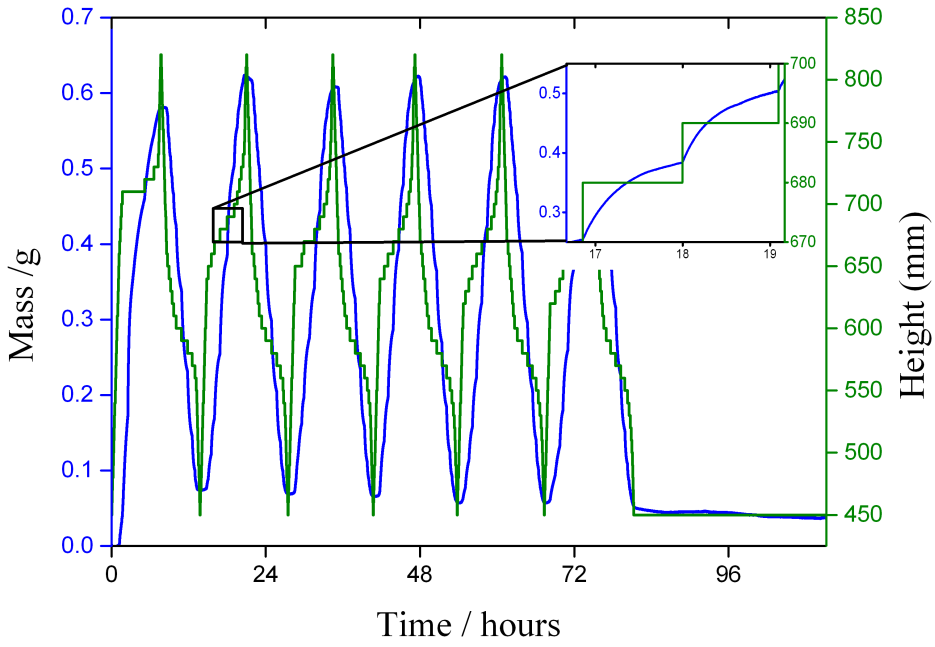

Figure 4.3: Raw data obtained from CPSC experiment. Mass of oil recovered (blue) and height of the translation stage (green) with time. The inset is a close up of each step. The convergence of the mass curve coincides with increasing the height of the translation stage.

might be caused from measuring the heights manually. The oil saturation change at a given translation stage height, which corresponds to the reference height (and thus the reference pressure) sets the zero capillary pressure. The height of the stage when the water is able to displace the oil during the imbibition phase, and the oil replaces the water during the drainage phase gives the zero point. The height is very reproducible, with the same value (650 mm) being observed for each of 4 calibration measurements, one of which is shown in figure 4.4. What can been seen from this plot, is that even with an empty cell, a hysteresis corresponding to 10 mm is measured. This is caused by the step height used for the pressure ramp protocol, and the ideal zero point is likely between these two values. For the calibration of the experiments the height at which the empty cell imbibies the water was used as the zero capillary pressure value. The geometry of the set-up, that is the cell position, oil and water levels with respect to their containers, is not changed when performing the experiments with beads, preserving the calibration.

4.1.4 Effect of the thresholding criteria

Capillary hysteresis is a permanent hysteresis [100], which means that the hysteresis does not vanish when the waiting time is increased. If the waiting time is too small, the measured hysteresis would be time dependant. Therefore in order to optimise the experimental protocol the minimum waiting time at each step, once a stable value is reached should be used.

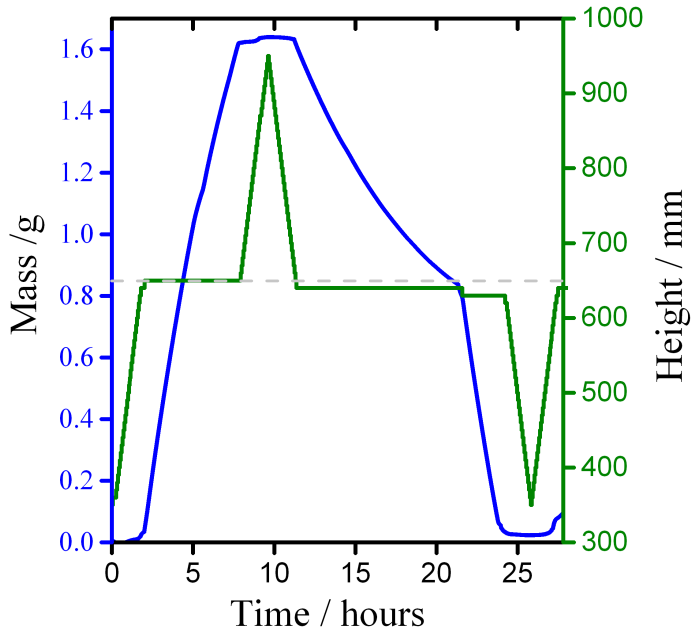

Figure 4.4: Measurement of capillary pressure saturation on an empty cell. The pressure at which the oil is displaced by the water is determined to be the zero capillary pressure reference.

The minimum waiting time, used in the measurement of Capillary Pressure Saturation curves employed in this investigation, is determined by thresholding criteria which decides when all imbibition and/or drainage events at a given pressure have finished. The threshold is defined as the standard deviation of the measured mass on the analytical balance for a given counting time. In our experiments the threshold is set as 0.0005 g/200 s, that is the standard deviation of the mass must be less than 0.0005g over a measurement time of 200 s. To check the validity of these values as thresholding criteria, experiments were also run using values of 0.0005 g/400 s and 0.0005 g/600 s. The different hysteresis loops recorded for these cycles can been seen in figure 4.5. The irreducible saturations (S_{water} and S_{oil}) and hysteresis loop opening was compared for the different counting times and the differences measured between experiments were within the experimental variation for a single experiment. Therefore the counting time of 200 s was deemed to be sufficiently long to determined the end of drainage and imbibition events for a given pressure.

4.1.5 Properties of the non-aqueous phase

The important properties of the non-aqueous phase is that is has a constant interfacial tension (IFT) and that it has a low vapour pressure, so there is no loss of mass due to evaporation during the experiment. It would also be beneficial if the liquid was non-toxic. For these purposes, hexadecane was chosen as the oily phase.

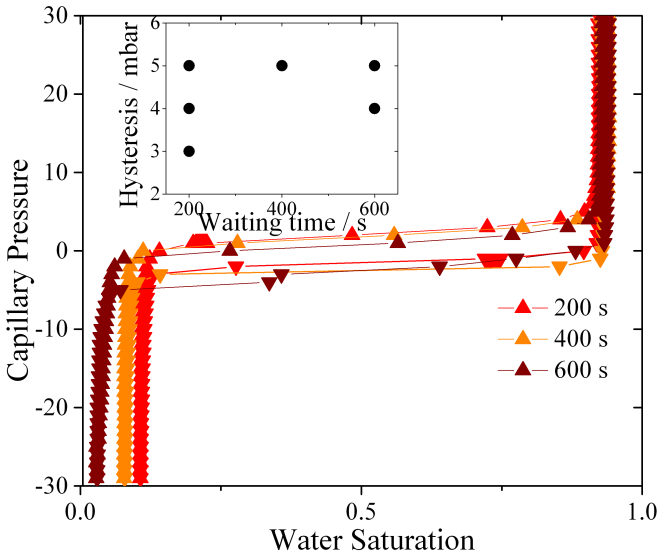

Figure 4.5: Three capillary pressure saturation cycles, measured for the same mixed gold sample, taken using different thresholds (indicated by colour). The inset shows the hysteresis loop opening value versus the threshold waiting time. The differences observed were within the experimental scatter.

Alkane content

99% hexadecane (Sigma Aldrich) and 95% hexadecane (Alfa Aesar) were trialled to determine if the alkane fractions were important. The oils were purified by running them through an alumina column to remove the surfactants. The interfacial tension was measured by the pendant drop method, before and after the purification against millipore water. The results are shown in figure 4.6 and indicate that this both a necessary and successful purification step. The listed purity of the hexadecane refers to the alkane fraction, i.e what is the maximum percentage of short or longer change alkanes allowed in the liquid. It is not expected that long chain alkanes of similar length would make a large impact on the interfacial tension [110], and after purification there was no measured difference between the two oils. Therefore it was decided that the more economical 95% hexadecane was suitable for our experiments.

Identification and elimination of trace surfactants

The purity of the non-aqueous phase was determined by the interfacial tension (IFT) using the pendant drop method. After it was noticed that there was a substantial drop in IFT for the oil phase after a CPSC measurement compared to the filtered hexadecane. To isolate the source of the contamination each component of the cell was degassed and rested in filtered hexadecane for 24 hours and then the IFT of the liquid measured. The results of the IFT tension measurements for each component are listed in table 4.2.

In the original design of the cell, a soft inner tubing made from Tygon-F4040A plastic, a typical material used for transporting fuels and oils was used instead of the Teflon tubing

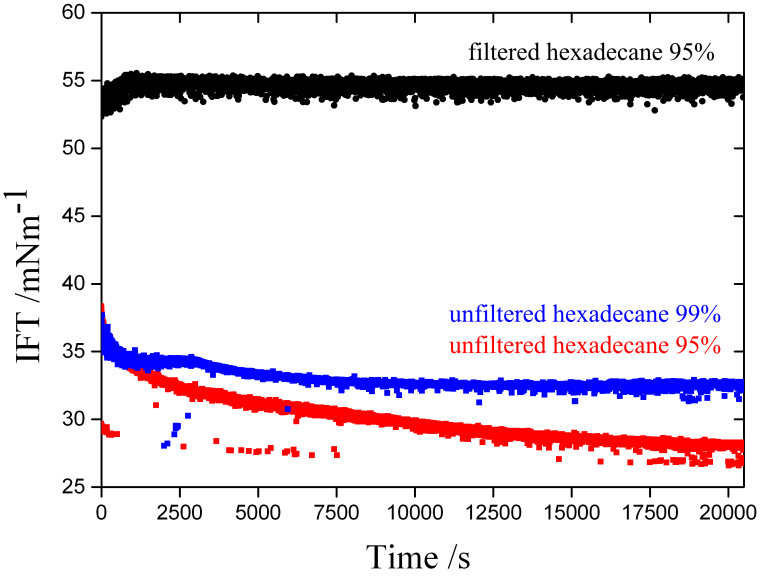

Figure 4.6: Interfacial tension measurements of hexadecane 95% and 99% before filtrations and 95% hexadecane after filtration. The unfiltered hexadecanes have a low starting value, and continue to decrease over time. The filtered hexadecane has a much higher initial IFT and remains constant over the 20,000 seconds of the measurement.

to create the inner cell surface. Tygon-F4040A has very good resistive properties towards alkanes and does not swell in hexadecane, unlike many plastics. However, as can be seen from table 4.2 measurement of the hexadecane in which Tygon-F4040A tubing had been soaked for 24 hours had a substantially lower IFT, and was the tubing was clearly contaminating the oil.

The only component which caused a major drop in the IFT of hexadecane with water was the Tygon tubing. To eliminate this source of contamination all seals and the inner tubing was changed to Teflon.

Table 4.2: Interfacial tension of millipore water/ hexadecane after each component of the cell had been soaked in the hexadecane for 24 hours.

Cell Component	IFT [mNm^{-1}]
Filtered Hexadecane	54
PEEK tubing	53
hydrophilic membrane	52
hydrophobic membrane	54
teflon seals	50
Tygon-F4040A	21

Bead coatings as possible sources of contamination

To investigate if the thiol and silane coatings used to render the beads hydrophobic were potential sources of contamination samples of silver and silane coated beads were degassed in hexadecane, rested for 24 hours and then the interfacial tension measured. The results are shown in table 4.3. The interfacial tension of the hexadecane remained constant after soaking the beads in the oil and therefore it was concluding, there was no significant degradation of the coating over a period of 24 hours.

Table 4.3: Interfacial tension of millipore water/ hexadecane after coated beads had been soaked in the hexadecane for 24 hours.

Coating	IFT [mNm^{-1}]
glass	52
Silver(thiol)	51
silane	52

4.2 Results and Discussion

This section discusses the results obtained from the capillary pressure saturation (CPS) measurements for the samples with different correlation lengths (as described in chapter 3).

First the important features of a capillary pressure saturation curve need to be identified. Figure 4.7 is a typical capillary pressure saturation curve measured for a sample of patchy beads. After the first initial imbibition branch of the curve, the following drainage and imbibition fall on top of each other, indicated the experiment is now in a steady cycle. The multiple cycles (up to six) per experiments are able to be measured due to the efficiency of the pressure protocol used.

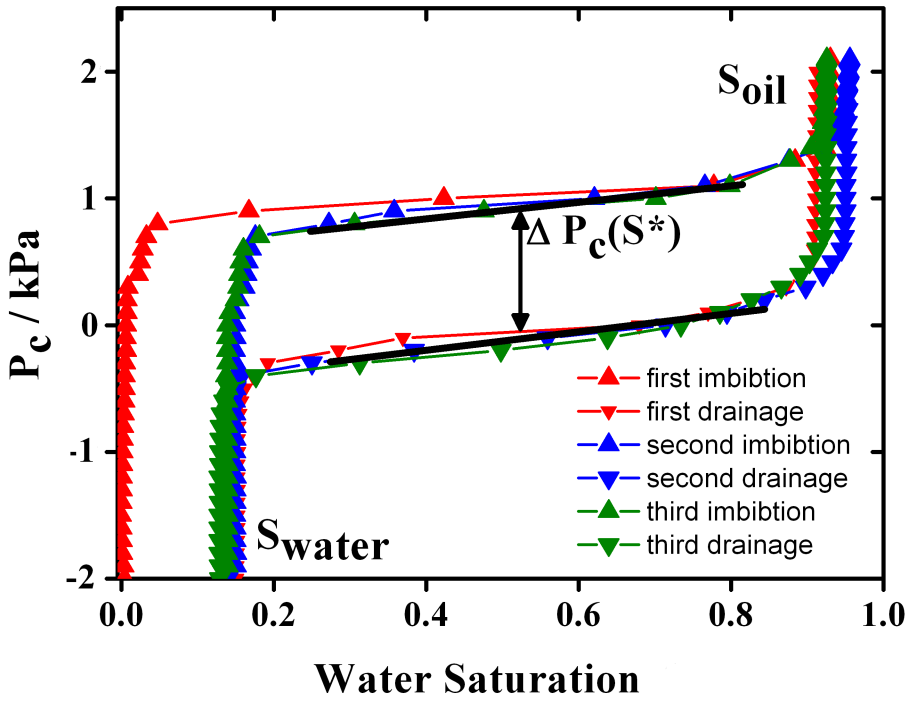

Figure 4.7: Measured CPSC for a patchy sample. The irreducible oil saturation, S_{oil}, is defined as the volume of water remaining when no more mass changes are recorded at high capillary pressure and S_{water} is the corresponding irreducible water saturation occurring at low capillary pressures. The hysteresis loop opening, ΔP_c, is taken as the distance between the imbibition and drainage curves at the point $S^* = (S_{\text{water}} + S_{\text{oil}})/2$. The colour scheme, used for all CPSC plots is red for the first imbibition/drainage cycle. Blue for the second and green for the third. Upwards pointing triangles represent water invasion (also referred to as imbibition) and downwards arrows refer to oil invasion (also referred to as drainage).

4.2.1 Influence of correlation length

Capillary Pressure Saturation experiments were performed for each sample type multiple times to ensure reproducibility. From each curve the irreducible oil S_{oil}, irreducible water

saturations S_{water} and the hysteresis loop opening ΔP_c measured as the distance between the linear regions of the imbibition and drainage curves at $S^* = (S_{water} + S_{oil})/2$ are extracted. Representative CPS curves for each sample type are shown in figure 4.8.

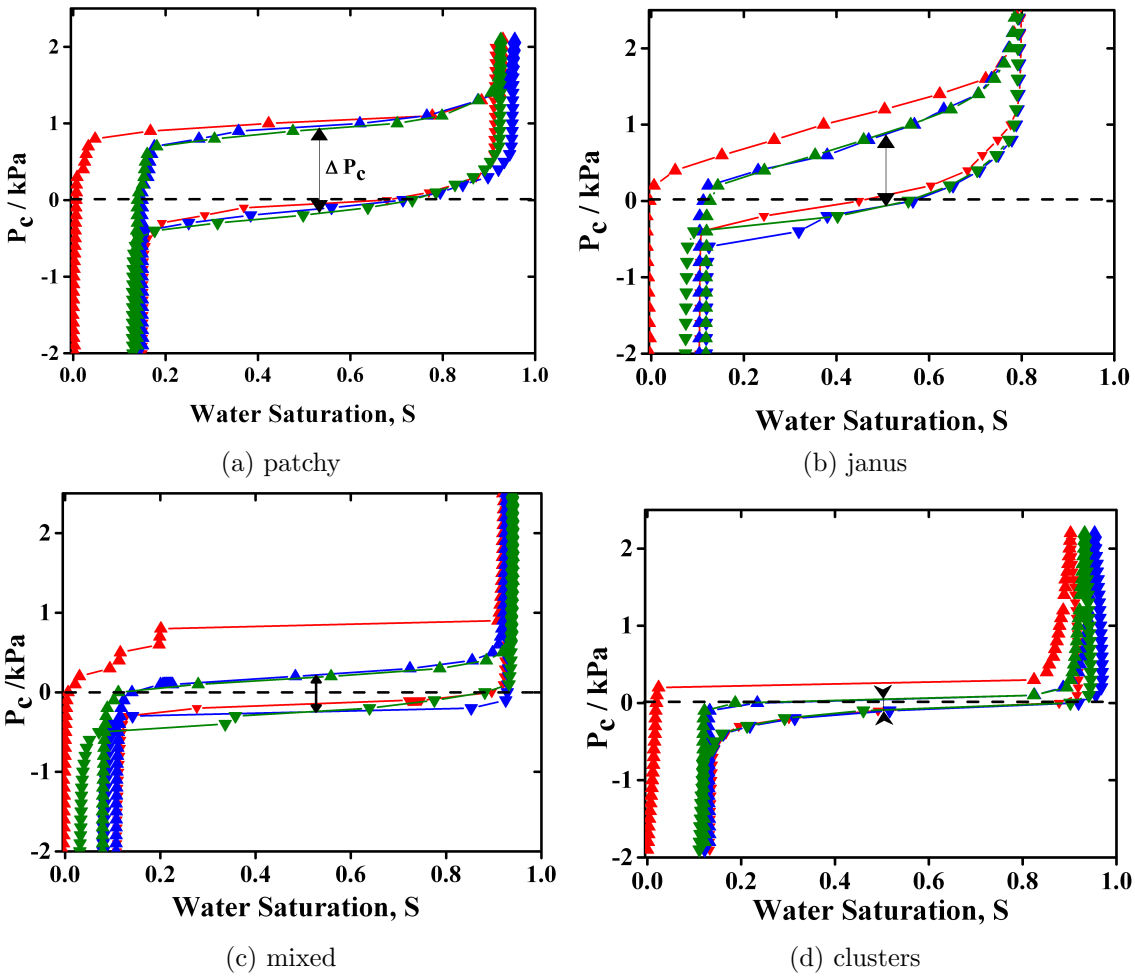

Figure 4.8: Capillary pressure saturation curves for each sample type. The patchy beads used in this experiment had a ctms coating, and the janus, mixed and cluster samples displayed here were created with the gold-thiol surface treatment.

Wettability according to AH and USBM

The wettability, according to the AH (Ammot-Harvey) and USBM classifications of the samples were calculated from the measured capillary pressure saturation curves. The classifications are shown in table 4.4. The sample composition is known to be mixed with 50:50 ratios of hydrophilic to hydrophobic surfaces and the AH and USBM indexes would be expected to be zero for all samples. Instead, what is seen, is that the samples have different qualitative wetting classifications based on these measurements, although, with the exception of the

patchy samples, the variation between multiple samples of the same sort is as large as the deviations from 0. This might be in part due to the finite sample size, i.e larger bead packs might generate less varied results. But, what is clearly seen, is that neither the AH, or USBM describes the differences between the CPS curves shown in figure 4.8. As both these indices mainly describe the average position of the curve compared to $P_c = 0$, this is not unexpected.

Table 4.4: Calculated wettability using Amott-Harvey and USBM methods for all samples. The wettability classifications are ow = oil wetting, wow = weakly oil wetting, ww = water wetting and www = weakly water wetting

Sample type	USMB	Amott Harvey	wettability
Patchy	-1	-0.3 ±0.1	ow
. Janus	-0.67 ± 0.18	-0.1 ±0.1	ow/wow
Mixed	0.3 ± 0.3	0.1 ±0.1	www
Clusters	0.4 ± 0.3	0 ±0.1	ww/www

Irreducible saturations

The irreducible saturations S_{oil} and S_{water} for oil and water respectively are plotted against the wetting correlation length to determine whether this has an impact in the amount of trapped oil or water in the bead pack as shown in Figure 4.9. There is no clear trend observed due to the correlation length and no systematic deviations between the irreducible saturations for different coating types. There is significant scatter in the values of the irreducible water saturations across all samples. The irreducible oil saturations for samples with a wetting correlation length of less that a bead diameter, also do not show a trend, being all around 10% of the interstitial volume of the bead pack, with the exception of the cluster samples which show high variability, also within a single experiment.

Recently studies of trapped phases in glass bead packs found that a single ganglia could constitute the majority or the remaining phase. [54, 64, 111] The authors used sample sizes of a similar order of magnitude to our experiment. Because the largest ganglia, or trapped fluid blob will be the easiest to mobilise, it is not far fetched to imagine the scatter in residual saturations between experiments, and in the case of the clusters samples, even during a single experiment, could be explained by the difference of only a few ganglia. This point will be addressed further in the following chapter, chapter 5.

It is important to remember that while the irreducible saturations measured in these experiments may seem low compared to core flooding experiments where up to 50% of the oil remains trapped in core [6, 112] there is a fundamental difference between CPS experiments and core flooding. The membranes at the top and bottom of the cell which block the flow of their respective non-wetting phase. What this means, is that even after percolation of the invading fluid e.g water, further displacement of the other phase, e.g oil, continues with increasing pressure until all of the oil droplets are disconnected from the oil reservoir at

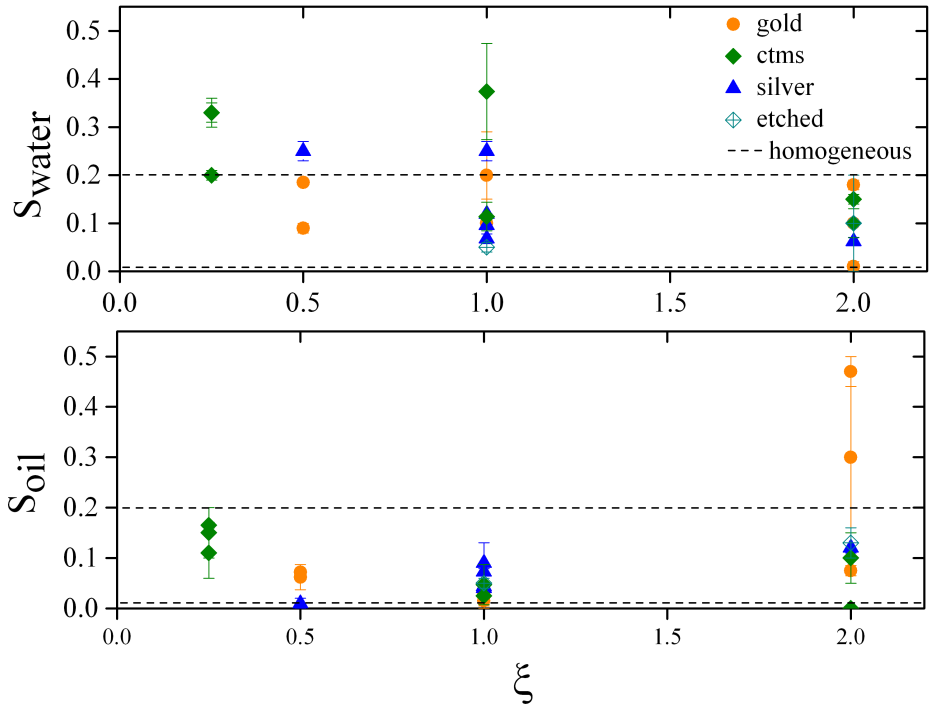

Figure 4.9: Comparison of irreducible water and oil saturations (S_{water} and S_{oil}) normalised by the pore volume within the cell. The error bars are calculated as the standard deviation between the values of the irreducible saturations on successive cycles of the same experiment.

the top. This understandably results in a much lower residual saturation, compared to the volume of oil remaining in the sample at the time of water percolation, or breakthrough as it is often referred to in petroleum engineering literature. Possible ideas to measure where the breakthrough even would occur involve conductivity measurements, such as Archie number measurements [45]. Most of the oil in a reservoir is produced prior to the breakthrough event, and after breakthrough problems with produced water decrease the economy of the recovery process, so understanding which factors enhance percolation (and thus a breakthrough event) and which inhibit is very indeed interesting. Such questions could be addresses in the future with modifications to the existing experimental set-up. One possibility is the inclusion of electrodes to measure the conductivity of the cell. Percolation of the water phase (with added electrolytes) would correspond to a large increase in the conductivity of the cell.

Wetting correlation length

What is clearly sensitive towards the wettability correlation length (Fig. 4.10) is the hysteresis loop opening, that is the shape of the imbibition and drainage profiles. The hysteresis decreases when the correlation length is increased. This is a very robust behaviour observed for the three types of coating. These observations are in agreement with the experimental

findings of Fatt and Klikkov [55], and the numerical results of Sorbie et. al [67] that changing the spatial relationship of water and oil wet beads (that is, having the smallest fraction oil wet and the larger beads water wet and vice versa) significantly effects the shape of the displacement profile. Both of these studies correlate the pore throat size with the wettability, and conclude therefore wettability is important. However, our results demonstrate that even in a homogeneous pore-throat system, wetting domains play an enormous role in the multiphase flow profile, and that the size of wetting domains is important.

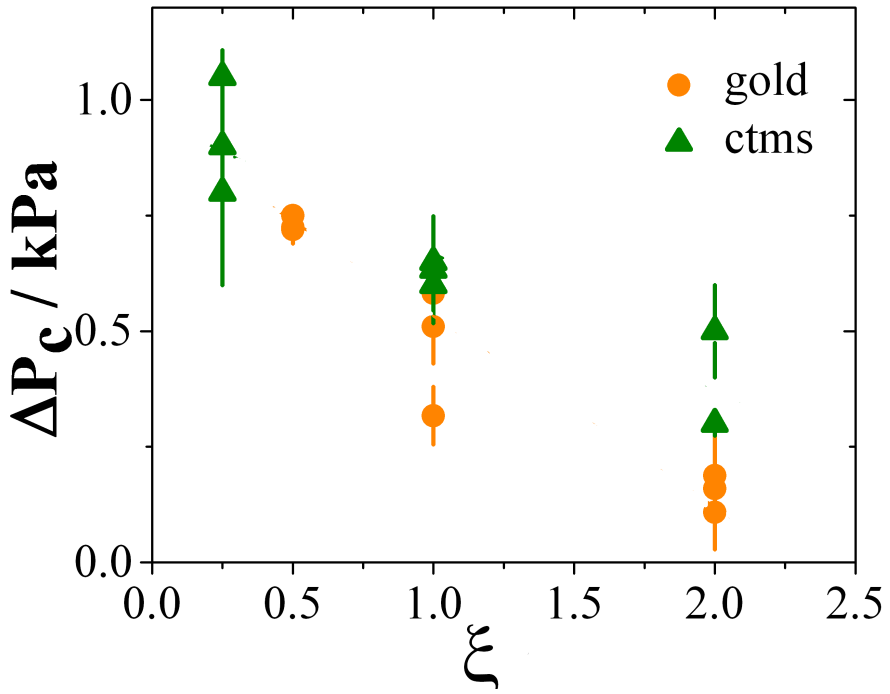

Figure 4.10: Hysteresis loop opening of the capillary pressure saturation curves. There is one data point for each individual experiment. The error bars are calculated as the difference between the hysteresis measured for successive cycles. A monotonic decrease in ΔP_c with increasing correlation length is observed.

As mentioned in section 4.1.4, capillary hysteresis, is a permanent hysteresis. It arises from the dissipative work which occurs from moving contact lines over the bead surfaces. Contact line pinning is particularly strong at junctions between wetting heterogeneities. The number of junctions per bead is inversely proportional to the wetting correlation length, ξ. So patchy samples have multiple pinning sites per bead, and indeed within even a pore space, whereas for mixed samples there are no wetting junctions at which the contact lines can become pinned. Figure 4.10 therefore demonstrates that there is a strong correlation between the increase of pinning sites and the energy dissipation. This shows that the effect of pinning starts to dominate when the wetting heterogeneity is of the order of a pore dimensions. This behaviour is robust, occurring for both types of coatings. On the other hand, mixed and cluster samples have hysteresis loop openings ($\Delta P_c(S^*)$) on the same order as homogeneous

samples (0.4 ± 0.1 kPa). This indicates that when the wetting heterogeneities are larger than the pore diameter, i.e pores have constant wettability, contact line pinning does not dominate the dynamics. In only this case, $\xi \geq 1$, an accurate description of the wetting heterogeneities does not appear to be important, and contact angle averaging techniques [36, 37] are valid.

Influence of surface roughness on capillary hysteresis

Bead samples with rough surfaces, the silver and etched samples were investigated to determine the effect of surface roughness on the measured capillary hysteresis. The results are shown in figure 4.11. Surface roughness, and implicitly, contact angle hysteresis does not appear to play a large role in determining the capillary pressure hysteresis. It was initially thought that because in general rough surfaces exhibit higher contact angle hysteresis rough samples would also show increased capillary hysteresis behaviour. However, the same trends, decreasing hysteresis with increasing ξ, were also observed for both the silver samples and for etched glass beads coated in silane. This is consistent with the previous findings that surface roughness [113] and contact angle hysteresis [50] are minor effects, compared to the advancing contact angle which appeared to be the control parameter for the measured capillary pressure saturation curves. As there is no significant difference between the advancing contact angles for samples of the sample treatment variety (gold, silver, silane) it can be concluded that the spatial arrangement of wetting surfaces, that is, the wetting correlation length that is the major factor influencing the hysteresis in the capillary pressure saturations measurements.

One possible explanation the lack of increase of capillary hysteresis with surface roughness is that thick wetting films which can form on rough surfaces can reduce the contact line pinning on the beads surfaces [113]. Dullien et al. visualised these thick films inside etched bead packs by adding styrene monomer to the oil phase which was polymerised with UV at the end of the experiment. The beads were extracted and the surfaces imaged with SEM. In the case of thick wetting films, it is expected that the dominant mechanism for capillary hysteresis is again the contact line pinning at the wetting junctions, which would also be a natural boundary for wetting films.

Summary

To summarise the main result of this section: the hysteresis loop opening, $\Delta P_c(S^*)$ is sensitive towards the wetting correlation length, particularly when the size of the wetting heterogeneities is less than a single pore. The average hysteresis loop opening values for each sample type, average over several experiments are plotted in figure 4.12. Another way of describing the correlation length would be to refer to the density of contact line pining sites. Assuming that an interface moving over a chemically heterogeneous surface becomes pinned at the boundaries of two different wetting surfaces, then it is fair to say that the density of pinning sites is inversely proportional to the correlation length. That is, the smaller the spa-

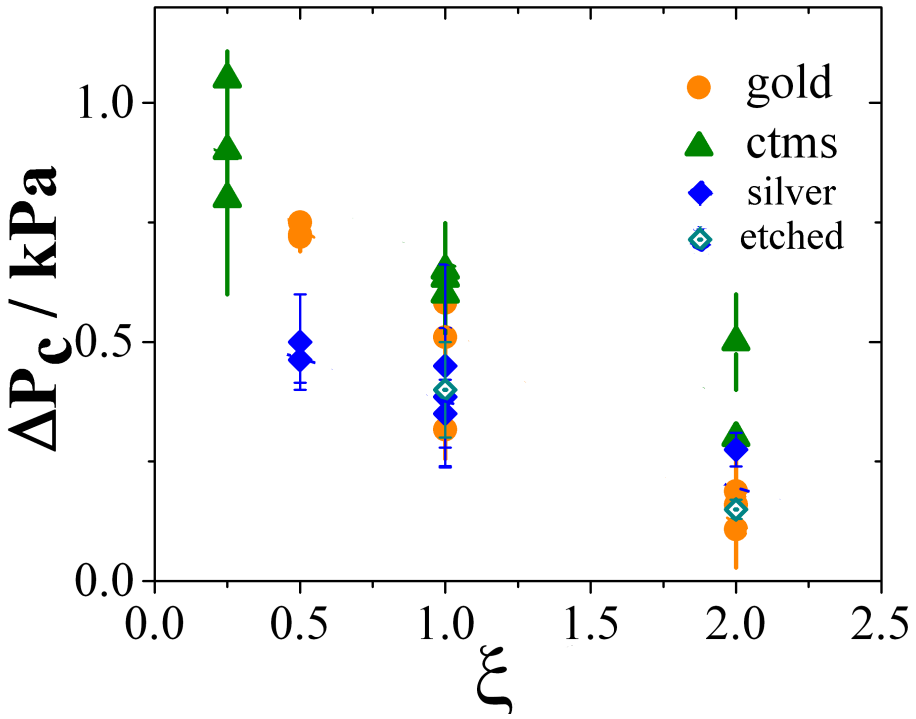

Figure 4.11: Hysteresis Loop Opening of the capillary pressure saturation curves, for all sample types, the smooth samples, gold and CTMS and the rough samples silver and etched. Each data point represents an individual experiment. The error bars are calculated as the difference between the hysteresis measured for successive cycles. Again, a monotonic decrease of ΔP_c with increasing ξ is observed.

tial wetting domains are, the more boundaries that exist within the same area, and therefore a higher density of pinning sites. The pinning of contact lines seems to depend more on the spatial extension of the wetting areas than more local quantities such as surface roughness..

Experiments by Dufour and Baret have directly observed contact line pinning on single janus beads at the gold-thiol/glass junction (figure 4.13). A bead is pulled through a hexadecane/water interface and at the wetting domain boundary contact angle pinning can be observed by an increase in the contact angle.

Assuming that contact line pinning is the major source of capillary hysteresis in these heterogeneous systems, simple sketches of the pore structures of the different samples help to clarify why there is more hysteresis in the patchy and janus samples, compared to the mixed and clusters. A schematic of the different possibilities for pores containing wetting heterogeneities is shown in figure 4.14. For clarity the picture has been drawn in 2D and the pore is approximated by the triangle between three beads, whereas in a 3D bead pack a good approximation of a pore would be the tetrahedra formed between four beads. The clusters and mixed samples are comprised of pores of both types of homogeneous wettability, as well as mixtures of both types of beads. The difference between the clusters and the mixed

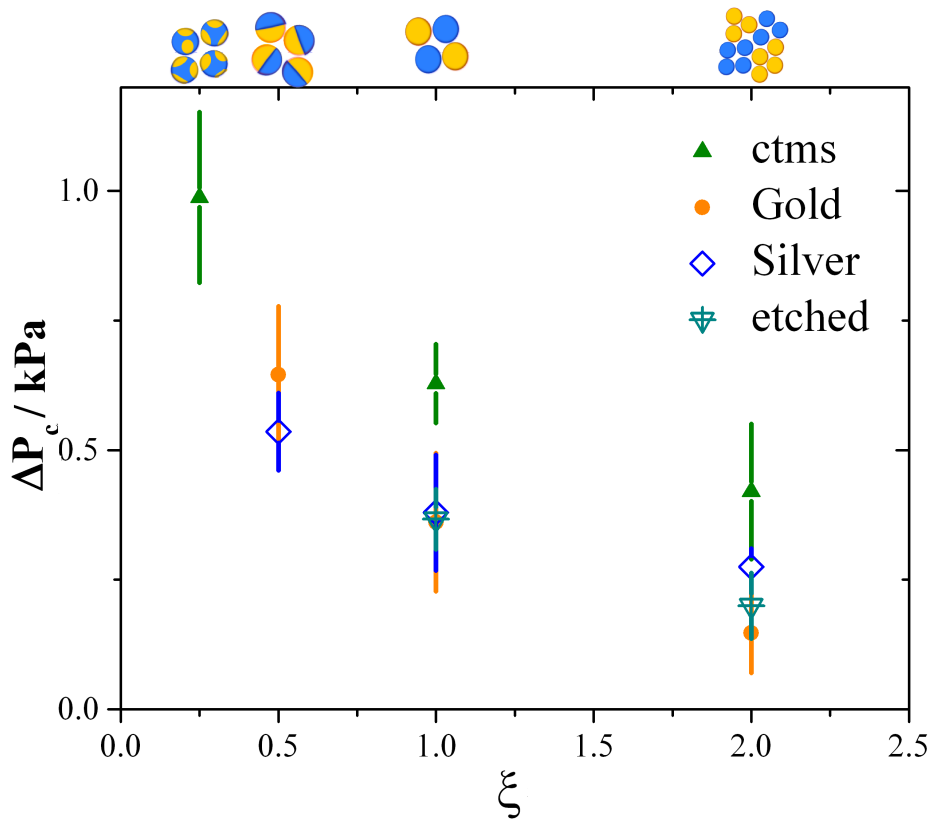

Figure 4.12: Averaged values for the hysteresis loop opening for each sample type. Error bars are calculated as the difference between all cycles of all samples. The trend of decreasing hysteresis loop opening with increasing correlation length is robust; with the same trends observed for each sample regardless of the coating type.

sample is that the cluster sample would contain more of the homogeneous pores (both oil and water wet) compared to the mixed sample. The janus samples have pores which are all a kind of mixed wettability. It is possible, that the beads could arrange such that they also formed a homogeneous pore structure (i.e all blue faces in, all yellow faces away from the pore) however, this kind of ordering is not widespread as evidenced by the correlation length for janus bead packs which do not show any further correlations after a bead diameter. Much more likely is that the beads are oriented so that for at least one, but potentially on of the beads, the boundary to the wetting heterogeneity is present inside the pore. This is also true for the patchy sample, but as the heterogeneities are small still, there could be two heterogeneities arising from the same bead inside the pore. From this sketch it is clear to see that an interface moving through a patchy pore could be pinned several times significantly increasing energy dissipation. For the mixed and cluster samples there are no sharp domain lines inside the pore. This is most likely the reason why contact angle averaging theories appear to be valid for the mixed type samples, as contact line pinning is not the dominant source of dissipation. In natural systems however, which do not contain only smooth surfaces

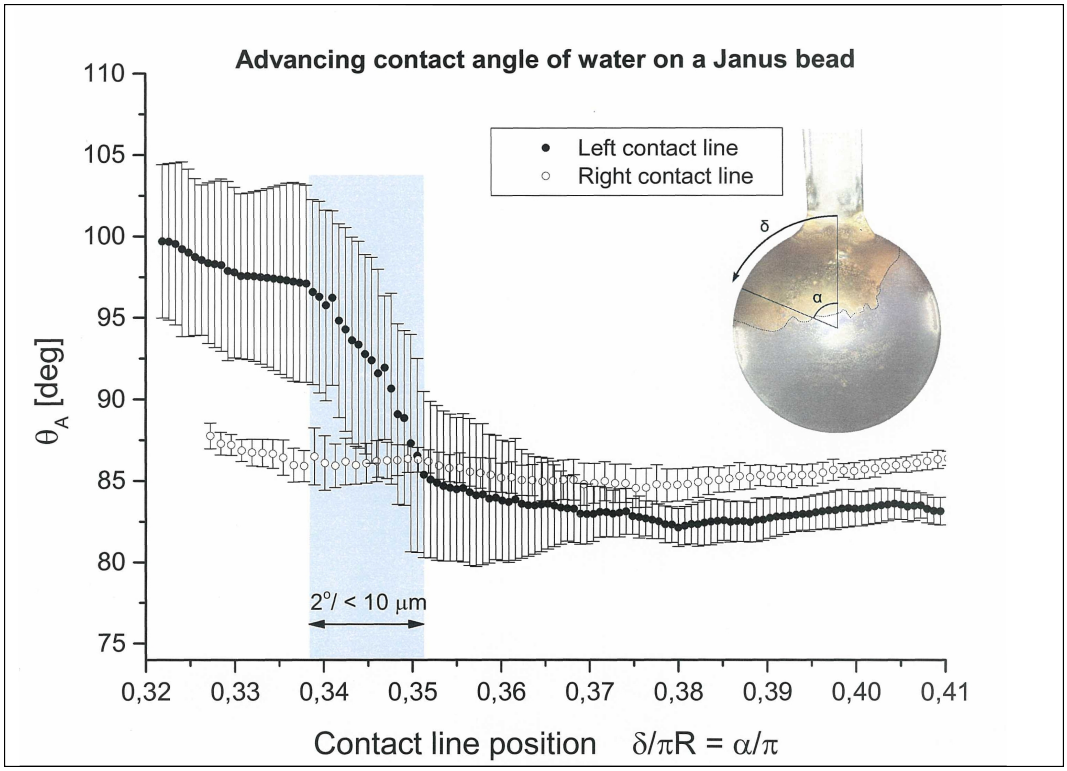

Figure 4.13: Pinning of the contact line at the wetting domain boundary on a single janus grain, diameter of 350 μm, measured by Renaud Dufour. The bead is pulled slowly through a hexadecane/water interface and the contact angle measured on a goniometer. As the interface reaches the domain boundary pinning is observed, evidenced by the step between the two equilibrium contact angles of the gold and glass surfaces.

like bead packs, wetting transitions are quite likely to occur inside pores, and have sharp boundaries so simple mixed bead models poorly represent natural mixed wet porous media.

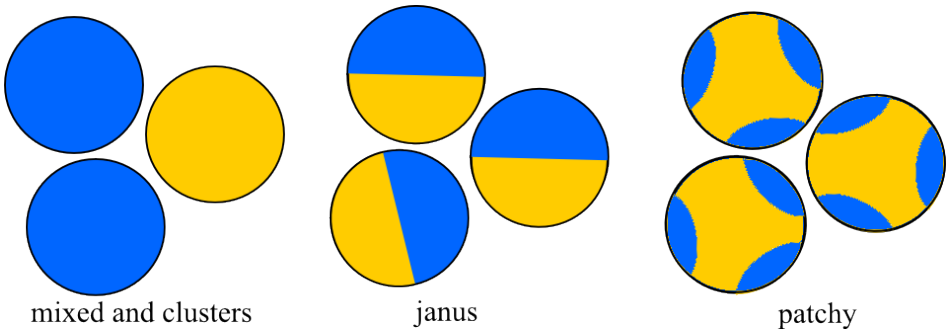

Figure 4.14: 2D cartoon illustrating possible pores that can be formed by the different beads. The potential for pinning sites within the pore is highest for the patchy and then the janus samples. The two colours blue and yellow represent the surfaces of different wettabilities. Pinning sites are located at the junction of the two colours.

4.2.2 Influence of cycle number

As mentioned in section 4.1.2, one of the benefits of this experimental protocol is that the dramatically reduced time scales allows for the measurement of multiple loops of the capillary pressure saturation curves. This allows the opportunity to also investigate the ageing behaviour of the fluid distributions inside the medium as the liquids are pumped in and out.

Hysteresis loop opening

Looking first at the evolution of the hysteresis loop opening with multiple cycle number (figure. 4.15) it can been seen that the hysteresis loop opening is quite stable with a slight tendency to decrease with increasing cycles. One possible explanation for this is the formation of wetting films [113, 114], allowing the liquid to invade more easily and might allow an easier reconnection of similarly wetting pores.

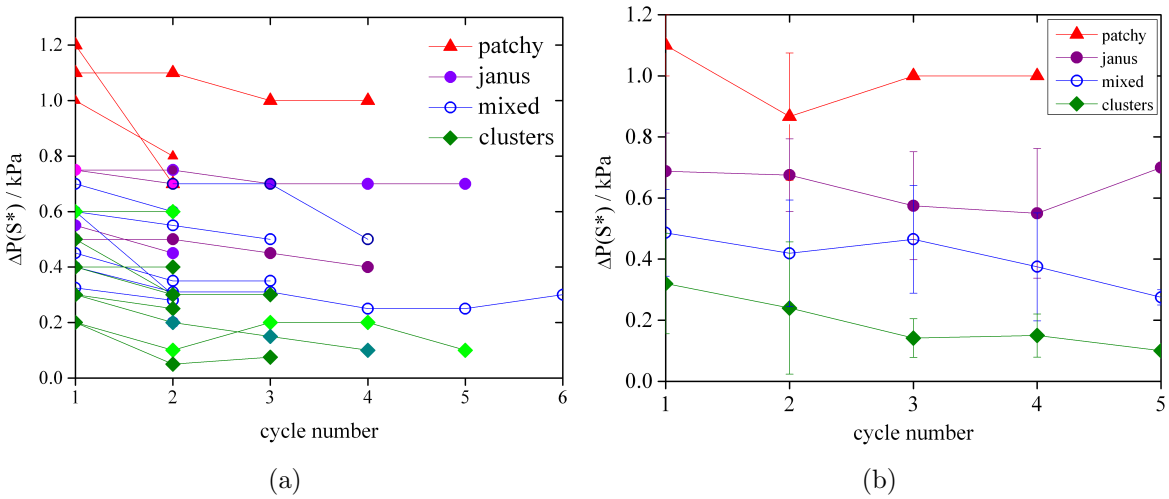

Figure 4.15: Hysteresis loop opening $\Delta P_c(S^*)$ for (a) different samples, representing all coating types, at each cycle number and (b) averaged over every experiment of that sample type. There is no significant trends with cycle number of the capillary hysteresis.

Irreducible saturations

The final oil and water saturations (S_{oil} and S_{water}) as a function of the cycle number are also investigated and the results are shown in figures 4.17 and 4.16. Again no systematic variation of the residual saturations with progressing cycles is observed. With the exception of the cluster samples, the saturations remain fairly constant throughout an experiment. At this point it not possible to determine if it is the same ganglia which are always trapped.

We can conclude from this that once the capillary pressure saturation curves reach second or third cycle they are in a stable state and very reproducible loops are obtained. What is

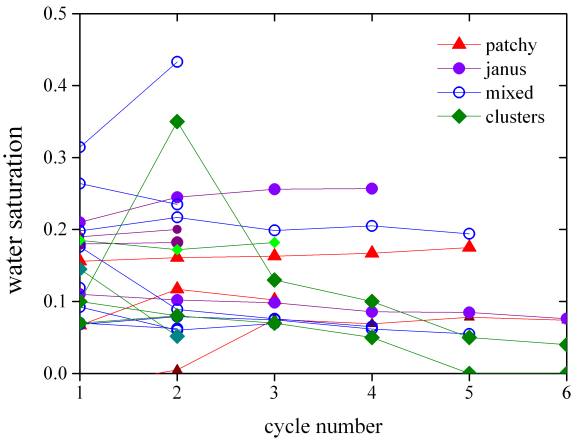

Figure 4.16: S_{water} for all samples with progressing cycle number. There is no detectable trend for the samples, and the irreducible water saturations remain fairly constant throughout single experiments, with the exception of one cluster sample.

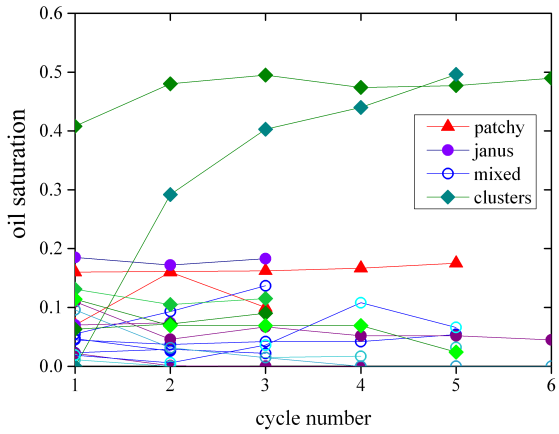

Figure 4.17: S_{oil} for all samples with progressing cycle number. There is no detectable trend for the irreducible values with cycle number. There is considerably more scatter in the values measured between experiments compared to the residual oil values, but again in general, with the exception of one of the cluster samples, the irreducible oil saturations remain fairly constant throughout an experiment.

however not clear is that just because the macroscopic behaviour remains stable that microscopically the same process (i.e same fluid path through the same) is occurring repeatedly on each cycle.

4.2.3 Effect of porosity

It was mentioned in chapter 2 that the liquid movement through a single pore can be approximated by a capillary, and modelled using a standard capillary pressure equation 2.2 (where

r is the typical pore throat radius). From this equation is it clear that the size of the pore will affect the pressure, and a logical extension is that the porosity of a bead pack will affect the capillary hysteresis. It would be difficult and also impractical to pre-measure the weight of the beads prior to an experiment, as making sure ever pre-weighed bead ended up inside the experimental cell would be practically impossible, so rather, the porosity of the samples are estimated by the height of beads in the cell when filling, and controlled by measuring the weight of dried beads recovered from the sample after the experiment. Figure 4.18 shows the hysteresis measured for each sample type, with the approximate porosity values. The porosities shown here are calculated using the the known volume of the cell, assuming it is a perfect cylinder. However, from tomographic imaging of the cell, some bending of the membranes could be observed, resulting in the volume being less that the estimated volume. Therefore the calculated porosities are likely higher than the actual values. The porosity could be estimated locally from the bead pack images taken with the tomography. The values measured by image processing from the tomography images of bead packs are given in table 4.5. These values are on the same order as those calculated from the mass of the beads.

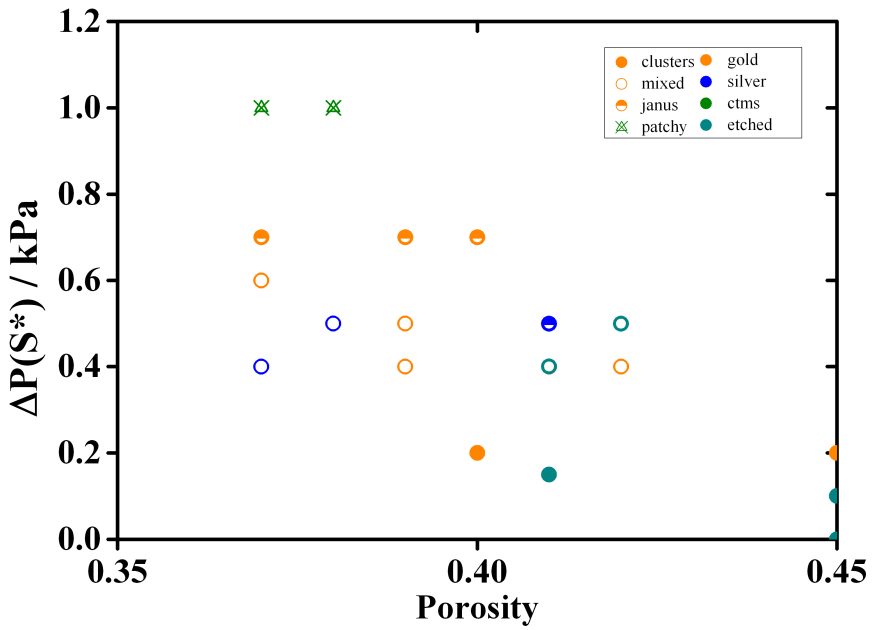

Figure 4.18: Hysteresis loop opening vs porosity

Again the residual saturations were also plotted against the porosity of the sample, but no trend was observed.

sample	porosity %
patchy	43
janus	39
mixed	36
clusters	45

Table 4.5: porosity of bead samples measured from x-ray tomography

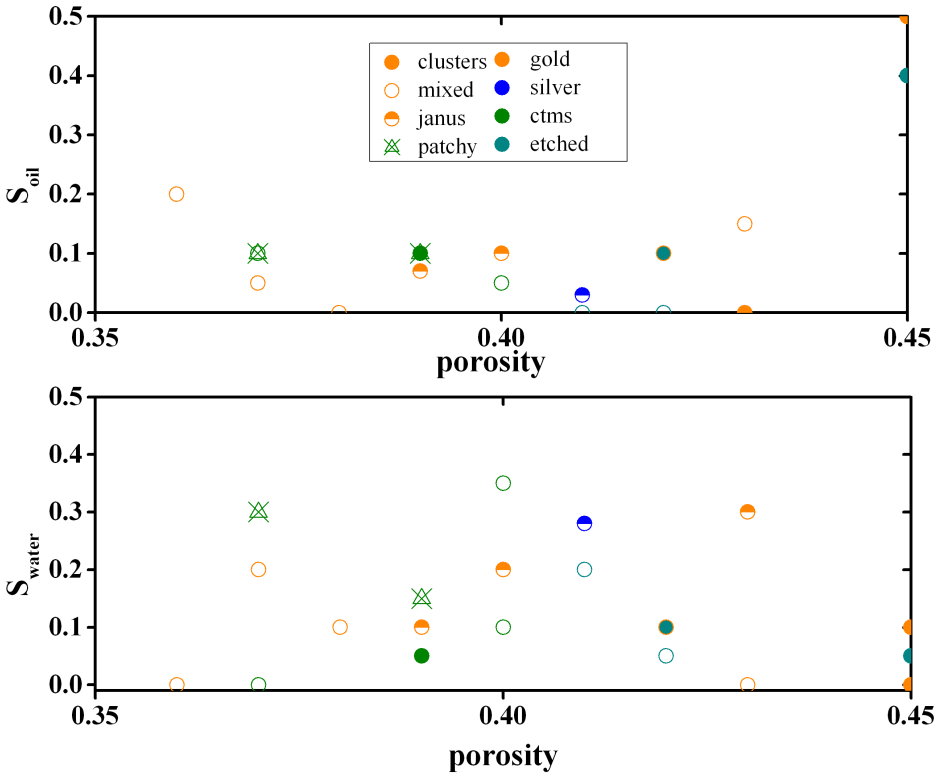

Figure 4.19: Residual saturations plotted against the porosity of the sample. Similarly to the correlation length the residual saturations do not appear to depend strongly on the density of the bead pack.

4.2.4 Layered samples

So far all the samples discussed had a mixed wettability with a random spatial arrangement, and a correlation length much smaller than the sample size. It was found that the once the wetting heterogeneities reached the order of a pore size they no longer dominated the capillary hysteresis of the sample. It is also interesting to see if this effect persists when the heterogeneities also become very large. A proposed idea to explain the validity of contact angle averaging techniques for mixed samples is the presence of continuous paths of both water and oil wet surfaces. Sample containing very large heterogeneities may not have such paths available, in which case the size of the heterogeneity may again be important. To test this hypothesis layered samples were prepared and an example CPS curve is shown in

figure 4.20. The layers were created by filling beads up to a certain height of the cell, and the wetting correlation length is assumed to be on the order of the sample size. The filling order was hydrophilic/hydrophobic.

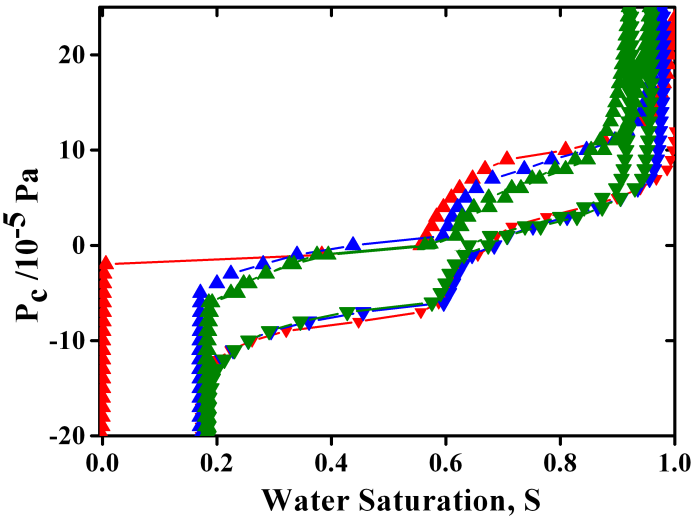

Figure 4.20: CPSC measurements of a layered sample with a hydrophilic/hydrophobic filling order. There is a clear step in the middle, which is attributed to contact line pinning at the junction of the wetting layers. The colors of the curve correspond to red: first imbibition and drainage, blue: second cycle and green: third cycle. Upwards arrow correspond to imbibition data points, and downwards triangles correspond to drainage.

What can be seen here, is again a clear effect of the correlation length. Although the correlation length is much larger than pore size these curves look significantly different from the mixed samples and homogeneous cases. For samples of two layers a clear step can be seen at the wetting junction, most likely also attributed to pinning of the interface. Again, this occurs in layered samples because there is a sharp change in the wettability of the sample which the moving liquid front must cross. While a correlation length for these samples was not measured, as the heterogeneity is itself on the order of the sample size, these samples indicated that it is not just small wetting heterogeneities which must be accounted for but also very large ones. While locally each section of the packing can be treated as homogeneous, a global average contact angle treatment of these samples would clearly not capture the behaviour measured here.

Dynamic X-ray tomography imaging of water invasion into a layered sample have shown that first the water invades all the water wet layers and then only secondly the oil wet layers [93]. This appears to also be the case in our samples. This presents an interesting experimental technique or creating samples in which the invasion of water into the porous media from different directions can be controlled. This is illustrated in figure 4.21. For instance a sample of hydrophobic or mixed wet beads with hydrophilic layers on the top and bottom will be invading from both sides, and by using vertical layers at the sides, invasion

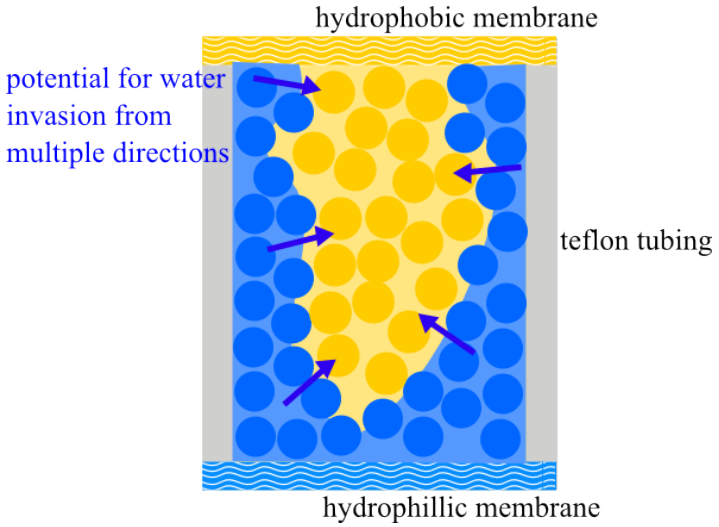

Figure 4.21: Schematic showing how vertical and horizontal layers of beads (shown in blue) could be used to create samples where the liquid front invades from several sides of the sample, rather than just from the bottom. Water is shown in blue, oil in orange, and the arrows show the possibility for the front to invade the central part of the sample the bottom and sides.

from all sides at once. This could be used to control the invasion process to create advancing interfaces with specific properties [115], or alternatively useful when comparing experimental results to numerics with periodic boundary conditions.

4.3 Summary and open questions

In this section I have explained the investigation of a series of porous samples with the same average wettability, but different spatial arrangements of the wetting surfaces. These spatial arrangements, which are defined by the wetting correlation length ξ, correspond to the density of contact line pinning sites within the pore space.

For the samples with correlation lengths of less than 1, high values of capillary hysteresis in the system are measured. This correlation between high hysteresis values and contact line pinning sites indicates that contact line pinning is the dominant mechanism of dissipative work as the interface is advanced through the sample. This effect is found for samples with different coatings and surface roughness, and does not appear to depends specifically on the contact angle of the individual surfaces, provided the surface patches are either hydrophilic or hydrophobic (do not have a contact angle of 90°).

For samples with correlation lengths close to one (mixed and cluster samples), significant deviations of the hysteresis loop opening from those of homogeneous samples was not observed. The proposed explanation of this is due to the lack of contact line pinning sites within single pores. Accurate descriptions of the wettability at this length scale appear to be less important. For these samples, with wetting heterogeneities on the order of the pore,

models which use contact angle averaging appear to still be valid. Once the heterogeneity becomes very large, such as the layered sample, the correlation length again appears to be important with differences in the CPSC observed. However as the heterogeneity is on the order of the sample size it is difficult to separate this effect from potential finite size effects of the measurement.

What has been clearly demonstrated in this chapter is that the wetting correlation does affect the fluid displacement profiles of the two phases through mixed wetting porous media. It is also known that the hysteresis opening is related to the interfacial area. It is still not yet clear what effect the correlation length has on the advancing interface, which has significant impacts on the residual oil saturations.

To address this issue fluid-fluid distributions for the four sample types was imaged with X-ray tomography at different water saturations. These experiments and the findings are discussed in the next chapter (Chapter 5).

Chapter 5

Tomographic imaging of liquid fronts

As discussed in chapter 4 it was found that the wetting correlation length controls the flow dissipation. To further understand this process, and the mechanism behind the flow dissipation the fluid-fluid distributions inside the packings were imaged.

In this chapter, X-ray tomography is used as a tool to visualise the liquid-liquid distributions inside the different model porous media in combination with the capillary pressure saturation experiments described in the previous chapter. The images were processed and the moving liquid fronts extracted. These fronts were analysed using the Minkowski measures, which are quantitative shape descriptors, and the differences of the the moving fronts through different samples are related to the correlation length ξ.

It is useful to remember that although the goal of the experiments is to understand local flow properties of individual pore displacements, these experiments are carried out at low capillary numbers ($\sim 10^{-6}$) and are in the quasi-static regime.

5.1 Combined imaging and CPS measurements

For the X-ray experiments a second cell, made of PEEK (Poly-ether-ether-ketone) was used as it is transparent to X-rays and resistant to solvents. PEEK is a very hard plastic, and will not deform under pressure (unlike softer plastics such as Teflon). Most importantly, PEEK does not release surfactants/plasticisers into the hexadecane, unlike many plastics, which would contaminate the oil. Therefore it is suitable for use in these experiments. A 3D drawing of the cell is shown in figure 5.1 b.

The CPS experiment is performed, according to the procedure described in the previous chapter. When the liquid reaches a certain saturation, determined by the balance reading, the cell is disconnected from the two liquid reservoirs using the two three way valves to prevent any liquid loss, or introduction of air. The sample is then placed inside the Nanotom, while

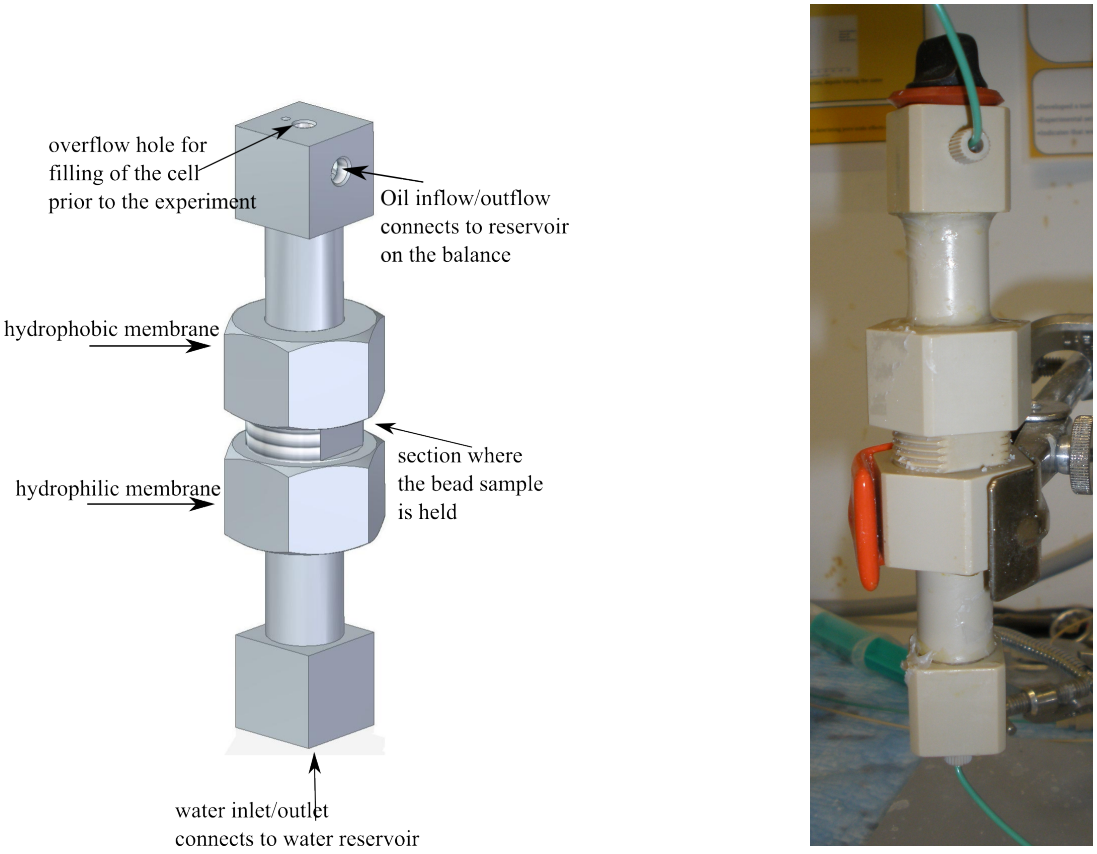

Figure 5.1: (a) 3D drawing of the PEEK cell used for these experiments and (b) photograph of the same cell connected to the CPS-apparatus.

taking care to ensure the same alignment is used between successive imaging of the same sample and a tomography is taken. The cell is then reconnected to the oil reservoirs, all tubing is flushed to remove air bubbles and the experiment is re-started. An example CPS curve, made with this stop-start protocol is shown in figure 5.2 and the corresponding images are shown in figure 5.3. Ideally a full cycle could be imaged, but due to possible introduction of air bubbles in the reconnection stage sometimes this is not possible, leaving the cycle incomplete. In this case, a new sample is prepared and the experiment is started again.

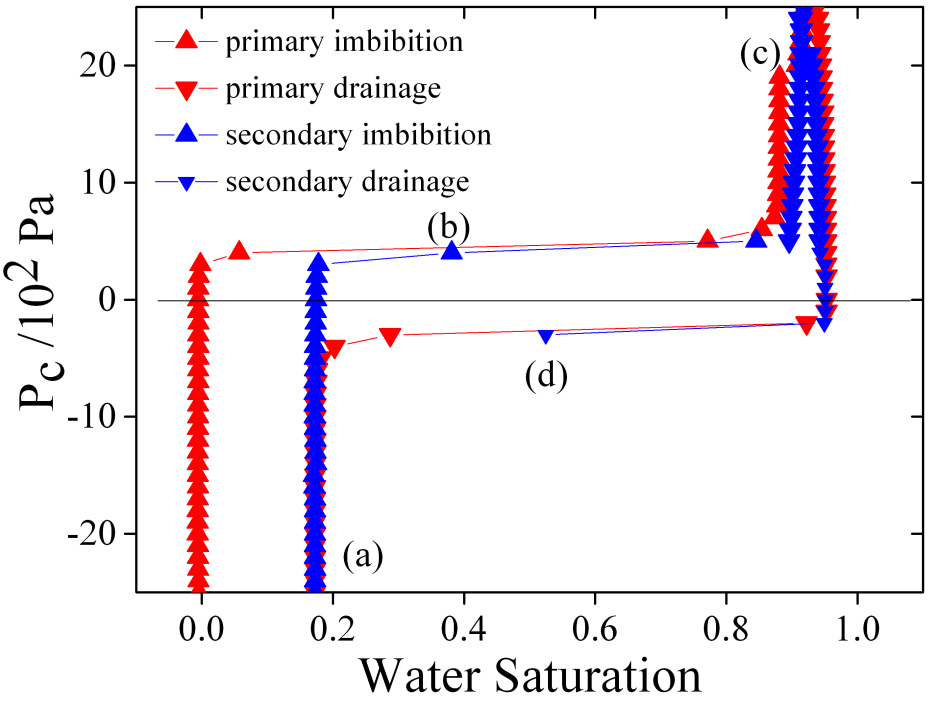

Figure 5.2: CPSC curve from combined CPS-tomography experiment on a janus sample. The labels a), b), c) and d) indicated the points where the experiment was paused and the images made. The corresponding snapshots (a-d) are shown below in figure 5.3.

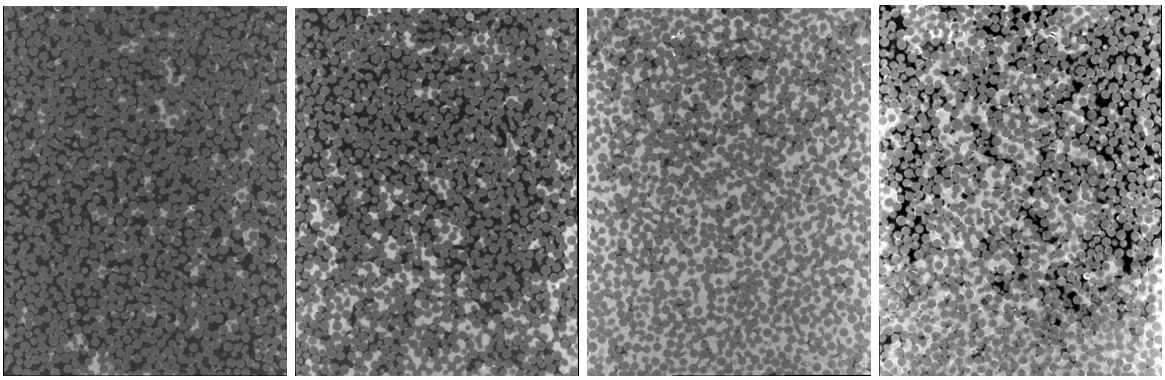

(a) irreducible water (b) secondary imbibtion (c) irreducible oil (d) secondary drainage

Figure 5.3: Snapshots of the CPS experiment, imaged with X-ray tomography, at the points labelled on the CPS curve in figure 5.2. The black phase is the hexadecane, the grey disks are the glass beads and the white phase is the water with 2 M KI added to increase x-ray absorption.

5.1.1 Identification of the liquid phases

After acquisition of the images, the physical data is extracted from the images using an work flow similar to the one illustrated in chapter 2. Noise is removed from the images via bilateral filtering, and the individual components (water, oil and beads) selected via grey value thresholding.

In order to evaluate the quality of the segmentation the volumes of the segmented phase were compared with the liquid volumes measured from the analytical balance. This comparison is shown in figure 5.4. The volume of the segmented phase is then compared with the measured mass from the balance. The error bars are obtained by varying the grey value thresholds to the minimum and maximum values that still produce a visually good segmentation, and determining the difference in segmented volume. For more detailed explanation of this, see appendix A. This methodology, external validation of the image processing, has been previously reported [46, 59] and is considered necessary to reduce potential errors.

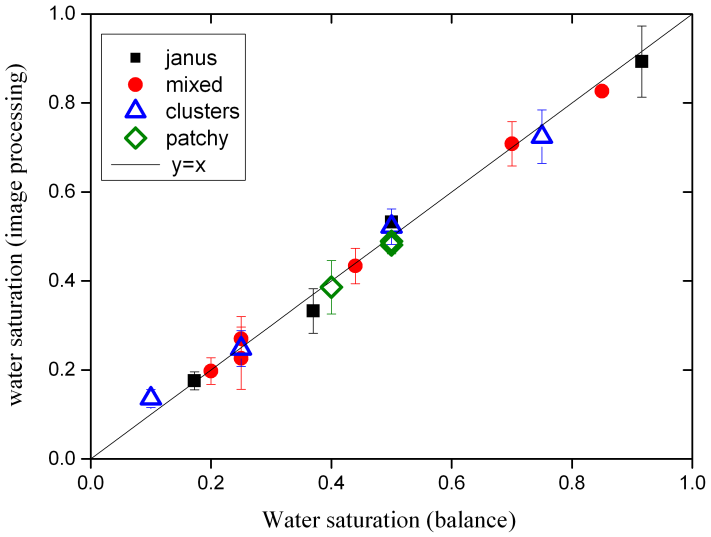

Figure 5.4: Water saturation of the sample calculated by image segmentation compared with the water saturation calculated from the mass measurements during the CPS experiment.

Figure 5.5 shows the water distributions inside the four different sample types at low water saturations ($\sim$ approximately 30%). It is very difficult to see a difference between the water distributions in the four packings, with the exception that the droplets in the cluster packings appear to be larger. Therefore in order to understand why the samples behave differently, the connectivity of both the liquid phases should be considered. This is discussed in the following section (section 5.2.

Having developed a generic processing work flow for all images and successfully segmented the two liquid phases the images can now be analysed. The purpose of these experiments is

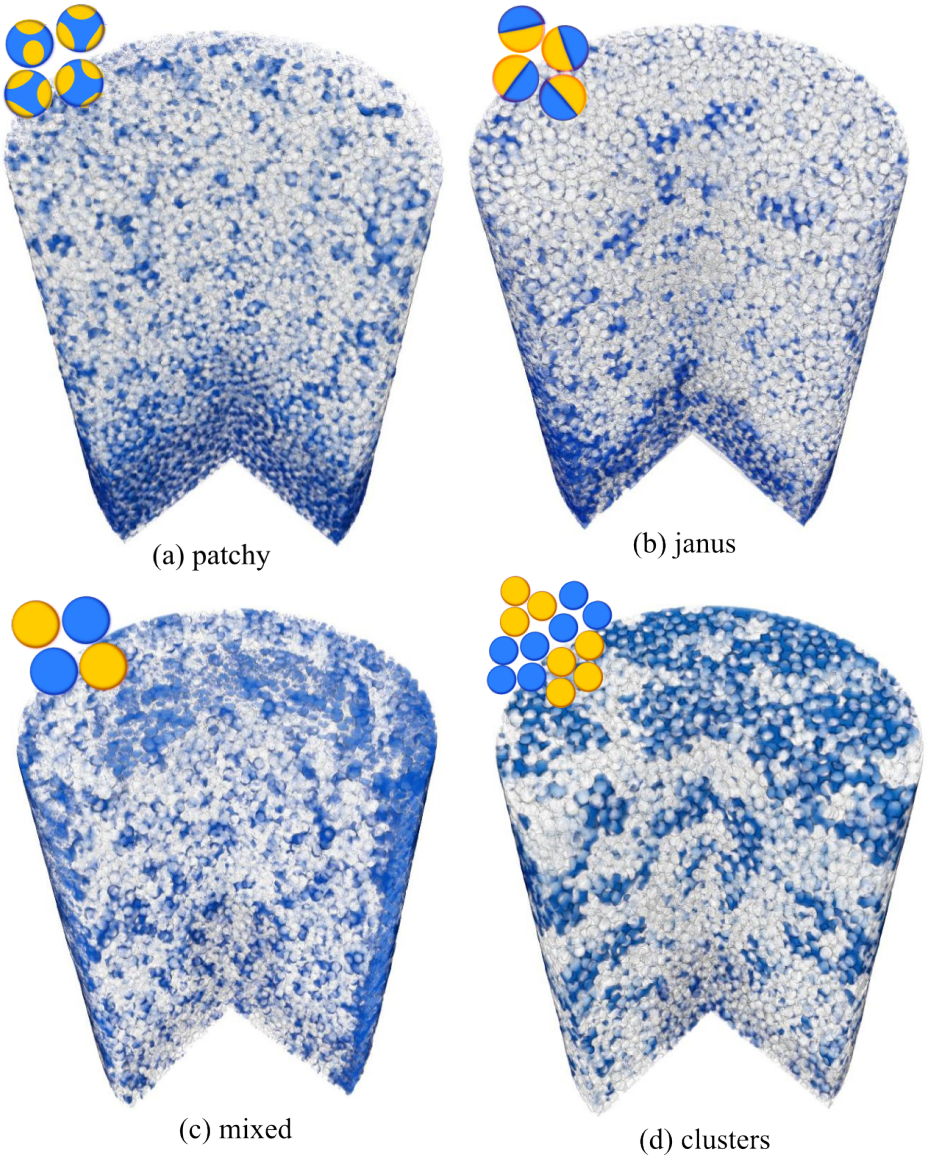

Figure 5.5: 3D volume rendering of sample beads (white) and water (blue) at low water saturations. A segment of the volume has been removed to allow visualisation of the interior liquid structure. Little difference between the samples can been seen by eye.

to elucidate the mechanism behind the flow dissipation. As stated in chapter 4, the proposed mechanism for flow dissipation is contact line pinning at the heterogeneity junctions. If this local effect is causing larger scale changes in the flow, it is expected to be related to the interfacial area [116]. Therefore, the first parameter of interest is the interfacial area.

5.2 Identification of the active interface

Invasion of a pore by either water or oil can only happen at the water-oil interface. Therefore it is the interface which controls the capillary pressure saturation behaviour, and the shape and size of the interface should be related to the hysteresis loop opening, ΔP (as described in chapter 4). For a drainage or imbibition event to happen, the liquid must be able to provide a pressure at the interface. This can only happen if the invading liquid is connected to the reservoir and the displaced liquid is connected to the drainage point. Indeed, this is why droplets become trapped in porous media. Once the droplet is disconnected from the continuous fluid phase, there is no mechanism to further apply pressure on it and it is unlikely move. Strictly speaking, droplets might be mobilised due to a viscous pressure drop and inertial effects which might be caused by the local increased velocity of fluid moving into a pore during a Haine's jump. However, we assume any such effects to be relatively minor. Therefore, oil-water interfaces which arise from these disconnected droplets are not expected to contribute very much to the capillary hysteresis, and rather the active interface, or liquid front, between the two connected liquid bodies is expected to contribute. A chart showing the work flow is presented in figure 5.6, and example images from each step are shown in figure 5.7.

Image processing

The active interface of the drainage/imbibition processing was identified using the following steps. Firstly the water and oil phase are segmented. The most important thing of this step is that the interfaces of the regions are clearly visible. The inclusion or exclusion of voxels due to noise are not so important as they are eliminated in the further processing steps. Each phase is first segmented using grey value thresholding. Then, each binary image is converted to a label image which assigns a different number to each connected region; this is visualised with different colours (see figure 5.7 a). The largest region from each section is identified and selected. This region is then dilated by 1 voxel using a 3D-18 neighbours criteria. The overlapping regions of these two selections are then calculated and said to be the active interface. The size of the interface is calculated by counting the number of voxels in the overlapping regions.

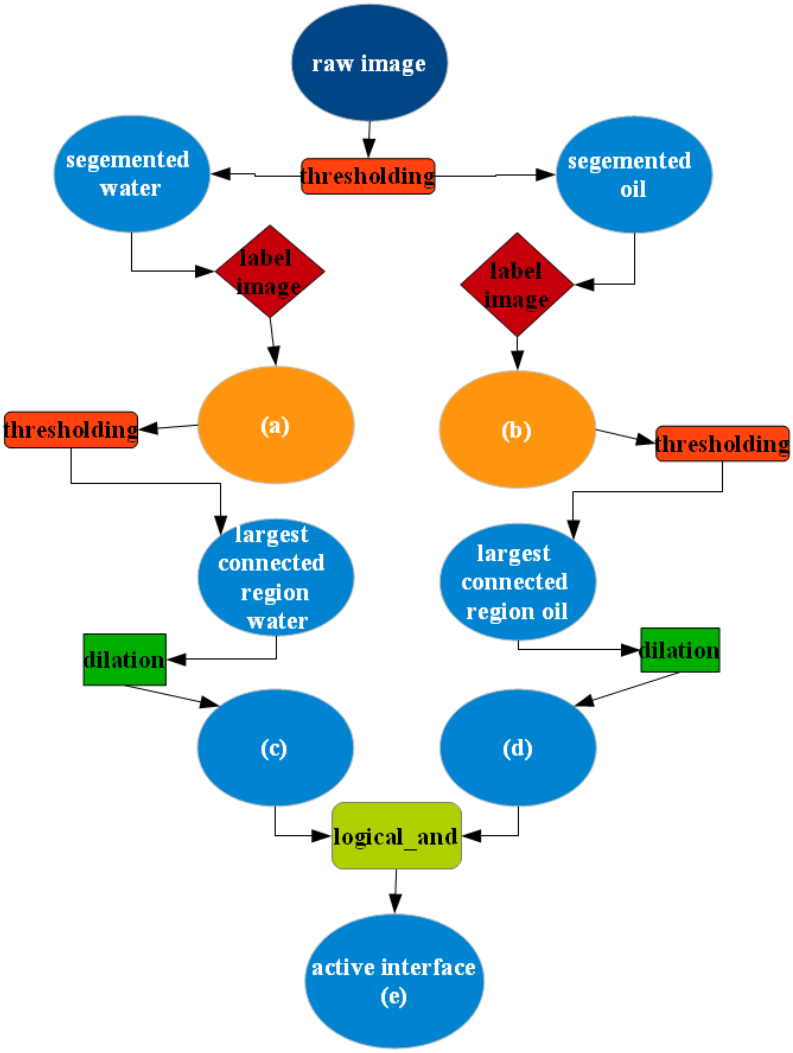

Figure 5.6: Work flow for identifying the active interfaces. The images corresponding the the letters a-e are displayed in figure 5.7

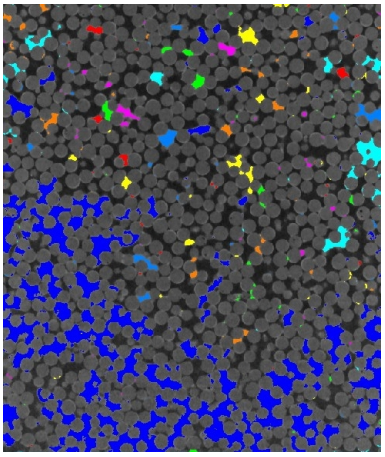

(a) labelled water phase

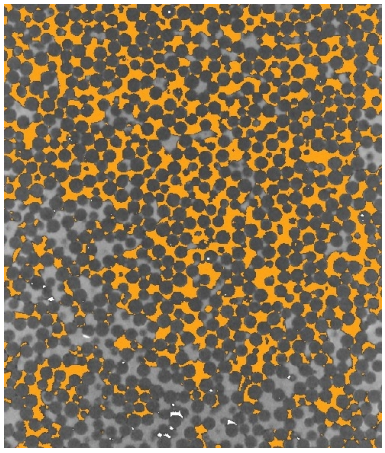

(b) labelled oil phase

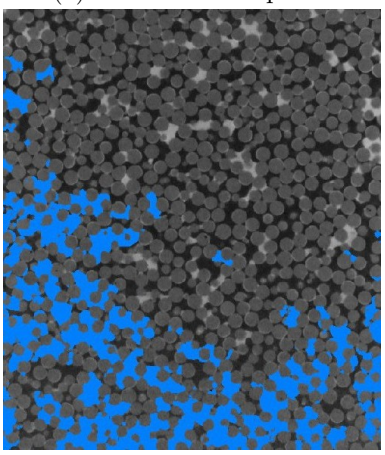

(c) largest connected region dilated

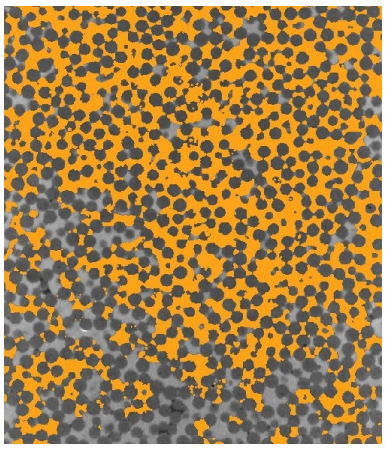

(d) largest connected region dilated

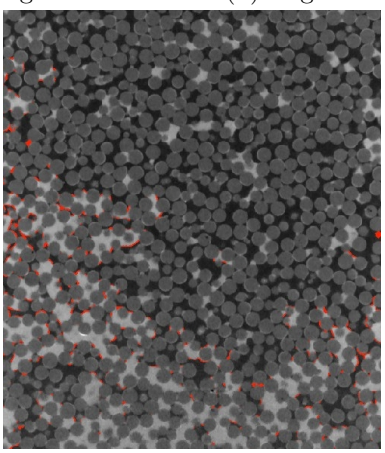

(e) active interface identified

Figure 5.7: Example images showing the identification of the active interface for a water invasion into a sample of janus beads.

5.2.1 Active interface at 30% water saturation

The active interface is extracted from each of the samples and overlaid on top of the image. An example 2D slice for each sample is shown in figure 5.8. Already from the 2D slice it can be seen that there are qualitative differences in the shapes of the active interfaces, with the patchy and janus interfaces looking smooth, and the mixed and clusters have rougher, more fingered interfaces. To fully appreciate the macroscopic differences in the interfaces it is better to visualise the interfaces in 3D. This is shown in figure 5.9.

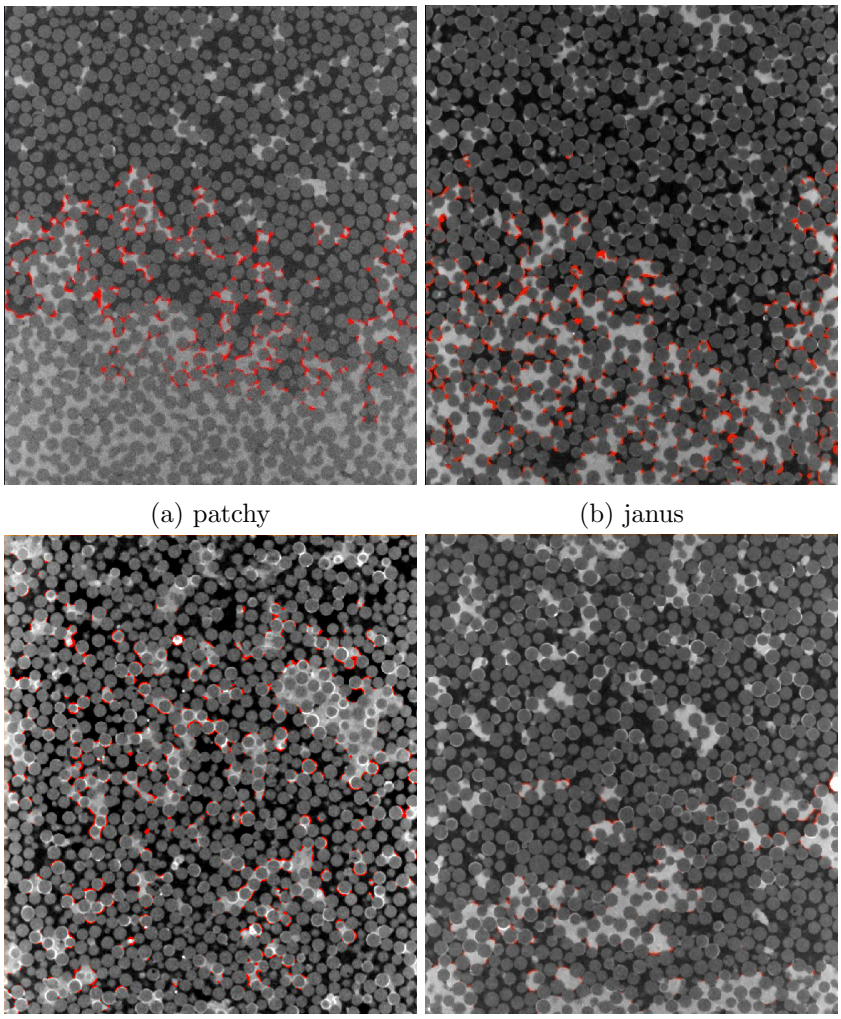

(a) patchy (b) janus

(c) mixed (d) cluster

Figure 5.8: Identification of the active interfaces from tomography images containing approximately 30% water. The active interface is highlighted in red.

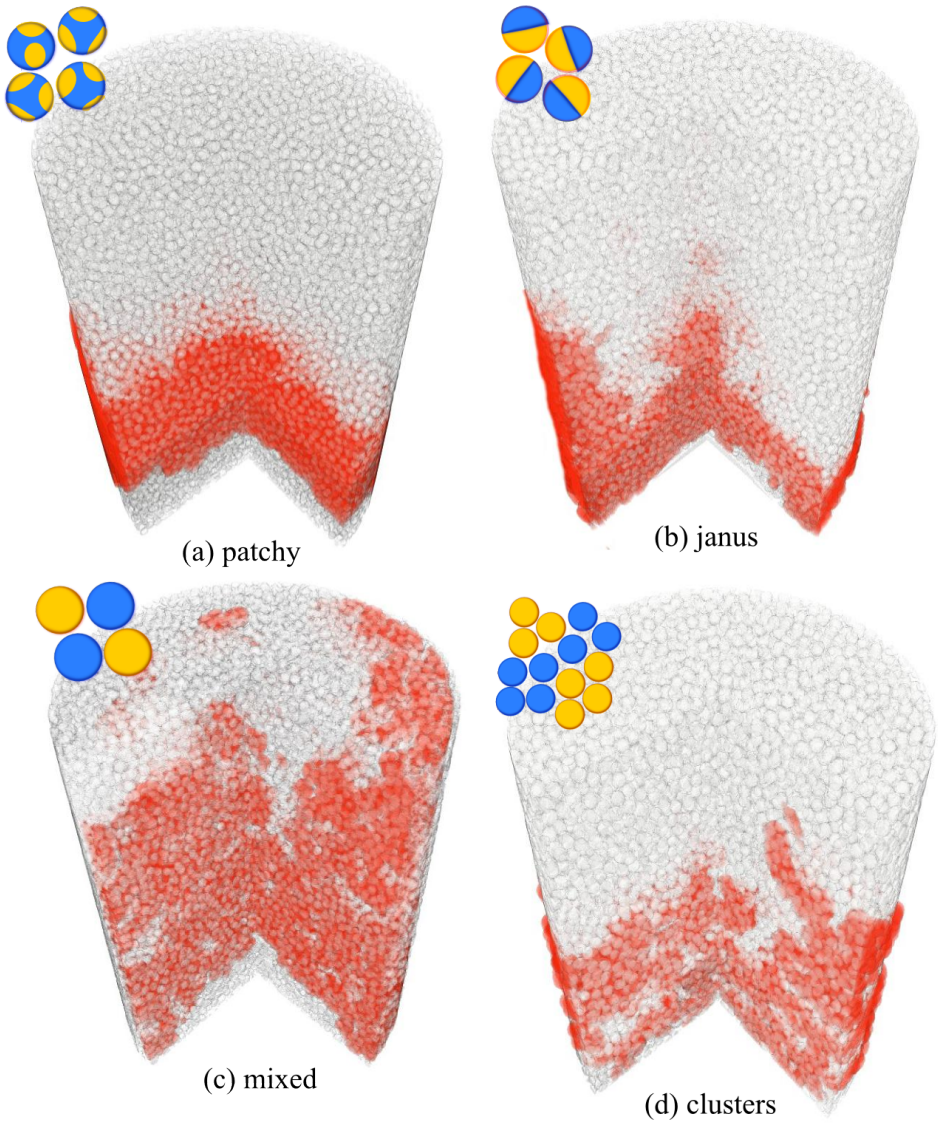

Figure 5.9: 3D volume rendering of sample beads (white) and the active interface (red) at approximately 30% water saturation. The interface is dilated by ten voxels (equal to one grain diameter) for visualisation purposes.

5.2.2 Active Interface at 50% water saturation

The same general trend for interfaces at higher water saturations is also observed. Figures 5.10 and 5.11 show the 2D and 3D representations of the interfaces at 50% water saturation in each of the samples. The patchy and janus samples still have more compact fronts whereas the mixed and clusters show a larger extent of fingering.

Although it has not been specifically measured, from the imaging of the tomography fronts, it is easy to extrapolate that the samples have different percolation thresholds, for example, the images of the mixed active interface at only $sim30\%$ water saturation reveal that the

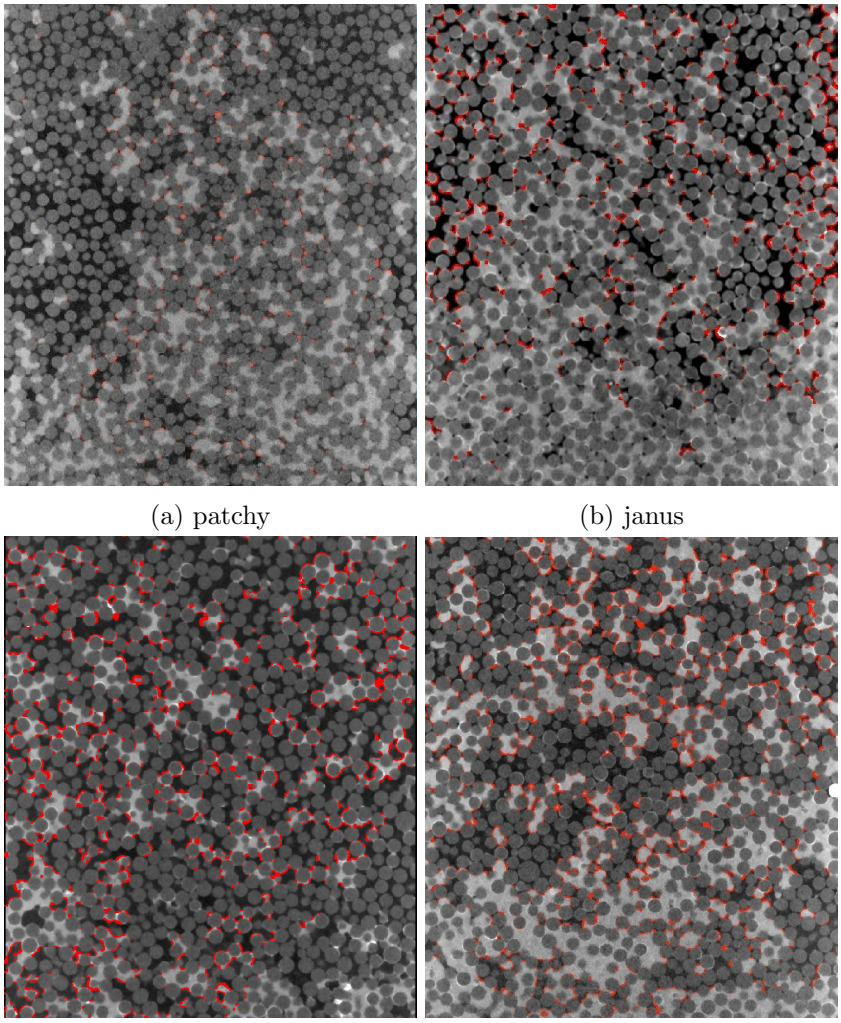

(a) patchy (b) janus

(c) mixed (d) cluster

Figure 5.10: Tomography of samples with 50% water content measured during the CPSC experiment. The active interface is identified and highlighted in red.

active interface extends the entire length of the packing, whereas for the other samples, this doesn't occur until higher saturations. By 50% water saturation, all four samples show percolation. A specific investigation of the effect of the wetting correlation length on the percolation threshold could be interesting for future studies, but is however not presented here.

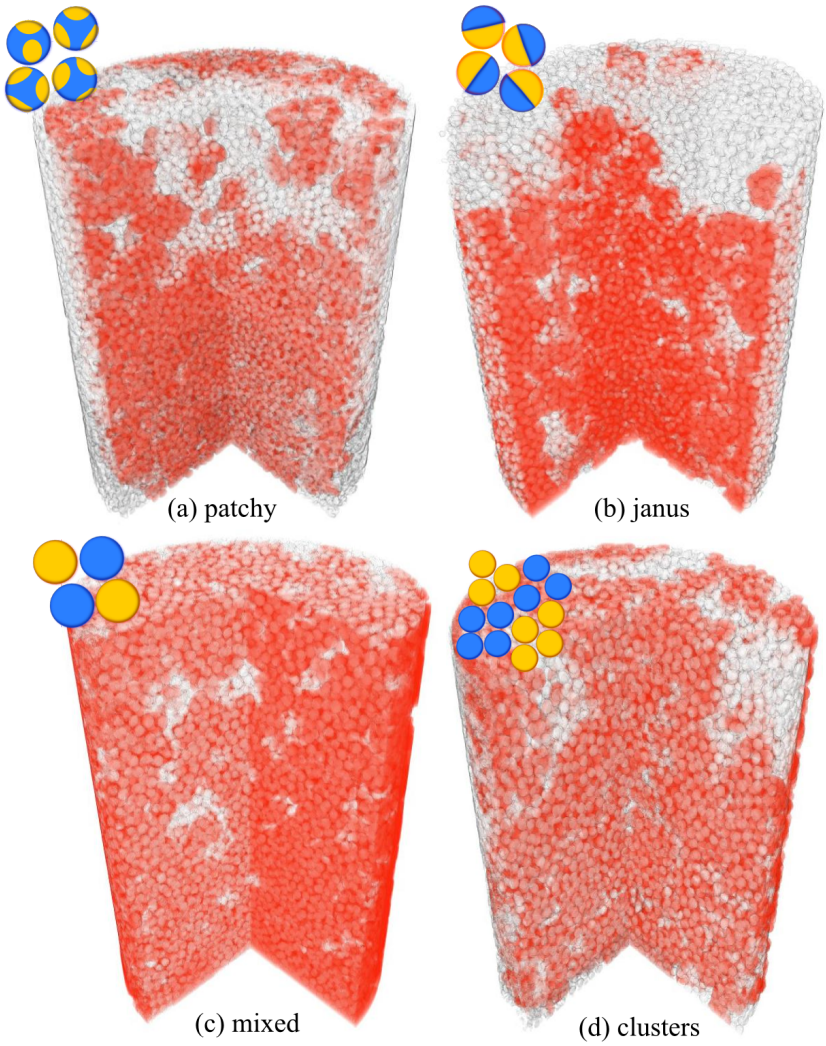

Figure 5.11: 3D volume rendering of sample beads (white) and the active interface (red) at 50% water saturation. The interface is dilated by ten voxels (equal to one grain diameter) for visualisation purposes. The same trend as for the low saturations is conserved with samples with small correlation lengths having smoother interfaces.

Just by looking at the images of the invading fronts, it seems that the shape of the active interface depends upon the correlation length. However to fully discern the effect of the wetting correlation length on the propagation of the invading phase, it is necessary to determined quantitative descriptions of the active interface. The obvious starting place, is to compare the sizes of the interfaces for the different samples. This was achieved by counting the number of voxels in each interface and plotting the size against the water saturation (see figure 5.12).

It is helpful to first consider how such a curve should look. At the beginning when there is only one phase (oil) present in the system, obviously the interfacial area between water and oil is zero. As the water content increases, so too must the interface. At a certain point however, when there becomes more water than oil, this interface must decrease again, and finally at the end of the water invasion when there is only oil remaining in trapped droplets the interface should be again at a minimum. Therefore, it is expected that the active interface starts at a very low value, increases to a maximum around 50% water saturation and then decreases again as the oil content decreases. This shape of the interfacial area curve has been reported in studies with homogeneously wettable bead packs [46–48].

The evolution of the interface during the CPS experiment is shown in 5.12. Only the interface between the water and oil connected to the liquid reservoirs, and not including any interfaces arising from disconnected droplets is considered. While the expected shape of the size of the interface with respect to water content is observed for the janus samples, the other data all falls within the noise and the expected trends are not seen in figure 5.12. This parameter, the interfacial area, is extremely sensitive towards the segmentation parameters, as indicated by the error bars. In fact, most of the data all falls within this range. For the patchy samples, there is no trend detected above the noise, and the values obtained for the interfacial area are seemingly constant, at least within the noise.

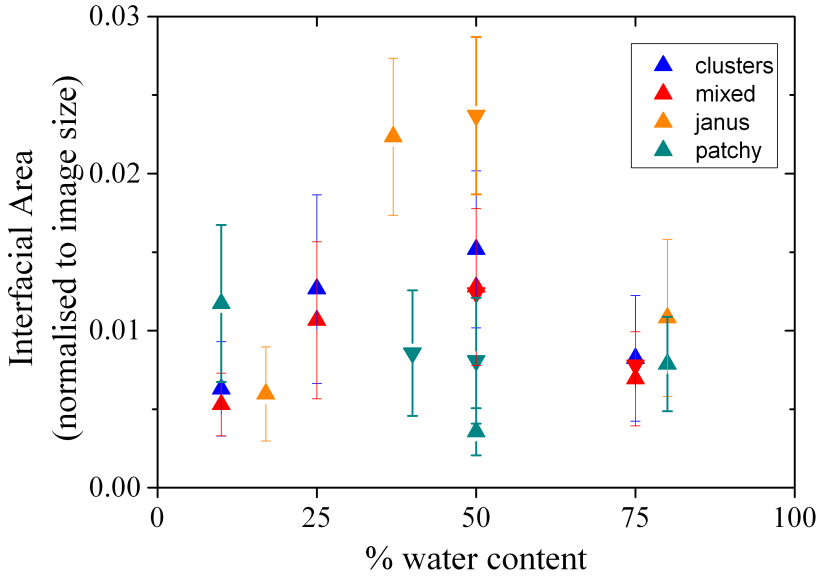

Figure 5.12: Active interfacial areas for water and oil, for different sample types. Upwards triangles represent images taken during water invasion, and downwards triangles represent images taken during oil invasion. The error bars represent the range of areas calculated for different 'good'segmentation values.

While it is observed that for low and high water saturations the interfacial areas are lower there is no trend observed in the active interfacial areas with ξ. Therefore, simply, the interfacial area alone is not sufficient to explain the CPS experimental results and a more in depth shape description is necessary.

5.3 Minkowski measures of water-oil interface

As shown in section 5.2 the interfacial area alone is insufficient to describe the development of the liquid fronts. Therefore, a more sophisticated analysis is required. Rather than describing each individual feature on a local scale, it would be preferable to describe the enveloping shape for the liquid front at the sample scale. To do this, a coarse graining technique [117] is used to analyse the overall shape of the liquid front.

To quantitatively analyse the shape of the liquid fronts in more detail the first three of the Minkowski measures [118]- volume, surface area and the Euler characteristic, χ, are employed. Interfacial curvatures were not measured as the resolution of the tomography is not high enough to accurately extract the curvature of individual liquid bridges [47].

5.3.1 Inflation of the interface

The idea of coarse graining the interface works like this: each voxel of the extracted interface is used as a seed. From these seeds spheres of radius c are grown. c is expressed in terms of bead diameters. That is, c = 1, is the same diameter as a typical bead. Practically this is achieved by thresholding a euclidean-distance-map (EDM, see appendix A) of the seed points.

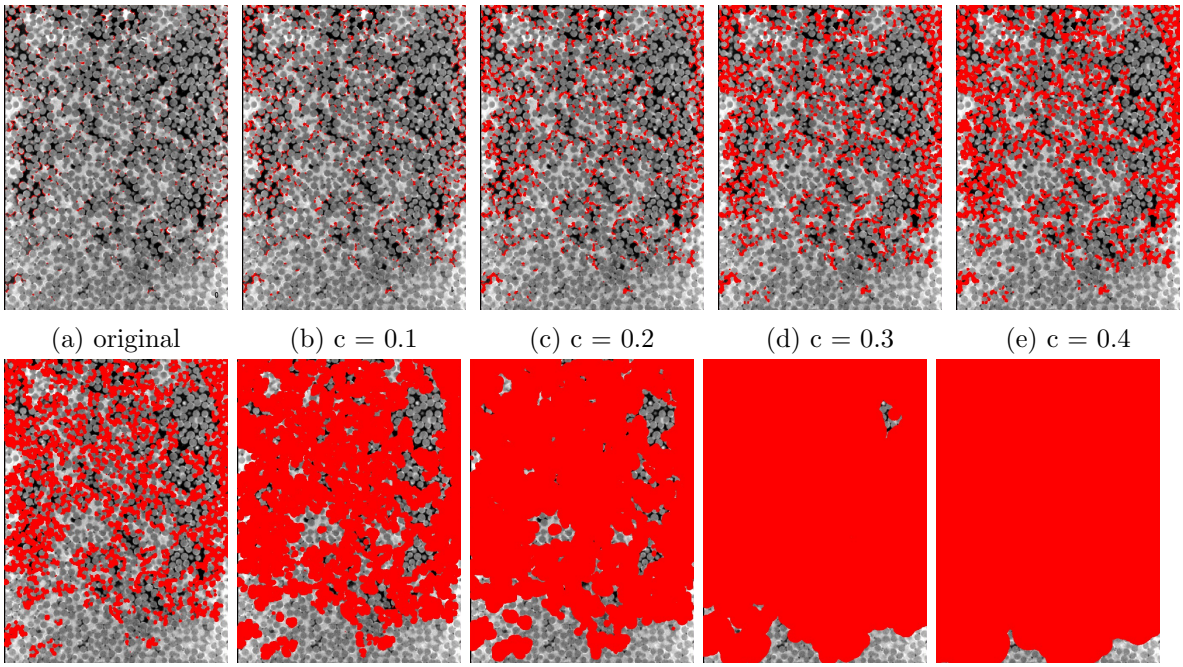

(a) original (b) c = 0.1 (c) c = 0.2 (d) c = 0.3 (e) c = 0.4

(f) c = 0.5 (g) c = 1.0 (h) c = 1.5 (i) c = 3 (j) c = 5

Figure 5.13: Dilation of interfaces by factor c (c = number of voxels/no. of voxels for a bead diameter). Interfaces are dilated by placing a sphere of radius c, at each seed point. Minkowski scalars (volume, surface and Euler characteristic) are calculated on the dilated images. Here XZ slices from janus sample at 50% water saturation are shown.

The interface shape is characterised by the union of all the spheres, counting the regions from overlapping spheres only once. In practise the sphere-growth method is the same principle as dilating the active interface. This can been seen in figure 5.13.

The Minkowski measures of the extracted interfaces were calculated using Bilimbi, an open source software package [119, 120], with a modification which converts voxel data to triangulated surfaces required for calculating surface areas and euler numbers. These measures are used to obtain quantitative shape information about the liquid fronts. First the general features of all curves will be explained, and the differences between the curves for different samples .

5.3.2 Volume and surface area measures

Volume

The first and most intuitive measure, to understand is the the collective volume curve (figure 5.14). It is simply union of all voxels in the collection of spheres grow around every seed, (That is, voxels in overlapping spheres are only counted once). As the dilation factor is increased the volume increases, as expected. At first the volume increase is linear as the separate regions are growing. Then as the regions start to merge the growth of the volume decreases. The increase in volume continues until all the holes are filled inside the object. At this point the growth of the volume becomes very slow, as the object can only grow from its surface. Eventually, for sufficiently large sphere radius (for these samples this occurs at c = 20) the entire volume of the image would be filled and there would be no more growth. So in all cases, both low water saturations ($\sim$ 30%. figure. 5.14 a), and 50% water saturation (figure 5.15 a), there is initially a rapid growth of volume, slowing as the spheres begin to overlap and converging at the total volume of the image.

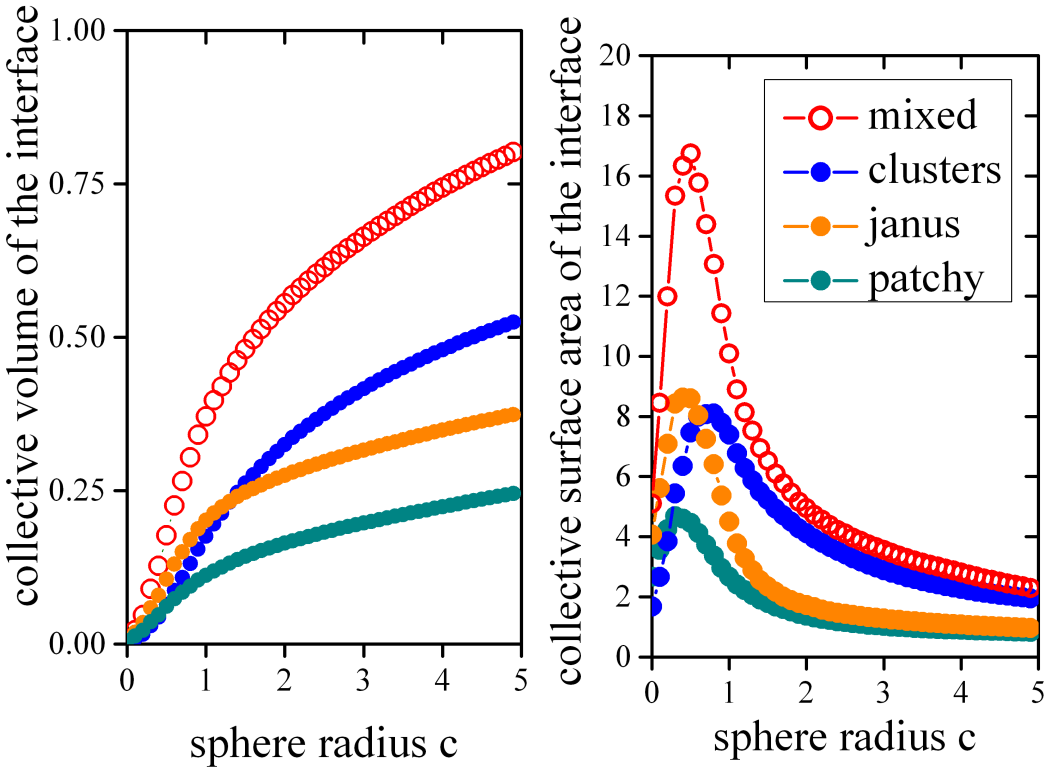

(a) volume (b) surface area

Figure 5.14: First two Minkowski measures for samples with low water saturations: (a) the volume and (b) surface area scalars, plotted as a function of the sphere radius, c.

In this way, it can be understood that the volume of the collective spheres at any given radius conveys information about the initial spatial distribution of the seeds. For values around

c=1, the collective volume derived from seeds which are far apart will be larger than that of seeds which are close together. This is because the growing spheres from widely distributed seeds will only begin to overlap at larger sphere radii compared to a dense distribution of seed points. Seeds which are close together overlap quickly and thus the collective volume will grow at a slower rate. Interfaces which are highly fingered will have more internal holes than interfaces which are compact. Therefore it is expected that highly fingered interfaces continue to have large volume gains, also at higher sphere radii compared to compact interfaces.

Applying this information to our four different samples, it can be deduced that the mixed sample exhibits the most fingered interface, with seed points being the furthest apart. The collective volume continues to grow rapidly until very large sphere radii indicating a rough interface. The cluster sample shows a reasonably fingered interface, with seed points not as widely disperse as the mixed sample, but more so than the janus and patchy. The janus and patchy samples, the samples with wetting correlation lengths of less than one, which exhibited large values of capillary hysteresis have the most compact fronts. The difference in the interfaces between with respect to ξ are more pronounced for the low water saturations than the 50% water saturations. This is because at 50% water saturation all the front has percolated all samples, and the maximum interfacial area has already been reached.

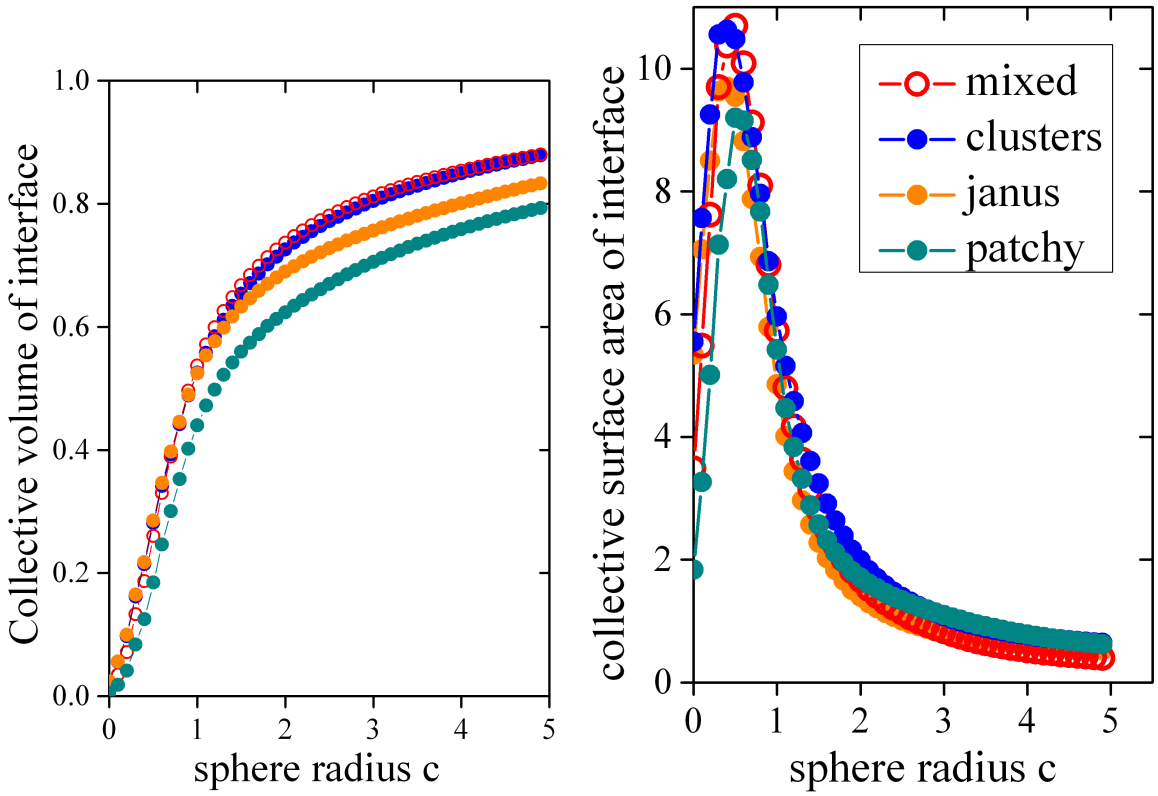

(a) volume (b) surface area

Figure 5.15: First two Minkowski measures for samples with 50% water saturation: (a) the volume and (b) surface area scalars, plotted as a function of the sphere radius, c. Shows smoothening of the interface for small correlation lengths.

Surface area

The evolution of the collective surface area curves with increasing sphere radii can be understood in a similar way to the collective volume curves. The surface area value is calculated as the enveloping surface of all the spheres.[1]

The evolution of the collective surface area with increasing sphere radius also proceeds as expected. Initially the surface area grows rapidly until all the spheres are joined into a single object. The surface area also includes the internal surface area of the enveloping shape of the interface. Once all the spheres are joined, further sphere growth begins to close the internal holes of the interface, causing the total surface area to decrease again. Eventually the surface area converges to a finite value as the collective spheres form a solid object. The first shape information that can be interpreted from these curves comes from the height of the peak.

[1]Specifically this is done from the triangulated surface using the marching cubes algorithm, which locally approximates the shape of the object inside a cube with a polygon which is selected from a library of possible shapes. This method has been reported several times as suitable for analysis of the type presented here. [28, 46, 47]

For samples which have dense seeds it would be expected that the peak position is earlier compared with samples with more dispersed seeds. At low water saturations (figure 5.14 b) we see that janus and patchy samples have peaks corresponding to $\sim$ c = 0.3, compared to mixed and cluster samples with peaks at $\sim$c = 0.8. At 50% saturations there is no detectable difference in peak position (figure 5.15 b). The second piece of information comes from the height of the peak. The more fingered an interface is, the more internal surface area it will have as the spheres begin to overlap. Applying this interpretation to the collective surface area curves displayed in figures 5.14 and 5.15 the same trends as determined by the volume scalar can be seen. Mixed samples have the most diffuse and fingered interfaces, followed by clusters and then janus and patchy which have quite compact fronts.

These curves also explain why no trends could be detected from just the voxel counting of the interface. The total shape, cannot be described from this one number alone. The volume and surface areas of the seed points are all quite similar, and further more, depend very strongly on the exact thresholds used for the segmentation. What described the shape however, is not the number of seeds, but how they are spatially distributed. It was only by analysing this feature that the differences in the shapes of the interface could be quantitatively differentiated.

Sensitivity towards segmentation

Realising now that the initial seed values are very sensitive towards the thresholding parameters used in the identification of the active interface, it is pertinent to ask, how sensitive are the Minkowski measures towards the threshold values? One of the steps in the identification of the active interface is the selection of the largest connected region. It is easy to imagine that small changes in the thresholding values could distort which regions are included in this selection, and which not. In fact varying the threshold parameters slightly the number of voxels included in the extracted liquid front can double. Of course, the segmentation is always controlled by the known volumes of the phases (see fig. 5.4), but very small errors in volume, might still have a large impact on the surface area.

To evaluate how sensitive the Minkowski measures are, liquid fronts were extracted using different values for the oil and water thresholds (for details see appendix A) and the Minkowski measures calculated. The number and size of the segmented volumes was found to be highly sensitive on the thresholding parameters. This result can been seen in figures 5.16 which displays the sensitivity of the initial seeds on the threshold parameters. On the other hand, the Minkowski analysis is robust towards these errors as shown in figure 5.17. The overlapping of the Minkowski measures for the three interfaces extracted with different thresholds confirm that this method of shape analysis is robust towards the segmentation parameters.

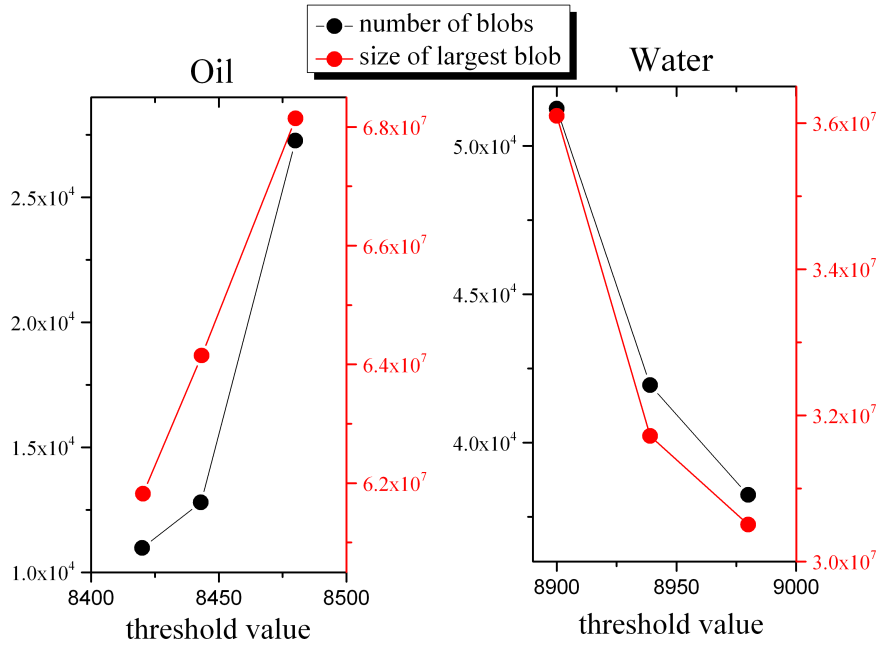

Figure 5.16: Volume of the largest connected blob, (black) and number of individual blobs (red) identified for segmentations using different thresholds. The volume of the blobs is sensitive to the threshold parameter used changing on the order of 10%, whereas the number is highly sensitive changing by a factor of two..

Imbibition vs drainage: up vs down

Lastly, the Minkowski measures can be employed to determine any differences in the fronts between the water invasion (imbibtion) or oil invasion (drainage). By eye, it is not obvious that the interfaces from these samples have the same shape. The interfaces, dilated to a value of c = 1, imaged at 50% water saturation are shown in figure 5.18. The collective volume and surface area curves for a mixed sample at 50% and 75% water saturation are shown in figure 5.19. No difference is observed in the collective properties of the fronts.

This symmetry in the front morphology is possible in these packings because the system itself is inherently symmetric- that is, there are equally many wetting and non-wetting pores regardless of which fluid is invading. This symmetry is not observed in samples with homogeneous wettability [46]. What might potentially be symmetry breaking in our experimental set up is gravity, as there is a difference in density between the two phases, particularly so in the case of the salt solutions used for the tomographic imaging. However, no differences between the Minkowski measures for the drainage and imbibition of mixed samples at the same water saturations are observed, it can be concluded that gravity, and the density difference of the liquids, does not play a significant role in the obtained results. This indicates that the front morphology, after the first imbibition at least, is influenced primarily by the sizes of the wetting domains, through contact line pinning, and not by the history of the invading liquids.

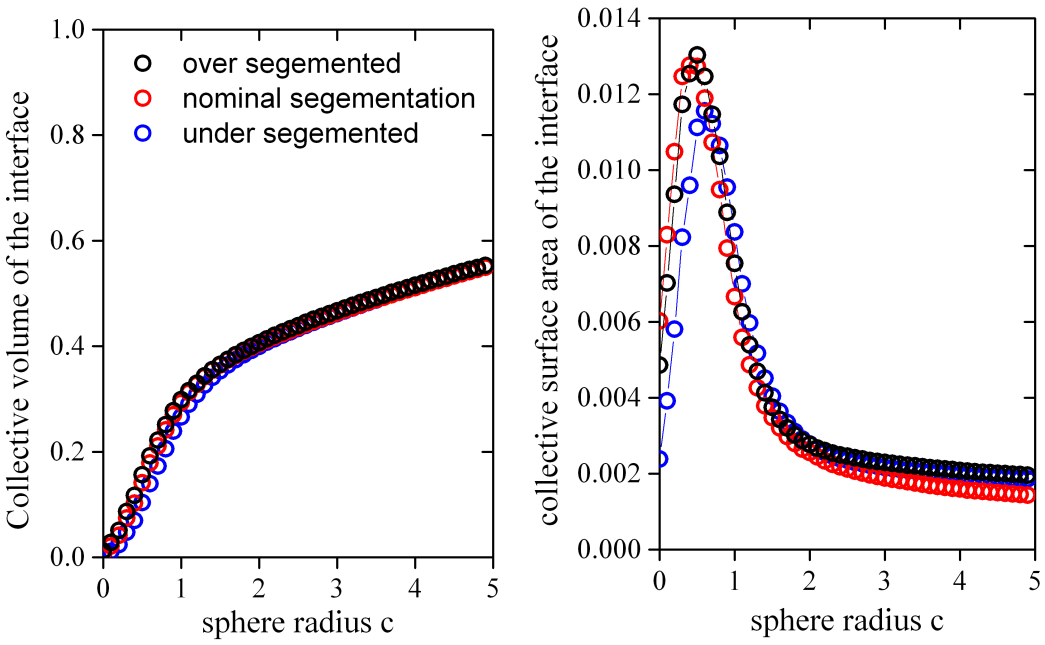

(a) volume measure

(b) surface area measure

Figure 5.17: Collective volume and surface area measurements of the interface for janus sample using different segmentation protocols. For small c, there are small differences in the curves, however these difference become increasingly small with increasing c, and the final values of the Minkowski measures are identical for the three different segmentations used. The surface area appears to be more sensitive than the volume measure but both measures are robust to small differences in the segmentation protocol.

(a) water invasion
flow upwards

(b) oil invasion
flow downwards

Figure 5.18: Mixed sample at 50% water saturations imaged during the water invasion and oil invasion parts of the CPS cycle.

This is in agreement with the observation that after the initial water invasion, the capillary pressure saturation curves do not substantially change between subsequent imbibition/drainage cycles. This suggests that once the system has been 'initialised', that is both phases have been in contact with the beads, the distribution of wettabilities dominates the flow behaviour. not the sample history, at least at the sample scale.

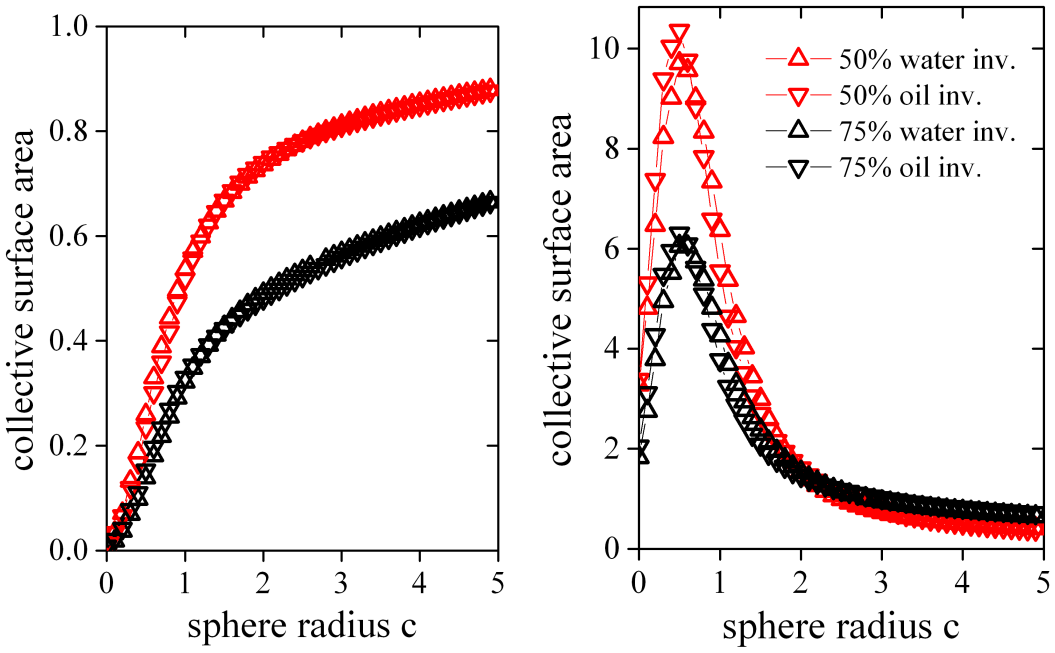

(a) volume measure

(b) surface area measure

Figure 5.19: Collective volume (a) and surface area (b) curves for mixed sample with 50% (red) and 75% (black) water saturations for both water (upwards arrows) and oil (downwards arrows) invasion. There is no difference in the shapes of these interfaces due to directionality of the fluid invasion.

The collective volume and surface area curves obtained for the four different sample types confirm the impression that the roughness, or extent of fingering of the liquid front is proportional to the wetting correlation length. At this point, there is still one more Minkowski measure which can provide quantitative shape information about the moving interfaces, that is the Euler characteristic.

5.3.3 Euler characteristic

Roughly speaking the Euler characteristic, χ, describes the number of holes a collection of objects have. It is topologically invariant and describes the shape of the object regardless of bending, or twisting. For a closed surface, such as a sphere, the Euler characteristic, written as χ is 2. For every hole that appears in the surface 2 is subtracted from the characteristic, so for example a torus, or doughnut shape, has an Euler characteristic of $\chi = 2 - 2 = 0$, a double torus has an Euler characteristic of $\chi = 2 - 2 - 2 = -2$ and a triple torus has a

$\chi = 2 - 2 - 2 - 2 = -4$. The Euler characteristic is additive, that is the Euler characteristic of a collection of objects is the sum of all the Euler characteristics of the individual objects. This is illustrated in figure 5.20. The Euler characteristic of a hollow sphere, that is an object with two closed faces, but no holes, or handles is the sum of two spheres: 4.

(a) six rum balls (multiple spheres) $\chi = 12$

(b) Truffle, (sphere) $\chi = 2$

(c) Doughnut, (torus) $\chi = 0$

(d) Pretzel (triple torus) $\chi = -4$

Figure 5.20: Euler characteristic of different shapes[2]

Figure 5.21 shows the Euler characteristic, χ, of the active interface inside a packing of janus beads at 50% water saturation. It is useful to first describe the general evolution of the Euler number with the increasing dilation factor and then compare the differences between packings. In the beginning, (label A) with a sphere radius of c=0, there are many separate objects. The Euler characteristic is the number of object minus the number of handles. For the janus sample the individual pieces of the interface have several handles in them, and the initial point is a negative number. However, is should be noted, that this value is highly sensitive to the segmentation protocol and does not really provide any information about the front shape. The section from A and B shows a sharply decreasing χ. As the spheres at each seed point are dilated, the individual objects begin to merge. This has two effects: as the objects begin to merge, there are less total objects, so the positive contribution to the euler characteristic is decreased; and secondly the number of holes per object increases. At this point there are less objects, and in general each object has more holes so the overall result is for an increasingly negative χ.

The section between labels B and C of figure 5.21 shows a sharp increase in χ. For these values of c there are only a few objects, one very large object with many handles, and still a few separate small objects. As the spheres continue to grow the handles within the object start to become separated from each other, creating enclosures. The effect of these enclosures,

[2]Photo credit for images:
a) http://www.babble.com/best-recipes/easy-no-bake-chocolate-rum-balls/,
b) http://beerntsens.com/viewproduct.asp?Productno=293,
c)http://www.npr.org/blogs/health/2012/04/17/150823790/seniors-in-medicare-doughnut-hole-more-likely-to-stop-heart-drugs
d) http://http://originalsuperpretzel.blogspot.de/2013/01/add-super-twist-to-big-game.html3

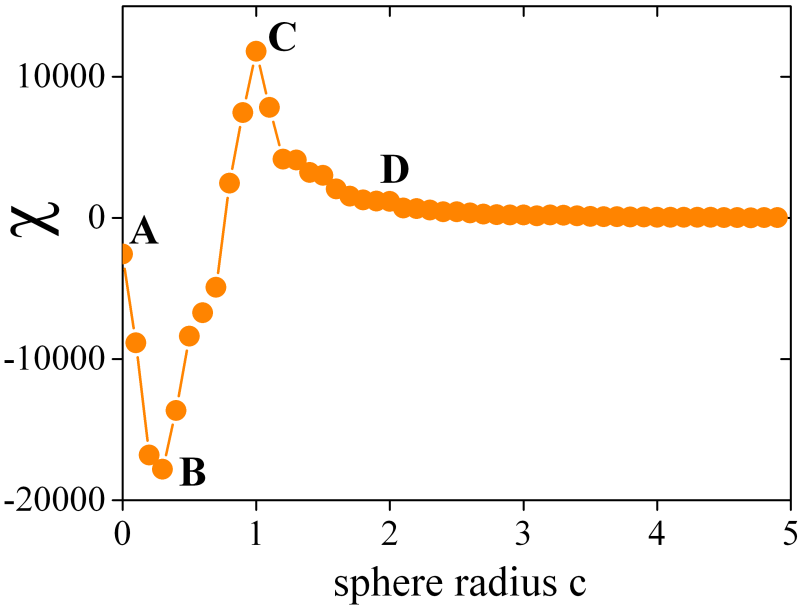

Figure 5.21: Euler characteristic for the inflated interface of a janus sample.

can be calculated by remembering the Euler characteristic of the hollow sphere. The hollow sphere which has two fully closed surfaces has a $\chi = 4$. So as the spheres continue to grow, more and more of the handles are either converted into enclosures (become separated from the background), or they are simply filled in. χ becomes increasingly positive until it reaches its maximum, which for all samples occurs at a sphere radius of c=1 voxels. After reaching the a high positive value due to multiple enclosures inside the collective interface, χ then decreases as all the holes and enclosures become filled in and the collective interface becomes a single, solid object. This can been seen in section between labels C and D in figure 5.21.

Now that the general features of the Euler characteristic curves with respect to the inflating interfaces (sphere radius) can be understood, the implications of the differences between the curves can be related to the interface shape. The Euler characteristic describes a more local property, that is the number of holes and inclusions of the interfaces compared to the volume and surface area measures. Unfortunately this also means it is more sensitive to the exact segmentation, particularly at values of low dilation (small c) as there are many 'nearly 'connected objects. Therefore the most robust and reliable portion of the curve to analyse is when all the objects are already connected after several dilation steps. The collective χ curves are plotted again, with the relevant area magnified in figure 5.22.

The height of the peak at c=1 in fiugre 5.22 is proportional to the number of completely included areas inside the interface, which is again proportional to how rough the interface is. The enveloping front shapes for mixed samples have more holes than for janus, and for patchy the least number of holes are incorporated into the interface. For the 30% saturated samples, the Euler characteristic for the clusters has a different shape, with the trough occurring at

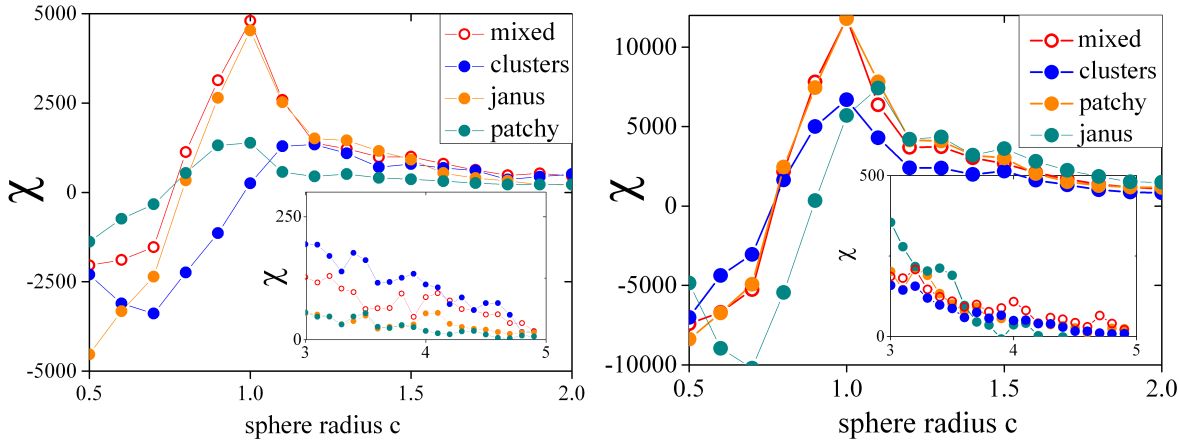

(a) 30% water saturations

(b) 50% water saturations

Figure 5.22: Euler characteristic of the collective interface. The insets show the tails of the distributions, and at high values of c which describe the enveloping shape of the interface.

higher c, than for the other samples. To understand this feature label images of the interface and background were made for the cluster and janus samples. These are shown in figure 5.23 at c=0.3, c=0.6 and c=1. The behaviour of the janus sample, fits the general profile previously described. At c=0.3, nearly all objects are connected, and there are many holes in the objects. The cluster samples however show many different objects (indicated by the different colours in the label image of the interface). This means that the original seed points are further apart, and at this dilation factor, have not yet merged. At a dilation of c=1, all the individual objects are now connected. However, unlike the other samples no peak is observed. It is now useful to compare the label images of the background for both samples. The labelled image of the janus sample shows several enclosures (that is, where the parts of the background have become cut of from the edges). These enclosures are highlighted in green. The cluster sample however, has none of these enclosures. This can be interpreted from the fact that the seed points begin further apart than for the janus sample and for clusters, at the dilation factor in which the handles close up, the interior volume is also filled. The insets to figures 5.22 a and b, show that for the interfaces at 30% water saturation, for $c \geq 2$, where the collective spheres approximate well the enveloping shape of the interface, clusters and mixed samples have larger Euler numbers, and patchy and janus samples have smaller. In the case of the 50% saturations, all the samples fall onto the same curve from $c = 3$.

The Euler characteristic is consistent, although less straightforward to interpret, with the information provided by the volume and surface area measures. The roughness of the developing front depends upon the wetting correlation length of the samples.

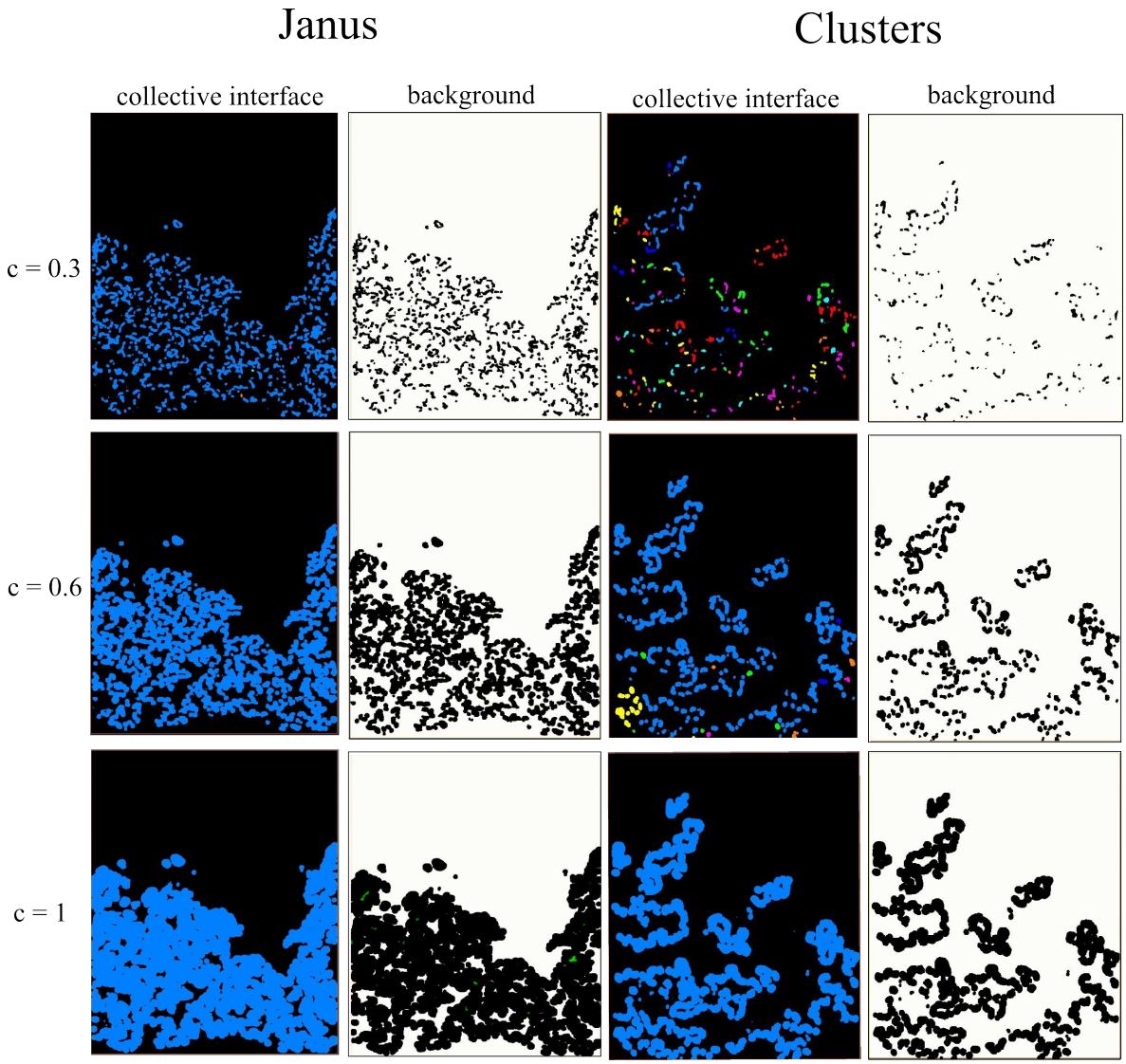

Figure 5.23: Labelled images of the collective interface and background for janus and clusters samples, for sphere radii of c=0.3, c = 0.6 and c=1. The labelled images of the interfaces show separated objects in different colours. In the first row, for clusters there are many separate objects, resulting in a high positive Euler characteristic, whereas for janus, almost all objects are joined. At c=0.6, both samples show similar characteristics, one large object for the interface, and completely connected background. For c=1, for the janus sample, it can be seen that portions of the background have become isolated due to the merging spheres at the interface. These sections are highlighted in green. This is not observed for the cluster sample.

Physical interpretation

How can this observation be understood? These experiments are performed at low capillary numbers, which means that the advanced of the liquid is dominated by capillarity. Therefore the roughness of the fronts is due to capillary fingering, which occurs due to local geometry of the pores at the interface. As mentioned in chapter 2 from the ideal capillary pressure equation we can predict that the front advance proceeds through first the small wettable pores , than large wettable pores, and then large non-wettable pores and lastly the small non-wettable. If the front always progresses through the pores in this order (dynamic x-ray experiments show that for invasion of a non-wetting fluid this appears to be the case [93] it can be understood how the fingering develops. In the case where there are heterogeneities within the pores, contact line pinning halts this advance and suppresses the fingering effects. The smoothening of the fronts are therefore consistent with the increase in dissipation of the interfacial advance measured in chapter 4. Both the increase in dissipation and the smoothening of the interface can be attributed to the pinning of contact lines at the wetting-non wetting surface junctions.

X-ray tomography imaging of the fluid interface at intermediate water saturations has been used to correlate the shape of the invading liquid front with the energy dissipation measured by the CPS experiments. It can also be employed to investigate the liquid distributions at the irreducible saturations.

5.4 Analysis of droplets at the irreducible saturations

This section addresses questions regarding the irreducible saturations. From the CPS experiments the volumes of trapped phase inside the packings did not appear to depend upon the wetting correlation lengths, and a large experimental scatter was observed. While there were no differences in the total volume of trapped phase due to correlation length it is perceivable that droplets comprising of the same total volume might be distributed in different ways. For applications such as oil recovery, the mobilisation of trapped ganglia is considered very important as up to 70% of the oil can remain trapped in these ganglia or droplets inside the reservoir [6]. Therefore, X-ray tomography was used to investigate the structure of the trapped droplets, to understand why the volume of trapped phase does not appear to depend on the wetting correlation length, and to explain the large scatter measured in these volumes between experiments.

Previous studies of this nature have found that very large amounts of the irreducible saturation can be in only a few ganglia [54, 64, 111] this was proposed in chapter 4 as a possible explanation for the scatter observed between experiments.

At the points during a CPS experiment when the irreducible water or oil saturation is reached (see figure 5.2, the sample cell is disconnected from the experimental apparatus, and imaged. By eye, it would be difficult to determine if there are any differences between the droplet shapes and sizes for different porous sample types, so again numerical analysis is used to quantify any differences in the droplets. 2D slices of the irreducible oil saturations are shown below in figure 5.24.

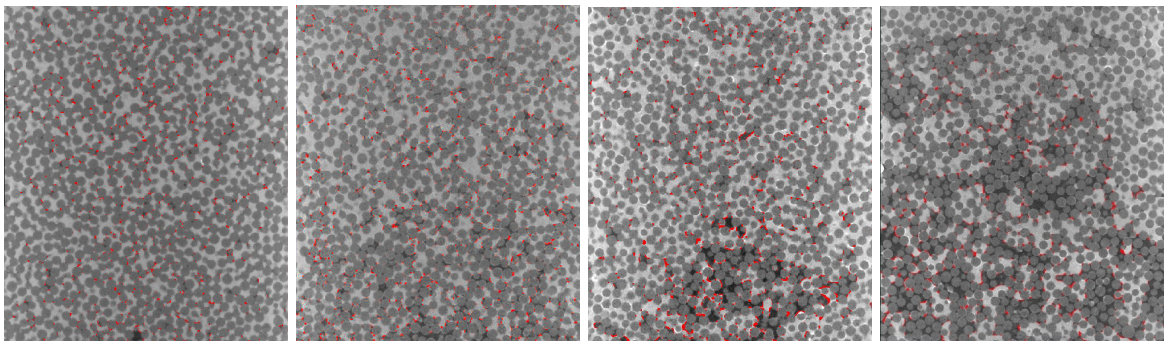

(a) patchy (b) janus (c) mixed (d) clusters

Figure 5.24: Irreducible oil saturations- the oil is dark grey, beads grey and water the brightest phase. The oil/water interfaces are highlighted in red.

There is a large range of values for the droplet sizes found in the packings and it is found that the largest droplet can comprise most of the irreducible phase. This is shown in figure 5.26 for the irreducible water and oil saturations of different packings and the results found here are comparative to literature results for systems of similar sizes [54, 64, 111]. This confirms the previously stated suspicion that the scatter between experiments could arise

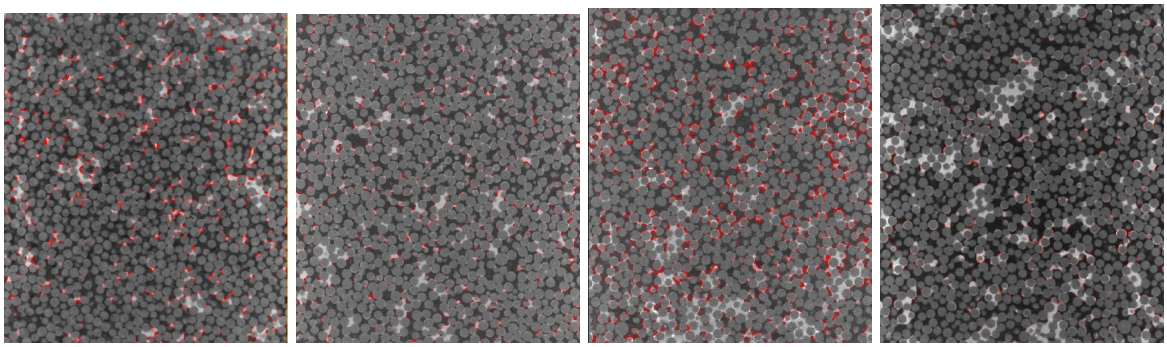

(a) patchy (b) janus (c) mixed (d) clusters

Figure 5.25: Irreducible water saturations- the oil is dark grey, beads grey and water the brightest phase. The oil/water interfaces are highlighted in red

from the mobilisation or trapping of just a single ganglia between experiments causing large differences in volumes of the irreducible phase. These values suggest that the sample size is simply too small to obtain any reasonable statistics on the trapped droplet distributions. To make any statements about the structure of the trapped phase with respect to the porous media properties, larger systems are required to obtain more statistics.

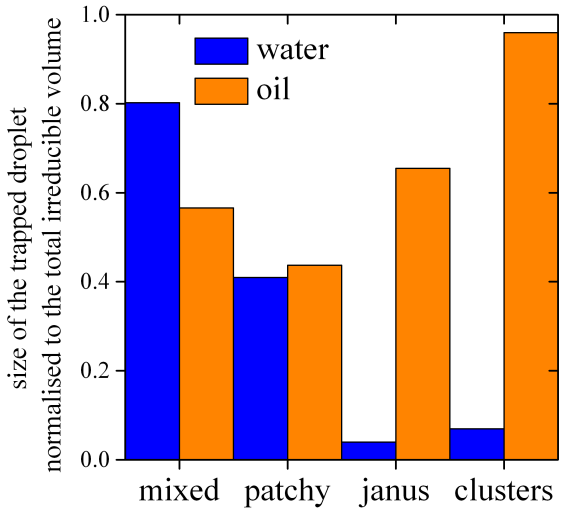

Figure 5.26: Bar graph showing the size of the largest droplet of the irreducible phase, normalised to the total volume of the irreducible phase. The largest droplet often comprises the majority of the trapped phase

The first analysis was extraction of the droplets themselves and calculating the size distributions- shown below in figure 5.28. To understand the shapes of the trapped water droplets at the irreducible water saturation from a cluster sample were rendered in 3D and are shown in figure 5.27. The shapes of the droplets are dictated by the constraints of the bead packings, and do not appear to depend on the wetting correlation length.

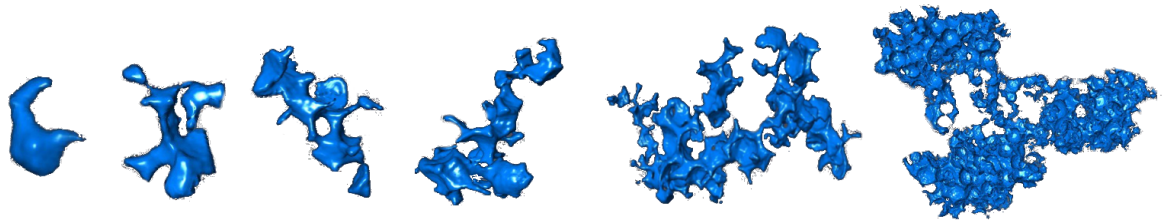

Figure 5.27: Individual water droplets, or ganglia, extracted from a cluster sample at the irreducible water saturation. Droplets range in size from leftmost: approximately one a pore volume (0.35 of a bead volume), to rightmost: spanning many pores ($\sim$ 500 bead volumes.

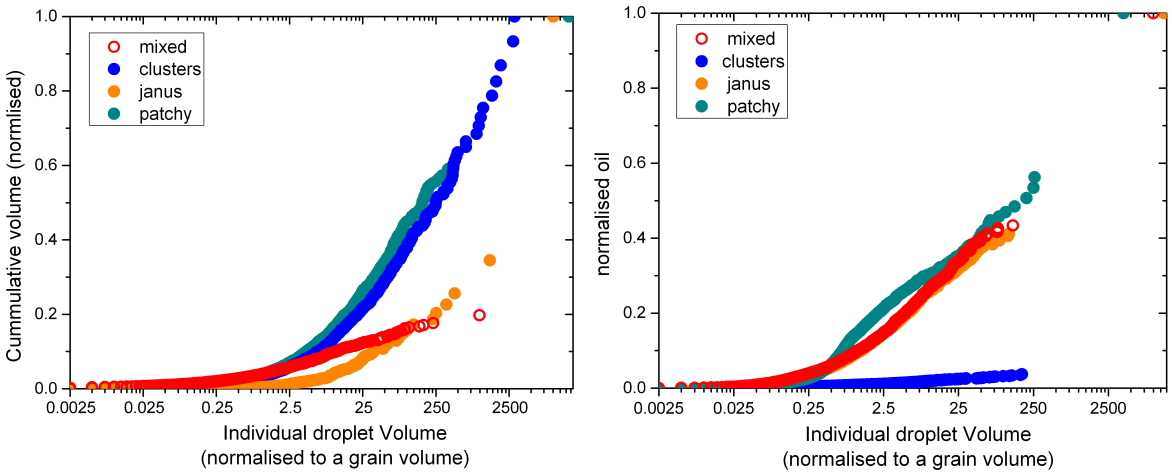

(a) residual water

(b) residual oil

Figure 5.28: Normalised cumulative size distributions of residual oil and water droplets.

What can be immediately seen from figure 5.28 is that there is no monotonic trend in the droplet sizes based on the correlation length. The scatter seen between the samples is of the same order as the scatter of these values which was observed in the CPS experiment. For completeness the Minkowski shape analysis was also performed on the liquid-liquid interfaces arising from the trapped droplets (shown in figures 5.30 and 5.29), but as expected from figure 5.26, the interfaces are dominated by one single large droplet. Thus, no structural difference in the trapped droplets due to the correlation length were able to be observed.

These measurements show is that the system size is too small to capture reasonable statistics regarding the distribution of trapped droplets. For a system of a similar size, this same problem was recently reported by Georgiadis and coworkers [54]. This observation is also consistent with the experimental scatter measured for the residual saturations (as described in chapter 4). While these experiments do not rule out that there is an effect of the wetting correlation on the structure and distributions of trapped ganglia in the porous media, at this time no effect was able to be observed. An alternative method, using ripened emulsions inside mixed and janus packings was used to prepare droplets with a narrower size

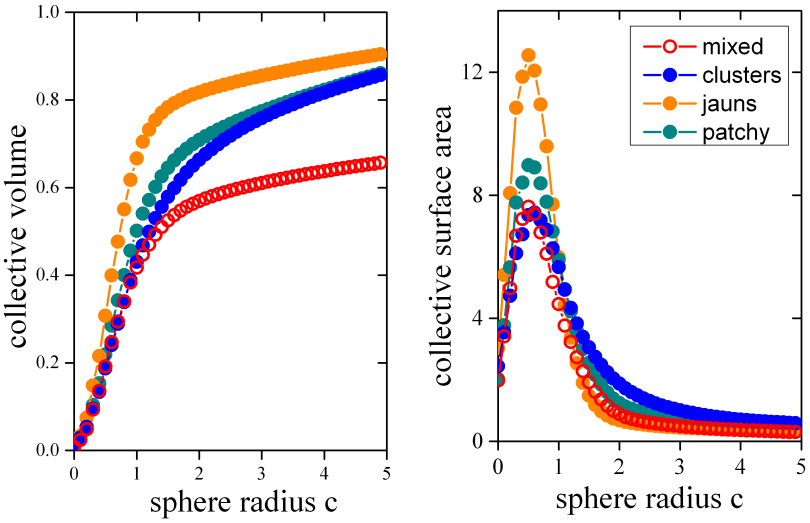

Figure 5.29: Minkowski scalars of the residual oil saturations

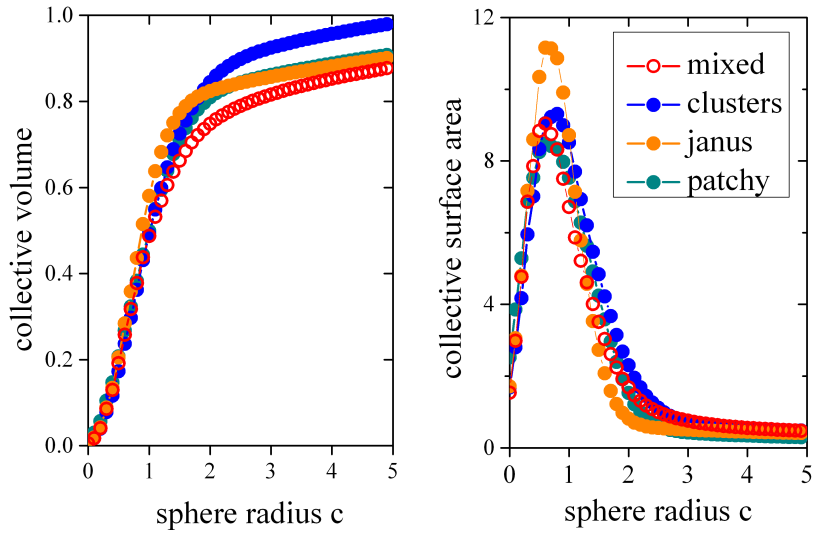

Figure 5.30: Minkowski volume and surface area scalars of the residual water saturations

distribution. However as the amount of trapped phase was very small, these results are not comparable. The experimental details and results are described in appendix C.

5.5 Summary

This chapter has dealt with the investigation into the liquid front morphology development during a capillary pressure saturation experiment using X-ray tomography. Samples were imaged at set stages of the imbibition and drainage cycles and the fronts analysed using the Minkowski measures. The front morphology at both ∼30% and ∼50% water saturations was observed to be dependant on the wetting correlation length ξ. The smoothening of the fronts is consistent with the hysteresis measurements made in chapter 4. Flow dissipation at small ξ is dominated by the pinning of contact lines at the wetting heterogeneity junctions. The fronts imaged at small ξ are smoother, caused by pinning of contact lines at wetting heterogeneity junctions. For larger ξ more fingered fronts are obtained, as there is less pinning, and dissipation of energy can is no longer dominated by contact line pinning.

Secondly the structure of trapped droplets at the irreducible saturations was investigated. By the mass measurements (chapter 4) there was no trend seen due to the correlation length, and a very large experimental scatter. It was found that very large volumes of irreducible saturation were present in just a few ganglia- in agreement with the literature [54,64,111]. This is proposed as an explanation for the large experimental scatter in the irreducible volumes, as the difference between successive experiments can be explained by mobilisation, or not, of a single ganglia. Perhaps some differences could be revealed with higher resolution x-ray tomography, where contact angles and average curvature (Minkowski tensors [47, 120]) might be extracted, but the major problem appears to be due to the limited system size.

Chapter 6

Wettability of polymer brush modified surfaces

In this chapter polymer and polyelectrolyte brushes are used to investigate two different questions regarding wetting heterogeneities in natural porous media. The first question regards the LoSal effect, and if it is possible to create a surface which exhibits a water in oil contact angle shift in the presence of salts. The second question address creating surfaces, and eventually bead pack with very small wetting heterogeneities (relative to a pore size) in order to study systems with very small wetting correlation lengths.

Firstly in section 6.1 a general introduction to polymer and polyelectrolyte brushes is and the synthesis of the brush systems used in these experiments is presented. Then the wettability of the brush systems in the presence of salt solutions is measured and the potential for such systems to mimic the LoSal effect is described in section 6.2.1. Lastly in section 6.3, the use of partially modified surfaces is presented as a means to create surface with heterogeneities on a small length scale.

The work described in this chapter was performed in a 2 month period during a short scientific stay at the BioMaGUNE in San Sebastien, Spain, under the supervision of Dr. Sergio Moya.

6.1 Polymer and polyelectrolyte brushes

Polymer brushes are polymers which are densely tethered to a surface. The close proximity of the polymers to one another forces them to adopted a straight conformation, pointing away from the surface- like the bristles of a brush, resulting in the name polymer brushes. This brush structure occurs when when the film is placed in a good solvent, that is, the polymer and solvent favourably interact. More formally put, the conformation of the brush is the result of the force balance between the osmotic force exerted on the brush by its neighbouring brushes and the elastic free energy increase which occurs when the chains become

overstretched [121, 122]. The conformation of the polymer depends on its interaction with the solvent. In a good solvent (strong/favourable interactions between the solvent and the brush) the polymer has an extended stretched conformation, whereas in a poor solvent the brush adapts a coiled conformation. These conformation changes can be used to tune the wettability of a brush modified film [123–125].

When the polymer chain is charged, such in the case of polyelectrolyte brushes there are additional electrostatic repulsions which contribute to forcing the polymer into a straight configuration. The addition of salt allows for these charges to be screened, reducing electrostatic repulsion and allowing the polymer to adopt a coiled conformation. [126]. This effect may also be produced by changing the species of the counter ion in solution. [126].

The chosen system for this investigation were polyelectrolyte surfaces which have been experimentally shown to have a counter ion dependant wettability [127–129]. However, almost all systems reported with a switchable wettability are air/water systems [127–131], and often require the addition of 'large cations', charged organic molecules which may also act as surfactants.

Typically there are two approaches used for polymer brush synthesis- the *grafting to* and *grafting from* methods. The grafting to approach uses polymers which were grown in solution and are then attached to the surface. While synthetically straightforward, stearic repulsions between large polymers reduce the efficiency of coupling reactions, and limit the density of films which can be formed in this way [123, 132]. The other approach, the grafting from method, grows the brush directly on the surface. Grafting from preparation of brushes results in homogeneous films of homogeneous composition and well controlled thickness [132]. The thickness of the film grown using the grafting from method can be controlled using 'living polymerisation techniques' . Depending on the desired products, this can be achieved in different ways such as: living anionic or cationic polymerisation [133], or ring opening metathesis polymerisation (ROMP) [134]. The most popular technique, and also the method used in this work is a living radical polymerisation.

6.1.1 Living radical polymerisation

Living radical polymerisation is where the growth of the polymer chain occurs via radical addition, and the chain growth is controlled using a radical transfer mediator, or catalyst. In a standard radical polymerisation the competing effects of polymerisation and termination reactions result in polydisperse products. The standard radical polymerisation process is indicated in figure 6.1. For applications where a small polydispersity of product is required, it is desirable to control the growth process via living techniques. In the case of surface initiated polymerisation, living radical polymerisation is employed to ensure brushes of the same length, thus yielding homogeneous coatings.

Living radical polymerisation refers to polymerisation techniques which control the growth

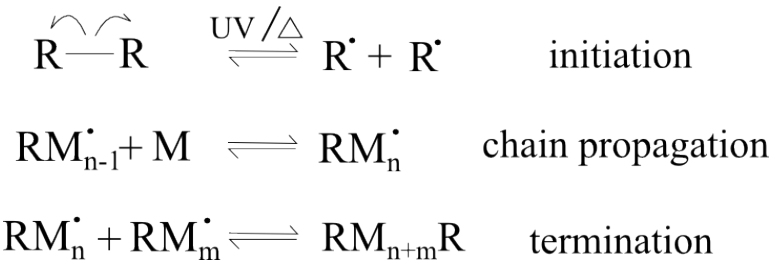

Figure 6.1: reaction schematic of radical polymerisation. The initiator molecule decays, in the presence of an external stimulus such as UV light, or heat forming two radicals. These radicals react with the monomer unit, denoted by M, propagating the chain growth. Two radicals can recombine at any time, terminating the reaction. If there is no control of the termination reactions the resulting polymers have a large polydispersity.

of the polymer by blocking the termination reaction. The radical is transferred from the growing polymer to new monomer through a catalyst. There are a range of these techniques such as NMP (Nitroxide-mediated polymerisation), RAFT (Radical addition-fragmentation chain transfer), and ATRP (Atomic transfer radical polymerisation).

Each method has advantages and drawbacks and depending on the desired products different methods are more suitable. Several comparisons of these different methods have been published, and such an example can be found in reference [123]. For this work brush growth is achieved by ATRP. ATRP uses the equilibrium between a dormant and active catalyst (usually copper(II)/copper(I)) to control the rate of polymerisation. The advantages of of ATRP are that it works at room temperature, does not require anhydrous conditions, requires initiators that are easy to synthesise. The only potential difficulty is the oxygen sensitivity of the Cu(I) catalyst, meaning the reaction must be performed under inert conditions, however this also provides an easy method of quenching the reaction, as exposure to air will oxidise the Cu(I) catalyst terminating the reaction. The growth of brushes on a surface is achieved by first tethering the initiator to the surface, by forming a self assembled monolayer of APTES (3-aminopropyltriethoxysilane) to which the initiator molecule is couple. This is known as SI-ATPR (Surface Initiated Atomic Transfer Radical Polymerisation).

For growth of polymer brushes on surfaces SI-ATRP, which stands for Surface Initiated Atomic Transfer Radical Polymerisation is used. The control of the radicals, and thus the addition of new monomer to the polymer chain is facilitated by the equilibrium between the active Cu(I)-bipyridyl complex and the dormant Cu(II)-bipyridyl complex resulting low polydispersity polymers. The reaction schematic is drawn in figure 6.2.

6.1.2 Synthesis of brushes

The synthesis of the brushes can be divided into three steps. First the substrates need to be activated. This is achieved by forming a monolayer of APTES (3-aminoproplytriethoxysilane). Then, the polymerisation initiator, in this work BIBA (bromoisobutyrylbromide) is attached

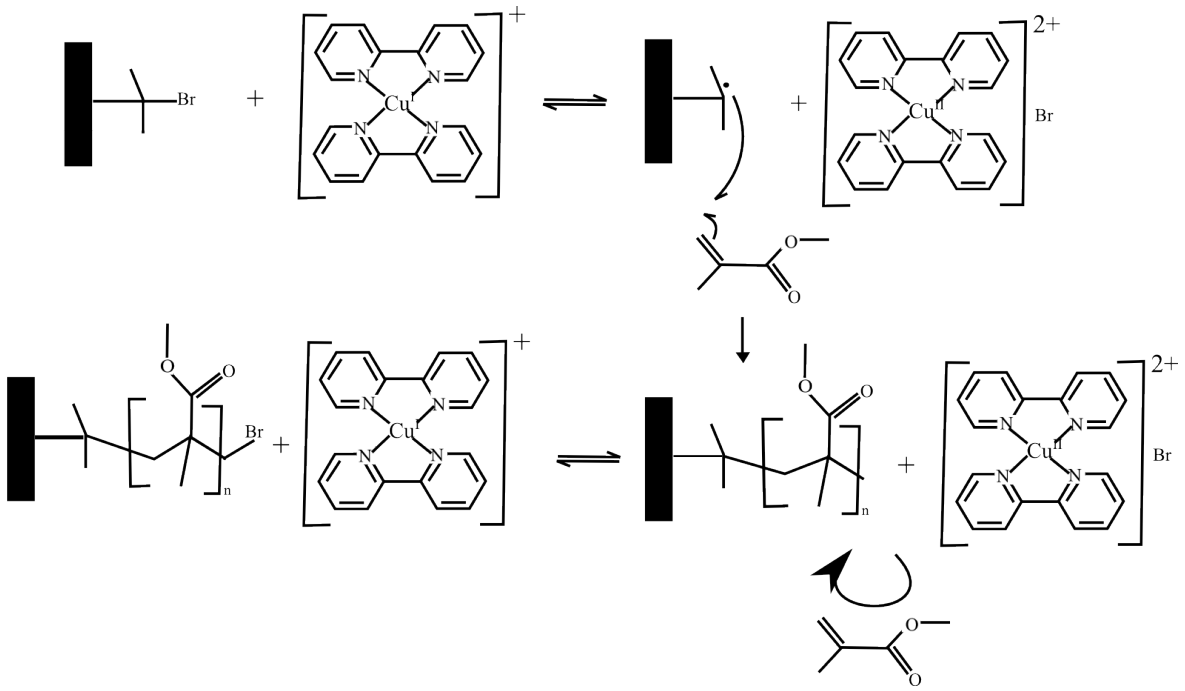

Figure 6.2: Reaction scheme of ATRP. The initiator is tethered, via APTES, to the glass surface, here represented as the solid black rectangle. First the catalyst solution is added to the reaction vessel containing the activated surfaces. The transfer of a radical from the initiator to the Cu(I)-bipy complex results in the surface tethered radical and a Cu(II)-bipy complex, and from here chain growth at the surface proceeds. Monomer (here methylmethacrylate is drawn) is added to the solution and chain growth proceeds via radical addition. The equilibrium between the Cu(I)-bipy complex and the dormant chain and the Cu(II)-bipy complex and the active chain controls the growth of the polymer. Termination of the polymer growth occurs when the Cu(I) catalyst is quenched by exposure to oxygen.

to the silane. After tethering of the initiator to the surface the polymer brush can be grown using ATRP. The following paragraphs describe the details of each step.

Preparation of substrates

Silicon and glass wafers were pre-cleaned by sonnicating in acetone (5 min), then ethanol (5 min), then nanopore water (5 min), dried under nitrogen and then cleaned in the Plasma cleaner (20 min).

To initiate the glass slides for polymerisation the cleaned slides were immersed in a 1% APTES solution in toluene (30 min) at room temperature. Following this, the slides were cleaned by sonnication in acetone (3 min) and then ethanol (3 min) and then dried in the oven at 60°C (4 hours).

Wafers were then placed in a conical flask, taking care that none of the wafers touch, and the flask was placed in an ice bath. 15 mL of DCM (Dichloromethane) and 0.6 mL of TEA (triethylamine) was poured on top of the wafers. These concentrations are such that the initiator is in excess, and up to ten 1 x 2 cm glass slides were initiated in such a solution.

0.6 mL of BIBA (bromoisobutyrylbromide) was added to 15 mL of DCM in a seperating funnel. The neck of the funnel was placed inside the neck of the flask and sealed to prevent any vapour from escaping. The BIBA solution was then added drop wise to the flask with the wafers (over approx. 10 min). After 2 hours the flask was removed from the ice bath and allowed to warm to room temperature over night. The reaction solution was then decanted and the wafers rinsed in nanopore water, sonnicated in acetone and then ethanol, (1 min each), and then dried under N_2.

For characterisation purposes, the contact angle of glass slides modified with an initiator layer was measured to have an advancing angle of $90\pm5^\circ$ and a receding angle of $60\pm5^\circ$ for air/water systems. The preperation and initiation of the glass sides is the same for all the polymer brush systems used in this series of experiments. Several types of polymers van be grown from these initiated substrates depending on the monomer (and solvent) used in the subsequent steps.

PSPM, Poly(3-sulfopropylmethacrylate)

The structure of PSPM is shown in figure 6.3. PSPM Brushes: Initiated glass slides were de-oxygenated by blowing N_2 through a conical flask containing the wafers. Solvent was prepared with 9 mL of DMF (dimethylformamide) and 6 ML of H_2O and degassed by bubbling N_2 through the solvent for 30 min. 8.9 mg of Cu(II)Cl_2, 33.2 mg Cu(I)Cl and 123,67 mg Bipy (bipyridine), added to 5 mL of Solvent in a dry flask. 1.576 g of monomer was transferred to the flask with with wafers and washed using 5 mL of solvent. The catalytic solution was then added and brushes were grown for 2 hours. After this time the reaction was quenched by opening the flask to air, the films collected, rinsed in nanpore water and dried with N_2. PSPM brushes prepared in this way had a dry film thickness measured by AFM and ellipsometry of 26 nm.

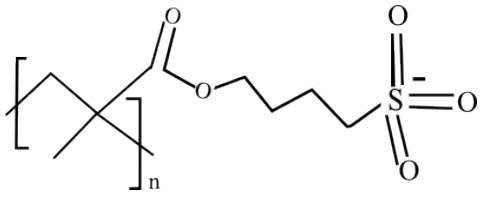

Figure 6.3: Molecular structure of PSPM Poly(3-sulfopropylmethacrylate)

PMETAC, Poly([(2-methacroloyloxy)ethyl]triammonium chloride))

The structure of PMETAC is shown in figure 6.4. PMETAC Brushes:In a round bottom flask 30 mL of solvent was made up from 15 mL of MeOH and 15 mL of nanopore H_2O and is degassed by bubbling with nitrogen gas for 30 min. 100 mg of CuCl and 300 mg of bipy (bipyridine) were then added to a second degassed 2-neck flask with 5 mL of degassed solvent

under stirring. The initiated wafers were placed in a conical flask, and oxygen removed blowing nitrogen through the flask. 3.34 mL of METAC monomer was added to the catalyst solution and then immediately transferred to the wafer containing flask. Brush growth proceeded for 2 hours and then the polymerisation was quenched. The wafers were rinsed in nanopore water and dried with N_2. Brushes prepared in this way had dry film thickness's measured by AFM and ellipsometry of 3 nm.

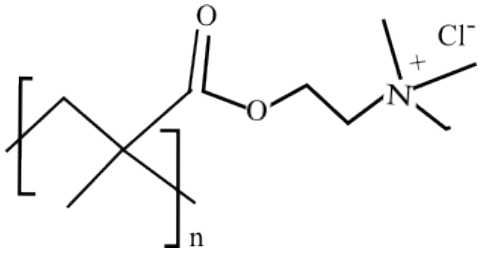

Figure 6.4: Molecular structure of PMETAC Poly([(2-methacroloyloxy)ethyl]triammonium chloride))

PMMA, Poly(methylmethacrylate)

The structure of PMMA is shown in figure 6.5. A flask containing the initiated glass slides was de-oxygenated by flushing with N_2 for 30 minutes. The solvent consisting of 9 mL DMF and 6 mL H_2O was concurrently de-oxygenated by bubbling with N_2 for the same amount of time. To 10 mL of the de-oxygenated solvent 33.2 mg of Cu(I)Cl, 8.9 mg of Cu(II)Cl_2 and 123.67 mg of Bipy were added. The catalytic solution was transferred with a cannula to the flask containing the glass slides. To the remaining 5 mL of de-oxygenated solvent 424 mL (398.87 mg) of MMA (Methylmethacrylate) was added and then transferred directly to the flask containing the slides. Polymerisation proceeded for 2 hours before quenching the reaction. The films were collected, rinsed in ethanol and dried under N_2. The dry film thickness was measured by ellipsometry to be 47 nm.

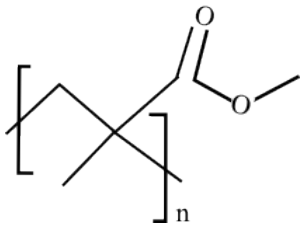

Figure 6.5: Molecular structure of PMMA (Polymethymethacrylate)

Block co-polymers

Block Co-polymers were prepared by sequential polymerisation reactions of the same surfaces. The first block was grown using the procedure as listed above, then the substrate rinsed and

dried, and then placed back inside a flask with a nitrogen atmosphere. The new monomer and catalyst solutions were then added and the second and third blocks allowed to grow for 2 hours. The easy attachment of multiple blocks to the polymers is facilitated by the bromine group which remains at the end of the polymer chain (shown in figure 6.2), and is used to re-initiate the polymerisation. For addition of PSPM blocks, only the Cu(I) catalyst was used without addition of the Cu(II) compound, as the initiation of the bromine from the polymer is not as efficient as from BIBA. Polymerisation of PSPM as a monoblock using only the Cu(I) catalyst, with no additional Cu(II), resulted in 53 nm thick films.

Di and triblock copolymers were synthesised: PMMA-PSPM, PSPM-PMMA, PMETAC-PMMA, PMETAC-PMMA-PMETAC, PSPM-PMMA-PSPM, and PSPM-PMMA-PMETAC.

6.2 Stimuli sensitive wettability and the 'LoSal' effect

Smart surfaces, or surfaces which can change their wettability in the presence of an external stimuli, have been gaining more and more attention in the last decade due to applications such as smart membrane material [135], drug delivery, or biocatalysis [136]. Polymer brushes are a popular way to create surfaces which exhibit wettability changes in response to their surrounding environment. Contact angle shifts of these systems have been achieved by changing solvents [124, 125, 137], temperature [138, 139], UV light [140, 141], or salinity [127–131].

As discussed in chapter 1, the wettability of a surface inside porous media dictates the flow patterns of immiscible liquids through such media. Mixed wettability inside natural porous media, such as aquifers or oil reservoirs occurs due to the adsorption of organic compounds to the rock surfaces during diagenesis. The previous chapters described the wetting heterogeneities in for model systems that were created using simple hydrophobic surface coatings. However, the wettability of natural systems, caused by for example asphaltene adsorption [142, 143] also changes in the presence of different liquids. This has been empirically observed in what is called the LoSal effect [75]. The LoSal effect refers to an increase in the amount of recovered oil when a core is flooded with low salinity water, compared with sea water flooding. The increase in oil has been ascribed to a local change in contact angle at the rock surface when low salinity water is used [76, 77]. Recent work on this topic has shown that the presence of divalent cations increases adsorption of organic compounds, such as stearic acid or crude oil components at liquid liquid interfaces [78, 79] and mineral surfaces [80, 81]. It has been found that when these surfaces are washed with low salinity water these organic compounds can be removed.

While this mechanism has been examined on a molecular level, using chemical force spectroscopy [80, 81], ellipsometry and AFM [78, 79], the effect of a change in contact angle on the morphology of trapped droplets inside a porous media has not yet been examined. Experiments on two phase flow in 2D micromodels [144] and in 3D homogeneously wetting bead

packs [93] have observed significant changes in final oil saturations and front morphology of the invading liquid when the three phase contact angle is increased above 90°. Empirical studies of core floods with low salinity water report that the most significant oil recovery gains occur when the rock is initially mixed wet, and becomes more water wetting [76, 77]. Therefore we also expect that morphological changes in trapped droplets, leading to remobilisation of ganglia occurs also around contact angle shifts close to 90°

The bead packs used for the flow experiments (as described in chapters 4 and 5, consist of approximately 150,000 beads. To conduct experiments on this scale, with treated beads which had a coating that exhibited a wettability change in the presence of salt the coating methods needs to be upscalable. The following section describes the attempts to achieve a switchable wettability using the polymer brush films.

6.2.1 Wetability of Polymer Brush films

The advancing and receding contact angles for all the different brush types synthesised (section 6.1 were measured against air and oil and are shown in figure 6.6. Advancing and receding contact angles were measured by increasing and decreasing the volume of a sessile drop on a plain surface (drop volume ∼20 μL with ±2 μL increases/decreases), in air and under oil. The images are collected using Data Physics OCA5 goniometer and drop profiles fitted using a circle profile using the commercial software SCA. For every contact angle measurement, of each brush/solution system described in this chapter, at least ten measurements were taken and the average and standard deviation were plotted.

As seem in figure 6.6, the end group of the brush appears dominates the wettability of the surface. Block co-polymers ending in PSPM are hydrophilic in both oil and water and have contact angles similar to PSPM. For PMETAC the contact angles seem to be more sensitive to the prior blocks. This is easy to understand because PSPM grows faster and the brush component is much longer compared to the PMETAC blocks. In oil, the PMETAC block appears to collapse and the contact angles measured for PSPM-PMMA-PMETAC appear like those measured for the single PSPM blocks. In general, the contact angles of all polymers except the PMMA ending blocks appear hydrophilic in both air and oil (CA < 90°) and the contact angle hysteresis of all systems is large. In order to reproduce the LoSal effect we are searching for a system which becomes increasing hydrophobic in the presence of salts. As mentioned previously, we expect contact angles shifts occur either side of 90° to be the most interesting to test mobilisation of droplets trapped inside bead packs.

The contact angles measured against water have the brush surface in the hydrated state. To achieve the contact angle shift, salt solutions are added to the polymer brush surfaces, to collapse the brushes and increase the hydrophobicity of the surface. The contact angles measured in air are in agreement with previously reported values of 28° for PSPM [128], 78° for PMMA [145] and 40° for PMETAC [146].

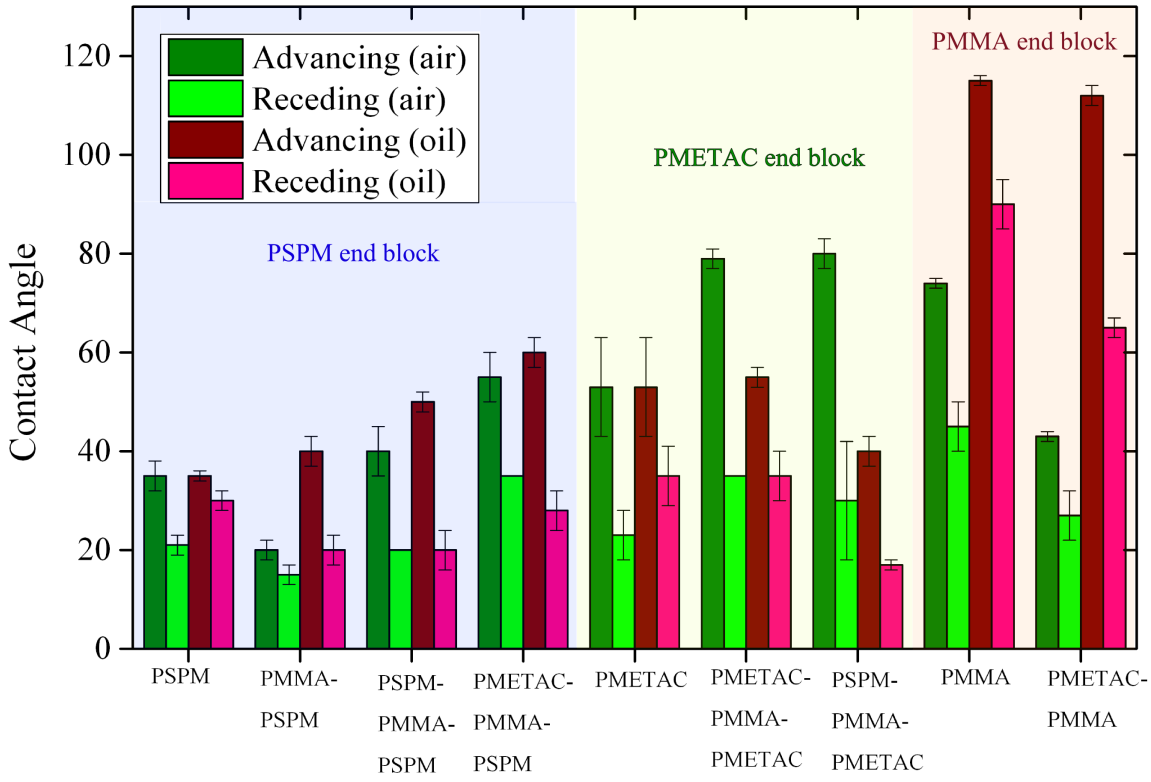

Figure 6.6: Advancing and receding contact angles measured in air and water (green) and oil in water (red) for polyelectrolyte brush films. The error bars show the standard deviation between ten measurements.

While the PMMA brushes and PMMA terminated blocks give the highest contact angles, and indeed the only ones above 90°, PMMA is uncharged (see figure 6.5). Therefore, it seems unlikely that increasing ionic strength will facilitate a further collapse of the brushes. Therefore the initial investigation focussed on the polyelectrolyte brushes in saline solutions. To force a hydrophobic collapse of the brushes the polyelectrolyte films were soaked in salty solutions for ten minutes, rinsed quickly in nanopore water, to prevent salt crystallisation upon drying/addition of oil and then placed in an oil bath. The advancing and receding contact angles against the salt solutions were then measured.

Salt type

Polyelectrolyte brushes have a wettability which depends upon the conformation of the brushes. For these surfaces it has been shown that changing the type of counter ion of the brush can dramatically change the conformation of the brushes [126, 127, 147–149], and thus the air/water contact angle.

Figure 6.7 shows the contact angles measured for PSPM and PMETAC polyelectrolyte brushes in the presence of different salt solutions. Salts were chosen that would appear in

natural sea water (NaCl, $MgCl_2$, $MgSO_4$, $CaCl_2$, KCl and $LiClO_4$) and selected such that both anions and cations could be tested. The effect of these salts on the polyelectrolyte films was investigated by first soaked in a 1 M solution of the different salts, and the advancing and receding contact angles of the salt solution in oil (octadecane) were measured. The results of these measurements are shown in figures 6.7.

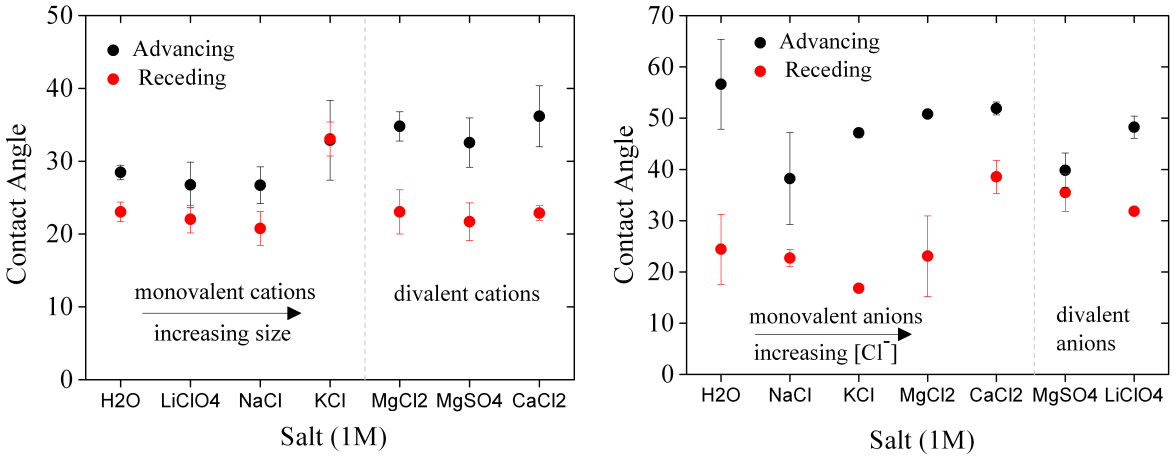

(a) PSPM (b) PMETAC

Figure 6.7: Advancing and receding contact angles measured on (a) PSPM and (b) PMETAC surfaces after soaking in 1 M salt solutions. Each data point consists of more than ten measurements, and the error bars are the standard deviation.

PSPM is a negatively charged polyelectrolyte and so the interaction of the salt is largely through the cations. A larger shift in contact angle is observed for monovalent larger cation, K^+, compared to Na^+ and Li^+. Both the divalent cations tested appear Mg^{2+} and Ca^{2+} appears to cause an increase in advancing contact angle. This indicates that both the size of the ion and the valency are important.

For PMETAC systems, all of the contact angles measured in salt solutions under oil showed lower contact angles compared with those obtained in after soaking in water (see figure 6.7b). This is not intuitive to explain. The PMETAC may be so poorly solvated by the oil, that the brushes are already in a collapsed state when the salt solution is added. PMETAC has a positively charged backbone, so the counter ions in solution will be anions. Unlike the PSPM, there does not seem to be a difference between the monovalent and divalent anions, in the advancing contact angles for PMETAC. What is instead seen is the effect of increasing concentration of Cl^- ions, ($MgCl_2$ and $CaCl_2$ have 2 M of Cl^-), although this is not particularly strong. There does not seem to be a strong difference between wettabiliy of PMETAC filsm soaked in salt solutions with either monovalent or divalent cations.

What is noticeable for both mono-block brush systems are the large values for contact angle hysteresis, for PSPM on the order of 10° and for PMETAC as large as 30°. While for capillary pressure saturation experiments (see chapter 4) it has been determined that advanc-

ing contact angle rather than contact angle hysteresis is the control parameter for the fluid displacement profile [49, 50], what effect this would have on changing droplet morphologies due to a local contact angle change is unclear.

Even for the collapsed state of the brush, indicated by the contact angle shift, the contact angles are still very hydrophilic ∼35° for PSPM and ∼50° for PMETAC as seen in figure 6.7. From the initial contact angle survey of the different brush types (figure 6.6), PMMA and PMETAC-PMMA had much higher contact angles. Therefore it was considered that using blocks of polyelectrolytes and PMMA might be able to create a contact angle shift from hydrophilic to hydrophobic. The idea is that when the polyelectrolyte block collapses the PMMA will then dominate the wetting characteristics. Brushes consisting of differently wetting blocks have been reported [150] to have solvent dependant conformations caused by phase segregation of the differently wettable blocks. Four tri-block polymers films were created, PSPM-PMMA-PSPM, PMETAC-PMMA-PSPM, PSPM-PMMA-PMETAC and PMETAC-PMMA-PMETAC.

PMMA, PMMA-PSPM and PMETAC-PMMA-PSPM

First the mono-PMMA block brushes and the di-block PMMA-PSPM were tested for sensitivity towards NaCl. The results are shown in figure 6.8. Then the tri-block structure PMETAC-PMMA-PSPM was also tested for salt sensitivity and the results are shown in figure 6.9.

The PMMA showed little sensitivity towards the NaCl with a slight decrease in advancing contact angle, whereas the PMMA-PSPM behaved exactly like the PSPM mono block, with a decrease of the same order on addition of NaCl. Therefore it was concluded that the PSPM block on top of the PMMA was of a thickness which meant, even on PSPM collapse, the PMMA was not visible to the liquids. This was also seen for the tri-block structure PMETAC-PMMA-PSPM (figure 6.9). This suggests that for a switchable wettability due to the presence of a lower block in the brush structure the upper block needs to be short. The chain length of any polyelectrolyte could be optimised by changing either the reaction conditions (i.e percentage catalyst used) or the growth time. However, due to the limited time for these experiments that was not investigated further. Rather, the tri-block systems ending in the short PMETAC blocks were used (PSPM-PMMA-PMETAC and PMETAC-PMMA-PMETAC).

PSPM-PMMA-PMETAC

Before the wettability testing with different saline solutions could be formed, an unforeseen problem concerning the PSPM-PMMA-PMETAC films was encountered. The problem with this system was the extreme ageing of these films when measured under oil. This is perhaps why oil/water contact angles are rarely reported in the literature. Figure 6.10 shows the

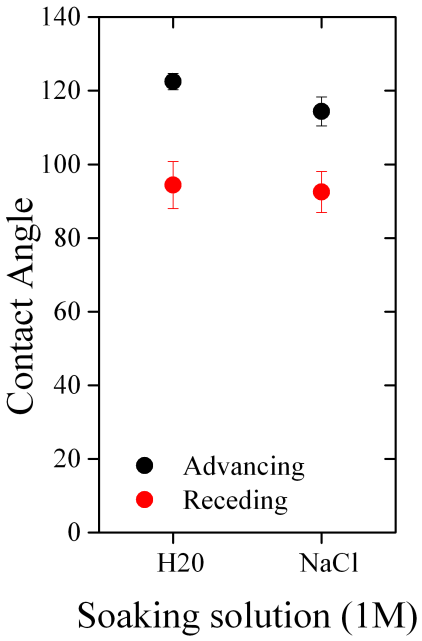

(a) PMMA

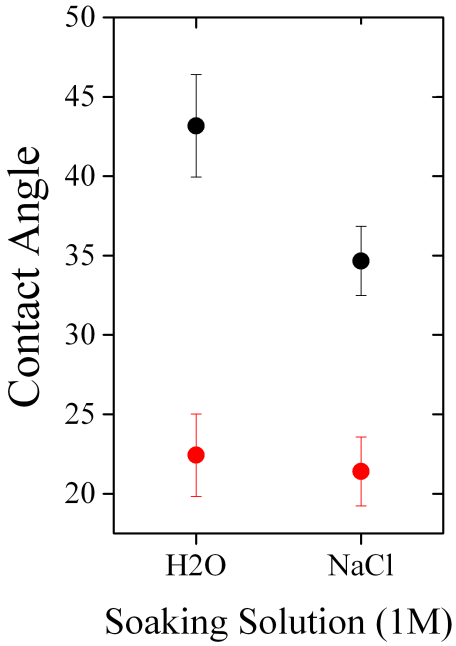

(b) PMMA-PSPM

Figure 6.8: PMMA and PMMA-PSPM contact angles measured water in oil and NaCl in oil. Neither systems exhibits a strong wettability change due to the presence of salt.

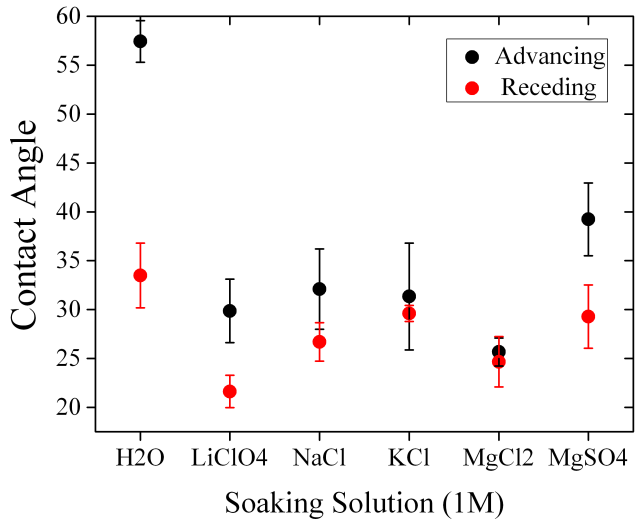

Figure 6.9: Change in contact angles for salt solutions measured under oil. The triblock system appears to behave like the mono PSPM block, in that, for at least this system, the contact angles seem closest to PSPM and the top block appears to dominate the wetting behaviour.

ageing behaviour of a PSPM-PMMA-PMETAC film for water in oil contact angles measured. These measurements were made by placing new droplets on the surface that was being aged

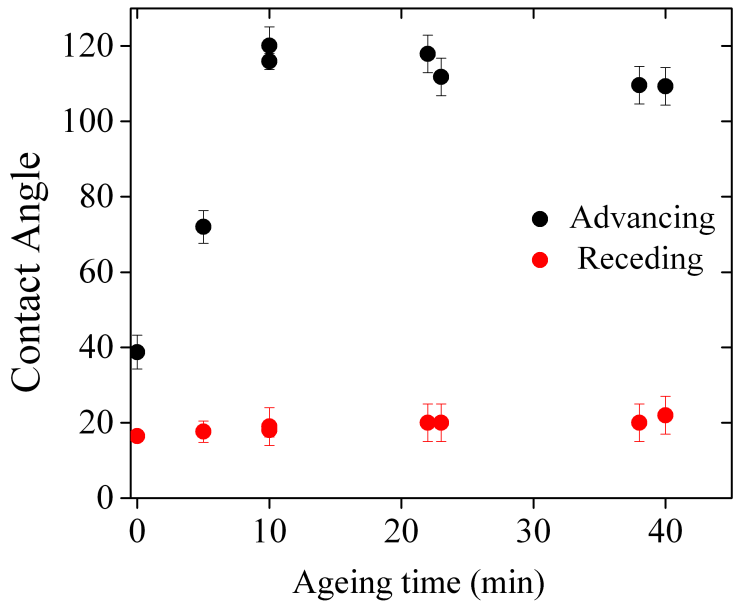

Figure 6.10: Ageing behaviour of PSPM-PMMA-PMETAC films under oil. The contact angle increases dramatically over the first ten minutes, then appears to reach a stable value. The change in the advancing contact angle is significant, from very hydrophilic to hydrophobic, although the receding contact angle appears to remain constant at around 20°.

in the oil. In the beginning hydrophilic contact angles are recorded, but within 10 minutes the advancing angle has increased to something hydrophobic. After 10 minutes the contact angle appears to be is relatively stable at around 110 degrees.

The initial contact angles measured are on the order of those measured for PSPM in oil, where are the final ones are more similar to those of PMMA. Therefore it appears that when measured directly after placing in the oil the brush behaviour is dominated by the PSPM block, but after ageing in the oil, it could be expected that the PSPM block collapses, and the brush behaviour is then dominated by the PMMA block. PMMA does not appear very sensitive towards salt concentration, as it does not qualitatively change when soaked in 1 M NaCl (see figure 6.8). Therefore the PSPM-PMMA-PMETAC system, which appears like PMMA after ageing for more than ten minutes in oil is not a promising system and further salt tests were not carried out. The cause of the ageing is no doubt very interesting, but unfortunately for now, the mechanism could not be determined. Perhaps, as was suggested for the PMMA-PSPM system, this response might be due to the relative lengths of the brushes. In this case tuning the relative lengths may provide a means of optimising the desired response. However, at this time, this was not investigated.

PMETAC-PMMA-PMETAC

The other brush system which showed promising behaviour from the oil/water contact angles was the PMETAC-PMMA-PMETAC block system. Like the PSPM-PMMA-PMETAC block system, the contact angle measured under oil were smaller than those measured under air, suggesting that when this system is in air, the PMMA block is very visible to the droplet, and under oil the PMETAC block dominated the interaction more. Unlike the PSPM-PMMA-PMETAC system, this system did not dramatic changes in the contact angle over time. The advancing and receding contact angles under oil for the tri block polymer matched those of the single PMETAC block. However, unlike the single PMETAC block, the tri block polymer was observed to have an increase in contact angle with the addition of salt. The contact angles measured of 1 M salt solutions under oil for PMETAC-PMMA-PMETAC films are shown in figure 6.11. Again, the contact angle hysteresis is very high. However, this system does show a shift in the advancing contact angle in the presence of salt to values close to 90°. Therefore these systems may be of interest to create switchable wettability inside a bead pack. To further investigate the effect of salt concentrations the contact angles were then measured against 0.1, 0.5 and 1 M concentration. The results of these experiments are shown in figure 6.12. The behaviour appears quite complicated. For $MgCl_2$ and $LiClO_4$ the contact angles decrease with increasing salt concentration. For NaCl there are slight increases with increasing salt concentration, but the most interesting solution is the $MgSO_4$ which exhibits a significant increase between 0.1 M $MgSO_4$ and 0.5 M $MgSO_4$. To understand what is happening to the polymer brush film with the increasing salinity experiments for this system (PMETAC-PMMA-PMETAC in $MgSO_4$ solutions), QCMD measurements of the film were made.

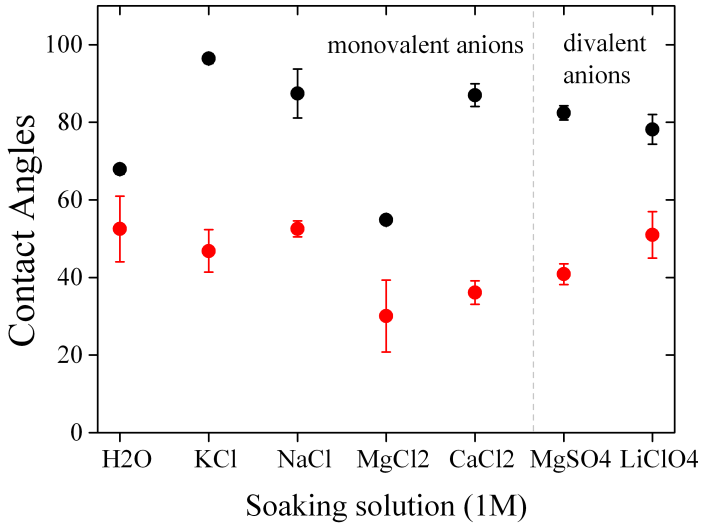

Figure 6.11: Contact angles of salt solutions (1 M) measured against PMETAC-PMMA-PMETAC polymer brush films under oil. The advancing contact angles are shown in black and the receding contact angles shown in red.

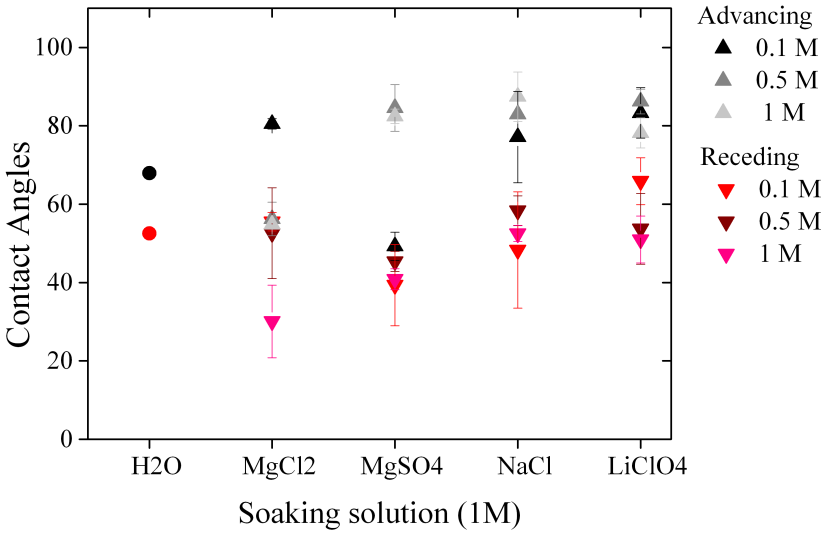

Figure 6.12: Contact angles of salt solutions with different concentrations measured against PMETAC-PMMA-PMETAC polymer brush films under oil. The most interesting salt solution appears to be $MgSO_4$, as the film becomes increasingly hydrophobic with increasing salt concentration.

6.2.2 QCMD experiments

To directly observe the effect of the salt on the films, polymer brushes were grown on QCMD (Quartz Crystal Microbalance with Dissipation measurement, from Qsense) sensors and then flushed with salt solutions to measure the response of the film. Collapse of polyelectrolyte PMETAC and PSPM films with addition of salt has been previously observed using simultaneous ellipsometry and QCMD, where the loss of mass was observed to coincide with a decrease of film thickness [148, 149] and is attributed to the loss of water molecules from the hydrated bruses upon collapse. QCMD is therefore an interesting way to observe the behaviour of the block co-polymer systems when introduced to saline solutions.

Quartz Crystal Microbalance measures the resonance of a quartz crystal using the piezoelectric effect. The resonant frequency of the crystal is proportional to the mass, and thus as more mass is deposited during polymerisation on the crystal the frequency changes proportionally. The dissipation of the resonance can be related to the viscoelastic properties of the film on the substrate, and as a rule of thumb, a decrease in dissipation indicates an increase in the rigidity of the film. By fitting the QCMD data, quantitative analysis of the deposited films is possible, however in the proof of concept experiments shown in this section only qualitative behaviour is discussed. Figure 6.13 shows a photo and schematic of the experimental set up used and two QCMD sensors on which the polymer brushes were grown. Figures 6.14 shows an example experiment where the growth of PSPM was monitored using QCMD. The rate of change of the frequency of the QCMD sensor is proportional to the rate of mass deposition, or in other words polymer growth [147, 148].

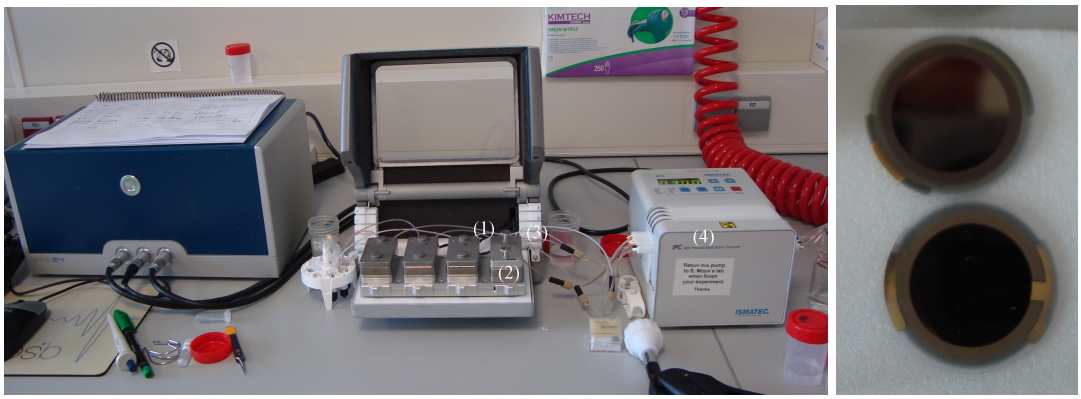

(a) photo of the QCMD set up (b) QCMD sensors

Figure 6.13: Experimental QCMD set up (a) and (b) sensors used to monitor the growth of polymer brushes. The catalyst and monomer solutions are pumped from (1) to (3) into the QCMD chamber (3) using a peristaltic pump (4). The mass deposited on the QCMD sensor, a silicon wafer on top of a quartz piezo, is measured by the change in the frequency of the sensor. For this set-up there are four QCMD chambers, and four experiments can be run in parallel.

Once the brushes are grown and the polymerisation quenched, the sensors are placed again inside the QCMD. An example of a salt flushing experiment can be seen in figure 6.15, where

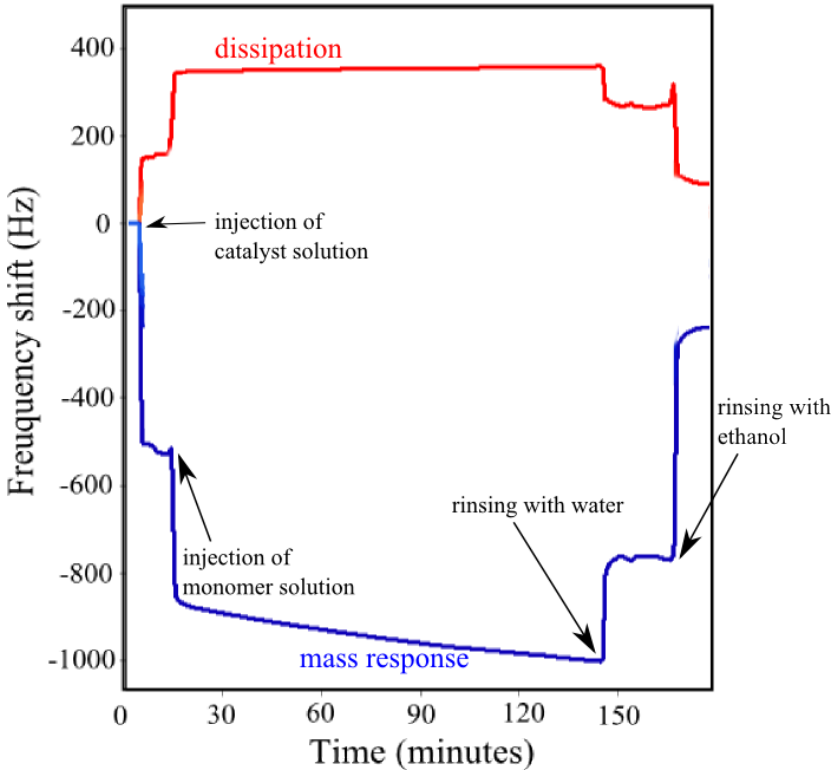

Figure 6.14: PSPM brush growth was monitored by QCMD. The blue curve represent resonant frequency of the sensor and the red curve represent the dissipation of the frequency. The decrease in frequency during the reaction time is proportional to the mass deposited on the film. The different stages of the reaction are indicated in on the figure.

increasing concentrations of $MgSO_4$ were flushed through the QCMD cell. From the contact angle experiments described in section 6.2.1 it was determined that PMETAC-PMMA-PMETAC interacted with $MgSO_4$ to produce the type of wettability switch of interest for potential applications of this study. This system was now tested with QCMD to determine what the effect of the $MgSO_4$ on the brush film is, and if the change in contact angle, can indeed be correlated to the expulsion of water from the film due to polymer collapse. The results of this experiment are shown in figure 6.15.

What seems quite interesting is that the mass response appears to be fast with the change in solution as shown for the 0.1 M $MgSO_4$ and 0.5 M $MgSO_4$ injections as shown in figure 6.15b.

Studies on the loss of water content from PMETAC films [149] found that the loss of water by PMETAC films at 0.1 M NaCl was approximately 30%, and this did not increase largely with increasing salt concentration. This is perhaps also why a contact angle shift for the PMETAC-PMMA-PMETAC system can be observed from H_2O to 0.1 M $MgSO_4$ but there are not very large further increases in the advancing contact angle for increasing salt

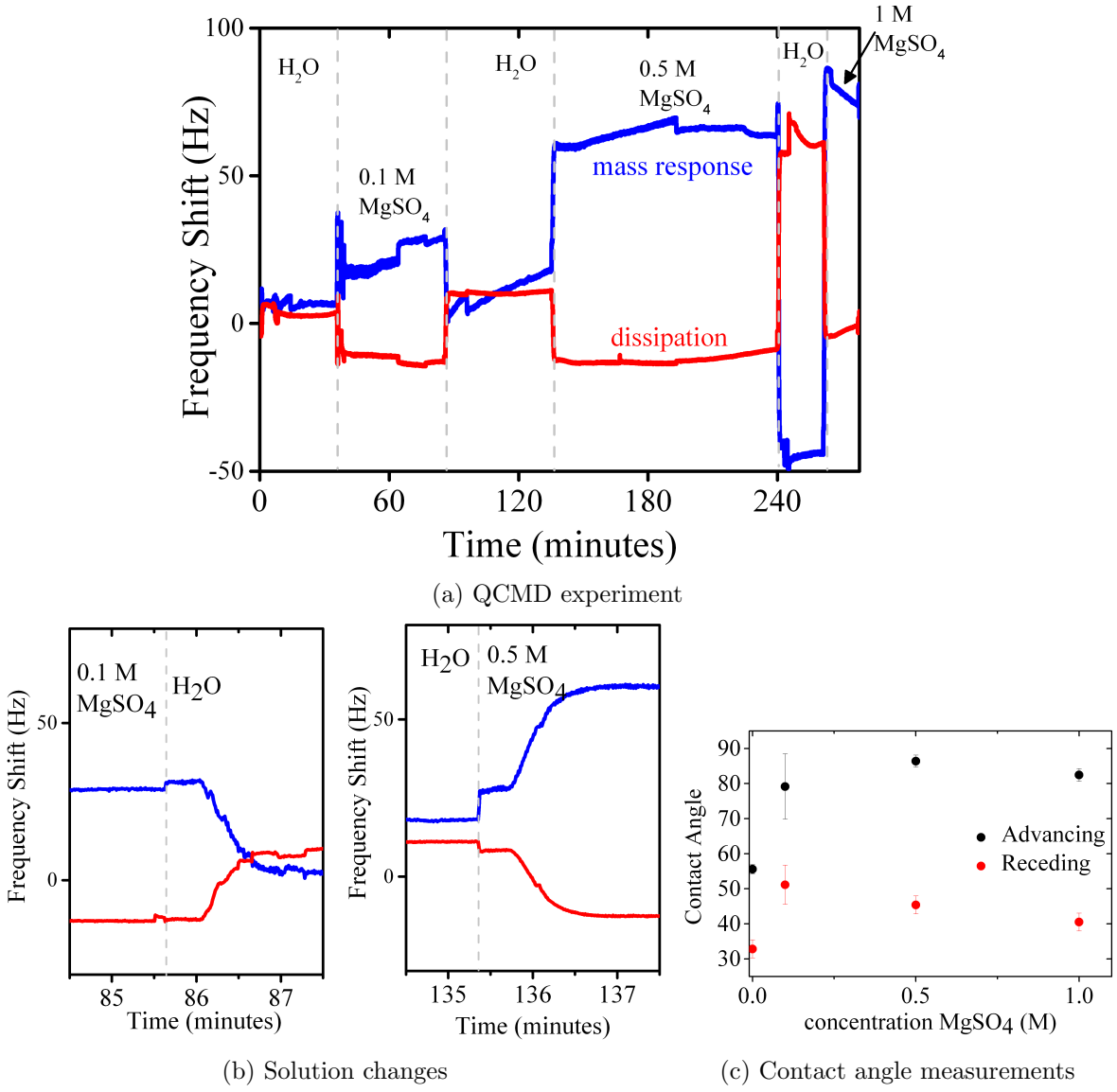

(a) QCMD experiment

(b) Solution changes

(c) Contact angle measurements

Figure 6.15: (a) Response of tri-block co polymer PMETAC-PMMA-PMETAC to $MgSO_4$ solution of 0.1 and 0.5 M and 1 M concentration. An increase in frequency corresponds to a decrease in mass. When the salt solution is added, there is a positive frequency shift. This indicates a loss of mass on the sensor, caused by collapse of the film and expulsion of the adsorbed water molecules inside the film. (b) zoomed in views of the transition between 0.1 M $MgSO_4$ and H_2O and H_2O and 0.5 M $MgSO_4$. It appears that there is a finite time required for changes in the brush film to occur. (c) Contact angle response to different concentrations of $MgSO_4$ measured under oil for a PMETAC-PMMA-PMETAC film.

concentration (shown in figure 6.15c). After rinsing with water the third time, the frequency shifts to negative values compared to the original water rinsing. This might be a sign of ageing of the film, or a kind of hysteresis behaviour, and further study of the film behaviour would be required to characterise this. The film was then flushed again with 1M $MgSO_4$, and again a decrease in mass of the film is observed, but the experiment was then stopped as

the mass changes were no longer considered to be reliable due to the unknown state of the brushes.

Before implementation of these types of coatings into bead packs, a considerable amount of work is still required to better characterise the interactions between the block co polymers and the salt solutions. However, so far it has been possible to create a 'switchable surface' which exhibits the right qualitative behaviour. This response could be optimised by tuning the relative lengths of the brushes or perhaps the grafting density. Another possibility which was no investigated here, is forming mixed films of brushes, rather than the blocks. Such systems of, for example PMMA and PMETAC may also interesting to study in this context.

6.3 Heterogeneous surfaces with small characteristic length scale

The second part of this chapter deals with creating wetting heterogeneities on surface which have are randomly distributed and have a small length scale.

The main body of work in this thesis dealt with wetting heterogeneities that were on the order of a bead size (correlation lengths from 0.25 to 2). It was found that for smaller correlation lengths the heterogeneities appeared to dominated the flow dissipation and control the shape of the invading liquid front. For the larger heterogeneities, with correlation lengths greater than 1, the wetting heterogeneities don't appear to change the local flow behaviour. It appears that at around correlation lengths of one, a transition occurs, between strong pinning on contact lines at boundaries to the wetting heterogeneities, and systems in which contact angle averaging simplifications appear to be valid. There is however, potentially another transition region, when heterogeneities become very small.

In natural samples heterogeneities exist on all length scales. These can be very small (just a few μm) as shown in chapter 1, figure 1.1 and have been measured by chemical force spectroscopy. Small heterogeneities on the surface lead to local contact angle hysteresis (as described in chapter 2). This is caused by local pinning of the contact lines at these heterogeneities. For two phase flow through bead packs, heterogeneities on the order of a bead size significantly influence the invading liquid morphology due the pinning of contact lines. However, as these heterogeneities become smaller, the effect of contact line pinning should also decrease. It could be expected that once heterogeneities become very small, contact lines moving over the heterogeneous surface would also not become pinned, and rather, the fluid would experience a type of average surface energy and hysteresis. In the following section, a method to prepare surfaces with small, but controllable length scale of wetting heterogeneities is discussed.

6.3.1 Towards smaller length scales

Towards this end, creating surfaces with small wetting heterogeneoties, that are controlled but randomly spatially distributed (not patterned), a self-assembly approach was tested. Self assembled monolayers of two types of silanes were made, one containing a chemical handle (an amine group, APTES) and the other a passive silane (propyltriethoxysilane, PTES). The structures of the two silanes used are shown in figure 6.16. To the active silane an initiator molecule for a polymerisation reaction was attached and from these tethered initiators polymer brushes were grown using the reaction protocols outlines in section 6.1.2.

For a fully activated surface, that is, if every silane had a polymer growing from it, the polymers form a brush like configuration. That is, they are forced outwards by the size exclusion effects from their neighbours, and have a structure somewhat resembling a

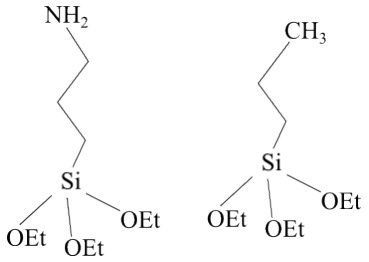

Figure 6.16: APTES, 3-aminopropyltriethoxysilane the active silane and PTS, propyltriethoxysilane the passive silane used in the formation of mixed silane layers.

hairbrush. In this case however, there are very few polymers and each polymer is free to take its energetically minimal conformation. In a wetting solvent, the polymer would have an extended form, and in a non-wetting solvent, the polymer would collapse, forming mushroom like structures on the surface [150].

For these specific experiments, a 1:99 ratio of active silane (APTES) to passive silane (PTES) was used. While this does not mean there is 1% active silane deposited on the surface, perhaps they do not mix, or the adsorption of one is energetically more favourable. Unfortunately, this was not investigated at this time, although XPS experiments indicated there can be substantial variation between the solution composition and the eventual surface composition. The polymer used was PSPM. PSPM completely modified surfaces were measured to have a contact angle of 30° (see figure 6.6. Patchy films were imaged with AFM and the surface heterogeneities can be seen in figure 6.17. The size of the patch was controlled by the growth time of the brush, and the number of patches controlled by the percentage of initiator present on the surface. It can be seen in figure 6.18 that the patch heights, are much higher than what would be expected for a fully coated PSPM film, which after 2 hours is only ∼30 nm thick. One possible explanation for this, is that the isolated brushes are in contact with much more monomer than in the film growth and the reaction is not sterically hindered by the presence of neighbouring brushes. For instance ATRP synthesis of free PSPM in solution polymers on average 130 nm long [151] after 45 minutes reaction time. Another contibuting factor might be the relatively large amount of catalyst present as same reaction concentrations were used as for a fully initiated film. Contact angle measurements showed a direct correlation between the growth time of the brush (i.e size of the patch) and the average contact angle measured for the system. This is shown in figure 6.19. The contact angle measured for just the silanated film (prior to the addition of the initiator of polymer growth) was measured to be 73±4°. These results, shown in figure 6.19, indicate that even at a low density of attachment the PSPM patches dominate the surface, and after 15 minutes of growth, the contact angles of ∼ are similar to those measured for a fully covered PSPM film.

While it is clear from figure 6.19 that the growth time of PSPM is correlated the to the average contact angle measured, the effect of the size of the patches alone cannot be

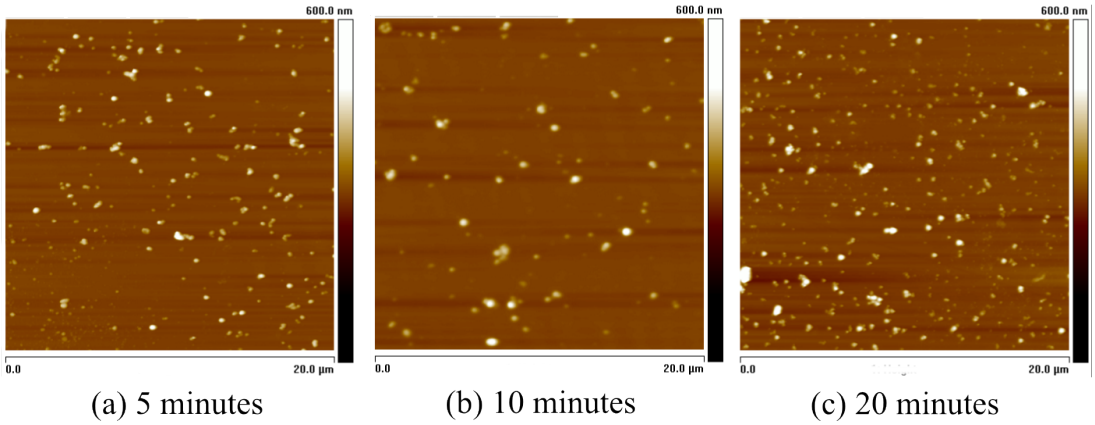

Figure 6.17: AFM images showing increasing size of patches on the surface of a treated silicon wafer. The time of the growth period is indicated above the AFM image.

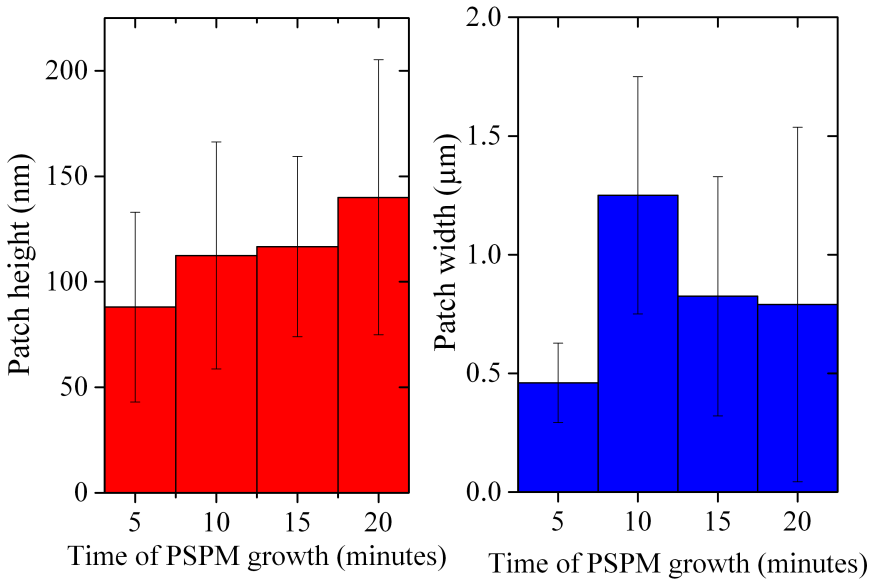

Figure 6.18: Patch heights and widths were extracted from AFM line profiles. The large error bars (standard deviation) result from the small number of patches measured per sample.

commented upon. This is because, as the PSPM chains become longer, the total amount of surface they can cover also increases. Therefore the decrease in contact angle, is probably due to a general increase in the coverage of the surface by the hydrophilic polyelectrolyte, rather than the increase in patch size. Samples with the same total coverage but different patch sizes could be made by tuning the original amount of initiator.

These are some proof of concept results, and more work is required, however it does appear

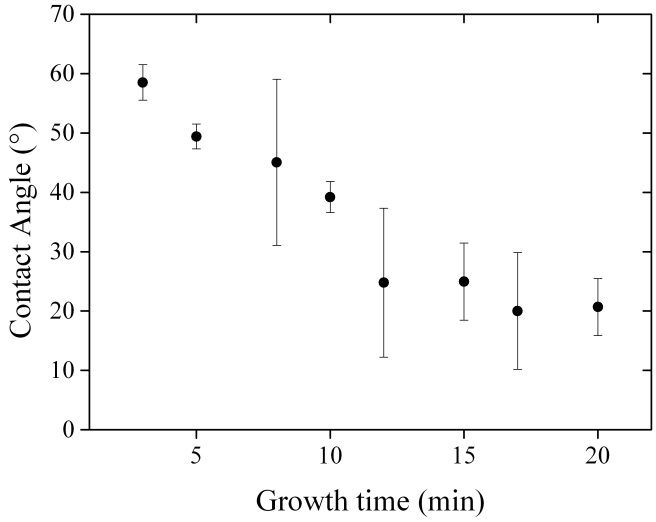

Figure 6.19: Measurement of contact angles (water in octadecane) show a decreasing average contact angle with increasing patch size, and after 20 minutes of growth, the PSPM patchy surface has a contact angle similar to that for a completely covered PSPM surface.

to be a interesting way to access very small, but still randomly distributed correlation lengths. This technique is also scalable, and such coatings can be made on non-planar surfaces, suitable for bead pack modifications.

Creating a patterned wettability of a defined length scale might also be achieved using micro-contact printing. Patterns with domain sizes as low as hundreds of microns are possible [152], although the up scaling of such a process seems limited, and treatments to bead surfaces for sample scale testing seems difficult. Therefore the above mentioned method has great potential for testing the full parameter space of the correlation length; not just on flat surfaces, but also on bead packs.

6.4 Summary

This chapter described the initial investigation into creating a switchable wetting surface using polymer brush films which would exhibit a wettability change from hydrophilic to hydrophobic in the presence of oil and water due to the salinity of the water phase. This was attempted using polyelectrolyte brushes grown on glass surfaces. In this work, only small salts were used, and not large organic ions which may act like surfactants. Although the hydrophobic collapse for polyelectrolyte brush systems such as PSPM and PMETAC has been previously observed under air [127, 128], a wettability transition was not measured under oil. This is most likely due to the poor interaction of the polyelectrolytes with the oil, forcing them already into a collapsed state, prior to the addition of salt solutions.

To overcome this a wetting transition based on the partial phase separation of a block copolymer between water and oil was then attempted. A wettability transition of a tri-block PMETAC-PMMA-PMETAC brush system was able to be observed upon the addition of salt, and in particular the addition of $MgSO_4$ trigged a concentration dependant response of the brushes which could also be measured by QCMD. For tri-block copolymers it appears that the relative lengths of the blocks are important as when long PSPM end blocks were used, no wettability transition was observed. The desired response of the brushs could be potentially optimised by tuning the lengths of the different blocks.

A second system was prepared in which patches of PSPM were grown on partially activated surface. The location of the patches depends on the self organisation of a mixed silane layer. This results in brushes tethered at random points on the surface. The preliminary results suggest that the size of the patches can be controlled by the growth time of the brush. The water in oil contact angle of the patchy surfaces was also found to be proportional to the growth time, and therefore the amount of polymer on the surface. Despite the low amounts of brushes grown (1% surface can tether a brush) the surface appeared very hydrophilic, and after 15 minutes growth exhibited the same contact angles are a fully coated PSPM surface. Mixed silane films appear to be a useful way of created randomly distributed patterns, and in conjunction with living polymerisation techniques such as ATRP, patches of a tunable size can be created.

Chapter 7

Conclusions and outlook

7.1 Conclusions

This thesis describes, to the best of the author's knowledge, the first experimental investigation into the effect of wetting heterogeneities, with defined spatial domains, inside porous media. The effect of the wetting heterogeneities was measured on the sample scale flow properties of two immiscible liquids.

At the beginning of this work, four questions were asked:

- What is the effect of pore scale wetting heterogeneities on the sample scale flow properties?
- What are useful model porous media systems to investigate this?
- Is there a model surface which mimics the LoSal effect?
- What are the implications for natural systems?

These questions were investigated by measuring model bead packs with wetting heterogeneities from sub-pore domains to heterogeneities which spanned several neighbouring pores. The effect of these domains was measured by capillary pressure saturation curves and x-ray tomography. It was found that sub-pore scale wetting heterogeneities cause an increase in energy dissipation of two phase flow through a porous media, due to the pinning of contact lines at the heterogeneity junctions.

A useful model system to investigate this effect, needs to capture the relevant parameter space for the size wetting heterogeneity. Because previous studies had only focussed on heterogeneities above a pore, it was decided here to look below and above this particular size. This study was the first of its type to introduce wettability heterogeneities on individual grains, where the patch sizes were systematically varied from the space of less than a single pore, to extending of several neighbouring pores. All of the samples had the same average

wettability. In this way the specific question of the role of ξ was able to be addressed, isolated from any further effects potentially caused by different average wettabilities inside the packings. The samples, were able to be described using a simple scalar quantity, the wetting correlation length ξ, a measure of the average wetting domain size inside bead packings comprised of $\sim$150,000 beads.

Two separate measurements were used to quantify the effect of the wetting domain sizes of the flow properties of two immiscible fluids. First the capillary pressure saturation curves, a standard measurement of wettability at the sample scale, were measured. These curves showed a monotonic increase in capillary hysteresis for samples with decreasing correlation lengths. This trend was robust towards difference surface treatments of the glass beads used, and no significant effect of surface roughness was observed. The second measurement, imaging of the liquid front, showed smoothening of the invading liquid fronts inside samples with small correlation lengths. Both of these observations can be understood as dissipation of the flow of the invading liquid, caused by contact line pinning at the wetting heterogeneity junctions. The correlation length, which describes the average size of these domains, is proportional to the density of pinning sites and therefore is a useful descriptor of the mixed-wet systems.

Previous studies of mixed wettability, had only focussed on heterogeneities which were larger than single pores. The parameter space studied here appears to capture the transition from a size of heterogeneity where pinning of the interface occurs and dominates the flow dissipation (i.e ξ <1 janus and patchy), to a size of heterogeneity where the average wettability appears to acceptably describe the local environment (i.e $\xi \geq 1$, mixed and clusters).

Using the living radical polymerisation method SI-ATRP, two types of coatings on glass surfaces were developed. The first used block copolymer brushes to create a wettability transition in the presence of saline solutions. The change in wettability could be attributed to the collapse of the polymer brushes, coinciding with expulsion of water from the brush films. This type of surface was proposed as a potential candidate to investigate the LoSal effect on a pore and larger scale. The second type of treatment created using SI-ATRP used mixed silane films with only small percentages of initiator to create very hydrophilic islands on an otherwise more hydrophobic surface. It was found that the average wettability of the surface could be controlled by the growth time of the polymer brush islands. This appeared to be a useful way of creating samples with $\xi \ll 1$. These proof of concept experiments demonstrate the utility of surface modifications using polymer brushes and are suitable for upscaling for the coating of glass beads for bead pack experiments.

What are the implications of these results for natural systems? The first, and most obvious, is that for a sample with unknown distribution of wettabilities, assumptions based on the validity of contact angle averaging simplifications may not hold. While it is not easy to measure the wettability distributions of unknown rock samples, it is relatively easy to measure the geometry (i.e pore throat network) using x-ray microtomography. Furthermore numerical

predictions of capillary pressure saturation curves for rocks with the exact same geometries can be compared to the experimentally measured ones to better asses the wetting condition. Based on the results of this work strong deviations from the predicted hysteresis loop opening would suggest the presence of sub-pore wetting heterogeneities. In this way, understanding how the wetting heterogeneities affect the shape of the capillary pressure saturation curve, even for simple bead packs, can contribute to the characterisation of samples with unknown wetting distributions.

7.2 Ongoing and future work

Percolation thresholds

In this work it was reported that there is no significant difference between the irreducible saturations for samples with different correlation lengths. However, this does not mean that there are no significant implications for potential applications such as oil recovery. In a core flood, or indeed in the field, there is no hydrophobic membrane at the top of the sample preventing the outflow of water. Thus, once the percolation threshold is reached, that is– water has a complete connected pathway through the entire porous media– both water and oil be produced. In industry this is referred to as the 'breakthrough' event. Once there is a complete connected water pathway through the media, the path of least resistance for incoming water is simply along these channels. Indeed, the breakthrough event corresponds with a dramatic reduction in produced oil [153], not to mention other problems such as the what to do with the produced water. Therefore, understanding when breakthrough is going to happen is crucial to predicting the economic viability of a project. While it was not specifically investigated in this work, the tomography indicated that there are different percolation thresholds for samples with different correlation lengths. Indeed, compact fronts would be expected to percolate at larger saturations compared with highly fingered fronts. Investigation of effect of the correlation length on the percolation threshold could be performed by more frequent imaging (either in increments of 5% water saturation, or indeed continuous imaging) or by incorporation of electrodes in the CPS cell to measure percolation by the conductivity of the cell. Percolation of the aqueous phase (with added electrolytes) should coincide with a sharp increase in conductivity.

Small limits of ξ

For very small correlation lengths it is expected that interfaces moving over surfaces with very small heterogeneities would experience an average surface energy, rather than feel the effect of each individual patch. The development of a potential technique to probe very small wetting heterogeneities was described in chapter 6 but no testing of moving interfaces was yet performed. Coating bead packs with such, or similar surfaces is one way of mapping the size limits of the wetting heterogeneities to cause pinning of the interface.

Non-random wetting correlations

The model porous media investigated in this work are all spatially random, that is, for wetting correlation lengths smaller than a grain there is no larger ordering, and no correlation between the size of the opening in the porous media and the wettability. This is not necessarily the case in natural mixed wetting porous media. As described in chapter 1, the development of mixed wettability inside an oil reservoir follows certain chemical processes [142, 143, 154],

which is believed to result in a porous media where the small throats are oil wet and the pore bodies are water wet. This process is represented in figure 7.1. In the previous chapters the design and characterisation of samples with random spatial heterogeneities is discussed. Here the word random refers to the fact that there is no orientational ordering of the beads. However, it is also possible to create samples where the patches of opposite wettability are exclusive located at the contact points between beads. Such samples will have the small gaps between beads wet by water and the larger pore bodies will be oil wet.

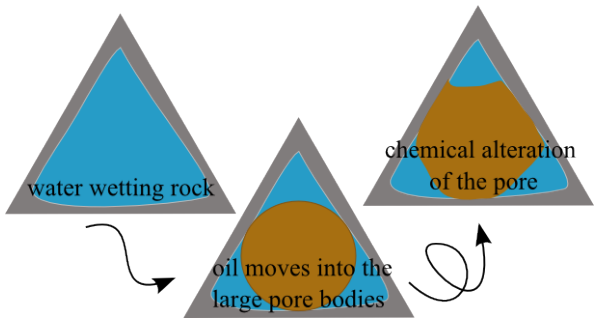

Figure 7.1: Cartoon of a pore (represented by the triangle) inside an oil reservoir which develops mixed wettability of a distinct pattern due to the history of occupying fluids. The pore is initially filled with water. As the oil is formed underground it rises due its lower density and is able to invade the larger pores. Over time chemical components from the oil phase move onto the surface of the pore wall, changing the wettability of the surface. The resulting pore has water wet gutters, or throats, and an oil wet pore body.

The beads are created in the same way as the patchy samples (see section 3.3.1), that is small quantities of liquid is introduced as a mask, prior to surface modification. To create the correlation between the wettability of the surface and the size of the pore opening, the beads are held in place while the silane solution and mask are removed (by drying). Great care is then taken to introduce the hexadecane back into the packing without disturbing the contacts of the beads. In this way, samples can be created where the throats, that is the contact points between the beads, which create the smallest openings, are water wet, and the rest of the pore body is wet by oil. These samples are called 'Knackstedt ' as they were inspired by the methodology presented in reference: [155]. This is the closest approximation of the natural mixed wettability scenario [26] illustrated in figure 7.1. Tomography taken of a ripened emulsion inside such a packing revealed that the oil preferred to reside in the oil wetting pores, and not in the water wet contact points between beads. An example of this is shown in figure 7.2. Such a system may also be of interest to prepare bead packs with 'trapped ganglia 'for mobilisation studies.

Previous experimental work to address this kind of distribution of wettabilities was creating using bead packs made of large oil wetting beads, and small water wetting beads- to create smaller water wetting pore and larger oil wetting pores. However, apart from any potential aggregation/segregation effects which are common for bidisperse bead packs, studying the

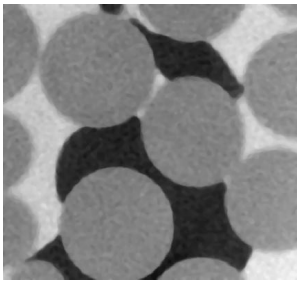

(a) 2D slice from tomography image

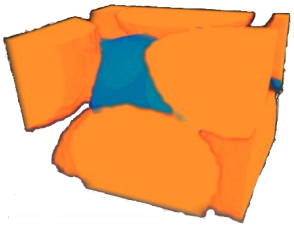

(b) 3D volume rendering

Figure 7.2: a) slice from tomography image showing beads with a patterned-mixed wettability beads filled with water (white) and oil (black) and b) 3D volume rendering of an oil droplet, contained inside the oil wetting pore body formed between four beads, but not wetting the bridges, which are water wetting.

fluid behaviour on monodisperse bead packs with a wetting heterogeneity allows the specific effect of the wetting heterogeneity to be studied and decoupled from any effects caused by the wider distribution of pore sizes.

For completion, opposite wetting samples, with oil wetting throats and water wetting pore can also be made. Reverse-Knackstedt beads can be made by stirring through small amounts of silane. Characterisation of such samples would be possible by tagging the silanes with a fluorescent molecule, e.g rhodamine, and visualising the bead pack using confocal microscopy. This step would be necessary to ensure there is not migration of the silane during the curing, and indeed all the silane remains in the location of the liquid bridges. Figure 7.3 shows fluorescently tagged janus beads. Such images could also be used for reverse-Knackstedt beads to characterise the location and spatial extension of hydrophobic patches.

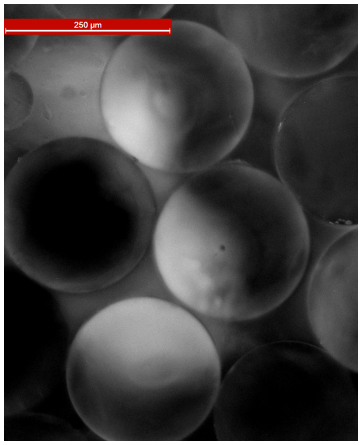

Figure 7.3: Fluorescent janus beads were prepared by first half coating the beads with APTES and then attaching rhodamine-isothiocyanante as a fluorescent tag. This is proposed as a method of characterising the reverse-Knackstedt beads. Scale bar is 250μm.

Appendix A

Imaging processing details

A.1 Glossary of image processing terms

voxel
A three dimensional pixel. 3D volume images are made up of volume pixels, i.e voxels.

binary image
A binary image consists of only black and white voxels. They are typically made by thresholding a greyvalue image.

thresholding
Thresholding refers to the binarisation of an image by setting all values above a certain grey value to 1 and all below to 0. The thresholding value used is determined from the grey value histogram and the accuracy of the segmentation determined by visual inspection.

neighbourhood
The neighbourhood of a voxel defines how many of the surrounding voxels are considered connected to it. In 3D, the neighbourhood can be 6 (voxels which share a face are connected), 18 (voxels which share a face or an edge are connected) or 26 (voxels which share a face, edge or corner are connected). Neighbourhoods are important for morphological transformations such as erosion and dilation.

dilation
Dilation is the expansion of a binary region by a set number of voxels. This can be done with different neighbourhood criteria. The choice of neighbourhood criteria will change result, meaning that this operation is not shape preserving.

erosion
Erosion refers to the procedure of reducing the size of an object by one layer at the boundaries. Like dilation, erosion depends on the choice of neighbourhood and is not necessarily shape preserving.

Label image
A label image is an image where each discrete region within the image is given a separate number. Connected regions are labelled by the same number. In this work a 26 neighbourhood criteria is used for label images.

Bilateral filter

An edge preserving filter which replaces the greyvalue of each voxel by a weighted average within a given kernel size. The weights used for averaging depend on the nearest distance to a boundary. In this way, voxels corresponding to the edge of an object are excluded from the filtering, and unlike standard median filters, the edges of the image remain unblurred.

despeckle filter

The despeckle filter is used to remove isolated speckles on noise. It works by calculating the mean and variance of voxels within a certain volume. Then voxels within this specified size are replaced with the mean value of all voxels within that area if the difference between the input and the mean is greater than the variance in the area. Otherwise the voxels are unchanged.

Euclidian distance map

Calculates a Euclidean distance map (EDM) based on voxelised data. The Euclidian distance map is a grey valued image, calculated from a binary image, where the value of the voxel represents the distance to the boundary of an object. The distance map can be calculated for either phase- inside, where the grey values represent the distance from the center of an object to its boundary and the background remains black; or outside where the objects remain white, and the greyvalue of the background corresponds to the distance between a background voxel and a boundary of an object. Thresholding an 'inside 'distance map can be used to erode images, and thresholding an 'outside 'distance map can be used to dilate images. Unlike erosion and dilation there is no shape dependence on the neighbourhood criteria.

hole fill

Hole filling algorithm works by flooding the background of an image step-wise until all areas which cannot be connected to the background in any way are determined. Then these holes are retrospectively filled. The algorithm used here, uses a 26 neighbours criteria for determining which areas can be reached, and which not.

closing

Closing is the combination of a dilation followed by an erosion step. The purpose of this is to close holes and voxels which are separated by a small gap. During the dilation step where all regions are expanded by the set number of voxels, regions which are close together but not touching will be merged. The newly merged areas remain connected during the subsequent erosion step.

opening

Opening refers to a sequential erosion and then dilation step. The effect of opening is to remove small connections between large objects.

binseperate

The binseperate command computes watershed lines for a binary image and then subtracts these lines from the image returning separated features. Watershed lines are calculated by first creating an Euclidean distance map of the image. The distance map is then inverted. The grey value image can be considered like a topological map. Now, the darkest voxels in the inverted distance map will correspond to centres of the objects

in the original image. These points are used as seeds for water flooding of the image. The seeds grow (or the regions are flooded) until two regions hit each other. The line of contact it taken as the watershed line.

logical and
This voxel by voxel operation takes two binary images and returns an image containing only the non zero voxels which are in both images.

logical sub
Performs a logical subtraction of one image to another.

logical not
performs a point wise inversion of a binary image

A.2 Image processing of samples for correlation length calculations

Mixed Correlation

To calculate the mixed correlation length samples were made with glass and basalt beads. Basalt beads have a higher X-ray absorption and so appear brighter in the tomography. This makes the segmentation of the different surfaces much easier. Glass beads and basalt beads were segmented separately using grey value thresholding. The holes from the beads (naturally occurring in the sample) were removed from the image using the hole_fill filter and then the basalt bead surface was identified by eroding the beads by one voxel and subtracting that from the segmented beads.

The segmentation of the glass beads proved slightly more difficult, as the grey values of the surface of the basalt beads matched perfectly with the grey values of the bulk glass, however these erroneous surface voxels were removed by applying an 1 voxel sized opening (erosion followed by a dilation step) transformation. The hole-filling algorithm, while successful for the basalt beads, was not able to remove all of the defects in the glass beads, as many of the air pockets also extend to the surface. These defects were removed using a closing filter with a kernel size of 3 x 3 x 3 voxels. Following these image processing steps, the segmented glass beads surface was extracted by subtracting a 1 voxel eroded image of the beads from the bead volume.

Cluster correlation

Basalt and glass clusters were made using NOA glue as the binding agent, and sieved with a 1 mm sieve before UV curing. They were then packed and compressed inside a sample tube and imaged using X-ray tomography. The different types of beads were identified using the same protocol as described for the mixed sample and the correlation length calculated from the extracted surfaces of both types of beads.

Janus correlation

To obtain the correlation length for janus beads, glass beads sputtered with a thick layer of gold (approx. 1 μm) were imaged and the surfaces extracted. The gold surface was extracted by grey value thresholding and the glass surface was extracted by first segmenting the whole beads, dilating the surface to also include to gold layer and then subtracting the bead image from the dilated image. This gives ring around the edge of the bead. Then the gold layers are subtracted from the glass surfaces giving the two surfaces of the coated and uncoated hemispheres separately segmented.

Patchy correlation

Etched silver samples (preparation is described in section 3.3.1) were used for the calculation of the ξ for patchy samples. These samples were also used for calibrating the mask volume to surface coverage. X-ray tomography was taken with resolution of 6 μm. The silver layers were segmented using grey value thresholding. Noise was removed using a despeckle filter. The extraction of the silver voxels was non trivial. This can be easily seen by first looking at the grey value histogram for a 2% masked sample, shown in figure A.2a. The air/beads

threshold is simple, and it is taken as the minimum between the two large peaks at a grey value of 7500. Thresholding of the silver layer is more complicated as there is no separation of the silver layers and the beads. This is because the outside most voxels of the glass beads are brighter than the bulk glass. These brighter glass voxels, cross into the darkest voxels of the silver layers. To determine the 'correct 'threshold value threshold images were made for the lowest grey value (no, or few bead voxels are included) which appeared to appropriately select the silver voxels and the highest grey value (no silver voxels are visably not included). The middle point between these two values was taken as the 'best 'threshold value. Images showing a 2D slice with the segmented silver layers overlaid for the lowest (blue), central (red) and highest (green) thresholds are shown in figure A.2b-d.

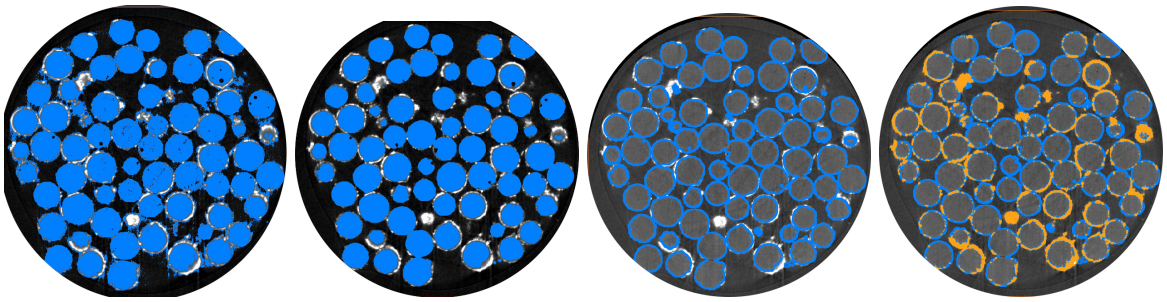

(a) thresholded (b) filtered and opened (c) surfaces extracted (d) silver and glass

Figure A.1: Workflow showing the detection of the non-silver surface voxels for patchy samples

Once the silver layers have been identified, the surfaces of the beads also have to been selected. This is done, by first segmenting the bulk glass. The grey values at the edge of the silver layers, correspond to some of the grey values of the bulk glass. This is shown in figure A.1a. The voxels labelled as glass are overlaid over the original tomography in blue. These erroneous voxels are easily removed using an opening step (just the like the foil on the kinder surprise egg from chapter 2). It can be seen in figure A.2, that the silver layers are quite thick. Therefore the bulk glass beads were dilated by 2 voxels, using an 18 neighbour criteria (so that the glass beads now encompass also the silver layer), and then the original voxels of the bead volume are subtracted from the dilated image. The silver voxels were then subtracted from the glass surface voxels to remove the overlapping regions. The images for the various stages of this work flow are shown in figure A.1.

The ratio between the now labelled glass and silver pixels were used to calibrate the surface coverage with respect to the volume of masking described in chapter 3, figure 3.9. The error bars for the surface coverage, were calculated from segmentation of the silver and beads using the highest and lowest possible grey values. The image processing sequence was repeated for all samples with different masks and the dependence of the surface coverage and correlation length for the different masking ratios calculated.

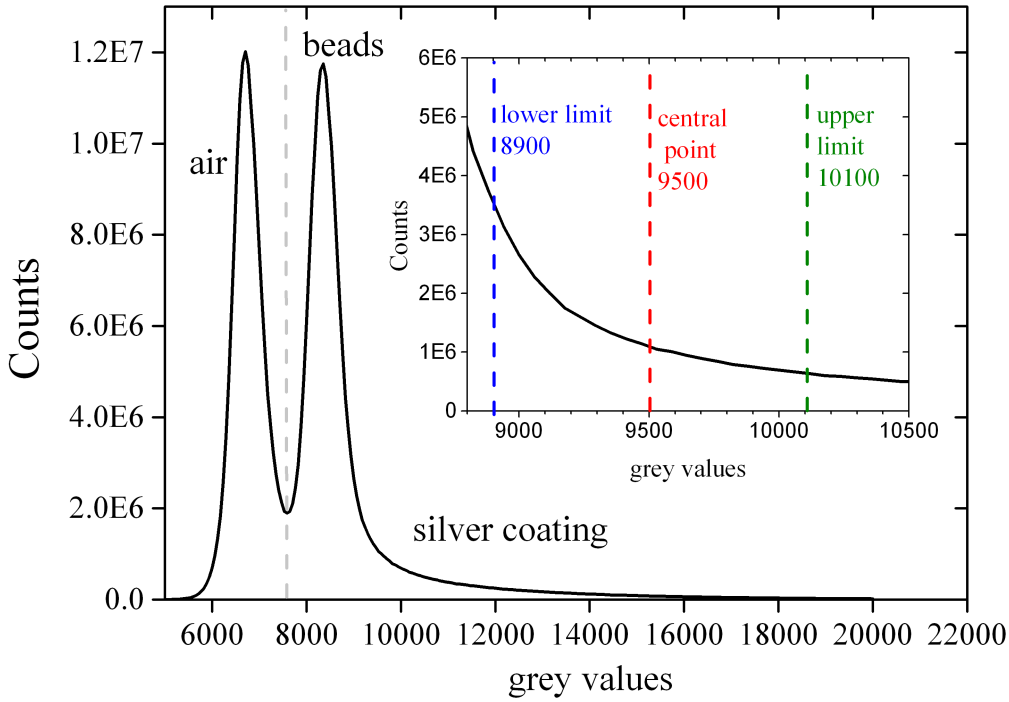

(a) grey value histogram with greyvalues corresponding to the air, beads and silver layers indicated. The grey dashed line shows the threshold value for the beads and the air. The inset shows the region where the silver layers start. There is no clear separation of the peak making segmentation difficult. The blue and green dashed lines indicate the lowest and highest visually acceptable segmentation.

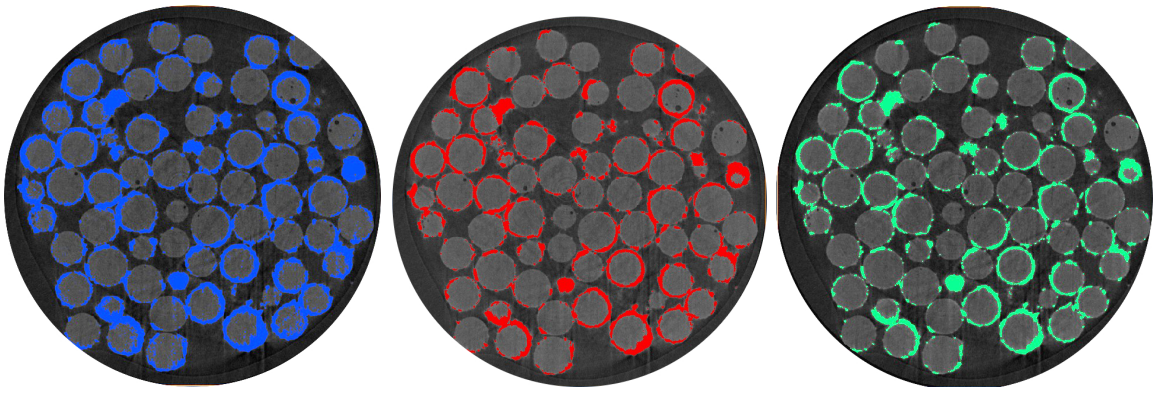

(b) lowest value (c) central value (d) highest value

Figure A.2: Grey value histogram and example 'acceptable ' segmentations of silver layers for a patchy sample made with 2.0% masking volume.

A.3 Image processing used for analysis of active interfaces and liquid fronts

As described in chapter 5, section 5.1.1, the volumes of each liquid were calculated from the segmentation of the phases. The correct segmentation was chosen using a similar methodology as for the silver surfaces described in section A.2 and the error bars (see figure 5.4) are calculated from the differences in volume of the highest and lowest segementations. An example for a liquid fronts in a janus bead pack is shown in figure A.3.

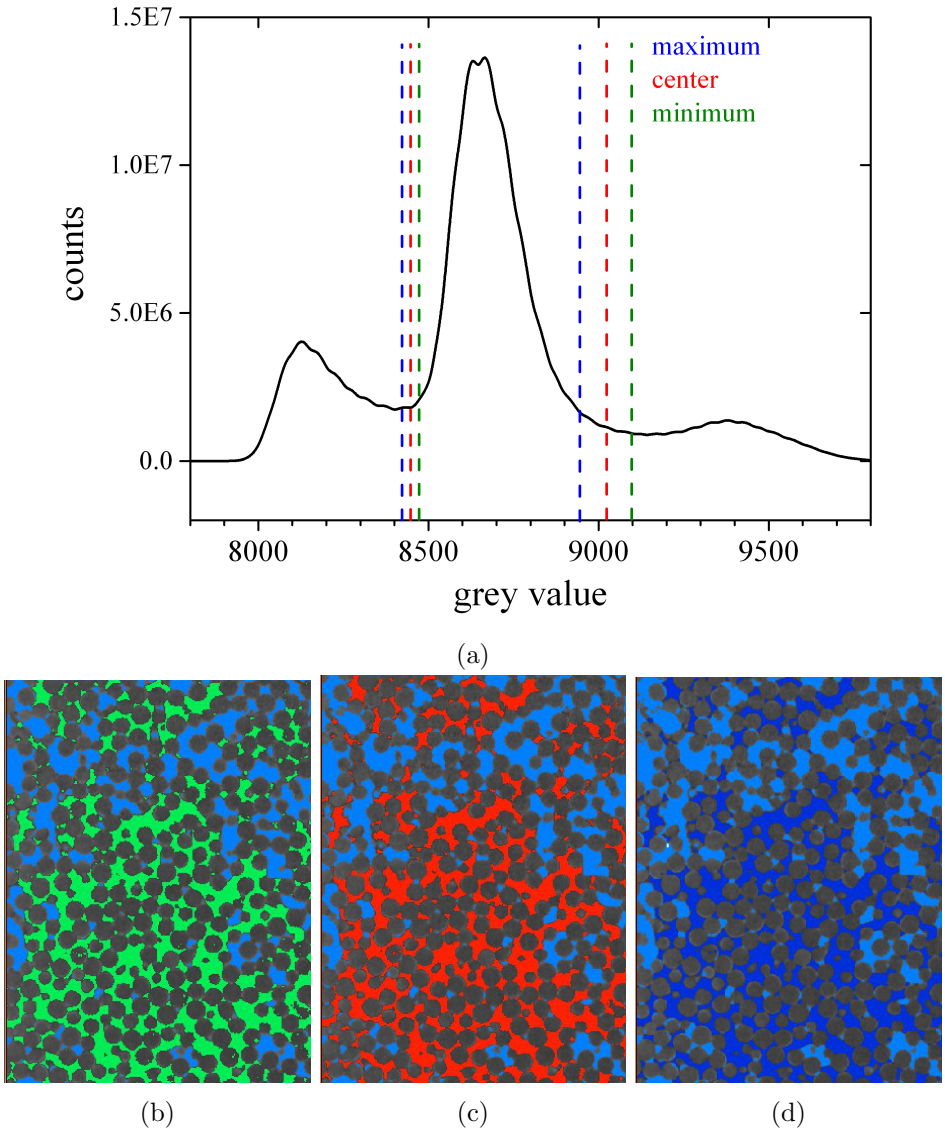

Figure A.3: (a) Greyvalue histogram showing the values for minimum and maximum visually acceptable segementations. The actual segmentation value was taken as the half way point between these two values (center value).(b)-(d) The segmentations overlaid over the raw data are shown, water phase in blue, and oil phase corresponding to the colour of the line indicating the value of the segmentation (i.e max, center, min)

Appendix B

Alternative janus preperation

The first method was to half embed the grains in wax droplets by pouring the grains through a layer of molten wax into a bath of cold water. The glass spheres, which are heavy sediment through the wax, dragging it with them by capillary forces. As the beads and wax hit the water, the contact area between the water and wax aims to be minimised, and the beads move to the outside of the wax droplet, forming Pickering emulsion like droplets. The molten wax solidifies in the cold water resulting in solid droplets covered by glass spheres, called 'divers'. (see fig. B.1). This method was inspired by the formation of 'Cartesian divers' in hexane and water [156], but hexane was substituted with paraffin wax (sigma aldrich) to allow collection of the divers, and surface modification of the glass beads (in this case by deposition of silver, and addition of hexadecane thiol).

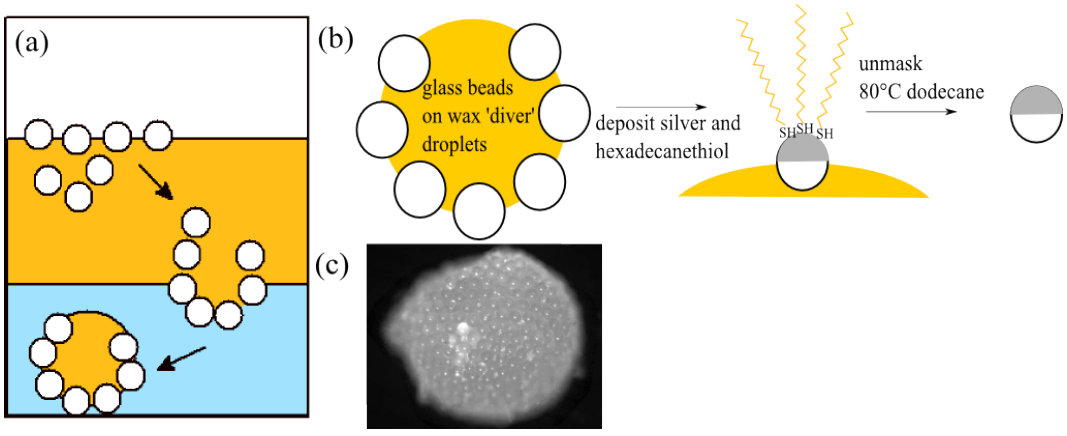

Figure B.1: Sketch of experiment procedure for formation of janus beads using the diver protocol. Left: glass spheres are poured through a layer of molton wax and sediment into a bath of cold water forming diver particles. Right: The glass beads on the surface of the wax droplets are modified. Removal of the wax results in half coated spheres.

To make sure there was sufficient removal of the wax from the uncoated surface, a control sample of janus beads was made, using the diver protocol, but without depositing silver and hexadecane thiol. After removal of the wax, qualitative testing of the spheres, by pouring into water, showed them to be water wetting. This was confirmed quantitatively using capillary pressure saturation measurements.

Based on the methodology of Jiang and Granick [157], it was also found that it was

possible to influence the amount of surface coverage of the grains by changing the composition of the water solution underneath the wax layer. Addition of different surfactants were able to influence the penetration of the glass beads into the wax layer, which in turn, influenced the coverage of the beads, as shown in figure B.2. The amount of surface coverage was quantified by first taking pictures of individual beads, and then counting the surface pixels which were coated. For each type of coating 50 beads were examined.

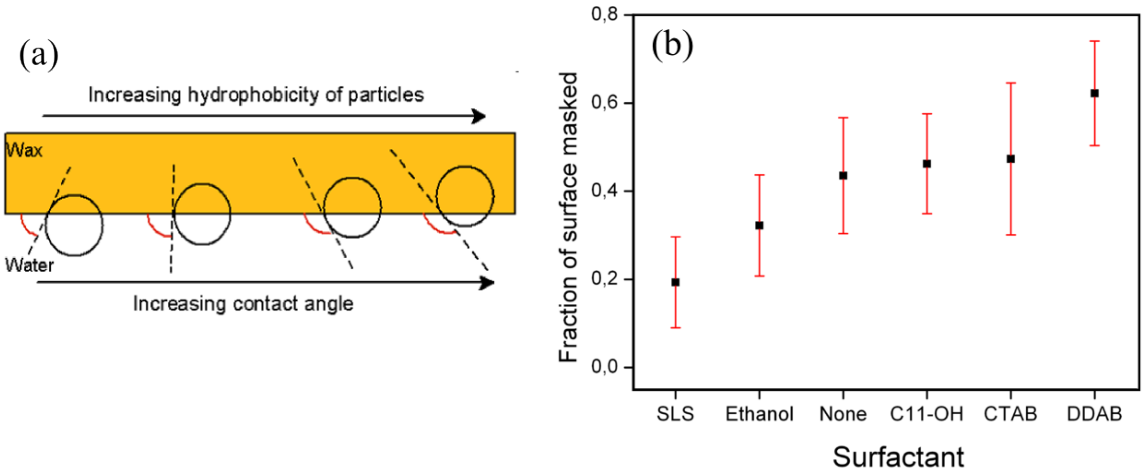

Figure B.2: (a) A cartoon showing increasing depth of penetration of glass beads into the wax with increasing hydrophobicity of the glass and (b) shows the amount of silver coverage on janus beads created with different surfaces the wax/water interface. Each data point consists of the average of 50 beads. Error bars represent the standard deviation of measured beads.

However a significant drawback to the diver method of masking was the small amount of samples recovered. The large beads, are held only loosely within the solidified wax droplets and often fall out during the coating process.

A perceived advantage of the water/wax masking method is the ability to upscale and produce large amounts of particles. However it turned out that for tomography purposes, the silver layers prepared on the wax droplets were not of good enough quality to be properly visualised. The binding of the glass beads inside the wax droplets is not very strong, and after multiple coatings and washings (3-5), so many beads had fallen out and could not be used, that the yields of samples prepared were inefficient.

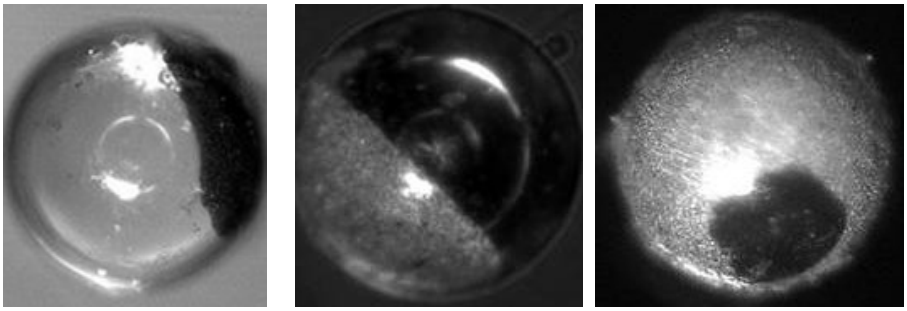

Figure B.3: Three glass beads (diameter = 250 μm) from wax droplets with different penetration depths.

Appendix C

Ripened emulsions in janus and mixed packings

In order to introduce randomly distributed droplets into a mixed wet packing where the minor phase (or irreducible phase) was of a total constant volume to specifically probe the effect of the wetting correlation length, oil in water emulsions were injected into bead packings. These emulsions were ripened inside the packing and imaged with x-ray tomography. The emulsions were prepared by sonnication of dodecane in water for 30 minutes. This process creates an oil in water and water in oil emulsion where the minor phase contributes a few volume percent [158].

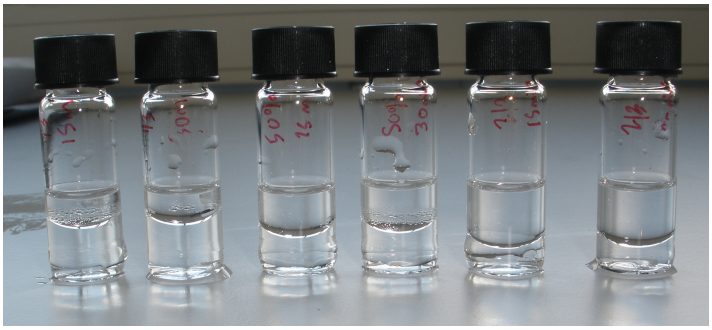

(a) water and dodecane prior to sonnication

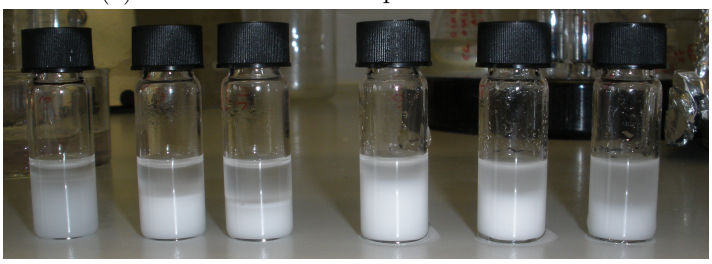

(b) after 30 minutes sonnication

Figure C.1: Before and after sonnication images of water and dodecane. The dispersion of one phase into the other can been seen by the milky appearance of the emulsion.

Dynamic light scattering (DLS) measurements of dodecane droplets in water were used to measure the size distribution of the dispersed phase. The dodecane droplets have an average

radius of 100 nm, and over the time period of the 10 measurements lasting in total ∼5 min, there was no significant ripening.

In our experiments however, we need x-ray contrast, so salt, in this case 1 M CsI was added to the aqueous phase. Unfortunately, this causes a rapid increase in the ripening of the emulsions. To reduce ripening of the emulsions prior to injections in the packings, the emulsions were cooled to zero degrees (freezing point of the dodecane (-9° C , and 1 M CsI -3.7° C). However the addition of salt decreases the stability of the emulsions. DLS measurements of dodecane in 1 M $CsI_{(aq)}$ showed ripening from an average radius of 1 μm to 4 μm over the time perious of 10 measurements. It should be noted, that although these droplets seem large, a droplet with radius 4μm still only comprises of 0.003% of a bead volume.

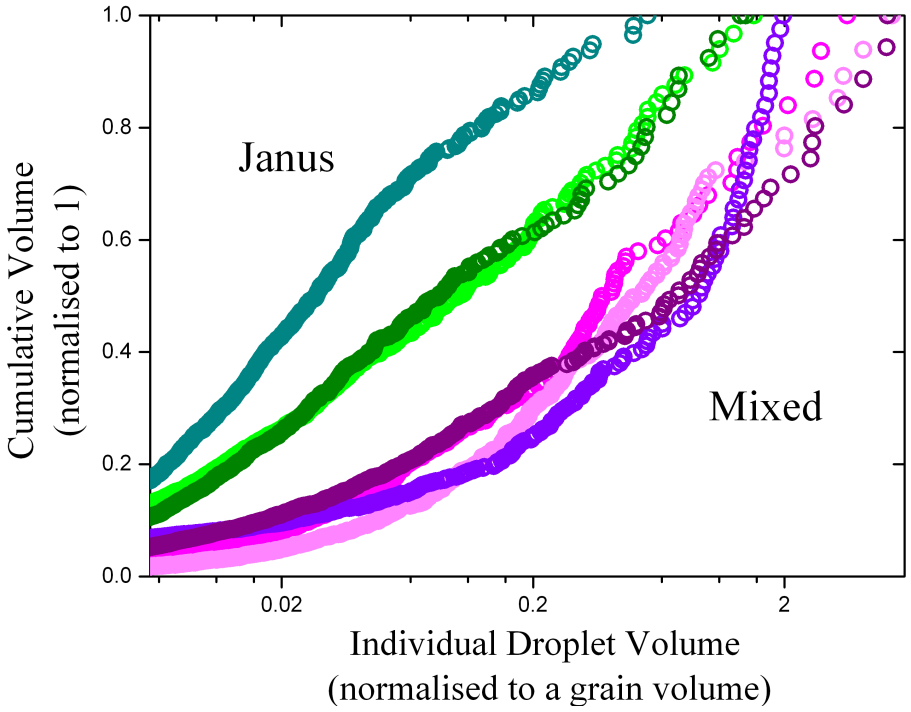

Figure C.2: Cumulative volume vs. individual droplet size for ripened emulsions inside janus (green curves) and mixed (purple curves) bead packs. In general the droplets formed inside the janus bead packs are smaller than those formed inside mixed packs.

From the cumulative volume distributions it appears that the droplets inside janus packings have a smaller individual characteristic volume than inside the clusters. This is intuitive as the droplets forming on the wetting surfaces inside mixed packings would have larger wettable areas on which to spread as they are growing. Further proof of this concept would be to examine the droplets ripened inside patchy and cluster packings to determine if the wetting correlation also controls the growth of droplets.

The advantages to the sonnicated emulsions techniques is that we are able to introduce similar amounts of the minor phase into the packings in a random way, allowing us to discriminate between the effect of the wetting heterogeneity on the surface and the individual flow characteristics of each experiments, as in the case of the irreducible saturations form the CPSC, where such large experimental scatter was observed, it is difficult to compare structure of droplets. A disadvantage to the emulsions method, is the very low amount of

residual phase which can be introduced in this manner. Even the largest droplets found in the systems have a volume of only 5 grain diameters, compared to the CPSC experiments where extended ganglia can be up to hundreds or even thousands of grain volumes (remember that the sample comprises of ∼150,000 grains). The even distribution of the droplets, not all of the phase being collected into a single ganglia allowed differences to be observed, however this is a property not necessarily true of natural systems. Furthermore, it may only be true that the correlation length dictates droplet sizes for droplets which are growing through ripening processes, and in a flow experiment, geometrical constraints are more important for pinch-off events, which separate droplets from the connected fluids. Trapped droplets arising from ripened emulsions inside the bead packings are not a realistic natural model system, due to the small amount of trapped phase, and the lack of very large droplets in the system. What was shown however is that it is possible create droplets with a characteristic size by changing the wetting properties of the porous media. Such a systems might also be useful to investigate the effect of the sizes of the trapped phase on their ability to be re-mobilised.

Bibliography

[1] W. He, J. Yi, and T. Van Nguyen, "Two-phase flow model of the cathode of PEM fuel cells using interdigitated flow fields," *AICHE journal*, vol. 46, no. 10, pp. 2053–2064, 2000.

[2] P. K. Sinha, P. P. Mukherjee, and C.-Y. Wang, "Impact of GDL structure and wettability on water management in polymer electrolyte fuel cells," *J. Mater. Chem.*, vol. 17, pp. 3089–3103, 2007.

[3] Z. Wang, C. Wang, and K. Chen, "Two-phase flow and transport in the air cathode of proton exchange membrane fuel cells," *Journal of Power Sources*, vol. 94, no. 1, pp. 40 – 50, 2001.

[4] M. Sahimi, "Flow phenomena in rocks: from continuum models to fractals, percolation, cellular automata, and simulated annealing," *Reviews of modern Physics*, vol. 65, pp. 1393–1534, 1993.

[5] S. Berg, H. Ott, S. A. Klapp, A. Schwing, R. Neiteler, N. Brussee, A. Makurat, L. Leu, F. Enzmann, J.-O. Schwarz, M. Kersten, S. Irvine, and M. Stampanoni, "Real-time 3d imaging of haines jumps in porous media flow," *PNAS*, vol. 110, pp. 3755–3759, 2013.

[6] I. Sandrea and R. Sandrea, "Global oil reserves - recovery factors leave vast target for EOR technologies," *Oil and Gas Journal*, vol. 105, pp. 1–8, 2007.

[7] N. R. Morrow, "Wettability and its effect on oil recovery," *Journal of Petroleum Technology*, vol. 42, pp. 1477–1484, 1990.

[8] W. Anderson, "Wettability literature survey- part 4: Effects of wettability on capillary pressure," *Journal of Petroleum Technology*, pp. 1283–1300, 1987.

[9] S. S. Datta, H. Chiang, T. S. Ramakrishnan, and D. A. Weitz, "Spatial fluctuations of fluid velocities in flow through a three-dimensional porous medium," *Physical Review Letters*, vol. 111, no. 6, 2013.

[10] B. Berkowitz, "Characterizing flow and transport in fractured geological media: A review," *Advances in Water Resources*, vol. 25, no. 812, pp. 861 – 884, 2002.

[11] K. T. MacQuarrie and K. U. Mayer, "Reactive transport modeling in fractured rock: A state-of-the-science review," *Earth-Science Reviews*, vol. 72, pp. 189–227, 2005.

[12] O. Sala, F. Chapin, J. Armesto, E. Berlow, J. Bloomfield, R. Dirzo, E. Huber-Sanwald, L. Huenneke, R. Jackson, A. Kinzig, R. Leemans, D. Lodge, H. Mooney, M. Oesterheld,

N. Poff, M. Sykes, B. Walker, M. Walker, and D. Wall, "Biodiversity - global biodiversity scenarios for the year 2100," *Science*, vol. 287, pp. 1770–1774, MAR 10 2000.

[13] M. J. Bickle, "Geolomedia carbon storage," *Nature Geoscience*, vol. 2, pp. 815–818, 2009.

[14] F. M. Orr, "Onshore geologic storage of CO2," *Science*, vol. 325, pp. 1656–1658, 2009.

[15] M. A. Shannon, P. W. Bohn, M. Elimelech, J. G. Georgiadis, and B. J. Marinas, "Science and techonology for water purification in the coming decades," *Nature*, vol. 452, pp. 301–310, 2008.

[16] A. J. Kota, G. Kwon, W. Choi, J. M. Mabry, and A. Tueja, "Hygro-respondive membranes for effective oil-water separation," *Nature Communications*, vol. 3, pp. 1025:1–8, 2012.

[17] J. Mueller, Y. Cen, and R. Davis, "Crossflow microfiltration of oily water," *Journal of Membrane Science*, vol. 129, no. 2, pp. 221–235, 1997.

[18] D. A. Weitz, J. P. Stokes, R. C. Ball, and A. P. Kushnick, "Dynamic capillary pressure in porous media: Origin of the viscous-fingering length scale.," *Physical Review Letters*, vol. 59, no. 26, pp. 2967–2970, 1987.

[19] W. Anderson, "Wettability literature survey - part 5: The effects of wettability on relative permeability.," *Journal of Petroleum Technology*, vol. 39, pp. 1453–1468, 1987.

[20] P. De Gennes, "Dynamic capillary pressure in porous media," *Europhysics Letters*, vol. 5, pp. 689–291, 1988.

[21] C. Cottin, H. Bodiguel, and A. Colin, "Influence of wetting conditions on drainage in porous media: a microfluidic study.," *Phys Rev E*, vol. 84, p. 026311, Aug 2011.

[22] M. Schneider, F. Osselin, A. Ballard, F. Rezgui, and P. Tabeling, "Wettability determination of core samples through visual rock and fluid imaging during fluid injection," *Journal of Petroleum Science and Engineering*, vol. 78, pp. 476–485, 2011.

[23] P. Jadhunandan and N. Morrow, "Effect of wettability on waterflood recovery for crude-oil/brine/rock systems," *SPE*, vol. 10, pp. 40–46, 1995.

[24] E. Nordgard, G. Sorland, and J. Sjoblom, "Behavior of asphaltene model compounds at w/o interfaces," *Langmuir*, vol. 26, no. 4, pp. 2352 – 2360, 2009.

[25] T. Hassenkam, L. L. Skovbjerg, and S. L. S. Stipp, "Probing the intrinsically oil-wet surfaces of pores in north sea chalk at subpore resolution," *PNAS*, vol. 106(15), pp. 6071–6076, 2009.

[26] P. Valvatne and M. Blunt, "Predictive pore scale modelling of two-phase flow in mixed wet media," *Water Resources Research*, vol. 40, pp. W07406–W07427, 2004.

[27] S. Zhang, R. E. Klimentidis, and P. Barthelemy, "Porosity and permeability analysis on nanscale fib-sem 3d imaging of shale rock," in *SCA Symposium 2011*, 2011.

[28] E. V. Lebedeva and A. Fogden, "Micro-CT and wettability analysis of oil reovery from sand packs and the effect of waterflood salinity and kaolinite," *Energy & Fuels*, vol. 25, pp. 5683–5694, 2011.

[29] M. Kumar and A. Fogden, "Patterned wettability of oil and water in porous media," *Langmuir*, vol. 26, pp. 1036–4047, 2010.

[30] N. R. Morrow and J. Buckley, "Wettability and oil recovery by imbibtion and viscous displacement from fractured and heterogeneous carbonates," tech. rep., University of Wyoming and New Mexico Petroleum Recovery Research Center, 2006.

[31] D. Wildenschild and A. P. Sheppard, "Xray imaging and analysis techniques for quantifying pore-scale structure and processes in subsurface porous medium systems," *Advances in Water Resources*, vol. 51, pp. 217–246, 2013.

[32] D. N. Rao, M. Girard, and S. G. Sayegh, "The influence of reservoir wettability on waterflood and miscible flood performance," *The Journal of Canadian Petroleum Technology*, vol. 31, pp. 47–55, 1992.

[33] T. Maldal, A. H. Gulbrandsen, and E. Gilje, "Correlation of capillary number curves and reminaing oil ssaturation for reservoir and model sandstones," *In Situ*, vol. 3, pp. 239–269, 1997.

[34] N. Wardlaw and M. McKeller, "Wettability and connate water saturation in hydrocarbon reservoirs with bitumen deposits," *Journal of Petroleum Science & Engineering*, vol. 20, pp. 141–146, 1998.

[35] S. MA, X. Zhang, N. Morrow, and X. Zhou, "Characterisation of wettability from spontaneous imbibtion measurements," *Journal of Canadian Petroleum Technology*, vol. 38, pp. 9447–13, 1999.

[36] P. Ustohal, F. Stauffer, and T. Dracos, "Measurement and modeling of hydraulic characteristics of unsaturated porous media with mixed wettability," *Journal of Contaminent Hydrology*, vol. 33, pp. 5–7, 1998.

[37] D. M. O'Carroll, L. M. Abriola, C. A. Polityka, S. A. Bradford, and A. H. Demond, "Prediction of two-phase capillay pressure-saturation relationships in fractional wettability systems," *Journal of Contaminant Hydrology*, vol. 77, pp. 247–270, 2005.

[38] L. A. Ferrand and M. A. Celia, "The effect of heterogeneity on the drainage capillary pressure-saturation relation," *Water Resources Research*, vol. 28, pp. 859–870, 1992.

[39] C. Miller, G. Christakos, P. Imhoff, J. McBride, and J. Pedit, "Multiphase flow and transport modeling in heterogeneous porous media: challenges and approaches," *Advances in Water Resources*, vol. 21, pp. 77–120, 1998.

[40] F. Fayers and T. Hewett, "A review of current trends in petroleum reservoir description and assessment of the impacts on oil recovery," *Advances in Water Resources*, vol. 15, pp. 341–365, 1992.

[41] S. Iglauer, S. Favretto, G. Spinelli, G. Schena, and M. J. Blunt, "X-ray tomography mmeasurement of power-law cluster size distributions for the nonwetting phase in sandstones," *Physical Review E*, vol. 82, pp. 056315–8, 2010.

[42] D. DiCarlo, A. Sahni, and M. Blunt, "Three-phase relative permeability of water-wet, oil-wet and mixed-wet sandpacks," *SPE Journal*, vol. 5, pp. 82–91, 2000.

[43] M. Kumar, J. P. Middleton, A. Sheppard, T. Senden, and M. A. Knackstedt, "Quantifying trapped residual oil in preservoir core material at the pore scale: Exploring the role of displacement rate, saturation history and wettability," *International Petroleum Technology Conference*, vol. 14001, pp. 14001–5, 2009.

[44] C. Cottin, H. Bodiguel, and A. Colin, "Drainage in two-dimensional porous media: from capillary fingering to viscous flow.," *Phys. Rev. E*, vol. 82, p. 046315, Oct 2010.

[45] B. Kozlov, M. H. Schneider, B. Montaron, M. Lagues, and P. Tabeling, "Archie's law in microsystems," *Transport in porous media*, vol. 95, pp. 1–20, 2012.

[46] K. A. Culligan, D. Wildenschilde, B. S. Christensen, W. G. Gray, M. L. Rivers, and A. F. Thompson, "Interfacial area measurement for unsaturation flow through a porous medium," *Water Resources Research*, vol. 40, p. W12413, 2004.

[47] R. T. Armstrong, M. L. Porter, and D. Wildenschild, "Linking pore-scale interfacial curvature to column-scale capillary pressure," *Advances in Water Resources*, vol. 46, pp. 55–62, 2012.

[48] C. J. Landry, Z. Karpyn, and M. Piri, "Pore-scale analysis of trapped immiscible fluid structure and fluid interfacial area in oil-wet and water-wet bead packs," *Geofluids*, vol. 11, pp. 209–227, 2011.

[49] F. Dullien and M. Fleury, "Analysis of the USBM wettability test," *Transport in porous media*, vol. 16, no. 2, pp. 175–188, 1994.

[50] Y.-W. Yang, G. Zografi, and E. Miller, "Capillary flow phenomena and wettability in porous media," *Journal of Colloid and Interface Science*, vol. 122, pp. 25–36, 1987.

[51] D. Wildenschild., T. Armstrong, A. L. Herring, I. M. Young, and J. W. Carey, "Exploring capillary trapping efficiency as a function of interfactial tension, viscosity and flow rate," *Energy Procedia*, vol. 4, p. 4945, 2011.

[52] N. Shahidzadeh-Bonn, E-Bertrand, J. Dauplait, J. Borgotti, P. Vie, and D. Bonn, "Gravity drainage in porous media: the effect of wetting," *Journal of Peteroleum Science and Engineering*, vol. 39, pp. 409–416, 2003.

[53] N. Smirnov, V. Nikitin, J. Legros, E. Istasse, L. Schramm, and F. Wassmuth, "Microgravity investigations of capillary-driven imbibtion and drainage in inhonoegneous porous media," *Acta Astronautica*, vol. 54, pp. 39–52, 2003.

[54] A. Georgiadis, S. Berg, A. Makuart, G. Maitland, and H. Ott, "Pore-scale micro-computer-tomography imaging: Nonwetting-phase cluster-size distribution during drainage and imbibition," *Physical Review E*, vol. 88, pp. 0330002–1 – 9, 2013.

[55] I. Fatt and W. Klikoff, "Effect of fractional wettability on multiphase flow through porous media," *Transaction of the American Institute of Mining and Metallurgical Engineers*, vol. 216, pp. 426–430, 1959.

[56] S. Bradforf and F. Leij, "Predicting two- and three fluid capillary pressure-saturation relations," *Environmental Science and Technology*, vol. 29(6), pp. 1446–1455, 1996.

[57] S. I. Hwang, K. P. Lee, D. S. Lee, and S. E. Powers, "Effects of fractional wettability on capillary pressure-saturation-relative permeability relations of two-fluid systems," *Advances in Water Resources*, vol. 29, pp. 212–266, 2006.

[58] D. M. O'Carroll, K. G. Mumford, L. M. Abriola, and J. I. Gerhard, "Influence of wettability variations on dynamics effects in capillary pressure," *Water Resources Research*, vol. 46, pp. W0850501–13, 2010.

[59] M. Scheel, *Experimental investigations of the mechanical properties of wet granular matter*. PhD thesis, Georg-August-Universität-Göttingen, 2009.

[60] W. Lindquist, S. Lee, D. Coker, k. Jones, and P. Spanne, "Media axis analysis of void structure in three dimensional tomographic images of porous media," *Journal of Geophysical Research*, vol. 101, pp. 8297–8310, 1996.

[61] X. Zhao, M. J. Blunt, and J. Yao, "Pore-scale modelling: Effects of wettability on waterflood oil recovery," *Journal of Peteroleum Science and Engineering*, vol. 71, pp. 169–178, 2010.

[62] M. J. Blunt, "Flow in porous media– pore-network models and multiphase flow," *Current Opinion in Colloid and Interface Science*, vol. 6, pp. 197–207, 2001.

[63] T. Ramstad, N. Idowu, C. Nardi, and P.-E. Oren, "Relative permeability calculations from two-phase flow simulations directly on digital images of porous rocks," *Transport in Porous Media*, vol. 94, pp. 487–504, 2012.

[64] M. Prodanovic, , W. Lindquistand, and R. Seright, "3d image-based characterization of fluid displacement in a berea core," *Advances in Water Resources*, vol. 30, no. 2, pp. 214 – 226, 2007.

[65] M. Knackstedt, A. Sheppard, and M. Sahimi, "Pore network modelling of two-phase flow in porous rock: the effect of correlation heterogeneity," *Advanced Water Resources*, vol. 24, pp. 257–77, 2001.

[66] R. D. Hazlett, S. Chen, and W. Soll, "Wettability and rate effects on immiscible displacement: Lattice boltzmann simulation in microtomographic images of reservoir rocks," *Journal of Petroleum Science & Engineering*, vol. 20, pp. 167–175, 1998.

[67] A. Dixit, J.S.Buckley, S. McDougall, and K. Sorbie, "Empirical measures of wettability in porous media and the relationship between them derived from pore-scale modelling," *Transport in porous media*, vol. 40, pp. 27–54, 2000.

[68] O. Gharbi and M. J. Blunt, "The impact of wettability and connectivity on relative permeability in carbonates: A pore network modelling analysis," *Water Resources Research*, vol. 48, pp. W12513–27, 2012.

[69] M. L. Porter, D. Wildenschild, C. Grant, and J. I. Gerhard, "Measurement and predicition of the relationship between capillary pressure, saturation and interfacial area in a napl-water-glass bead system," *Water Resources Research*, vol. 46, p. W08512, 2010.

[70] S. Sheppard, M. D. Mantle, A. J. Sederman, M. L. . Johns, and L. F. Gladden, "Magnitic resonance imaging study of complex fluid flow in porous media: flow patterns and quantitative saturation profiling of amphiphilic fracturing fluid displacement in sandstone cores," *Magentic Resonance Imagaing*, vol. 21, p. 364, 2003.

[71] M. H. Sankey, D. J. Holland, A. J. Sederman, and L. F. Gladden, "Magentic resonance velocity imaging of liquid and gas two-phase flow in packed beds," *Journal of Magnetic Resonance*, vol. 196, p. 142, 2008.

[72] L. Xu, S. Davies, A. B. Schofield, and D. A. Weitz, "Dynamics of drying in 3d porous media.," *Phys Rev Lett*, vol. 101, p. 094502, Aug 2008.

[73] A. T. Krummel, S. S. Datta, S. Münster, and D. A. Weitz, "Visualizing multiphase flow and trapped fluid configurations in a model three-dimensional porous medium," *AICHE journal*, vol. 59, pp. 1–8, 2013.

[74] S. S. Datta and D. A. Weitz, "Drainage in a model stratified porous medium," *Europhysics Letters*, vol. 101(1), p. 14002, 2013.

[75] M. Cissokho, S. Boussour, P. Cordier, H. Bertin, and G. Hamon, "Low salinity oil recovery on clayey sandstone: Experimental study," *Petrophysics*, vol. 51, pp. 305–313, October 2010.

[76] N. Hadia, T. Hansen, M. Tweheyo, and O. Torsaeter, "Influence of crude oil components on recovery by high and low salinity waterflooding," *Energy & Fuels*, vol. 26, pp. 4328–4335, 2012.

[77] B. S. Shiran and A. Skauge, "Enhanced oil recovery (eor) by combined low salinity water/polymer flooding," *Energy & Fuels*, vol. 27, pp. 1223–1235, 2013.

[78] A. M. Brzozowska, M. Duits, and F. Mugele, "Stability and interactions in mixed monolayers of fatty acid derivatives on artificial sea water," *Colloids and Surfaces, A: Physicochemical and Engineering Aspects*, vol. 443, pp. 200–211, 2013.

[79] N. Kumar, L. Wang, I. Siretanu, M. H. G. Duits, and F. Mugele, "Salt dependent stability of stearic acid langmuir-bkodgett films exposed to aqueous electrolytes," *Langmuir*, 2013.

[80] T. Hassenkam, C. Pederson, K. Dalby, T. Austad, and S. L. S. Stipp, "Pore scale observation of low salinity effects on outcrop and oil reservoir sandstone," *Colloids and Surfaces, A: Physicochemical and Engineering Aspects*, vol. 390, pp. 179–188, 2011.

[81] T. Hassenkam, A. Mitchell, C. Pederson, L. L. Skovbjerg, N. Bovet, and S. L. S. Stipp, "The low salinity effect observed on sandstone model surfaces," *Colloids and Surfaces, A: Physicochemical and Engineering Aspects*, vol. 403, pp. 79–86, 2012.

[82] M. Santini, M. Guilizzoni, and S. Fest-Santini, "X-ray computer microtomography for drop shape analysis and contact angle measurement," *Journal of Colloid and Interface Science*, vol. 409, pp. 204–210, 2013.

[83] A. Schmohl, A. Khan, and P. Hess, "Functionalization of oxidized silicon surfaces with methyl groups and their characterization," *Superlattices and Microstructures*, vol. 36, pp. 113 – 121, 2004.

[84] M. Miyama, Y. Yang, T. Yasuda, T. Okuno, and H. K. Yasuda, "Static and dynamic contact angles of water on polymeric surfaces," *Langmuir*, vol. 13, no. 20, pp. 5494–5503, 1997.

[85] C. D. Bain, E. B. Throughton, Y.-T. Tao, J. Evall, G. M. Whitesides, and R. G. Nuzzo, "Formation of monolayer films by the spontaneous assembly of organic thiols from solution on gold," *Journal of the American Chemical Society*, vol. 111, pp. 321–335, 1989.

[86] A. Ulman, "Formation and structure of self-assembled monolayers," *Chem. Rev.*, vol. 96, pp. 1533–1554, 1996.

[87] J. Drelich, J. L-Wilbur, J. D. Miller, and G. M. Whitesides, "Contact angles for liquid drops at a model heterogeneous surface consisting of alternating and parallel hydrophobic/hydrophilic strips," *Langmuir*, vol. 12, pp. 1913–1922, 1996.

[88] R. N. Wenzel, "Surface roughness and contact angle," *Journal of Physical Chemistry*, vol. 53, pp. 1466–1467, 1949.

[89] A. B. D. Cassie and S. Baxter, "Wettability of porous surfaces," *Transactions of the Faraday Society*, vol. 40, pp. 546–551, 1944.

[90] A. Tuteja, W. Choi, M. Ma, J. M. Mabry, S. A. Mazzella, G. C. Rutledge, G. H. McKinley, and R. E. Cohen, "Designing superoleophobic surfaces," *Science*, vol. 318, pp. 1618–1622, DEC 7 2007.

[91] A. Lafuma and D. Quere, "Superhydrophobic states," *Nature Materials*, vol. 2, pp. 457–460, 2003.

[92] H. B. Eral, G. Manukyan, and J.-M. Oh, "Wetting of a drop on a sphere," *Langmuir*, vol. 27, pp. 5340–5346, 2005.

[93] H. Scholl, K. Singh, A. Kabdenov, M. DiMichiel, M. Scheel, and R. Seeman, "Dynamic x-ray tomography investigations of two phase flow in porous media.".

[94] C. Semprebon and M. Brinkmann, "Contact angle on small spheres measured by meniscus deformation." in preperation.

[95] A. Siebold, A. Walliser, M. Nardin, M. Oppliger, and J. Schultz, "Capillary rise for thermodynamic characterization of solid particle surface," *Journal of Colloid and Interface Science*, vol. 186, pp. 60 – 70, 1997.

[96] W. Purcell, "Capillary pressures. Their measurement using mecury and the calculation of permeability therefrom," *Transaction of the American Institute of Mining and Metallurgical Engineers*, vol. 186(2), pp. 39–48, 1949.

[97] H. Princen, "Capillary pressure behavior in pores with curved triangular cross-section: effect of wettability and pore size distribution," *Colloids and Surfaces*, vol. 65, pp. 221–230, 1992.

[98] S. Levine, J. Lowndes, and P. Reed, "2.phase fluid-flow and hysteresis in a periodic capillary-tube," *Journal of Colloid and Interface Science*, vol. 77, no. 1, pp. 253–263, 1980.

[99] E. Amott, "Observations relating to the wettability of porous rock," *Transactions of the American Institute of Mining and Metallurgical Engineers*, vol. 216, pp. 156–162, 1959.

[100] N. Morrow, "Physics and thermodynamic of capillary action in porous media," *Industrial and Chemical Engineering Chemistry*, vol. 62, pp. 32–57, 1970.

[101] S. L. Wellington and H. Vinegar, "X-ray computerised tomography," *Journal of Petroleum Technology*, vol. 39, pp. 885–898, 1987.

[102] "http://www.ge-mcs.com/en/radiography-x-ray/ct-computed-tomography/nanotom-s.html."

[103] M. Neudecker, "Master-forschungspraktikum rntgentomographie." Lecture Notes, Georg-Augustus-Univerisitts Gttingen, 4 2012.

[104] S. W. Smith, *The scientist and Engineer's Guide to Digital Signal Processing*. California Technical Publishing, 1998.

[105] L. Bernard, S. Fave, and E. Norefalise, *Avizo 7 Reference Guide*. Visilog, 2011.

[106] Z.-j. Jiang and C.-y. Liu, "Seed-mediated growth technique for the preparation of a silver nanoshell on a silica sphere," *Journal of Physical Chemistry B*, vol. 107, pp. 12411–12515, September 2003.

[107] S. Utermann, P. Aurin, M. Brinkmann, C. Fischer, and S. Matthias, "Tailoring the frictional properties of granular media," *Physical Review E*, vol. 84, p. 031306, 2011.

[108] M. E. Ahmed and P. J. Van Geel, "Potential concerns related to using octadecyltrichlorosilane (ots) in rendering soils and porous ceramics hydrophobic," *Journal of Contaminant Hydrology*, vol. 110, pp. 22–33, 2009.

[109] C. Casagrande and M. Veyssie, "Grains janus: realisation and first observations of interfacial properties," *C.R Acad. Sci. Paris*, vol. 306, pp. 1432–1425, 1988.

[110] A. Goebel and K. Lunkenheimer, "Interfacial tension of the water/n-alkane interface," *Langmuir*, vol. 13, pp. 369–372, 1997.

[111] M. Prodanovic, W. Lindquist, and R. Seright, "Porous structure and fluid partitioning in polyethylene cores from 3d x-ray microtomographic imaging," *Journal of Colloid and Interface Science*, vol. 298, no. 1, pp. 282 – 297, 2006.

[112] M. Blunt, F. Fayers, and F. Orr, "Carbon-dioxide in enhanced oil-recovery," *Energy Conservation and Management*, vol. 34, no. 9-11, pp. 1197–1204, 1993.

[113] F. A. L. Dullien, C. Zarocone, I. F. Macdonald, A. Collins, and R. D. E. Bochard, "The effects of surface roughness on the capillary pressure curves and the heights of capillary rise in glass bead packs," *Journal of Colloid and Interface Science*, vol. 127, pp. 362–372, 1989.

[114] M. Han, S. Youssef, E. Rosenberg, and M. F. F. Levitz, "Deviation from archie's law in partially saturated porous media: Wetting film versus disconnectedness of the conducting phase," *Physical Review E*, vol. 79, p. 031127, 2009.

[115] G. Mason and D. W. Mellor, "Simulation of drainage and imbibtion in a random packing of equal spheres," *Journal of Colloid and Interface Science*, vol. 176, pp. 214–255, 1995.

[116] P. Reeves and M. Celia, "A functional relationship between capillary pressure, saturation and interfacial area as revealed by a pore-scale network model," *Water Resources Research*, vol. 32, pp. 2345–2358, 1996.

[117] K. Huang, M. Brinkmann, and S. Herminghaus, "Wet granular rafts: aggregation in two dimensions under shear flow," *Soft Matter*, vol. 8, pp. 11939–11948, 2012.

[118] D. Legland., K. Kieu, and M.-F-Devaux, "Computation of Minkowski measures on 2d and 3d binary images," *Image Analysis & Stereology*, vol. 26, pp. 83–92, June 2007.

[119] "http://www.theorie1.physik.uni-erlangen.de/research/karambola/."

[120] G. E. Schröder-Turk, W. Mickel, S. C. Kapfer, M. A. Klatt, F. M. Schaller, M. J. F. Hoffmann, N. Kleppmann, P. Armstrong, A. Inayat, D. Hug, M. Reichelsdorfer, W. Peukert, W. Schwieger, and K. Mecke, "Minkowski tensor shape analysis of cellular, granular and porous structures," *Advanced Materials*, vol. 23, no. 22-23, pp. 2535–2553, 2011.

[121] S. Alexander, "Adsoprtion of chain molecules with a polar head a scaling description," *Journal de Physique*, vol. 38, pp. 983–987, 1977.

[122] P. G. De Gennes, "Scaling theory of polymer adsoprtion," *Journal de Physique*, vol. 37, pp. 1445 –1452, 1976.

[123] S. Edmondson, V. L. Osborne, and W. T. Huck, "Polymer brushes via surface-initiated polymerizations," *Chemical Society Reviews*, vol. 33, pp. 14–22, 2004.

[124] Y. Liu, L. Mu, B. Liu, and J. Kong, "Controlled switchable surface," *Chemistry- A European Journal*, vol. 11, pp. 2622–2631, 2005.

[125] L. Zhang, Z. Zhang, and P. Wang, "Smart surfaces with switchable superolephilicity and superoleophobicity in aqueous media: towards controllable oil/water seperation," *NPG Asia Materials*, vol. 4, p. E8, 2012.

[126] S. E. Moya and J. Irigoyen, "Recent advances in the use of the quartz crystal microbalance with dissipation for the study of the collapse of polyelectrolyte brushes," *Journal of Polymer Science Part B: Polymer Physics*, vol. 51, no. 14, pp. 1068–1072, 2013.

[127] O. Azzoroni, S. Moya, T. Farhan, A. A. Brown, and W. T. Huck, "Switching the properties of polyelectrolyte brushes via "hydrophobic collapse"," *Macromolecules*, vol. 38, pp. 10192–10199, 2005.

[128] M. Doebbelin, G. Arias, I. Loinaz, I. Llarena, D. Mecerreyes, and S. E. Moya, "Tuning surface wettability of poly(3-sulfopropyl methacrylate) brushes by cationic surfactant-driven interactions," *Macromolecular Rapid Communications*, vol. 29, pp. 871–875, 2008.

[129] X. Wei and T. Ngai, "Ion-induced hydrophobic collapse of surface-confined polyelectrolyte brushes measured by total internal reflection microscopy," *Polymer Chemistry*, vol. 3, pp. 2121–2128, 2012.

[130] K.-S. Liao, H. Fu, A. Wan, J. D. Batteas, and D. E. Bergbreiter, "Designing surfaces with wettability that varies in response to solute identity and concentration," *Langmuir*, vol. 25, pp. 26–28, 2009.

[131] O. Azzaroni, A. A. Brown, and W. Huck, "Tunable wettability by clicking into polyelectrolyte brushes," *Advanced Materials*, vol. 19, pp. 151–154, 2007.

[132] R. Barbey, L. Lavanant, D. Paripovic, N. Schuewer, C. Sugnaux, S. Tugulu, and H.-A. Klok, "Polymer brushes via surface-initiated controlled radical polymerisation: Syntehsis, characterisation, properties, and applications," *Chemical Reviews*, vol. 109, pp. 5437–5527, 2009.

[133] R. Advincula, "Polymer brushes by anionic and cationic surface-initiated polymerisation (sip)," *Advances in Polymer Science*, vol. 197, pp. 107–136, 2006.

[134] M. Weck, J. J. Jackiw, R. R. Rossi, P. S. Weiss, and R. H. Grubbs, "Ring-opneing metathesis polymerisation from surfaces," *Journal of the American Chemical Society*, vol. 121, pp. 4088–4089, 1999.

[135] I. Luzinov, S. Minko, and V. Tsukruk, "Adaptive and responsive surfaces through controlled reorganization of interfacial polymer layers," *PROGRESS IN POLYMER SCIENCE*, vol. 29, no. 7, pp. 635–698, 2004.

[136] I. Y. Galaev and B. Mattiasson, "Smartpolymers and what they could do in biotechnology and medicine," *Trends in Biotechnology*, vol. 17, pp. 335–340, 1999.

[137] S. G. Boyes, A. M. Granville, M. Baum, B. Akgun, B. K. Mirous, and W. J. Brittain, "Polymer brushes-surface immobilized polymer," *Surface Science*, vol. 570, pp. 1–12, 2004.

[138] Y. Guo, F. Xia, L. Xu, J. Li, W. Yang, and L. Jiang, "Switchable wettability on cooperative dual-responsive poly-l-lysine surface," *Langmuir*, vol. 26, pp. 1024–1028, 2010.

[139] W. Sun, S. Zhou, B. You, and L. Wi, "A facile method for the fabrication of superhydrophobic films with multiresponsive and reversibly tunable wettability," *Journal of Materials Chemistry A*, vol. 1, pp. 3164–3154, 2013.

[140] B. Xin and J. Hao, "Reversibly switchable wettability," *Chemical Society Reviews*, vol. 39, pp. 769–782, 2010.

[141] A. Uyama, S. Yamazoe, S. Shigematsu, M. Morimoto, S. Yokojima, H. Mayama, Y. Kojima, S. Nakamura, and K. Uchida, "Reversible Photocontrol of Surface Wettability between Hydrophilic and Superhydrophobic Surfaces on an Asymmetric Diarylethene Solid Surface," *LANGMUIR*, vol. 27, pp. 6395–6400, MAY 17 2011.

[142] A. E. Pomerantz, M. R. Hammond, A. L. Morrow, O. C. Mullins, and R. N. Zare, "Two-step laser mass spectrometry of asphaltenes," *Journal of the American Chemical Society*, vol. 130, pp. 7216–7217, 2008.

[143] C. Becker, K. Qian, and D. H. Russel, "Molecular weight distribution of asphaltenes and deasphaltened oils studied by laser desorption ionization and ion mobility mass spectrometry," *Analytical Chemistry*, vol. 80, pp. 8592–8597, 2008.

[144] M. Jung, M. S. de la Lama, R. Seeman, and M. Brinkmann, "Two-phase flow in heterogeneious hele-shaw cells," research report, Max Planck Institute of Dynamics and Self Oraganisation, 2013.

[145] R.-V. Ostaci, D. Damiron, S. Capponi, G. Vignaud, L. Leger, Y. Grohens, and E. Drockenmuller, "Polymer brushes grafted to passivated silicon substrates using click chemistry," *Langmuir*, vol. 24, pp. 2732–2739, 2008.

[146] Xiaoling Wei and To Ngai, "Ion-induced hydrophobic collapse of surface-confined polyelectrolyte brushes measured by total internal reflection microscopy," *Polymer Chemistry*, vol. 3, pp. 2121–8, 2012 2012.

[147] S. Moya, A. Brown, O. Azzaroni, and W. Huck, "Following polymer brush growth using the quartz crystal microbalance technique," *Marcromolecular Rapid Communications*, vol. 26, pp. 1117–1121, 2003.

[148] J. I. Ramons and S. E. Moya, "Water content of hydrated polymer brushes measured by an in situ combination of a quartz crystal microbalance with dissipation monoitoring and spectroscopic ellipsometry," *Macromolecular Rapid Communications*, vol. 32, pp. 1972–1978, 2011.

[149] J. I. Ramos and S. E. Moya, "Effect of the density of ATRP thiol initiators in the yield and water content of grafted-from PMETAC brushes. a study by means of QCM-D and spectroscopic ellipsometry combined in a single device," *Macromolecular Chemistry and Physics*, vol. 213, no. 5, pp. 549–556, 2012.

[150] S. Minko, "Responsive polymer brushes," *Journal of Macromolecular Science, Part C: Polymer Reviews*, vol. 46, pp. 397–420, 2006.

[151] Y. Xu, A. Walther, and A. H. E. Mller, "Direct synthesis of poly(potassium 3-sulfopropyl methacrylate) cylindrical polymer brushes via atrp using a supramolecular complex with crown ether," *Macromolecular Rapid Communications*, vol. 31, pp. 1462–1467, 2010.

[152] A. Perl, D. N. Reinhoudt, and J. Huskens, "Microcontact printing: Limitations and achievements," *Advanced Materials*, vol. 21, pp. 2257–2268, 2009.

[153] R. A. Salathie, "Oil reovery by surface film drainage in mixed wettability rocks," *Journal of Petroleum Technology*, vol. 25, pp. 1216–1224, 1973.

[154] J. M. L. Michele M. Thomas, Jamie A. Clouse, "Adsorption of organic compounds on the carbonate minerals 1. model compounds and their influence on mineral wettability," *Chemical Geology*, vol. 109, pp. 201–213, 1993.

[155] M. Kumar, T. Senden, S. Latham, A. Sheppard, and M. . Knackstedt, "Designed for mixed wettability," *SPE Journal*, pp. 113862–71, 2008.

[156] J. Tavacoli, J. Thijssen, and P. Clegg, "A self-assembled automatic cartesian diver," in *Self Assembly- Soft Matter*, 2010.

[157] S. Jiang and S. Granick, "Controlling the geometry (janus balance) of amphiphilic colloidal particles," *Langmuir*, vol. 24, pp. 2438–2445, 2008.

[158] S. Horikoshi, Y. Akao, taku Ogura, H. Sakai, M. Abe, and N. Serpone, "On the stability of surfactant free water in oil emulsions and syntehsis of hollow SiO2 nanospheres," *Colloids and Surfaces, A: Physicochemical and Engineering Aspects*, vol. 372, pp. 55–60, 2010.

Acknowledgements

Firstly I would like to thank my thesis examiners Prof. Dr. Stephan Herminghaus and Prof. Dr. Gotz Eckold, and the members of my thesis committee for participating in the examination of my thesis. I would like to also acknowledge generous support from BP Exploration Operation Company Ltd. within the GeoMorph research project and the Max Planck Society for funding of my research.

I would like to thank my supervisor Matthias Schröter for help, advice and constant encouragement. Coming here, both to Germany and to a physics institute was a bit of a culture shock, so thank you for being patient with me, and helping me to catch up. I very much enjoyed the SMGM group meetings and retreats, which were as much full of laughter and fun, as serious science.

I would also like to thank my adopted supervisor Martin Brinkmann, whose ideas became the central point of this project and whose excitement and enthusiasm often overcame my reluctance to do something which seemed too difficult. Your help was often overwhelming but always appreciated.

Thanks goes incredibly much to Benoît Semin, with whom I worked, and who shared the trials and tribulations of some of these experiments. I couldn't have done it without you, and even though we spent a lot of time thinking it would never go anywhere, in the end it was worth it. I could always count on you for an honest appraisal of my work, and good advice.

I would like to thank Jean-Christophe Baret, for being a very enthusiastic and productive co-author on our paper, and helping me with writing the numerous reports during my time here. Thanks also for starting the runners group during the BP meetings.

I'm very grateful to Dr. Segio Moya, who hosted my in Spain at the BioMaGUNE in San Sebastien. Thank you to all the group members for making me feel welcome, and teaching me about Pinxo-Pote. Particular thanks goes to Joseba Irigoyen for the AFM measurements of the polymer brushes and Tanchen Ren for teaching me the polymer brush synthesis, and for the ellipsometry measurements.

Thanks goes to Wolf Keiderling and Udo Krafft for the design and building of the experimental CPS cells. Wolf, you were always so happy and helpful it was a joy to work with you. I would like to gratefully acknowledge Fabian Schaller who wrote the Bilimbi program used to calculate the Minkowski measures of the active interfaces, and Thomas Hiller and

Daniel Herde who wrote the program used to calculate the correlation length. I would also like to acknowledge Renaud Dufour for measurement of the contact angles on bead surfaces, and in particular the pinning of contact lines at wetting heterogeneities on janus beads and Cornelius Fischer for measuring the white light interferometry of the bead surfaces. I would also like to thank Mario Scheel for many useful discussions and advice.

To my wonderful proof readers, and there were a lot of you, Annika Döring, Thomas Hiller, Benoit Semin, Birte Riechers, Max Neudecker, Daniel Herde, Karsten Krüger, Logan Schultz, and Fabian Schaller, and of course my supervisors, thank you very much. I know it must have been tedious to read, sometimes multiple times, but I appreciated it, and the final result is all the better for it.

I'd like to thank my wonderful office mate Max: it was the best of times, it was the worst of times. But more often than not, we were laughing, so I guess we did all right. Our numerous conversations about grey values, the Nanotom filaments, latex hacks and German translations were put to good use, and I was proud that we had the best door in the institute. I would also like that thank our occasional office mate Karen for ever useful advice- from which image compression format was the best, to how maximise the impact factor of your CV, and where to find the best online knitting patterns. It was amazing and inspiring to have you as an office mate. Thanks also to the SMGM group (past and present) for useful discussions, and being a willing rent a crowd for practise talks.

To my friends, thank you for always being there for me. No one could get through this alone, and you support, love and encouragement, (and the occasional kick in the pants), was always much appreciated (eventually). I would like to thank Annika Döring, Kristian Dalle, Thomas Hiller, Jean-Francois Metayer, Birte Riechers, Fabian Schaller, and Shristi Upreti for significant enhancement of my non-scientific life.

And lastly, to my wonderful parents. Thank you for your constant love, support and belief in me. Without you I could have never come this far and I will always be grateful.